INVESTIGATING THE ROLE OF STRUCTURAL PARAMETERS INFLUENCING PHOTOCATALYTIC AND ELECTROCATALYTIC BEHAVIOUR OF BINARY AND TERNARY METAL OXIDES

ADITI VIJAY

A thesis submitted for the

partial fulfilment of the degree of Doctor of Philosophy

Institute of Nano Science and Technology Knowledge City, Sector 81, SAS Nagar, Manauli P.O., Mohali-140306, Punjab, India

Indian Institute of Science Education and Research (IISER) Mohali, Knowledge City, Sector 81, SAS Nagar, Manauli, P.O. 140306 Punjab, India.

May 2022

Dedicated to my lovely parents and husband for their continuing support, love, and encouragement

Declaration

The work presented in this thesis has been carried out by me under the guidance of Dr. Sonalika Vaidya at the Institute of Nano Science and Technology (INST) Mohali. This work has not been submitted in part or in full for a degree, a diploma, or a fellowship to any other university or institute. Whenever contributions of others are involved, every effort is made to indicate this clearly, with due acknowledgement of collaborative research and discussions. This thesis is a bonafide record of original work done by me. I have adequately cited and referenced the original sources.

Aditi Vijay

(Ph.D. Candidate)

In my capacity as the supervisor of the candidate's thesis work, I certify that the above statements by the candidate are true to the best of my knowledge.

Dr. Sonalika Vaidya

(Supervisor)

Scientist-D

Institute of Nanoscience and Technology, Mohali.

Acknowledgement

The completion of this thesis would not have been possible without the support and encouragement of some special people. Hence, I would like to take this opportunity to show my gratitude to those who have assisted me during my Ph.D. journey.

First of all, I would like to express my sincere gratitude to my Ph.D. supervisor, Dr. Sonalika Vaidya for her constant guidance, support and productive discussions throughout my Ph.D. journey. I am extremely grateful to my supervisor for her incredible patience, and continuous encouragement towards research.

I would like to thank my research committee members, Dr. Kamalakannan Kailasam and Dr. Ehesan Ali for their valuable suggestions during the yearly assessment.

I would like to acknowledge INST for providing financial support and instrumentation facility. I would like to express my sincere gratitude to Present Director, Prof. Amitava Patra and Past Director, Prof.A.K. Ganguli of INST for allowing me to pursue research at INST.

I would like to acknowledge our collaborators Dr. Ehesan Ali (Scientist-F at INST Mohali) and Aritra Mukhopadhyaya (INST Mohali) for performing theoretical studies in chapter 2, Prof. Santanu Pal (Associate Professor at Department of Chemical Sciences, IISER Mohali) for GISAXS study in chapter 4, Dr. Umberto Terranova (Lecturer in Chemistry and Physics at University of Buckingham) for performing theoretical studies (studies under progress) in chapter 4, Prof. K.V. Ramanujachary (Professor at Rowan University) and Prof. Samuel E. Lofland (Professor at Rowan University) for carrying out magnetic studies in chapter 6.

I would like to thank my present and past Labmates Dr. Pragya Shukla, Ruchi Verma, Anu Kumari, Shaswati Jyoti, Jasveer Kaur, Hitasha Shahi, Shanmuga Priya S, Ashwinder Kaur and Kadambari Bairagi for their support at the lab and fruitful scientific discussions.

Furthermore, I highly thank my friends at INST, Aashish Bhatt, Ashima Rawat, Ruby Gupta Soumadri Samanta, Venugopala Rao Battula, Sushil Kumar and Rimple Kalia for all the good times we spent at the INST campus and for helping me whenever I needed. I would like to thank

my best friend Akansha Tyagi for being there with me in every situation since our master's degree.

At last, I would like to thank my family for their constant support. My parents, Mr. Ram Prasad Vijayvergia and Mrs. Savitri Vijay, always encouraged me to pursue my dreams and supported me in good and bad times. They have taught me to be strong and courageous in every situation. I would also like to thank my brother, sister, and sister-in-law for their encouragement. I would also like to thank my parents-in-law for their incredible understanding and support throughout my Ph.D. journey. Finally, I would like to thank my husband Mr. Piyush Vijay for his unconditional love, kind support during tough times, and encouragement to do better. Words would never be enough to express how grateful I am to my husband for his patience and understanding.S

Table of Content

Chapter 2

Chapter 3

List of Tables

LIST OF FIGURES

Chapter 1

Introduction

Chapter 1

Introduction

1.1 Background:

1.1.1 Hydrogen - Imminent Fuel:

According to the world population forecast by United Nations in 2020[1] , the world's population is continuously expanding. The population of the world has raised almost three times since 1950. According to statistics (figure 1.1), the world's total population in 2020 was 7.75 billion and is expected to rise in the future decades, mainly because of the quick evolution of the developing countries. It is expected that the human population will exceed around 10.87 billion by 2100. The rise in the world's population over the decades and advancements in the new technologies has led to the rapid increase in the global energy demand and global warming.

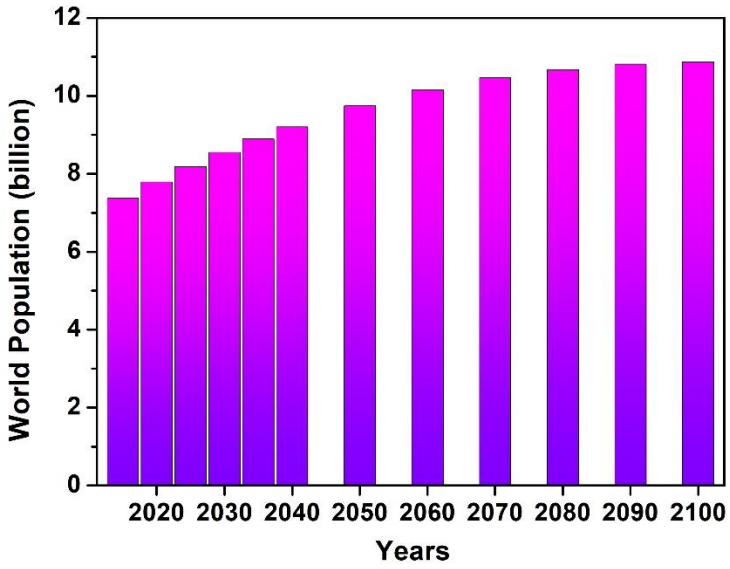

Figure 1.1 : World population statistics from 2015 to 2100 according to United Nations forecast.

The global energy consumption is projected to increase from 16 Terawatt (TW) in 2010 to 30 TW in 2050[2]. According to the renewable energy's global status report 2021, total energy consumption from 2009 to 2019 has increased from 320 ExaJoules to 382 ExaJoules. Out of the total energy consumption, the energy produced from fossil fuels which include coal, oil,

petroleum, and natural gas acquired a major part around 80.3% in 2009 (figure 1.2) and this percentage decreased to 0.1% in 2019. The share of renewable energy has moderately increased during this decade. This substantial reliance on fossil fuels for energy production is the major cause of their depletion and increase in global warming due to the emission of harmful gases such as CO_2. The slow progress in utilizing renewable energy resources to meet global energy demand is still a major concern. Therefore, there is an urge to develop clean and green renewable energy resources which can solve the energy and environmental-related issue and withstand for a longer duration.

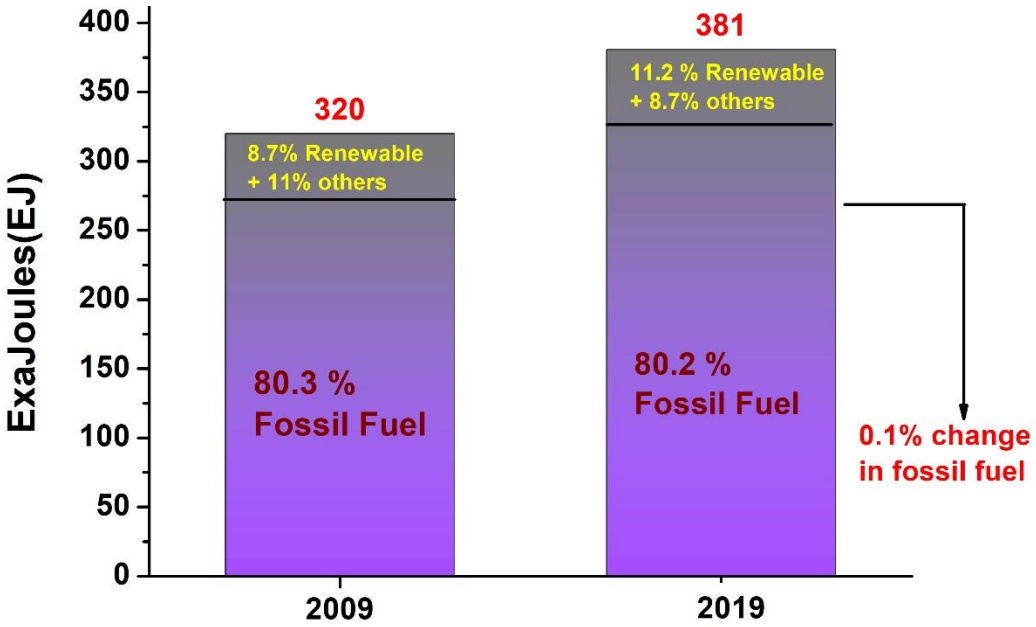

Figure 1.2 : Total Global Energy Consumption (including renewable energy share) in 2009 and 2019[2].

In this regard, Hydrogen has gained the world's attention as an alternative to fossil fuels for meeting global energy demand. It is a clean and green source of energy as it can be produced from renewable energy resources such as water which helps in shifting dependence from fossil fuels to infinite renewable resources of energy. Furthermore, hydrogen will help in controlling global warming by decarbonising the worldwide energy system.

There are several ways of producing hydrogen from fossil fuels and renewable energy resources. At present, hydrogen is mainly produced from petroleum and steam reforming of natural gas. The steam reforming process results in the emission of carbon dioxide gas. As water and the sun are the most abundant renewable resource available in the world, therefore utilizing them to produce hydrogen would be an appropriate strategy to tackle growing energy and environmental concerns. There are three possible ways through which hydrogen can be produced from renewable energy resources (figure 1.3):

1. Electrolysis of water (utilizing electricity produced from photovoltaics and wind energy etc.).
2. Water Splitting by Photocatalysis and Photoelectrochemical reactions by utilizing solar energy.
3. Biomass conversion (thermochemical).

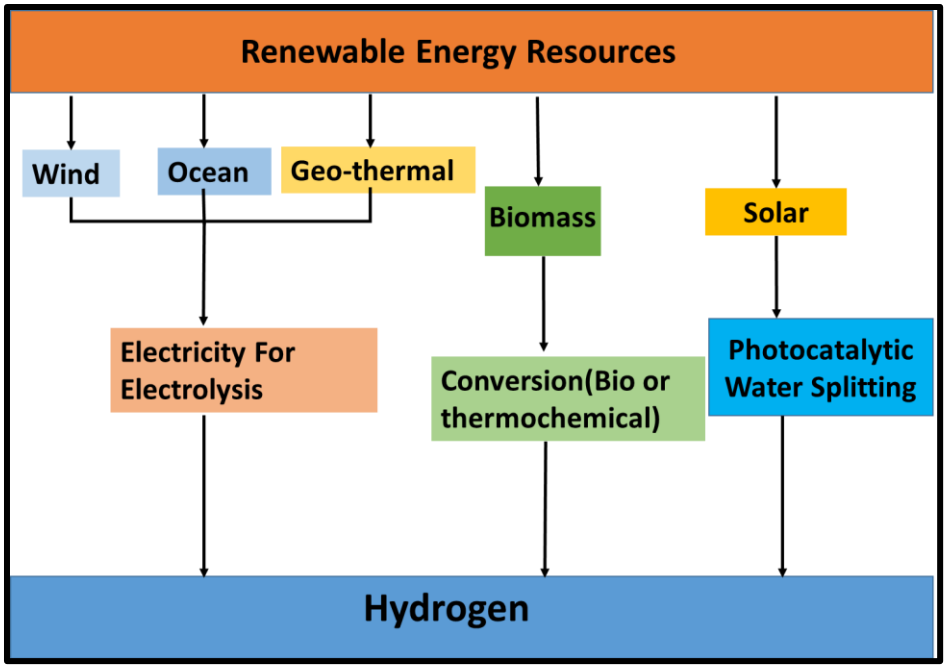

Figure 1.3 : Different ways of hydrogen production from renewable energy resources.

1.1.2 Water pollution and wastewater treatment:

The water resource is the most valuable natural resource for humankind as well as for plants and animals. Despite the abundance of water in nature (in the sea and oceans), drinking water is limited for humans. This is because most of the drinking water resources available are contaminated by rapid industrialization and global population growth. Thus, wastewater treatment has become one of the major concerns in the world.

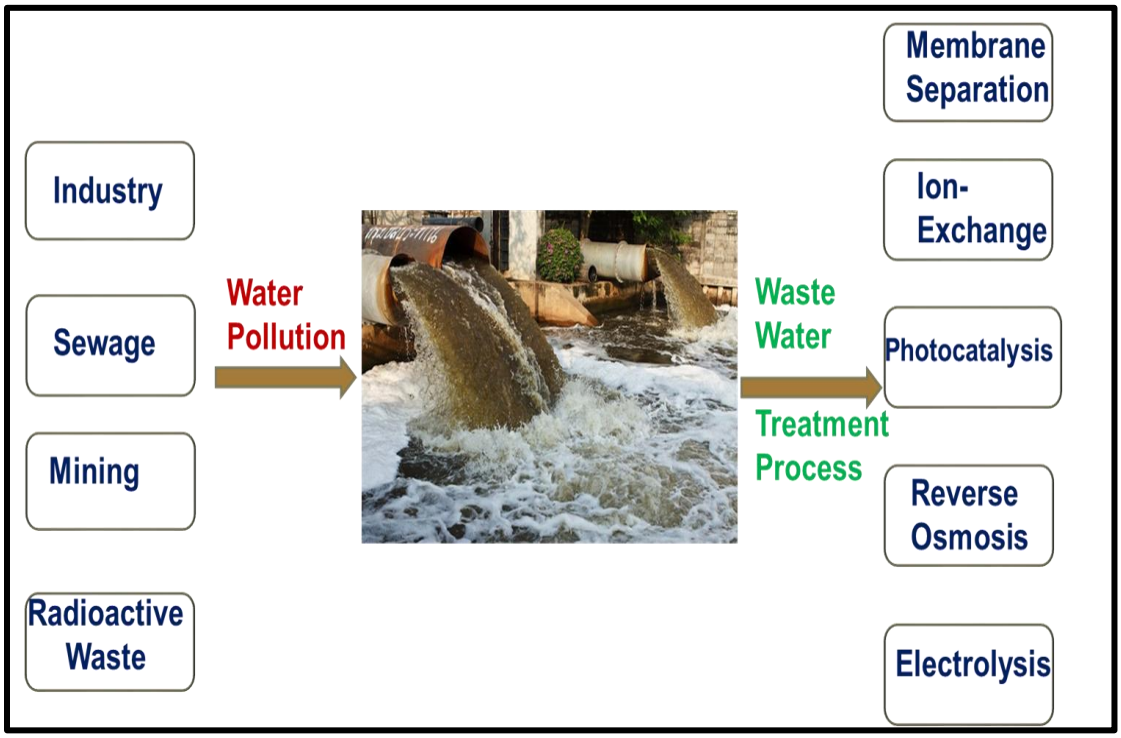

Figure 1.4: Sources of water pollution and effective treatment processes[3].

There are several sources of water pollution with major sources of pollution being industrial waste, sewage waste, mining waste, agricultural waste, marine dumping, nuclear waste, etc. (figure 1.4)[4]. Organic contaminants such as organic dyes contribute a major part to industrial waste towards water pollution.

During the past few decades, several techniques have been developed for the treatment of wastewater (figure 1.4). The conventional water treatment method includes filtration, membrane separation, and sedimentation technique which leads to the generation of secondary waste some of which contains toxic bacteria. Therefore, the development of green, clean and non-destructive techniques for the treatment of organic contaminants in the water is a need of the hour. In this

regard, Advanced Oxidative Processes (AOP)'s, which include O_3/UV and O_3/H_2O_2/UV treatment and Photocatalysis, have emerged as efficient techniques for wastewater treatment. Photocatalysis has several properties such as degradation or mineralization of organic pollutants, cost-effectiveness, reusability etc. which makes it a suitable technique for organic pollutant degradation.

Thus, from the above-discussed concerns regarding global energy and environmental issues, it can be concluded that Photocatalytic methods, for generating hydrogen and wastewater treatment and Electrochemical Methods for solving energy crisis (hydrogen and oxygen evolution which are used in fuel cells) have a great potential for solving the above-discussed issues. Hence, understanding their basic principle and accordingly designing the catalyst is of great importance.

1.2 Photocatalysis:

1.2.1 Photocatalytic water splitting:

Overall water splitting through UV-light induced electrolysis was first reported by Fujishima and Honda on TiO_2 electrodes in 1972[5]. Photocatalytic water splitting reaction termed artificial photosynthesis is an uphill reaction that requires Gibb's energy greater than 237 kJ to convert water into hydrogen and oxygen. Water can be split into hydrogen and oxygen by acquiring solar energy from the sun and chemical energy from semiconductor catalysts.

$$H_2O + \text{catalyst} \xrightarrow{h\nu} H_2 + O_2 \qquad (1.1)$$

In the Photocatalytic process, when the light of energy greater than the bandgap of the semiconductor is incident on the surface of the semiconductor, then the electron excites from the valence band to the conduction band of the semiconductor leaving the holes behind in the valence band. The excited electrons participate in the photo-reduction reaction at the conduction band. The entire process takes place in three main steps[6] (figure 1.5); i) generation of photo-induced charge carriers upon light irradiation, ii) separation of charge carriers and migration to their respective reaction site (holes at valence band and electrons at conduction band), simultaneously surfaces defects or other defects acts as recombination centres for photo-

generated charge carriers iii) photo-generated charge carriers participated in the reactions which occur at the surface of the catalyst.

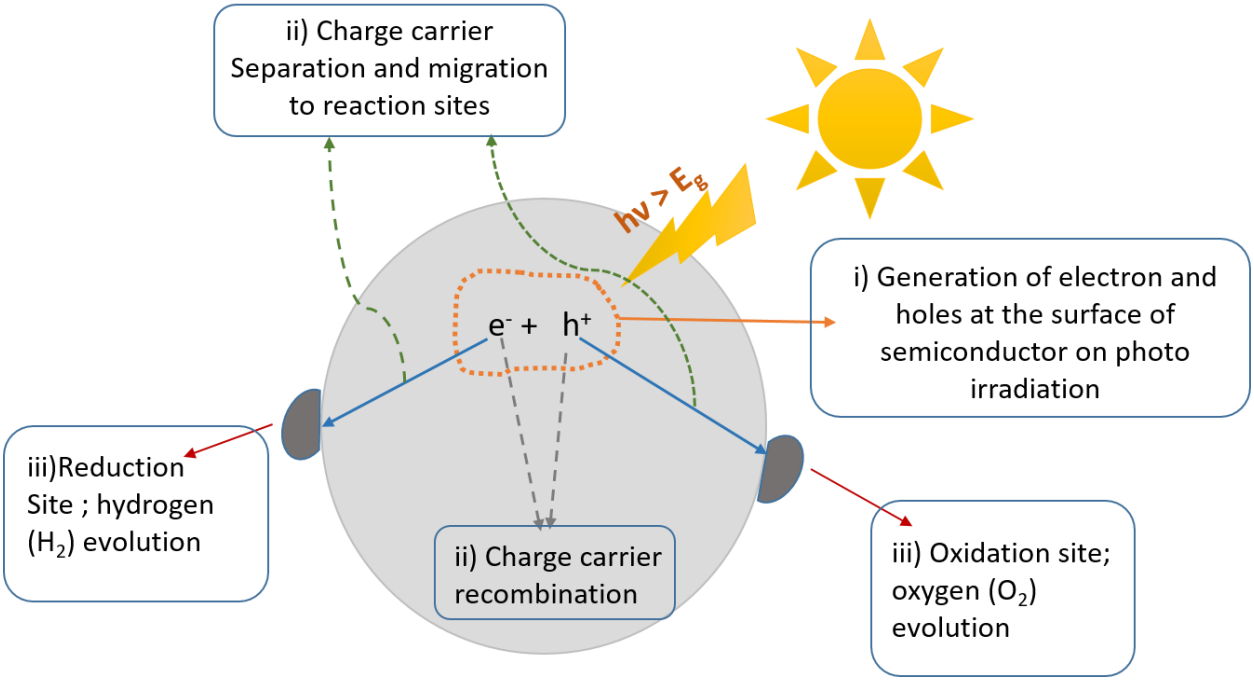

Figure 1.5: Process for Photocatalytic water splitting[6]

The water molecule is reduced by the electron present at the conduction band which leads to the formation of hydrogen, and H_2 whereas holes present at the valence band oxidize the water molecule to form O_2 for the overall water splitting reaction. The essential criteria for semiconductor photocatalyst for water splitting are to have a suitable bandgap and the band edge positions (conduction and valence band edge levels) vs NHE. For hydrogen evolution, the conduction band edge minimum position should be more negative than the redox potential for hydrogen (i.e. 0V vs. NHE (pH =0) whereas for oxygen evolution, the valence band maxima position should be more positive than the redox potential of oxygen 1.23 V vs. NHE (pH =0). Therefore, the minimum bandgap requirement or minimum photon energy required by semiconductor photocatalyst for water splitting is calculated to be 1.23 eV.

1.2.2 Photocatalytic degradation of Organic Contaminants:

Photocatalysis has proven to be one of the effective tools for the degradation of organic contaminants (such as dye) present in water caused by industrial waste. This process utilizes photon energy from the sun in presence of semiconductor catalysts (such as TiO_2) to speed up the process of degradation of organic contaminants. It is a thermodynamically downhill reaction, where Gibbs's free energy is negative ($\Delta G < 0$). There are mainly four kinds of the mechanism involved in the treatment of wastewater caused by the dye through photocatalyst, which includes a) Photo-decolourization, wherein the dye returns to its original form either through back reduction or oxidation process, b) Photo-degradation which involves decomposition of the dye to some other steady products. This process is generally termed as photocatalytic dye degradation, c) Photo-mineralization, in this case, there is the occurrence of complete decomposition of the dye into H_2O, CO_2, N_2 and NO_3^- etc., d) Photo-decomposition, where both the photo-degradation and photo-mineralization process occurred

Mechanism and basic principle:

There are mainly four steps involved in the photocatalytic dye degradation mechanism[7] (figure 1.6):

(i) When a light of energy (hν) incident on the surface of the semiconductor (SC) photocatalyst, then electrons(e^-) excite from the valence band (VB) to the conduction band (CB) leaving a hole behind in the valence band (h^+):

$$SC + h\nu \longrightarrow e^-(CB) + h^+(VB) \quad (1.2)$$

(ii) The holes (h^+) present at the valence band of the (VB) react with a water molecule to hydroxyl radical which has a superb oxidizing ability and reacts with adsorbed organic species (such as dye) to mineralize them.

$$H_2O + h^+(VB) \longrightarrow OH^\cdot + H^+ \quad (1.3)$$

(iii) The electrons e^- present at the conduction band (CB) react with dissolved oxygen to form superoxide radical ($O_2^{\cdot-}$). The superoxide radical ($O_2^{\cdot-}$) reacts with H^+ (hydrogen ion) to form hydroperoxyl radical ($HOO^\cdot$). After that successively formed hydrogen peroxide (H_2O_2) which further disassociates into hydroxyl radical ($OH^\cdot$).

$$O_2 + e^-(CB) \longrightarrow O_2^{\cdot -} \quad (1.4)$$

$$2O_2^{\cdot -} + 2H^+ \rightleftarrows 2HOO^{\cdot} \quad (1.5)$$

$$2HOO^{\cdot} \longrightarrow H_2O_2 + O_2 \quad (1.6)$$

$$H_2O_2 \longrightarrow 2OH^{\cdot} \quad (1.7)$$

(iv) Thus, both the hydroxyl radical present at conduction (CB) and valence band (VB) react with the dye molecule to dissociate it into various products such as water molecule (H_2O) or carbon dioxide (CO_2) or N_2 etc.

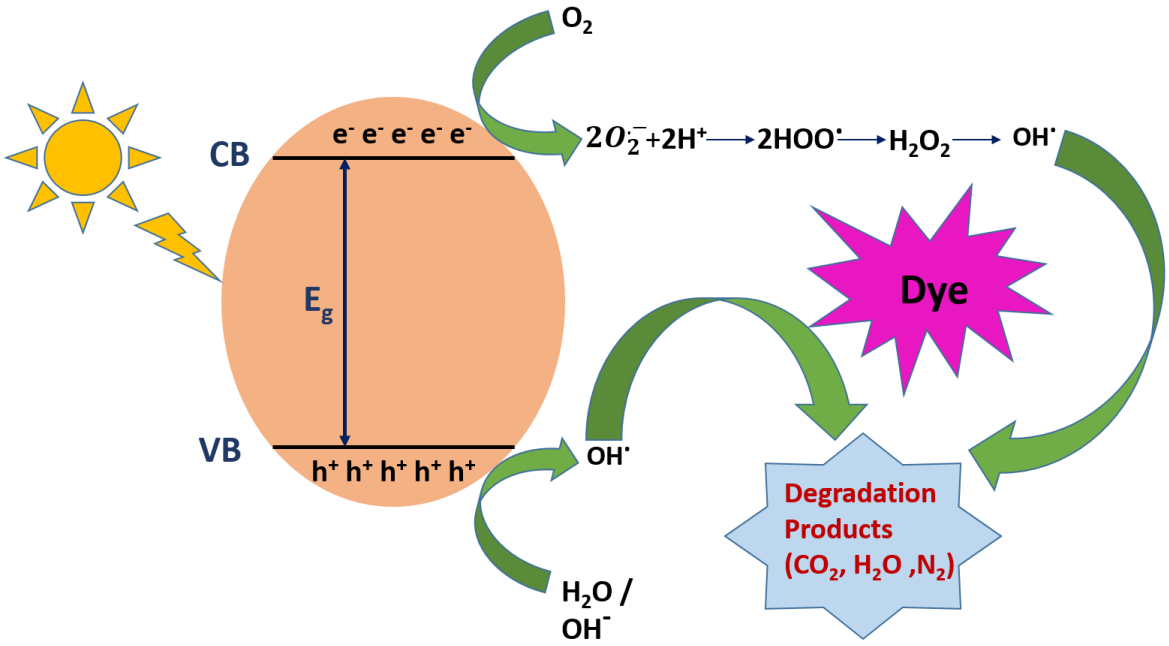

Figure 1.6: Photocatalytic dye-degradation mechanism on semiconductor photocatalyst.

During the past years, several photocatalysts have been developed for water splitting and dye degradation. TiO_2 has proven to be among the highly active photocatalyst over the decades due to its high photochemical stability and abundance[8]. TiO_2 has been modified to utilize the visible-light spectrum of the solar radiation using various methods such as deposition of metal (Pt, Pd and Ni) on the catalyst surface[9, 10], coupling with carbon nanomaterials (such as carbon nanotubes, carbon dots, graphene and g-C_3N_4 etc.)[11] and by the formation of binary composites with other metal oxides and metal dichalcogenides[12]. Several other metal oxides such as ZnO, Bi_2O_3, Bi_2WO_6, Nb_2O_5a and γ-Fe_2O_3 have shown good photocatalytic activity[13]. $SrTiO_3$ has

emerged as a highly efficient catalyst for overall water splitting when doped with Al [14,15]. Metal oxides such as WO_3[16], α-Fe_2O_3[17] and $BiVO_4$[18] are the most stable oxygen evolution photocatalyst due to high photochemical stability. $BiVO_4$ with a monoclinic crystal structure was observed to be highly active in water oxidation activity[19]. Lately, CoO nanoparticles[20] have been discovered as an efficient catalyst for overall water splitting without any co-catalyst. Several metal sulfides[21] (highly exposed to photo-corrosion), nitrides[22], oxysulfides[23] and metal oxynitrides[24] have been discovered as good photocatalysts. Metal oxide semiconductors have several advantages over others such as low cost, high abundance, high reusability, low toxicity and tunability. It has been observed that co-catalysts play an important role in improving overall splitting reaction. But the high cost of metal co-catalyst limits the practical use of several photocatalysts. *Therefore, developing a highly efficient catalyst without any metal co-catalyst is extremely required. In the present thesis, the focus is on studying the catalytic activity without any metal co-catalyst.*

1.3 Electrochemical Water Splitting:

Water electrolysis was first reported in 1789[25], since then it has been studied and applied broadly to form hydrogen efficiently with high purity. Electrochemical water splitting consists of two half–cell reactions, hydrogen evolution reaction (HER) occurring at the cathode and oxygen evolution reaction occurring at the anode (figure 1.7). Decomposition of water in hydrogen and oxygen is not a thermodynamically feasible process at ambient pressure and temperature but with the application of energy in the form of electricity, water splitting follows the given reactions;

i) In Acidic Condition:

At anode: $H_2O \longrightarrow O_2\,(g) + 4e^- + 4H^+$ ……... $E^o_{ox} = 1.23$ V (1.8)

At cathode: $2H^+ + 2e^- \longrightarrow H_2\,(g)$……. $E^o_{red} = 0$ V (1.9)

ii) In Alkaline Condition:

At anode: $4OH^- \longrightarrow O_2\,(g) + 4e^- + 2H_2O$ ……. $E^o_{ox} = 0.463$ V (1.10)

At cathode: $4H_2O + 4e^- \longrightarrow 2H_2\,(g) + 4OH^-$ ……. $E^o_{red} = -0.767$ V (1.11)

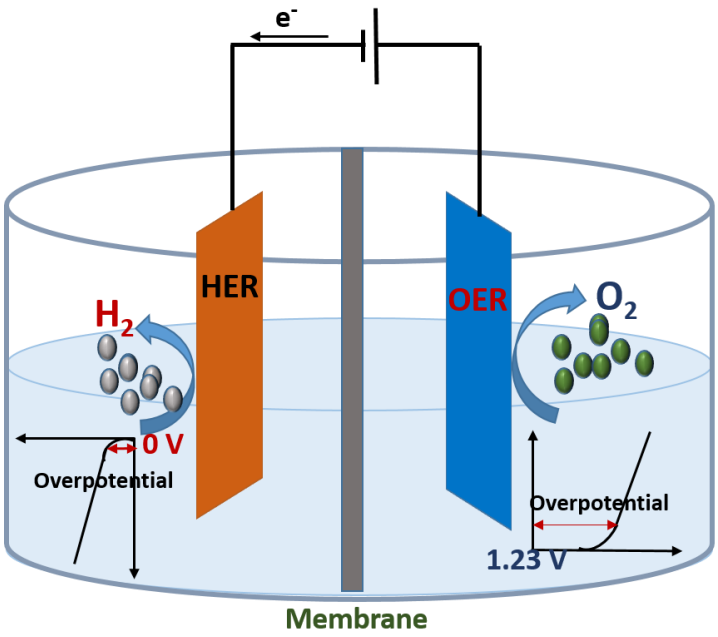

Figure 1.7: Schematic illustration of electrochemical water-splitting reaction.

From the equations for water splitting in acidic reaction (equations 1.8 and 1.9), it can be seen that OER (oxygen evolution reaction) is a four electron-proton coupled reaction whereas HER is a two-electron transfer process. OER requires a higher oxidation potential for the water-splitting reaction to proceed when compared with HER. Thus, the sluggish kinetics of OER creates a large energy barrier for overall water splitting to occur. Therefore, to improve the overall kinetics of the electrocatalytic water-splitting reaction, the main focus should be to reduce the higher overpotential for the OER reaction.

1.3.1 Electrocatalyst for Electrochemical Hydrogen Evolution Reaction (HER):

HER is one of the half-reactions of water electrolysis that occurs at the cathode. It is a two-electron transfer process. HER mechanism is highly dependent on the environment of the reaction set-up (such as the pH of the electrolyte).

In acidic conditions, there are three main processes namely, Volmer, preceded by Heyrovsky or Tafel steps followed during HER (equation 1.12, 1.13, and 1.1.4):

a) Volmer Step:

$$H^+ + e^- \longrightarrow H_{ad} \quad (1.12)$$

b) Heyrovsky step:

$$H^+ + e^- + H_{ad} \longrightarrow H_2 \quad (1.13)$$

c) Tafel step:

$$2H_{ad} \longrightarrow H_2 \quad (1.14)$$

In basic or alkaline conditions, two possible steps are given below:

a) Volmer Step:

$$H_2O + e^- \longrightarrow OH^- + H_{ad} \quad (1.15)$$

b) Heyrovsky step:

$$H_2O + e^- + H_{ad} \longrightarrow OH^- + H_2 \quad (1.16)$$

Here, H_{ad} denotes hydrogen adsorbed on the surface of the catalyst or at the reaction site.

There are two main kinds of electrocatalyst used for HER, a) precious noble metal-based catalyst and b) Non-noble based catalyst.

a) Noble metal-based catalyst for HER:

The noble metal-based catalyst for electrocatalytic HER includes noble metals such as Pt, Pd, Ru, Ir and Rh[26]. Amongst these, Pt shows remarkably high hydrogen evolution performance than other metal catalysts. However, these catalysts have limitations for their use in the commercial field (due to their high cost and storage issues). Therefore, to improve the usability of the noble metal-based catalyst, the focus has been shifted to using them with other transition metal-based catalysts. . Duan et al[27] have achieved remarkable enhancement in HER activity by alloying Pt nanowires with single-atom Ni. Subbaraman et. al[28]. have performed electrochemical HER on $Ni(OH)_2$ modified Pt surface and observed an eight-time increase in the efficiency of the HER. Another way to improve the alkaline efficiency of the metal-based catalyst is doping Pt with some other metal. Xie et.al[29] have synthesized N-Pt/Ni nanowires for HER and observed a very low overpotential of 13 mV at 10 mA/cm^2

b) Non-noble metal-based catalysts for HER:

Due to the high cost of Pt-based noble metal catalyst, the most abundant transition metal catalyst has been developed over the last few decades for electrocatalytic hydrogen evolution reactions. The non-noble metal-based catalyst consists of earth-abundant transition metals such as Co, Fe, Ni, W, Cu, and Mo[30, 31]. Miles et. al[32] reported that the catalytic activity of the transition metal oxides follows the order: Ni > Mo > Co > W > Fe > Cu. It has been reported that nickel-based alloys[33] are proven to be a good catalyst for electrochemical hydrogen evolution reaction due to several advantages such as cost-effectiveness, better corrosion resistance in basic media and competition with a noble metal catalyst in terms of activity. There are several binary and ternary alloys[34, 35, 36] that have been synthesized in this regard, NiMo, NiCo, NiZn, NiCr and NiFe etc. Among these, NiMo is found to be the better catalyst based on high activity, good stability and low charge-transfer resistance[37]. Apart from metal alloys, transition metal carbides[38] (such as MoC_2, WC, WC_2 and V_8C_7 etc.) transition metal phosphides[39] (Ni_2P, CoP, Co_2P, FeP, MoP etc.) and dichalcogenides[40 ,41] (MoS_2, $MoSe_2$, $MoTe_2$, WS_2, WSe_2 and WTe_2) have been developed for achieving high catalytic efficiency.

Several binary and ternary metal oxides including perovskite oxides, spinel oxides, ox hydroxides and hybrids containing oxides semiconductors have also emerged as good electrochemical HER catalyst[42]. Transition metal oxides[42] include WO_3, CoO, NiO and MoO_2 etc, spinel oxides[43] include Co_3O_4, $NiCo_2O_4$[44], $CoFe_2O_4$[45] and perovskite oxides (ABO_3) including $Ba_{0.5}Sr_{0.5}Co_{0.8}Fe_{0.2}O_{3-\delta}$[46] etc. have showed improved HER activity. Despite having lower catalytic activity, and electronic conductivity compared to metal-based catalysts, oxides have several advantages[42] such as low cost, structure diversity, easy synthesis and tunability which makes them one of the most efficient groups of catalysts for electrocatalytic HER.

1.3.2 Electrocatalyst for Electrochemical Oxygen Evolution Reaction (OER):

OER is another half-reaction of the overall water splitting reaction that occurs at the anode consisting of four electron-proton coupled reactions and has a high energy barrier ie.1.23 V which makes the OER reaction kinetically slow. OER consists of two kinds of pathways[47] for the production of molecular oxygen which involves adsorption of hydroxide (OH_{ads}) on the surface of the catalyst (*). In alkaline media, OER follows steps (from 1.17- 1.21):

$$OH^- + * \longrightarrow OH_{ads} + e^- \quad (1.17)$$

$$OH_{ads} + OH^- \longrightarrow O_{ads} + H_2O + e^- \quad (1.18)$$

First pathway:

$$O_{ads} + O_{ads} \longrightarrow O_2 \quad (1.19)$$

In the second pathway,

$$O_{ads} + OH^- \longrightarrow OOH_{ads} + e^- \quad (1.20)$$

$$OOH_{ads} + OH^- \longrightarrow O_2 + H_2O + e^- \quad (1.21)$$

Generally, the second pathway is more thermodynamically favoured for oxygen evolution in comparison to the first pathway. In acidic conditions, OER takes place in the following steps (from 1.22 -1.25);

$$2H_2O + * \longrightarrow OH_{ads} + H_2O + e^- + H^+ \quad (1.22)$$

$$OH_{ads} + H_2O \longrightarrow O_{ads} + H_2O + e^- + H^+ \quad (1.23)$$

$$O_{ads} + H_2O \longrightarrow OOH_{ads} + e^- + H^+ \quad (1.24)$$

$$OOH_{ads} \longrightarrow O_2 + e^- + H^+ \quad (1.25)$$

The main prerequisite for a material to be a better OER electrocatalyst is to have lower strength of the metal-OH bond, low cost, and stability in alkaline media. Highly active electrocatalysts for OER are mainly Ir and Ru based oxides such as IrO_2 and RuO_2 as they exhibit higher catalytic activity in alkaline electrolyte media. In addition to the noble metal-based catalysts which are highly expensive, research is going on for developing cost-effective metal oxide OER catalysts with higher stability. Recently, transition metals (Ni, Mn, Co and Fe) based oxides have gained popularity as an efficient catalyst for electrochemical OER. As OER activity depends on the M-OH bond strength, therefore OER activity of the transition metal hydroxy-oxides follows the order Ni > Co > Fe > Mn[48]. It has been reported that $NiFeO_x$ and $CoFeO_x$ are found to be the most active, non-noble metal-based and stable catalysts for OER in alkaline media[49, 50]. Due to the presence of an extended σ* band, perovskite oxides[51] such as $SrCoO_3$[52], $LaNiO_3$[53] and $LaMnO_3$[54] are the superior catalysts for OER. Spinel transition metal oxides[55] such as Co_3O_4, $ZnCo_2O_4$, $NiCo_2O_4$ and $MnCo_2O_4$ catalysts are considered to be one of the most efficient OER

catalysts where the presence of cations in octahedral sites determine the efficiency of OER catalyst.

As the slow reaction mechanism of OER limits the overall efficiency of water splitting, therefore it is important to focus on developing a catalyst with lower overpotential for OER.

1.4 Role of structural parameters in enhancing HER and OER efficiency of the photo- and electrocatalyst:

In recent past years, there has been the development of many novel catalysts discussed in sections 1.2 and 1.3 for both HER and OER. Several structural parameters are also responsible for affecting the photo- and electro-catalytic efficiency of the catalyst. Modification based on these parameters can improve the activity of the catalyst. These structural parameters include the size and morphology of the catalyst, surface area of the catalyst, the bandgap of the catalyst, crystal structure of the catalyst, exposed facets on the catalyst surface, preferred orientation along with a particular crystal plane (oriented assemblies) etc. Several external factors such as electric polarization, magnetic polarization, metal co-catalyst leading, type of scavenger or electrolyte used also affect the rate of the catalytic reaction.

1.4.1 Effect of size:

The size of the catalyst plays an important role in photocatalysis and electrocatalysis as catalysis is a surface phenomenon. Compared to the bulk catalyst, the nano-sized catalyst provides a higher surface to volume ratio, allowing a large number of reactants (or more reaction sites) to react at the surface simultaneously. Transport of charge carriers from bulk to the surface is also increased by decreasing the size of the catalyst in the nano-regime[56]. Photon absorption is increased in smaller size particles which is supposed to enhance the photocatalytic activity of the catalyst. However further decrease in particle size to quantum dots leads to photon scattering, thus decrease in photocatalytic activity.

Jakub Jirkovský et.al[57] mentioned that electrocatalytic oxygen evolution performance on $Ru_{0.8}Co_{0.2}O_{2-x}$ was observed to be higher in the case of smaller particle size of the catalyst which could be due to the presence of more number of reaction sites. Sanjit Saha et.al.[17] reported

that the smaller size of the particle is advantageous for electrocatalytic HER activity due to an increase in the facile flow of the electrolyte through the pores of the catalyst. However, a further decrease in the particle size from 30 nm to 12 nm led to an increase in the electrical conductivity and HER onset potential due to an increase in the bandgap energy as a result of quantum confinement. In another report by Towsend et.al.[58], the authors reported overall water splitting over nanoscale strontium titanate through photochemical and photo-electrochemical ways. They observed that when the size of the $SrTiO_3$ nanoparticles was reduced below 30 nm, the activity of the catalyst suddenly reduced which is a consequence of lower photon absorption and sluggish water oxidation potential.

1.4.2 Effect of morphology:

The morphology of the catalyst plays a critical role in increasing the efficiency of the catalyst and enables one to design the catalyst for a specific application. Specific surface area can be increased by changing the morphology which leads to an increase in the active site on the surface of the catalyst, thereby increasing the photocatalytic activity. Different morphologies of the catalyst have been designed for HER[59, 60], OER[61] and overall water splitting[62] of the catalyst.

Bora Seo et.al[63] reported that spherical shaped Ni_2P nanoparticles exhibited higher hydrogen evolution activity when compared with rods shaped morphology of Ni_2P. Meshram et.al[64] synthesized CuO with different morphologies such as spherical, platelet, sheet, and vesicular like structures and studied their photocatalytic performance. They observed that platelet-like morphology possesses a higher surface area and exhibited higher photocatalytic dye degradation efficiency than other morphologies. Zhang et al.[65] demonstrated that WO_3 nanorods delivered lower overpotential i.e. 83 mV for electrocatalytic hydrogen evolution reaction when compared with microplates morphology. Xu et al.[66] observed that VSe_2 with flakes –kind of morphology delivers high catalytic activity for hydrogen evolution reaction as compared to 1D nanobelt shaped structure. Swati Mohan et.al[67] studied electrochemical OER activity on different morphologies of IrO_2 nanostructures viz, nanoparticles, nanocubes and nanorods. They observed high OER activity for IrO_2 nanorods due to high electrochemical surface area, higher stability and low charge transfer resistance.

1.4.3 Effect of Crystal structure:

The crystal structure of the semiconductor affects the electronic band structure that can alter the bandgap or band positions of the semiconductor. Also, different surface arrangements of the atoms lead to a difference in adsorption of reactant molecules at the surface of the catalyst, charge separation and reduction abilities in surface reactions[68]. Therefore, several investigations were made on modifying the crystal structure and electronic structure of the catalyst for improving photo-and electrocatalytic activity.

Peng Li et.al[69] synthesized two different crystal structures viz. orthorhombic and cubic of perovskite $NaNbO_3$ to see their effect of them on photocatalytic hydrogen evolution activity. They observed higher photocatalytic activity in the case of cubic-$NaNbO_3$ compared to orthorhombic-$NaNbO_3$ which is because cubic-$NaNbO_3$ possesses a more dispersive conduction band than orthorhombic-$NaNbO_3$.This resulted in higher migration of photoinduced electrons. Changhong Wang et.al[70] reported the role of crystal structure in enhancing electrocatalytic oxygen evolution performance of hcp-Ni@NC in comparison to fcc-Ni@NC structures which could be due to change in the electronic state of the shell. It has been reported by Guan-Qun Han et.al[71] that the alpha phase of MnO_2 (α- MnO_2) nanostructures are more active for electrochemical oxygen evolution in comparison to the beta phase (β- MnO_2) due larger intrinsic activity of each manganese(Mn) atom in alpha (α- MnO_2) phase than beta phase (β- MnO_2). Cátia L.Ücker et.al[72] reported that pseudohexagonal type Nb_2O_5 showed better dye-degradation efficiency than the orthorhombic structure which is due to the low crystallinity and high surface area of pseudohexagonal type Nb_2O_5.

1.4.4 Effect of Exposed Facets:

The properties of a catalyst are highly dependent on the nature of exposed surfaces as it involves the arrangement of atoms on the surface and their coordination[73]. Adsorption and reduction of water molecules depend on the surface energy of the particular facet which could further improve the reaction rates. Moreover, oxidation and reduction reactions occurring at different facets improve charge separation efficiency and thus photocatalytic activity. Therefore, designing a catalyst with a specific crystal facet becomes remarkably essential.

Li Liu. Et al[74] synthesized Co_3O_4 crystals with four exposed crystal facets viz. {111}, {112}, {001}, {110} and studied their overall electrocatalytic water-splitting reaction. Co_3O_4 with {111} facet as exposed facet was found to have more active Co^{3+}, high surface energy and larger dangling bond density which resulted in higher activity both for HER and OER. Moussab Harb. et al.[75] investigated the impact of the exposed facets (including (010), (110), (001), and (121)) of $BiVO_4$ on photocatalytic water-splitting reaction. From DFT based calculations, the authors have predicted that the (001) surface of $BiVO_4$ is highly active for both hydrogen and oxygen evolution reactions whereas the (010) surface is only active for OER reaction. It has been reported[76] that hexagonal-WO_3 nanorods with (200) exposed facets showed better photocatalytic dye degradation activity than hexagonal-WO_3 nanosheets with (001) exposed facets due to high surface area and photo-induced charge separation. Jianan Li et.al.[77] reported that the development of facet junction between {001} and {111} facet in $ZnFe_2O_4$ nanoparticles improves the charge separation by reducing the recombination rate of photo-induced charge carriers thereby enhancing the photocatalytic degradation efficiency over gaseous toluene. Therefore, designing previously discovered catalysts with preferably exposed facets would be an effective strategy for regulating catalytic activity.

1.4.5 Effect of the electric Polarization:

The presence of the internal field within the crystal changes the band bending at the interfaces and provides a driving force for the separation of photogenerated electrons and holes which helps in improving the catalytic efficiency of the catalyst. The application of an external electric field or electrical polarization helps in further transfer of charge carries to opposite reaction sites and enhances the adsorption capacity of the charged ions on the surface. The role of electrical polarization is still not fully utilized in all aspects of photo and electrocatalysis, therefore utilizing external electric polarization would be an efficient strategy for designing the catalyst.

Yongfei Cui et.al[78] reported the photocatalytic dye decolourization activity of $BaTiO_3$ as a catalyst and observed that ferroelectric $BaTiO_3$ showed better catalytic activity than non-ferroelectric $BaTiO_3$ which could be due to the separation of photo-induced charge carriers as a result of the creation of space charge layer. Sangbaek Park et al.[79] studied the role of ferroelectric $K_{0.5}Na_{0.5}NbO_3$ catalyst on photocatalytic hydrogen evolution activity. They have observed a 7-fold increment in the hydrogen evolution activity in the case of polarized catalyst (polarized with

the help of the corona poling technique) which could be due to the presence of an internal dipole field resulting in the separation of charge carriers. Xiaoning Li et al.[80] reported the effect of ferroelectric polarization in enhancing electrochemical oxygen performance of $Bi_4Ti_3O_{12}\cdot(BiCoO_3)_2$ catalyst, where they observed a significant decrease in the overpotential value after polarization. They have explained these results based on improved charge adsorption capability in poled surfaces. H. S. Kushwaha et.al[81] reported the ferroelectric forward polarization enhanced electrochemical oxygen evolution performance of $Bi_{0.5}Na_{0.5}TiO_3$ catalyst. The increase in OER activity is observed mainly due to enhanced charge separation, adsorption of charged species on the surface of the poled catalyst and the reduction in charge transfer resistance, due to band bending in the poled catalyst. Thus, these studies suggest that ferroelectric polarization is a valuable strategy for improving catalytic activity.

Thus, it can be concluded that the photo-and electrocatalytic activity of the already discovered catalyst could be enhanced with proper modification in the structural parameters described above.

1.5 Aim of the thesis:

- As outlined in sections 1.1, 1.2 and 1.3, Photocatalytic and Electrocatalytic ways to generate alternative sources of energy i.e. Hydrogen Energy and removal of organic contaminants from water are important to solve the present energy crisis and water pollution problem. Thus, designing a highly active catalyst for hydrogen evolution and treating water pollution is the need of the hour. As water oxidation reaction limits the overall water splitting reaction due to its high overpotential, hence developing an efficient OER catalyst with low overpotential is also important.
- Since many past decades, several novel catalysts have been discovered for improving the efficiency of the catalyst which include noble metal, metal oxides, sulfides, carbides, nitrides and many more. Despite having low catalytic performance, binary and ternary metal oxides have emerged as the most stable, highly resistant to photo-corrosion, cost-efficient and abundant catalyst. As described in section 1.4, the designing of the catalyst includes several structural parameters and modification of which affects the catalytic

performance of the catalyst. Thus, the catalytic efficiency of the already developed metal oxides could be improved with the proper modification of the structural parameters.

- Thus, the objective of the present thesis is to establish the relationship between the influence of the structural parameters of the catalyst with the Photo- and Electrocatalytic activity of binary and ternary metal oxides for developing an efficient catalyst for the desired application.

1.6 Thesis Outline:

The present thesis is divided in to seven chapters including an introduction, experimental findings, results and a conclusion. A brief description of the chapters is given below;

Chapter 1 gives a basic introduction to fulfilling growing energy demand and remediation of water pollution through photo- and electrocatalytic water splitting and the role of various parameters influencing the catalytic reaction rate.

Chapter 2 entitled "Understanding the role of ionic flux on the polarity of the exposed surfaces of ZnO and its correlation with Photocatalytic dye degradation activity" provides a basic understanding of the growth of exposed surfaces in ZnO structures through the introduction of various monovalent and divalent fluxes such as NaCl, KCl, NaCl-KCl (eutectic-mixture), Na_2SO_4. The correlation between photocatalytic dye degradation activity and the nature of exposed surfaces was used to see the effect of ionic flux on the formation of exposed surfaces. DFT based theoretical calculations were also done to understand the role of surface energy in the growth mechanism of a particular facet evolved by the introduction of fluxes.

Chapter 3 gives an understanding on the synergism of several factors such as size, morphology, surface area and exposed facets in influencing the photocatalytic hydrogen evolution and dye degradation performance of $SrTiO_3$ nanostructures (synthesized using various polyols (including EG, PEG-300, PEG-400 and water) as a solvent in solvothermal reaction). Photoluminescence and photocurrent studies were also done to study the behaviour of photo-induced charge carriers in different $SrTiO_3$ nanostructures.

Chapter 4 describes the role of the oriented assembly of $SrTiO_3$ nanostructures along the (200) plane on the photocatalytic hydrogen evolution activity. Here, assembled structures of previously

synthesized (cube-shaped $SrTiO_3$ nanostructures synthesized in chapter 3) $SrTiO_3$ nanostructures were formed on glass substrate by functionalizing either glass substrate or $SrTiO_3$ nanostructures with IPTMS (3-iodo-propyl trimethoxysilane) as a linker and studied their role in enhancing photocatalytic hydrogen evolution reaction.

Chapter 5 of the thesis is focused on the role of different crystal structures in $Sr_{n+1}Ti_nO_{3n+1}$ (n= 1,2 and ∞) series on photocatalytic hydrogen evolution activity. Here, two types of structures namely the perovskite phase in $SrTiO_3$ (n =∞) and the Ruddlesden-popper phase in Sr_2TiO_4 (n= 1) and $Sr_3Ti_2O_7$ (n= 2) were synthesized through a modified hydrothermal method followed by calcination and studied their effect on photocatalytic hydrogen evolution performance.

Chapter 6 entitled "Role of crystal structure and electrical polarization of an electrocatalyst in enhancing Oxygen Evolution performance: Bi-Fe-O system as a case study'' described the effect of the different crystal structures of the Bi-Fe-O system (viz. rhombohedral crystal structure of $BiFeO_3$, orthogonal crystal structure of $Bi_2Fe_4O_9$ and cubic structure of $Bi_{25}FeO_{40}$) electrochemical oxygen evolution activity. As electrical polarization affects the adsorption capacity of charged ions on the surface of the catalyst and polarization also depends on the type of crystal structure, therefore we have also studied the effect of electrical polarization on oxygen evolution performance of three oxides viz., $BiFeO_3$, $Bi_2Fe_4O_9$ and $Bi_{25}FeO_{40}$.

Chapter 7 gives the summary of all experimental chapters and future prospects of the studies carried out in this thesis.

1.7 References:

1. Szmigiera, M. World population - forecast about the development 2015-2100. https://www.statista.com/statistics/262618/forecast-about-the-development-of-the-world-population/.
2. REN21, Renewable 2021 Global Status Report. **2021**.
3. Sharma, S.; Bhattacharya, A., Drinking water contamination and treatment techniques. *Applied Water Science* **2017,** *7* (3), 1043-1067.
4. Nathanson, J. A., water pollution , https://www.britannica.com/science/water-pollution. **2022**.
5. Fujishima, A.; Honda, K., Electrochemical Photolysis of Water at a Semiconductor Electrode. *Nature* **1972,** *238* (5358), 37-38.
6. Kudo, A.; Miseki, Y., Heterogeneous photocatalyst materials for water splitting. *Chemical Society Reviews* **2009,** *38* (1), 253-278.
7. Ajmal, A.; Majeed, I.; Malik, R. N.; Idriss, H.; Nadeem, M. A., Principles and mechanisms of photocatalytic dye degradation on TiO_2 based photocatalysts: a comparative overview. *RSC Advances* **2014,** *4* (70), 37003-37026.
8. Pulido Melián, E.; González Díaz, O.; Ortega Méndez, A.; López, C. R.; Nereida Suárez, M.; Doña Rodríguez, J. M.; Navío, J. A.; Fernández Hevia, D.; Pérez Peña, J., Efficient and affordable hydrogen production by water photo-splitting using TiO_2-based photocatalysts. *International Journal of Hydrogen Energy* **2013,** *38* (5), 2144-2155.
9. Ismail, A. A., Mesoporous PdO–TiO_2 nanocomposites with enhanced photocatalytic activity. *Applied Catalysis B: Environmental* **2012,** *117-118*, 67-72.
10. Huang, B.-S.; Chang, F.-Y.; Wey, M.-Y., Photocatalytic properties of redox-treated Pt/TiO_2 photocatalysts for H2 production from an aqueous methanol solution. *International Journal of Hydrogen Energy* **2010,** *35* (15), 7699-7705.
11. Al Mayyahi, A.; Everhart, B. M.; Shrestha, T. B.; Back, T. C.; Amama, P. B., Enhanced charge separation in TiO_2/nanocarbon hybrid photocatalysts through coupling with short carbon nanotubes. *RSC Advances* **2021,** *11* (19), 11702-11713.
12. Park, H.; Park, Y.; Kim, W.; Choi, W., Surface modification of TiO_2 photocatalyst for environmental applications. *Journal of Photochemistry and Photobiology C: Photochemistry Reviews* **2013,** *15*, 1-20.
13. Riente, P.; Noël, T., Application of metal oxide semiconductors in light-driven organic transformations. *Catalysis Science & Technology* **2019,** *9* (19), 5186-5232.
14. Zhao, Z.; Goncalves, R. V.; Barman, S. K.; Willard, E. J.; Byle, E.; Perry, R.; Wu, Z.; Huda, M. N.; Moulé, A. J.; Osterloh, F. E., Electronic structure basis for enhanced overall water splitting photocatalysis with aluminum doped $SrTiO_3$ in natural sunlight. *Energy & Environmental Science* **2019,** *12* (4), 1385-1395.
15. Qin, Y.; Fang, F.; Xie, Z.; Lin, H.; Zhang, K.; Yu, X.; Chang, K., La,Al-Codoped $SrTiO_3$ as a Photocatalyst in Overall Water Splitting: Significant Surface Engineering Effects on Defect Engineering. *ACS Catalysis* **2021,** *11* (18), 11429-11439.

16. Huang, Z.-F.; Song, J.; Pan, L.; Zhang, X.; Wang, L.; Zou, J.-J., Tungsten Oxides for Photocatalysis, Electrochemistry, and Phototherapy. *Advanced Materials* **2015,** *27* (36), 5309-5327.
17. Saha, S.; Kumar, J. S.; Chandra Murmu, N.; Samanta, P.; Kuila, T., Controlled electrodeposition of iron oxide/nickel oxide@Ni for the investigation of the effects of stoichiometry and particle size on energy storage and water splitting applications. *Journal of Materials Chemistry A* **2018,** *6* (20), 9657-9664.
18. Kudo, A.; Omori, K.; Kato, H., A Novel Aqueous Process for Preparation of Crystal Form-Controlled and Highly Crystalline $BiVO_4$ Powder from Layered Vanadates at Room Temperature and Its Photocatalytic and Photophysical Properties. *Journal of the American Chemical Society* **1999,** *121* (49), 11459-11467.
19. Kudo, A.; Ueda, K.; Kato, H.; Mikami, I., Photocatalytic O_2 evolution under visible light irradiation on $BiVO_4$ in aqueous $AgNO_3$ solution. *Catalysis Letters* **1998,** *53* (3), 229-230.
20. Liao, L.; Zhang, Q.; Su, Z.; Zhao, Z.; Wang, Y.; Li, Y.; Lu, X.; Wei, D.; Feng, G.; Yu, Q.; Cai, X.; Zhao, J.; Ren, Z.; Fang, H.; Robles-Hernandez, F.; Baldelli, S.; Bao, J., Efficient solar water-splitting using a nanocrystalline CoO photocatalyst. *Nature Nanotechnology* **2014,** *9* (1), 69-73.
21. Ikeue, K.; Shinmura, Y.; Machida, M., Ag-doped Mn–Cd sulfide as a visible-light-driven photocatalyst for H_2 evolution. *Applied Catalysis B: Environmental* **2012,** *123-124*, 84-88.
22. Suryawanshi, A.; Dhanasekaran, P.; Mhamane, D.; Kelkar, S.; Patil, S.; Gupta, N.; Ogale, S., Doubling of photocatalytic H_2 evolution from g-C_3N_4 via its nanocomposite formation with multiwall carbon nanotubes: Electronic and morphological effects. *International Journal of Hydrogen Energy* **2012,** *37* (12), 9584-9589.
23. Wang, Q.; Nakabayashi, M.; Hisatomi, T.; Sun, S.; Akiyama, S.; Wang, Z.; Pan, Z.; Xiao, X.; Watanabe, T.; Yamada, T.; Shibata, N.; Takata, T.; Domen, K., Oxysulfide photocatalyst for visible-light-driven overall water splitting. *Nature Materials* **2019,** *18* (8), 827-832.
24. Ahmed, M.; Xinxin, G., A review of metal oxynitrides for photocatalysis. *Inorganic Chemistry Frontiers* **2016,** *3* (5), 578-590.
25. Smolinka, T.; Bergmann, H.; Garche, J.; Kusnezoff, M., Chapter 4 - The history of water electrolysis from its beginnings to the present. In *Electrochemical Power Sources: Fundamentals, Systems, and Applications*, Smolinka, T.; Garche, J., Eds. Elsevier: **2022**; pp 83-164.
26. Li, C.; Baek, J.-B., Recent Advances in Noble Metal (Pt, Ru, and Ir)-Based Electrocatalysts for Efficient Hydrogen Evolution Reaction. *ACS Omega* **2020,** *5* (1), 31-40.
27. Li, M.; Duanmu, K.; Wan, C.; Cheng, T.; Zhang, L.; Dai, S.; Chen, W.; Zhao, Z.; Li, P.; Fei, H.; Zhu, Y.; Yu, R.; Luo, J.; Zang, K.; Lin, Z.; Ding, M.; Huang, J.; Sun, H.; Guo, J.; Pan, X.; Goddard, W. A.; Sautet, P.; Huang, Y.; Duan, X., Single-atom tailoring of platinum nanocatalysts for high-performance multifunctional electrocatalysis. *Nature Catalysis* **2019,** *2* (6), 495-503.
28. Subbaraman, R.; Tripkovic, D.; Strmcnik, D.; Chang, K.-C.; Uchimura, M.; Paulikas Arvydas, P.; Stamenkovic, V.; Markovic Nenad, M., Enhancing Hydrogen Evolution Activity in Water Splitting by Tailoring Li+-$Ni(OH)_2$-Pt Interfaces. *Science* **2011,** *334* (6060), 1256-1260.

29. Xie, Y.; Cai, J.; Wu, Y.; Zang, Y.; Zheng, X.; Ye, J.; Cui, P.; Niu, S.; Liu, Y.; Zhu, J.; Liu, X.; Wang, G. A.-O.; Qian, Y., Boosting Water Dissociation Kinetics on Pt-Ni Nanowires by N-Induced Orbital Tuning ,. *Advance Material* **2019,** *31* (16), 1807780.

30. Chen, Z.; Duan, X.; Wei, W.; Wang, S.; Ni, B.-J., Recent advances in transition metal-based electrocatalysts for alkaline hydrogen evolution. *Journal of Materials Chemistry A* **2019,** *7* (25), 14971-15005.

31. Zhang, K.; Zou, R., Advanced Transition Metal-Based OER Electrocatalysts: Current Status, Opportunities, and Challenges. *Small* **2021,** *17* (37), 2100129.

32. Miles, M. H.; Thomason, M. A., Periodic Variations of Overvoltages for Water Electrolysis in Acid Solutions from Cyclic Voltammetric Studies. *Journal of The Electrochemical Society* **1976,** *123* (10), 1459-1461.

33. Raj, I. A.; Vasu, K. I., Transition metal-based hydrogen electrodes in alkaline solution — electrocatalysis on nickel based binary alloy coatings. *Journal of Applied Electrochemistry* **1990,** *20* (1), 32-38.

34. Laszczyńska, A.; Szczygieł, I., Electrocatalytic activity for the hydrogen evolution of the electrodeposited Co–Ni–Mo, Co–Ni and Co–Mo alloy coatings. *International Journal of Hydrogen Energy* **2020,** *45* (1), 508-520.

35. Wang, G.; Li, W.; Huang, B.; Xiao, L.; Lu, J.; Zhuang, L., Exploring the Composition–Activity Relation of Ni–Cu Binary Alloy Electrocatalysts for Hydrogen Oxidation Reaction in Alkaline Media. *ACS Applied Energy Materials* **2019,** *2* (5), 3160-3165.

36. Xia, M.; Lei, T.; Lv, N.; Li, N., Synthesis and electrocatalytic hydrogen evolution performance of Ni–Mo–Cu alloy coating electrode. *International Journal of Hydrogen Energy* **2014,** *39* (10), 4794-4802.

37. Safizadeh, F.; Ghali, E.; Houlachi, G., Electrocatalysis developments for hydrogen evolution reaction in alkaline solutions – A Review. *International Journal of Hydrogen Energy* **2015,** *40* (1), 256-274.

38. Wan, C.; Regmi, Y. N.; Leonard, B. M., Multiple Phases of Molybdenum Carbide as Electrocatalysts for the Hydrogen Evolution Reaction. *Angewandte Chemie International Edition* **2014,** *53* (25), 6407-6410.

39. Read, C. G.; Callejas, J. F.; Holder, C. F.; Schaak, R. E., General Strategy for the Synthesis of Transition Metal Phosphide Films for Electrocatalytic Hydrogen and Oxygen Evolution. *ACS Applied Materials & Interfaces* **2016,** *8* (20), 12798-12803.

40. Voiry, D.; Yamaguchi, H.; Li, J.; Silva, R.; Alves, D. C. B.; Fujita, T.; Chen, M.; Asefa, T.; Shenoy, V. B.; Eda, G.; Chhowalla, M., Enhanced catalytic activity in strained chemically exfoliated WS_2 nanosheets for hydrogen evolution. *Nature Materials* **2013,** *12* (9), 850-855.

41. Lukowski, M. A.; Daniel, A. S.; Meng, F.; Forticaux, A.; Li, L.; Jin, S., Enhanced Hydrogen Evolution Catalysis from Chemically Exfoliated Metallic MoS_2 Nanosheets. *Journal of the American Chemical Society* **2013,** *135* (28), 10274-10277.

42. Zhu, Y.; Lin, Q.; Zhong, Y.; Tahini, H. A.; Shao, Z.; Wang, H., Metal oxide-based materials as an emerging family of hydrogen evolution electrocatalysts. *Energy & Environmental Science* **2020,** *13* (10), 3361-3392.

43. Mei, J.; Liao, T.; Ayoko, G. A.; Bell, J.; Sun, Z., Cobalt oxide-based nanoarchitectures for electrochemical energy applications. *Progress in Materials Science* **2019,** *103*, 596-677.

44. Gao, X.; Zhang, H.; Li, Q.; Yu, X.; Hong, Z.; Zhang, X.; Liang, C.; Lin, Z., Hierarchical $NiCo_2O_4$ Hollow Microcuboids as Bifunctional Electrocatalysts for Overall Water-Splitting. *Angewandte Chemie International Edition* **2016,** *55* (21), 6290-6294.

45. Wang, X.; Liu, Z.; Guo, Z.; Ge, L.; Liu, Z., NiO–$CoFe_2O_4$ electrocatalyst prepared on Ni foam by one-step hydrothermal method for efficient overall water splitting. *Journal of Materials Science* **2021,** *56* (14), 8575-8587.

46. Xu, X.; Su, C.; Shao, Z., Fundamental Understanding and Application of $Ba_{0.5}Sr_{0.5}Co_{0.8}Fe_{0.2}O_{3-\delta}$ Perovskite in Energy Storage and Conversion: Past, Present, and Future. *Energy & Fuels* **2021,** *35* (17), 13585-13609.

47. Bajdich, M.; García-Mota, M.; Vojvodic, A.; Nørskov, J. K.; Bell, A. T., Theoretical Investigation of the Activity of Cobalt Oxides for the Electrochemical Oxidation of Water. *Journal of the American Chemical Society* **2013,** *135* (36), 13521-13530.

48. Subbaraman, R.; Tripkovic, D.; Chang, K.-C.; Strmcnik, D.; Paulikas, A. P.; Hirunsit, P.; Chan, M.; Greeley, J.; Stamenkovic, V.; Markovic, N. M., Trends in activity for the water electrolyser reactions on 3d M(Ni,Co,Fe,Mn) hydr(oxy)oxide catalysts. *Nature Materials* **2012,** *11* (6), 550-557.

49. Trotochaud, L.; Young, S. L.; Ranney, J. K.; Boettcher, S. W., Nickel–Iron Oxyhydroxide Oxygen-Evolution Electrocatalysts: The Role of Intentional and Incidental Iron Incorporation. *Journal of the American Chemical Society* **2014,** *136* (18), 6744-6753.

50. Morales-Guio, C. G.; Liardet, L.; Hu, X., Oxidatively Electrodeposited Thin-Film Transition Metal (Oxy)hydroxides as Oxygen Evolution Catalysts. *Journal of the American Chemical Society* **2016,** *138* (28), 8946-8957.

51. Matsumoto, Y.; Yamada, S.; Nishida, T.; Sato, E., Oxygen Evolution on $La_{1-x}Sr_xFe_{1-y}Co_yO_3$ Series Oxides. *Journal of The Electrochemical Society* **1980,** *127* (11), 2360-2364.

52. Liu, Y.; Zhou, W.; Wu, P., Room-temperature ferromagnetism and optical properties in Mg-doped TiO2: A density functional theory investigation. *J. Appl. Phys.* **2014,** *115* (12), 123913.

53. Otagawa, T.; Bockris, J. O. M., Lanthanum Nickelate as Electrocatalyst: Oxygen Evolution. *Journal of The Electrochemical Society* **1982,** *129* (10), 2391-2392.

54. Ashok, A.; Kumar, A.; Bhosale, R. R.; Almomani, F.; Malik, S. S.; Suslov, S.; Tarlochan, F., Combustion synthesis of bifunctional $LaMO_3$ (M=Cr, Mn, Fe, Co, Ni) perovskites for oxygen reduction and oxygen evolution reaction in alkaline media. *Journal of Electroanalytical Chemistry* **2018,** *809*, 22-30.

55. Harada, M.; Kotegawa, F.; Kuwa, M., Structural Changes of Spinel MCo_2O_4 (M = Mn, Fe, Co, Ni, and Zn) Electrocatalysts during the Oxygen Evolution Reaction Investigated by In Situ X-ray Absorption Spectroscopy. *ACS Applied Energy Materials* **2022,** *5* (1), 278-294.

56. Amaechi, I. C.; Katoch, R.; Kolhatkar, G.; Sun, S.; Ruediger, A., Particle size effect on the photocatalytic kinetics of barium titanate powders. *Catalysis Science & Technology* **2020,** *10* (18), 6274-6284.

57. Jirkovský, J.; Makarova, M.; Krtil, P., Particle size dependence of oxygen evolution reaction on nanocrystalline RuO_2 and $Ru_{0.8}Co_{0.2}O_{2-x}$. *Electrochemistry Communications* **2006,** *8* (9), 1417-1422.

58. Townsend, T. K.; Browning, N. D.; Osterloh, F. E., Nanoscale Strontium Titanate Photocatalysts for Overall Water Splitting. *ACS Nano* **2012,** *6* (8), 7420-7426.

59. Wei, Z.; Mogan, T. R.; Wang, K.; Janczarek, M.; Kowalska, E., Morphology-Governed Performance of Multi-Dimensional Photocatalysts for Hydrogen Generation. *Energies* **2021,** *14* (21).

60. Luo, Y.; Tang, L.; Khan, U.; Yu, Q.; Cheng, H.-M.; Zou, X.; Liu, B., Morphology and surface chemistry engineering toward pH-universal catalysts for hydrogen evolution at high current density. *Nature Communications* **2019,** *10* (1), 269.

61. Wu, Z.; Vagin, M.; Boyd, R.; Bakhit, B.; Greczynski, G.; Odén, M.; Björk, E. M., Morphology effects on electrocatalysis of anodic water splitting on nickel (II) oxide. *Microporous and Mesoporous Materials* **2022,** *333*, 111734.

62. Bastús, N. G.; Comenge, J.; Puntes, V., Kinetically Controlled Seeded Growth Synthesis of Citrate-Stabilized Gold Nanoparticles of up to 200 nm: Size Focusing versus Ostwald Ripening. *Langmuir* **2011,** *27* (17), 11098-11105.

63. Seo, B.; Baek, D. S.; Sa, Y. J.; Joo, S. H., Shape effects of nickel phosphide nanocrystals on hydrogen evolution reaction. *CrystEngComm* **2016,** *18* (32), 6083-6089.

64. Meshram, S. P.; Adhyapak, P. V.; Mulik, U. P.; Amalnerkar, D. P., Facile synthesis of CuO nanomorphs and their morphology dependent sunlight driven photocatalytic properties. *Chemical Engineering Journal* **2012,** *204-206*, 158-168.

65. Zhang, X.; Jin, G.; Wang, D.; Chen, Z.; Zhao, M.; Xi, G., Crystallographic phase and morphology dependent hydrothermal synthesis of tungsten oxide for robust hydrogen evolution reaction. *Journal of Alloys and Compounds* **2021,** *875*, 160054.

66. Zhang, X.; Li, J.; Xiao, P.; Wu, Y.; Liu, Y.; Jiang, Y.; Wang, X.; Xiong, X.; Song, T.; Han, J.; Xiao, W., Morphology-Controlled Electrocatalytic Performance of Two-Dimensional VSe_2 Nanoflakes for Hydrogen Evolution Reactions. *ACS Applied Nano Materials* **2022,** *5* (2), 2087-2093.

67. Mohan, S.; Gupta, S. K.; Mao, Y., Morphology-oxygen evolution activity relationship of iridium(iv) oxide nanomaterials. *New Journal of Chemistry* **2022,** *46* (8), 3716-3726.

68. Bai, S.; Gao, C.; Low, J.; Xiong, Y., Crystal phase engineering on photocatalytic materials for energy and environmental applications. *Nano Research* **2019,** *12* (9), 2031-2054.

69. Li, P.; Ouyang, S.; Xi, G.; Kako, T.; Ye, J., The Effects of Crystal Structure and Electronic Structure on Photocatalytic H_2 Evolution and CO_2 Reduction over Two Phases of Perovskite-Structured $NaNbO_3$. *The Journal of Physical Chemistry C* **2012,** *116* (14), 7621-7628.

70. Wang, C.; Wang, Y.; Yang, H.; Zhang, Y.; Zhao, H.; Wang, Q., Revealing the Role of Electrocatalyst Crystal Structure on Oxygen Evolution Reaction with Nickel as an Example. *Small* **2018,** *14* (40), 1802895.

71. Han, G.-Q.; Liu, Y.-R.; Hu, W.-H.; Dong, B.; Li, X.; Shang, X.; Chai, Y.-M.; Liu, Y.-Q.; Liu, C.-G., Crystallographic structure and morphology transformation of MnO_2 nanorods as efficient electrocatalysts for oxygen evolution reaction. *Journal of The Electrochemical Society* **2015,** *163* (2), H67.

72. Ücker, C. L.; Riemke, F. C.; de Andrade Neto, N. F.; Santiago, A. d. A. G.; Siebeneichler, T. J.; Carreño, N. L. V.; Moreira, M. L.; Raubach, C. W.; Cava, S., Influence of Nb_2O_5 crystal structure on photocatalytic efficiency. *Chemical Physics Letters* **2021,** *764*, 138271.

73. Liu, G.; Yu, J. C.; Lu, G. Q.; Cheng, H.-M., Crystal facet engineering of semiconductor photocatalysts: motivations, advances and unique properties. *Chemical Communications* **2011,** *47* (24), 6763-6783.

74. Hui, A.; Ma, J.; Liu, J.; Bao, Y.; Zhang, J., Morphological evolution of Fe doped sea urchin-shaped ZnO nanoparticles with enhanced photocatalytic activity. *J. Alloys Compd.* **2017,** *696*, 639-647.

75. Lardhi, S.; Cavallo, L.; Harb, M., Significant Impact of Exposed Facets on the $BiVO_4$ Material Performance for Photocatalytic Water Splitting Reactions. *The Journal of Physical Chemistry Letters* **2020,** *11* (14), 5497-5503.

76. Wang, X.; Fan, H.; Ren, P., Effects of exposed facets on photocatalytic properties of WO_3. *Advanced Powder Technology* **2017,** *28* (10), 2549-2555.

77. Li, J.; Li, X.; Yin, Z.; Wang, X.; Ma, H.; Wang, L., Synergetic Effect of Facet Junction and Specific Facet Activation of $ZnFe_2O_4$ Nanoparticles on Photocatalytic Activity Improvement. *ACS Applied Materials & Interfaces* **2019,** *11* (32), 29004-29013.

78. Cui, Y.; Briscoe, J.; Dunn, S., Effect of Ferroelectricity on Solar-Light-Driven Photocatalytic Activity of $BaTiO_3$—Influence on the Carrier Separation and Stern Layer Formation. *Chemistry of Materials* **2013,** *25* (21), 4215-4223.

79. Park, S.; Lee, C. W.; Kang, M.-G.; Kim, S.; Kim, H. J.; Kwon, J. E.; Park, S. Y.; Kang, C.-Y.; Hong, K. S.; Nam, K. T., A ferroelectric photocatalyst for enhancing hydrogen evolution: polarized particulate suspension. *Physical Chemistry Chemical Physics* **2014,** *16* (22), 10408-10413.

80. Li, X.; Liu, H.; Chen, Z.; Wu, Q.; Yu, Z.; Yang, M.; Wang, X.; Cheng, Z.; Fu, Z.; Lu, Y., Enhancing oxygen evolution efficiency of multiferroic oxides by spintronic and ferroelectric polarization regulation. *Nature Communications* **2019,** *10* (1), 1409.

81. Kushwaha, H. S.; Halder, A.; Vaish, R., Ferroelectric electrocatalysts: a new class of materials for oxygen evolution reaction with synergistic effect of ferroelectric polarization. *Journal of Materials Science* **2018,** *53* (2), 1414-1423.

Chapter 2

Understanding the role of ionic flux on the polarity of the exposed surfaces of ZnO and its correlation with Photocatalytic dye degradation activity

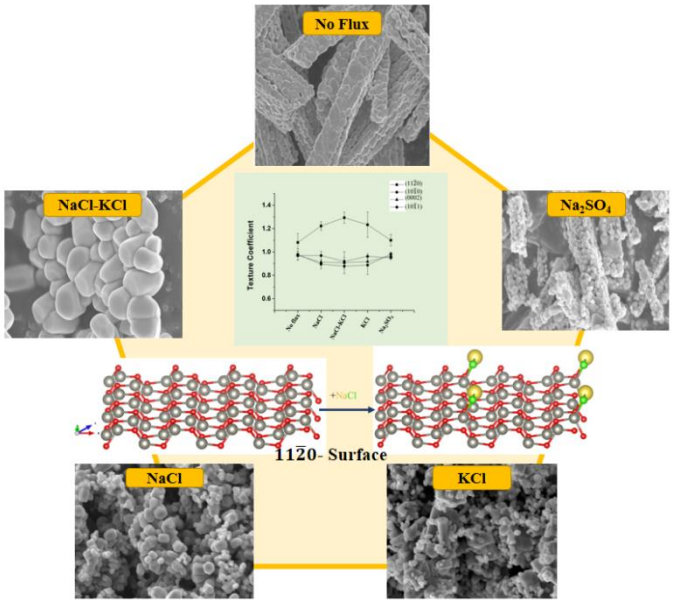

Chapter 2

Understanding the role of ionic flux on the polarity of the exposed surfaces of ZnO and its correlation with Photocatalytic dye degradation activity

ABSTRACT

The role of ionic flux in controlling the polarity of the surfaces of ZnO was evaluated, both experimentally and theoretically. Zinc oxide was synthesized by controlled decomposition of zinc oxalate nanorods in the presence of ionic flux. The degree of preferred orientation of a specific plane, for ZnO structures, was observed by calculating the texture coefficient. The presence of flux (NaCl, KCl, a mixture of NaCl-KCl and Na_2SO_4) during the decomposition of oxalate precursor led to the preferential growth of $(11\bar{2}0)$ planes. The value of texture coefficient was found to be high for the $(11\bar{2}0)$ plane when the decomposition was carried out in the presence of a mixture of NaCl and KCl when compared to their counterparts. A decrease in the value of texture coefficient for the $(11\bar{2}0)$ plane was observed when Na_2SO_4 was used as a flux, which was similar to the value obtained for ZnO synthesized in the absence of flux. The observations from the analysis of texture coefficient were correlated with photocatalytic degradation of Rhodamine B dye, by making use of the fact that the nature of exposed surfaces influences the catalytic activity of the material. On-site Coloumb correlations corrected density functional theory (DFT+U) based computational studies were performed to get theoretical insight into the role of ionic flux for surface reconstructions. The surface energies for different ZnO surfaces were computed in the presence and absence of the ionic flux. It was revealed that the pristine $(10\bar{1}0)$ surface is more stable compared to pristine $(11\bar{2}0)$ by 0.04 J/m^2 (surface energy), however, the scenario changed in the presence of the ionic flux, and $(11\bar{2}0)$ become more stable by 0.03 J/m^2. This indeed corroborated with our experimental observations and explained the fundamental role of ionic flux on the polarity of exposed surfaces of ZnO.

Keywords: A1. Texture Coefficient; A1. Flux; A1. The of surfaces A1. Surface Energy

2.1 Introduction:

The formation of structures with different surfaces (facets) is important as the polarity of these surfaces determines the catalytic activity of the nanomaterials. Capping agents like surfactants, organic ligands, inorganic ions, etc. have been used for controlling the shape and size of the material as these act as stabilizing agents and alter the growth rates of the surfaces. The growth rate also directs the shape of the particle. Selective desorption of the capping agents from the surface of the growing unit is one way to form faceted structures. For example, Ravi Shankar et.al have reported that amines were selectively removed from the facet of gold by ascorbic acid, which resulted in the formation of branched structure[1].

In a polycrystalline material preferred orientation is the tendency of the crystallites in a powder to be oriented in a preferred manner for a particular plane than others. It can also be defined as a crystallographic texture. Controlling the texture of the material helps in tailoring the properties of the material. This was demonstrated by Bahl et.al. in controlling the crystallographic texture of magnesium and its effect as a restorable biomaterial [2]. The authors have generated different textures by cutting an extruded rod of Mg in multiple directions. They found that the strength and the ductility of Mg were affected by the texture of the rod. In another report by Abhyankar et.al. [3], it was demonstrated that doping of W in SnO_2 led to a reduction in the value of texture coefficient for (110) plane and an increase in the value for the (200) plane. The outstanding effect observed on the gas sensing properties of the doped film was correlated to the change in the value of the texture coefficient. Sreeremya et.al.[4] have correlated the chemical reactivity of different shapes of CeO_2 with the type of crystal facets forming the nanostructures. They observed that there was a correlation between the sum of the texture coefficient for (200) and (220) planes with the soot combustion temperature for various nanocatalysts. Thus, it is important to control the crystallographic texture of the material. The present study deals with understanding the effect of various fluxes on the surfaces of ZnO. We have chosen ZnO as it is an n-type semiconductor with four major kinds of surfaces present for wurtzite ZnO[5-7] (figure 2.1) viz. (i) polar Zn-terminated (0001) surface. (ii) polar O-terminated $(000\bar{1})$ surface. (iii) non-polar $(11\bar{2}0)$ surface (iv) non-polar $(10\bar{1}0)$ surface.

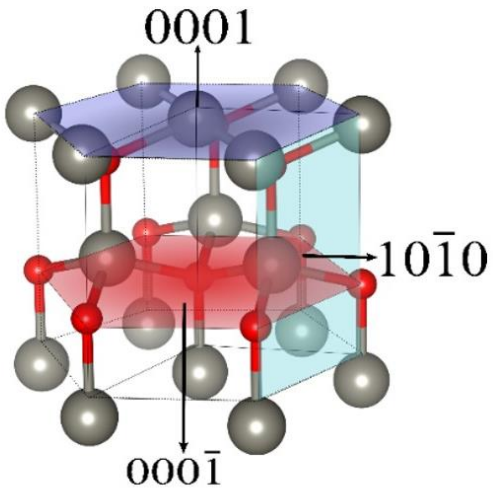

Figure 2.1 : The Hexagonal Wurtzite ZnO unit cell

Polar surfaces of ZnO are important for catalytic reactions. It has been observed by Huang *et.al*[8] that a large ratio of (0001) facet in ZnO led to high photodegradation of Rhodamine B (RhB) dye. They concluded that for different facets of ZnO, the order of photodegradation efficiencies was (0001)> $(10\bar{1}1)$ > $(10\bar{1}0)$. Tang *et.al* [6] have shown the importance of non-polar surfaces such as $(11\bar{2}0)$ of ZnO for adsorption of CO_2. In another report [9], it was reported that the predominance of $(10\bar{1}1)$ facets resulted in a higher value for current density for ZnO-based dye-sensitized solar cells. These examples illustrate that it is important to control the growth of the surfaces, as the application depends on the exposed surface of ZnO. To control the nature of exposed surfaces, it is important to control the surface energy which plays a major role in the relative stability of the surfaces. It has been known from the previous theoretical investigations [5-6] that the stability order of different unreconstructed and clean ZnO surfaces is $(10\bar{1}0)$> $(11\bar{2}0)$> (0001)> $(10\bar{1}1)$. The polarity of the polar surfaces has been attributed to the alternative stacking of tetra-coordinated Zn and O atoms along the c-axis. Such polar surfaces were classified as Tasker type-III surface that contains a permanent dipole moment inside the bulk unit cell.[7, 10] It is suggested that there must be some charge redistribution involved to stabilize the surfaces. Recently, Catlow *et al*.[7] have demonstrated from their stochastic sampling of the polar surfaces that surface reconstruction plays a significant role in stabilizing the polar ZnO surfaces. According to their study, a surface reconstruction is involved in redistributing the charges among the two polar planes (Zn terminated-0001 and O terminated $000\bar{1}$). Due to surface reconstruction, the surface

energy of the polar ZnO surfaces gets reduced and even becomes lower than the non-polar surfaces. As a consequence, they are expected to be exposed during crystal growth and should compete with non-polar surfaces. It is thus, important to understand the formation of exposed facets enabling one to control their growth and explore the properties that are dependent on the shape of the material. In this study, we have tried to understand the role of different fluxes in controlling the polarity of surfaces of ZnO, both experimentally and theoretically. Briefly, ZnO was synthesized by thermal decomposition of zinc oxalate in the presence of flux. The synthesis is carried out in the presence of flux because of two main reasons. Firstly, flux contains inorganic ions, and it is a well-known fact that inorganic ions influence the formation of the faceted structure by acting as a binding agent during the formation of nanostructures[11]. The presence of ions affects the growth of crystal structure through interaction between the characteristic surface with changes in surface hydration and ion solvation. Secondly, flux provides a molten (semi-liquid) environment during the formation of the material[12] and acts as a solvent. A solvent controls the polarity and viscosity of the medium affecting the structure of a specific morphology and crystal facet[13,14]. We utilized these properties of the flux for the formation of faceted structures of ZnO. The use of flux has been known for the synthesis of materials [15-17], however, there are very few reports wherein, flux has been used during the decomposition of the precursor for the formation of oxides. For instance, flux-assisted thermal decomposition of copper oxalate [18] and nickel oxalate [19] has been reported by Wang et. al. where NaCl was used as a flux and led to the formation of nanorods of CuO [18] and NiO [19] respectively. Jiang et.al.[20] in their paper have carried out the synthesis of ZnO nanowires by decomposition of zinc acetate in the presence of LiCl (molten salt). The authors obtained nanorods when decomposition of hydrated zinc acetate was carried out in the presence of LiCl. The authors have carried out a systematic study using HRTEM and SAED for analyzing the growth direction of ZnO nanowires and nanorods. In this study, we have used a different kind of flux during the decomposition of zinc oxalate and have evaluated the effect of these fluxes in controlling the polarity of the exposed facets. The degree of preferred orientation for a particular plane has been monitored experimentally by calculating the texture coefficient. It is known that if the value of the texture coefficient for a particular plane lies between zero and one, it signifies a lack of orientation of the grain in that direction. A value greater than 1 indicates that the crystallites have preferentially grown in a direction perpendicular to the hkl plane. For getting an understanding of how flux influences the degree of preferred orientation, theoretical studies were carried out to calculate the facet-dependent surface energy of different surfaces. The

effect of flux was evaluated by considering the change in surface energy due to the adsorption of ions on the relaxed surfaces. For calculating the surface energy, the unreconstructed and clean surface was used. To correlate our findings on the effect of flux on the degree of preferred orientation towards a particular plane, photodegradation of RhB was carried out with ZnO, synthesized under different flux conditions.

2.2 Experimental:

2.2.1 Materials:

Cetyltrimethylammonium bromide (CTAB) (SRL), Iso-octane (Merck), 1-butanol (Merck), Zinc nitrate hexahydrate (Sigma Aldrich), diammonium oxalate monohydrate (Merck), NaCl (Merck), KCl (Merck), Na_2SO_4 (Merck) were used. All the chemicals were used without further purification.

2.2.2 *Method:*

Zinc oxalate was prepared by two methods namely, reverse micellar method [21] and the co-precipitation method. Briefly, for the synthesis of zinc oxalate using reverse micelles: two microemulsions with cetyltrimethylammonium bromide (CTAB) as the surfactant (weight fraction 16.76%), 1-butanol as the cosurfactant (weight fraction 13.9%), iso-octane as the non-polar phase (weight fraction 59.29%) and 0.1M aqueous solutions (weight fraction 10.05%) of $Zn(NO_3)_2$ and $(NH_4)_2C_2O_4$ were prepared. The microemulsions were mixed and stirred overnight. The precursor was centrifuged, washed with a 1:1 chloroform/methanol mixture, and dried at room temperature. The oxalate precursor, synthesized using the reverse micellar route was heated at 850 ^oC for 12 h both in the absence[22] and presence of different flux. For the synthesis of zinc oxalate using the co-precipitation method, 0.1 M solution of Zn^{2+} and $C_2O_4^{2-}$ ions were mixed in equal volumes and stirred overnight. The precursor was centrifuged, washed with water and acetone, and dried at room temperature. Zinc oxalate, synthesized using the co-precipitation route, was heated at 850 ^oC for 12h in the presence and absence of flux. We have used four types of flux namely, a 1:1 mixture of NaCl-KCl, NaCl, KCl, and Na_2SO_4. The precursor to flux weight ratio was taken as 2:1. In a typical method, zinc oxalate prepared by either method mentioned above was ground with the flux in a mortar pestle to obtain a uniform mixture. The sample was put in a recrystallized alumina crucible and heated at a high temperature. The white product was washed with lukewarm distilled water, and centrifuged until no ions were detected (using silver nitrate/barium nitrate) in the solution. After the removal of ions, the product was washed with acetone and dried at 40 ^oC.

2.2.3 Characterization:

The crystallinity and the phase purity of ZnO were checked using Powder X-Ray Diffraction (PXRD) using Eco D8 Advance Bruker XRD with a Cu Kα radiation source (λ = 0.15418 nm) operated at 40 kV and 25 mA with a scanning step of 0.02. Texture coefficient was determined through PXRD, and calculated using the following expression:

$$TC_{(hkl)} = \frac{\frac{I_{m(hkl)}}{I_{o(hkl)}}}{\frac{1}{N}\sum_{1}^{N}\frac{I_{m(hkl)}}{I_{o(hkl)}}} \quad (2.1)$$

Where $I_{m\ (hkl)}$ is the measured intensity of the (hkl) plane

$I_{o\ (hkl)}$ is the standard intensity (JCPDS No. 01-079-0208) of the (hkl) plane

N is the number of peaks selected for determining the texture coefficient.

For calculating the texture coefficient of ZnO, intensities of four planes (N=4) were taken into account viz. $(10\bar{1}0)$, (0002), $(10\bar{1}1)$, and $(11\bar{2}0)$.

Lattice parameters for ZnO, obtained by decomposition of oxalate precursor synthesized using the reverse micellar method, were obtained using TOPAS software version 5, keeping sample displacement error into consideration. Sample displacement error is a phenomenon prevalent with the Bragg-Brento geometry in the PXRD instrument. This error results in the shifting of peaks by equal magnitudes either to the left or right of the actual peak position.

The morphology of zinc oxide nanoparticles was studied by JSM- 1T 300 JEOL Scanning Electron Microscope (SEM) and JEOL 7600F Field Emission Scanning Electron Microscope (FESEM) on powder mounted on carbon tape coated with gold. Transmission Electron Microscopy and Electron Diffraction studies were carried out on a JEOL JEM 2100 operated at 200 kV. Powder samples were dispersed in ethanol and a drop of the dispersed solution was put on a copper grid supported by a carbon film and dried. Nitrogen adsorption-desorption isotherms were recorded with Quanta Chrome Model Q2 equipment at liquid nitrogen temperature (77 K). The specific surface area was determined by the Brunauer–Emmett–Teller (BET) method.

2.2.4 Photocatalytic Activity:

For the photocatalytic degradation of RhB dye, 100 mg of the catalyst was dispersed in 100 mL of 8 μM (RhB) dye solution in a photocatalytic reactor, equipped with a water circulating jacket. The mixture was irradiated with UV light using a high-pressure Hg lamp (250 W). The adsorption capacity of the material was checked by allowing the sample to equilibrate in the dye solution for 30 minutes under dark conditions. After 30 minutes of stirring in the dark, the light source was switched on. The photodegradation of Rhodamine B dye in an aqueous solution was monitored using UV-visible spectroscopy.

2.3 Computational Methods and models:

2.3.1 Density Functional Theory (DFT) Calculations:

The DFT calculations were performed using the Vienna Ab-initio Simulation Package (VASP)[23-25]. In the calculations the valence electronic states are expanded with a plane-wave basis set, while the core electrons are treated with pseudopotential. The valence-core interaction was represented by full-potential Projected Augmented Wave (PAW) potential.[26] The Generalized Gradient Approximations (GGA)[27-28] was used to treat the exchange-correlation potentials with the Perdew, Bruke, and Ernzerof (PBE) functional.[29] A plane-wave cut-off of 400 eV was used to guarantee a good convergence of the total energy. The GGA functional overestimates the electron delocalization but underestimates the band gaps. To avoid this shortcoming and to treat strongly localized Zn 3d electrons, the on-site Coulomb correlations corrected GGA+U [30] methodology was adopted. The effective Hubbard U-parameter (U_{eff} =U-J) that is U_{eff} =7.5 eV was used for our calculations. The U value was adopted based on previous reports in the literature [6]. The convergence tolerance for the self-consistent electronic minimization was set to 10^{-5} eV/cycle. The K-points grid[26] was taken as (7x7x7) for the bulk and (7x7x1) for the surface. The optimized cell parameters are a=3.159 Å, c=5.056 Å and c/a=1.60035.

To compute the facet-dependent surface energy a supercell containing the facet of interest was created by incorporating a large vacuum (~12 Å) along the perpendicular

axis to the facets in the unit cell. Six double-layer slabs were taken to ensure the absence of interaction between two opposite surface terminations through the bulk. We kept the lowest 2 layers of the surface slabs fixed to their bulk position throughout all our calculations. The surface energy for a clean, converged slab in a vacuum is defined as.

$$\gamma = \frac{1}{2A}(E_{slab} - NE_{bulk}), \qquad (2.2)$$

Where A is the surface area of the slab. E_{slab} is the total energy of the slab. N is the number of the bulk unit in the slab. E_{bulk} is energy per bulk unit.

2.3.2 Modelling of surfaces in the presence of ionic flux

We used 6 double layer thick ZnO slabs with 2x2 repetition in x and y directions to simulate the ionic flux. The lower two layers were kept at a fixed bulk position. The remaining slabs were allowed to relax in the presence of the oppositely charged ions (e.g, Na^+ and Cl^- ions) kept on top of the ZnO dimers in the z-direction. After obtaining relaxed slab geometry in the presence of ionic flux, the ions were removed and the energy of the slab was recalculated to account for the change in the surface energy due to change in the structural parameters inserted by the ionic flux. To simulate the combined ionic flux by NaCl and KCl, we used the surface supercell with double repetition in x and y directions (4x4 surface supercell was used).

2.4 Results and Discussion

The phase purity and crystallinity of the precursor i.e. zinc oxalate and the product (ZnO), obtained after decomposition of the precursor under different conditions was evaluated using PXRD. The PXRD pattern of synthesized oxalate nanostructures is shown in figure 2.2 wherein reflections could be indexed to the monoclinic structure of zinc oxalate dihydrate.

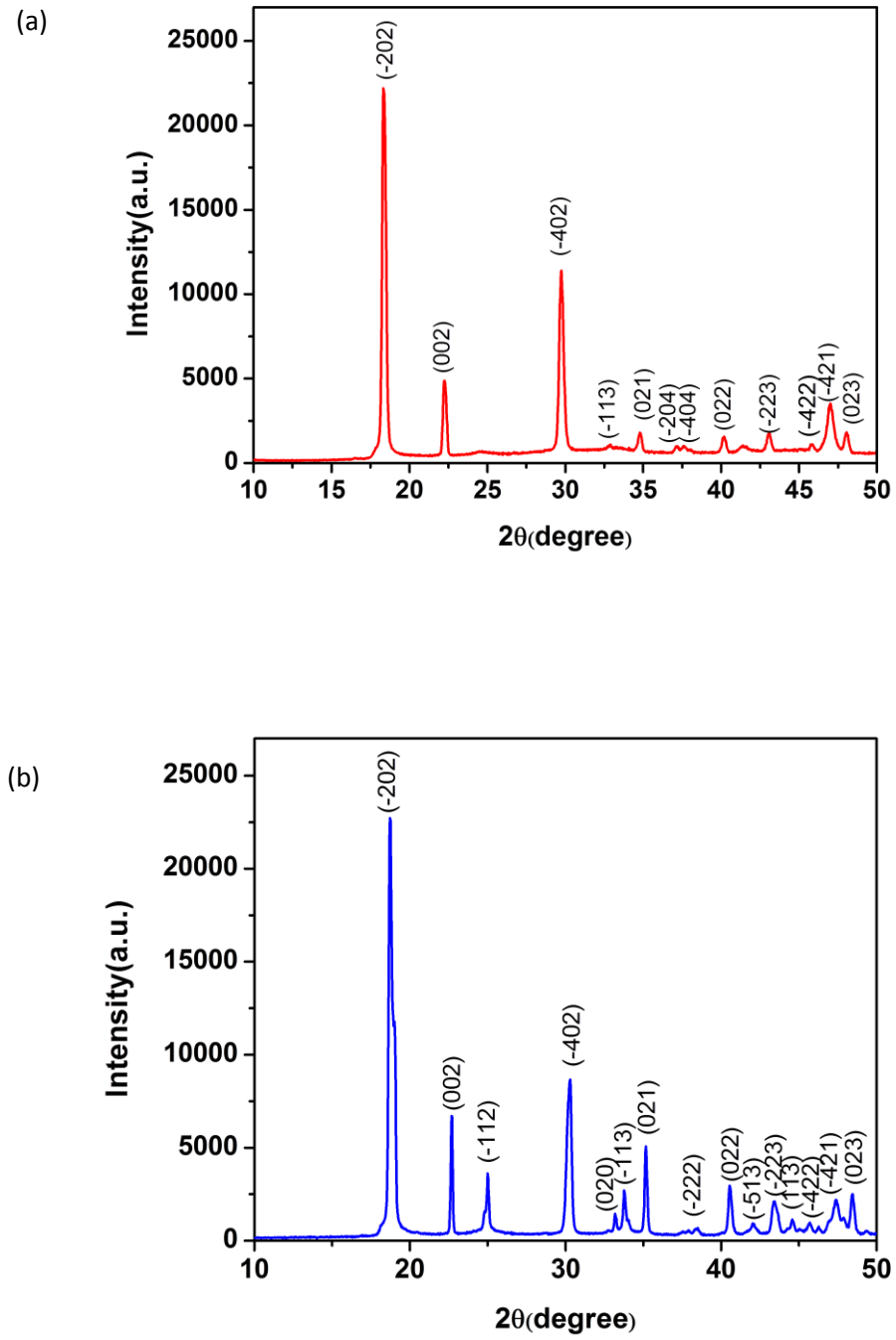

Figure 2.2: PXRD pattern of zinc oxalate synthesized using (a) reverse micellar method and (b) co-precipitation method.

Figure 2.3(a) and 2.3(b) showed the PXRD pattern of ZnO obtained by the decomposition of oxalate precursor synthesized using the reverse micellar method and co-precipitation method (in the presence and absence of flux), respectively.

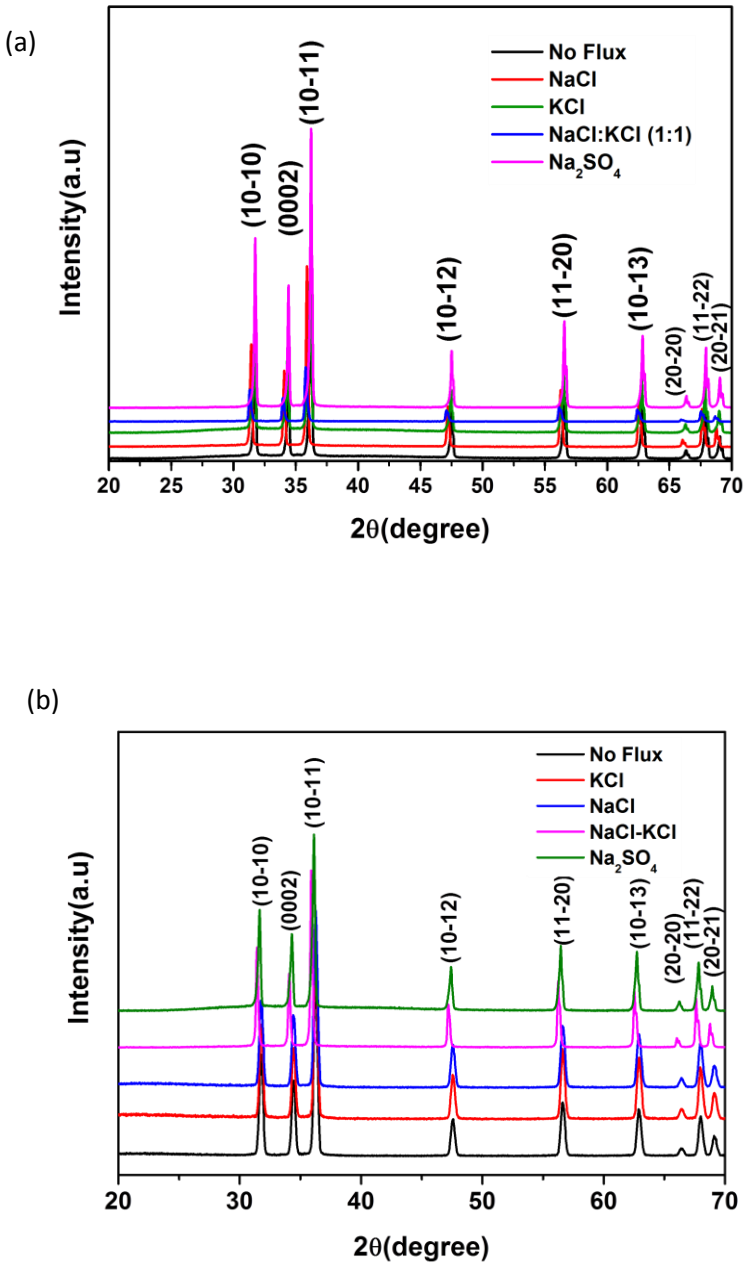

Figure 2.3: PXRD pattern of zinc oxide nanostructures formed by the decomposition of zinc oxalate synthesized using (a) reverse micellar method and (b) co-precipitation method.

The PXRD pattern shows the formation of crystalline ZnO (wurtzite). Lattice parameters were calculated by keeping sample displacement error into consideration which accounts for shifting of peaks by equal magnitudes either to left or right of the actual

peak position in Bragg-Brento geometry in the PXRD instrument. Lattice parameters for ZnO, obtained by decomposition of oxalate precursor synthesized using the reverse micellar method, have been tabulated in Table 2.1. No change in the lattice parameters was observed with the change in the nature of flux used for synthesizing ZnO.

Table 2.1**:** Refined lattice parameters (calculated from PXRD data) of ZnO obtained decomposition of zinc oxalate precursor (synthesized using reverse micellar route).

Flux	*Lattice Parameter*	
	a (Å)	*c (Å)*
No Flux	*3.25327(13)*	*5.2102(2)*
NaCl	*3.25015(7)*	*5.20628(13)*
KCl	*3.25316(17)*	*5.2110(3)*
NaCl-KCl	*3.25042(7)*	*5.20680(14)*
Na2SO4	*3.25061(10)*	*5.20654(18)*

The texture coefficient was calculated using equation 2.1. The value of the texture coefficient for all the plane was close to 1 (figure 2.4) for ZnO obtained using the two methods, in the absence of any flux. This suggests that the particles did not have a preferred orientation towards a particular plane and were randomly oriented. We then investigated the role of flux on the degree of preferred orientation of ZnO.

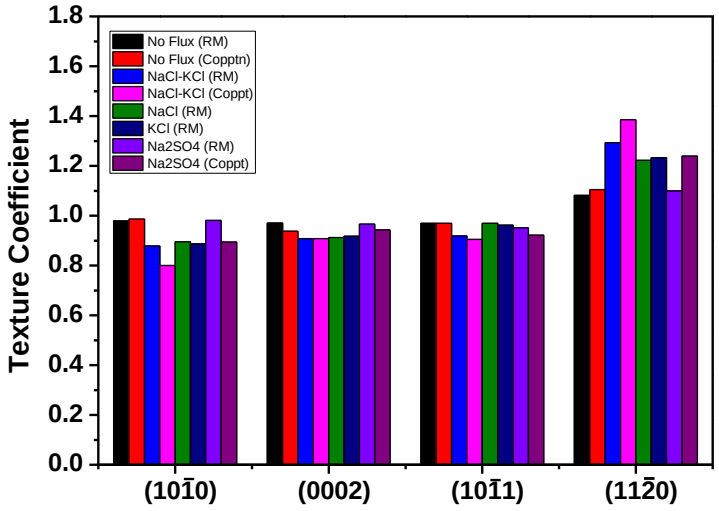

Figure 2.4: Plot of texture coefficient of different planes of ZnO obtained using the decomposition of zinc oxalate under different conditions. (RM: reverse micellar method; copptn: co-precipitation method)

From figure 2.4, it was interesting to observe that the texture coefficient shows the highest value for $(11\bar{2}0)$ plane (for samples obtained by decomposition of oxalate precursor in presence of flux) which suggests that ZnO was formed with a preferred orientation for $(11\bar{2}0)$ plane. It is to be noted that the value of texture coefficient for ZnO obtained from the decomposition of oxalate precursor which was synthesized using the co-precipitation method was high when compared to the ZnO obtained from oxalate synthesized using the reverse micellar method. Thus, it is to be noted that the methodology adopted for synthesizing the oxalate precursor played an important role in determining the degree of preferred orientation. To see the effect of the final morphology of the oxalate precursor on the size and shape of ZnO and its role on the texture coefficient, SEM studies were carried out on ZnO (obtained by decomposition of oxalate precursor, in absence of flux). Careful observations of SEM images show the formation of rods of zinc oxalate dihydrate (prepared using reverse micellar route) with an average length of ~20 μm and diameter ~5 μm (figure 2.5a). However, zinc oxalate with irregular shape (figure 2.5b) was formed by the co-precipitation method.

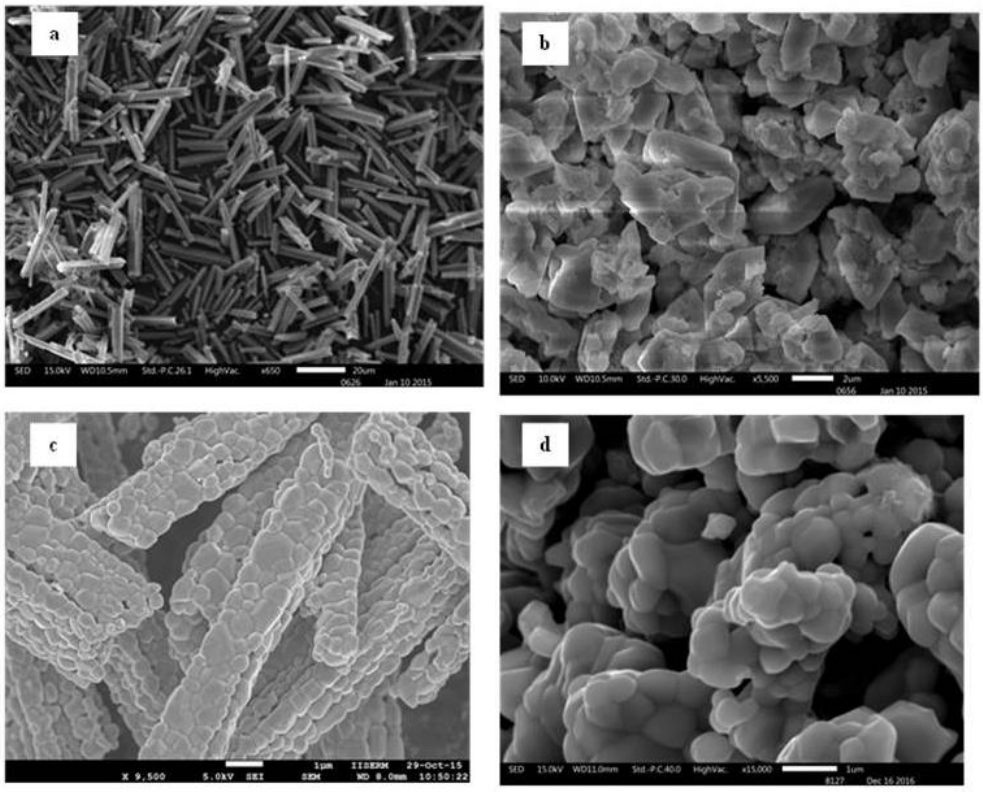

Figure 2.5: SEM images of zinc oxalate synthesized using (a) reverse micellar method and (b) co-precipitation method. SEM images of zinc oxide nanostructures obtained by decomposition of zinc oxalate (in the absence of flux) synthesized using (c) reverse micellar method and (d) co-precipitation method.

Figure 2.5c shows rods composed of assembled particles (average size ~350 nm) of ZnO when rods of zinc oxalate (synthesized using the reverse micellar method) were decomposed at 850 ^{o}C in the absence of any flux. Irregularly shaped particles (average size ~ 700 nm) with no clear facets and with diffused boundaries (figure 2.5d) were obtained when the oxalate precursor (synthesized using co-precipitation) was decomposed in the absence of any flux. It was observed that the oxide obtained from nanorods of oxalate precursor was smaller in size when compared with the size of oxide obtained from oxalate precursor synthesized using the co-precipitation method. It has also been previously observed that the size of the oxide nanostructures depends strongly on the morphology of the precursor [31,32]. The studies show that the growth of oxide nanostructures during decomposition of oxalate precursors is dependent on the morphology of the precursor. The growth of ZnO is somewhat restricted when the morphology is rod-shaped when compared to the irregular shaped particles. The rate of growth of nanostructures during their formation also governs the creation of texture and thereby preferred orientation of the material. Thus, based on the observations from SEM studies, even though the texture coefficient showed high value for $(11\bar{2}0)$ plane for ZnO formed from the oxalate precursor using the co-precipitation method, we chose to carry out further study on ZnO formed from the precursor synthesized using a reverse micellar method, mainly due to the morphology of oxalate precursor.

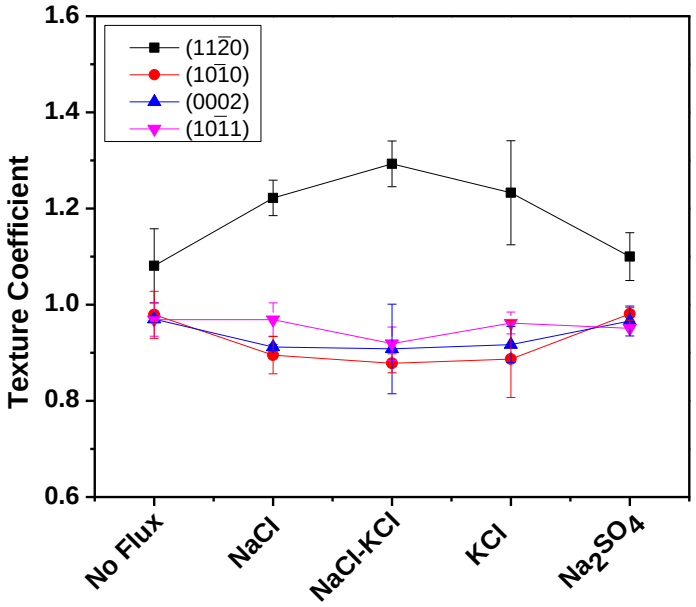

Figure 2.6: Variation of texture coefficient for $(10\bar{1}0)$, (0002), $(10\bar{1}1)$ and $(11\bar{2}0)$ planes with flux used during decomposition of zinc oxalate.

From figure 2.6, one observes that the value of texture coefficient for $(11\bar{2}0)$ plane is high when the decomposition was carried out in the presence of a mixture of NaCl and KCl when compared to using the pure halides i.e. only NaCl and only KCl. The melting point of pure NaCl is 800 ^{o}C, pure KCl is 770 ^{o}C and the eutectic mixture of NaCl and KCl is 657 ^{o}C. To compare the degree of preferred orientation of ZnO towards $(11\bar{2}0)$ plane, formed in the presence of flux, the reaction was carried out at 850 ^{o}C where all the three types of flux would be present in their molten state. However, the reaction temperature was just 50 ^{o}C and 80 ^{o}C higher than the melting temperature for NaCl and KCl flux while it was ~150 ^{o}C higher for the eutectic mixture as the flux.

Thus, it can be believed that a synergistic effect of a high difference between the melting temperature and the reaction temperature along with the effect of ions present in the flux could be the reason for the high degree of preferred orientation towards $(11\bar{2}0)$ plane. On changing the flux to Na_2SO_4, containing a divalent anion, a decrease in the value of texture coefficient for $(11\bar{2}0)$ plane was observed. A slight increase in the value of texture coefficient was observed for $(10\bar{1}0)$, (0002), $(10\bar{1}1)$ planes, for ZnO, synthesized in the presence of Na_2SO_4 flux, when compared with other flux. The value of the coefficient was found close to 1 and was quite similar to the value obtained for ZnO synthesized in the absence of flux. Thus, the change in the value of texture coefficient for ZnO synthesized under different flux suggests that the ions present in the flux played an important role in increasing the degree of preferred orientation towards $(11\bar{2}0)$ plane.

To see, whether the texture coefficients are influenced by size, shape or faceting behaviour of the particles, SEM studies were carried out on the decomposition of nanorods of zinc oxalate (synthesized using reverse micellar route) in the absence (figure 2.7a) and presence of various flux (figure 2.7b-e). The eutectic temperature gave (figure 2.7b), the majority of particles with sharp facets for ZnO obtained from decomposition of zinc oxalate (synthesized using the reverse micellar method) in the presence of 1:1 mixture of NaCl-KCl. In the case of decomposition of zinc oxalate (synthesized using the reverse micellar method) in the presence of only NaCl (figure 2.7c) and KCl (figure 2.7d), the majority of particles were formed with smooth edges and no sharp facets. The difference in the kind of particles obtained with only NaCl and KCl and their eutectic mixture could be the reason for obtaining a high value of texture coefficient for $(11\bar{2}0)$ plane for ZnO synthesized in the presence of a 1:1 mixture of NaCl-KCl as flux. When flux containing a divalent anion-Na_2SO_4 was used, particles assembled to form a rod-like structure (figure 2.7e), similar to the assembly obtained when ZnO was formed in the absence of any flux.

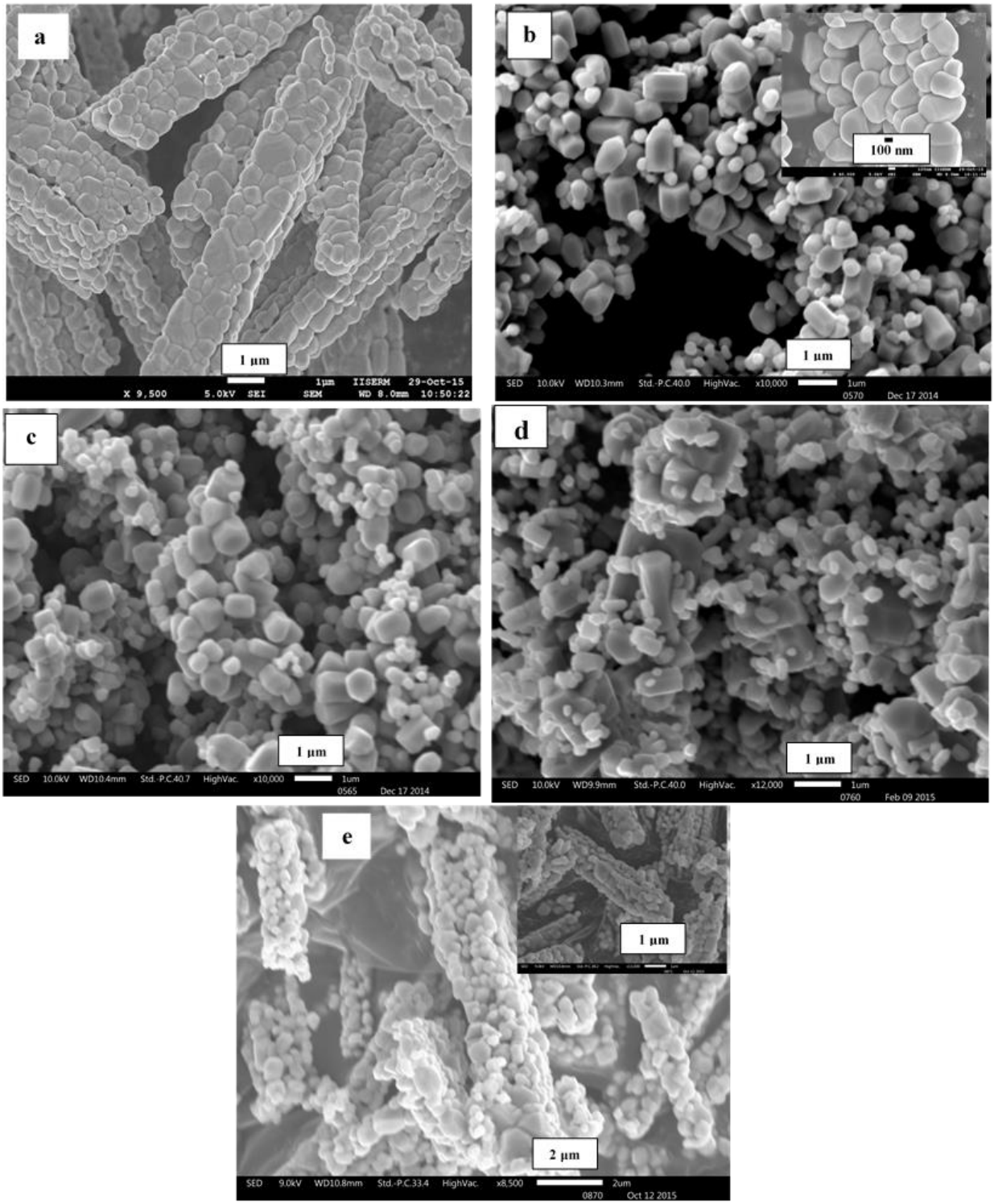

Figure 2.7: SEM images of ZnO obtained by decomposition of zinc oxalate (synthesized using reverse micellar route) in (a) absence of flux, with (b) 1:1 mixture of NaCl-KCl, (c) NaCl, (d) KCl and (e) Na_2SO_4 as flux.

The value of the texture coefficient was also quite similar to two kinds of ZnO indicating that Na_2SO_4 did not have any effect on the degree of preferred orientation. Preferred orientation in a polycrystalline sample indicates a preference of certain planes than exhibiting a random orientation and can be evaluated from XRD by calculating the texture coefficient. It is important to know the degree of preferred orientation of the material as it affects the macroscopic properties of the material. It is thus inferred that the nature of flux influences the polarity of the surface as indicated from the observed value of the texture coefficient, an indicator for the degree of preferred orientation. Flux contains inorganic ions which could have assisted in the growth of facets with preferred orientation. It is known that the ionic impurity also modifies the potential which arises due to concentration gradient in solution and consequently alters the crystal growth. Ubbelohde has mentioned that three types of ionic impurities, viz. (i) H^+ ion with common anion and OH^- ion when cation is common, (ii) high valent ions in a solution of low valent ions, and (iii) less mobile colloids capable of acting as ions, play an important role in altering the crystal growth. [33] Studies showing the influence of ions on the growth of structures with exposed facets have been cited in the literature. For instance, the effect of ions was also studied by Niu et.al. [34] wherein it was observed that the chloride ion in cetylpyridinium chloride dictated the morphology of the nanostructures to rhombic dodecahedron and octahedron. The introduction of KBr into the reaction solution led to the formation of cubic nanostructures. The authors reported that this could be because of preferential adsorption of Cl^- and Br^- ion on different facets. [34] Divalent ion has been shown to influence the morphology of the particles to rod shape. It was shown by Yang et.al.[35], that anions such as F^-, SO_4^{2-}, Cl^- ions influence the morphology of Ag nanostructures by either poisoning or enhancing the growth of crystal facet. It was believed that SO_4^{2-} ion acted as an ionic surfactant and thus led to the formation of the dendritic framework of Ag by reducing the corresponding surface energies and blocking the formation of crystal facets from adding fresh Ag atoms and nanoparticles. In another report by Liu et.al. [36], it was observed that selective adsorption of F^- ion on (0001) facets of TiO_2 resulted in lowering the surface energy of (0001) facet, leading to the formation of a truncated octahedron of TiO_2 with a large percentage of (0001) facet. Replacing F^- ion with SO_4^{2-} or acetate ion led to the formation of nanorods of TiO_2. In our studies, we observed a similar effect where replacing a monovalent anion, Cl^- with a divalent anion SO_4^{2-} led to rod shape. Thus, one can see that the type of ions has a major role in the morphology of the material. In our studies, the flux contains inorganic ions and also provides a molten environment. The presence of inorganic ions diffusing through the molten environment could have assisted in the nature of texture formed for ZnO.

To see the crystalline nature of ZnO, electron diffraction studies were performed on a single particle of ZnO synthesized using thermal decomposition of zinc oxalate nanorods in the absence of any flux and presence of a mixture of NaCl-KCl. We observed a well-defined spotted pattern in the electron diffraction, indicating that the particle focused during the analysis was single-crystalline. For ZnO synthesized in absence of any flux, the pattern could be indexed to $(1\bar{2}10)$ zone axis whereas for ZnO synthesized in presence of NaCl-KCl, the pattern could be indexed to $(1\bar{1}00)$ zone axis. The images of the particle and their corresponding electron diffraction pattern are shown in figure 2.8 (a-d).

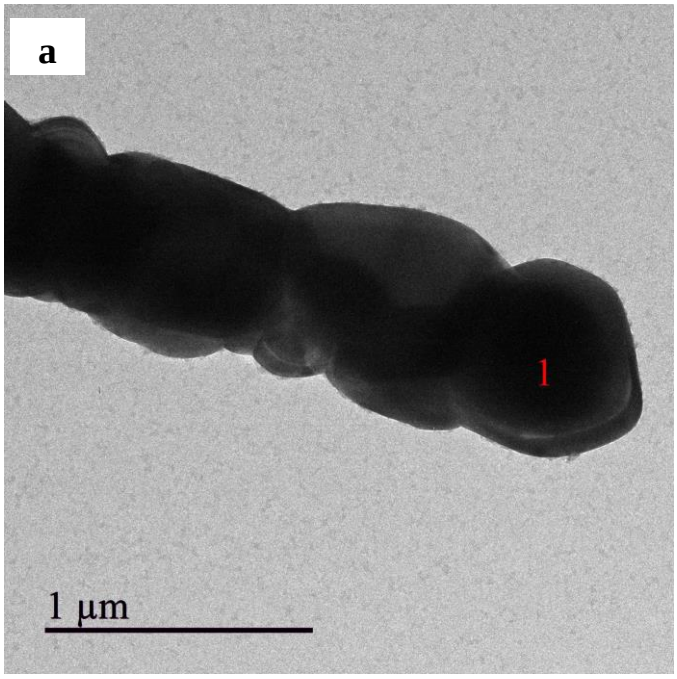

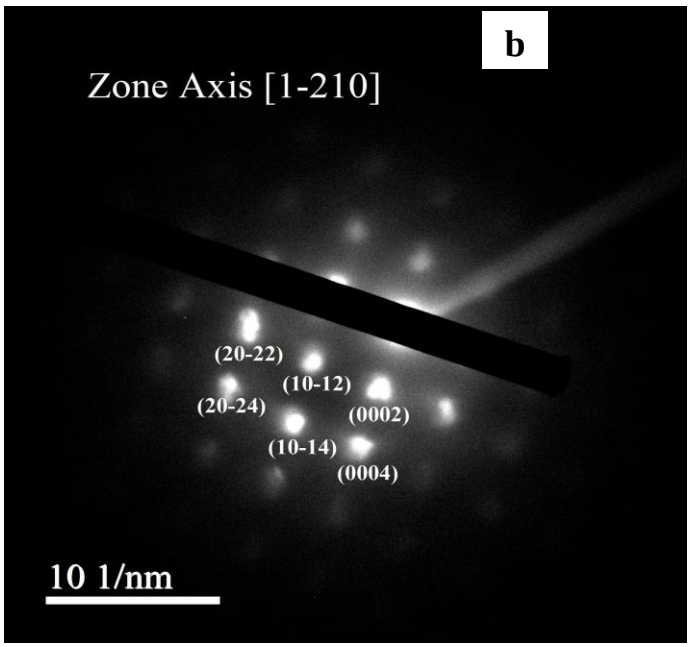

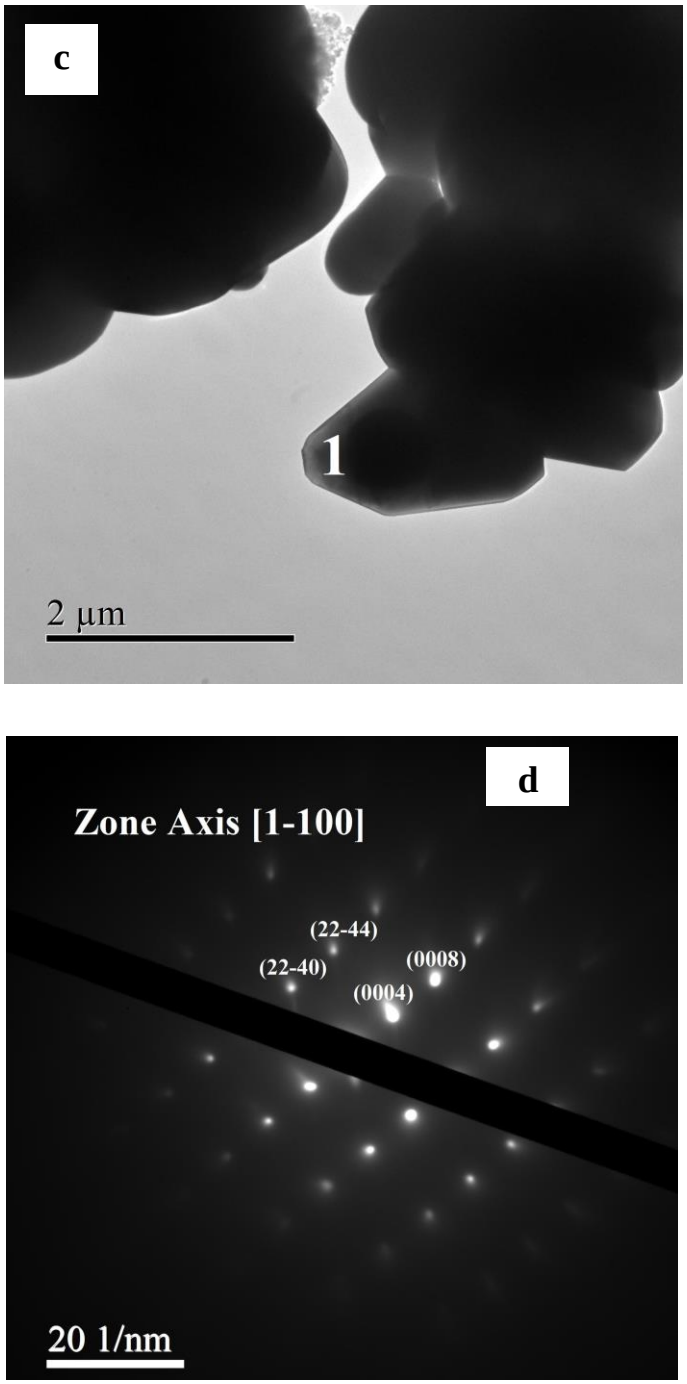

Figure 2.8 : TEM Image of ZnO synthesized using thermal decomposition of zinc oxalate nanorods (a) in absence of flux and (c) in presence of 1:1 NaCl-KCl. Electron Diffraction pattern obtained from particle marked 1 in the corresponding TEM for ZnO obtained using thermal decomposition of zinc oxalate nanorods (b) in absence of flux and (d) in presence of 1:1 NaCl-KCl.

Photocatalytic Studies

It has been previously reported that the nature of exposed surfaces influences the catalytic performance of the material[4, 37-40]. We used this approach to correlate our findings based on the analysis of the texture coefficient. For this, we carried out photodegradation of Rhodamine B dye using ZnO synthesized by decomposition of nanorods of zinc oxalate under various flux conditions.

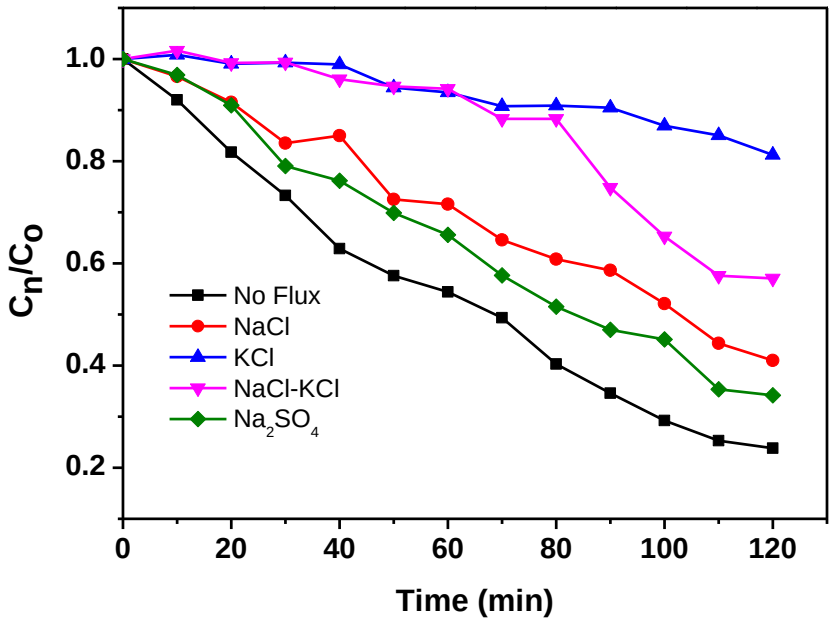

Figure 2.9: Photodegradation of Rhodamine B using ZnO obtained by decomposition of zinc oxalate (synthesized using reverse micellar route) in the absence of flux, with 1:1 mixture of NaCl-KCl, NaCl, KCl and Na_2SO_4 as flux.

It was observed (figure 2.9) that the photocatalytic activity of ZnO for the degradation of Rhodamine B dye followed the following order: No Flux > Na_2SO_4 > NaCl > NaCl-KCl > KCl. As observed from the order of texture coefficient, the order of degree of preferred orientation for non-polar $(11\bar{2}0)$ plane was NaCl-KCl > KCl > NaCl > Na_2SO_4 > No flux. The order of value of texture coefficient for polar (0002) plane was No Flux ≈ Na_2SO_4 > NaCl ≈ NaCl-KCl ≈ KCl. Thus, based on the above order, it can be inferred that though ZnO shows a greater degree of preferred orientation for $(11\bar{2}0)$ surface, the photocatalytic activity was greatly influenced by the number of particles with (0002) surfaces. Moreover, it can be

envisaged, the surface energy of (0002) is much higher than $(11\bar{2}0)$ and $(10\bar{1}0)$, suggesting that the (0001) exposed surfaces are more active for the catalytic reaction. It has also been reported[8] that polar exposed (0001) and $(000\bar{1})$ faces of ZnO are more active surfaces for photocatalysis. In our study, we observed that the order of photocatalytic activity for the degradation of Rhodamine B dye was also in agreement with the order of texture coefficient for (0002) plane. To ascertain whether the nature of the surfaces of ZnO is an influencing factor in the photodegradation of Rhodamine B, two other important factors viz. size distribution and surface area, which governs the catalytic behaviour were studied. Particle size distribution was plotted using SEM images (figure 2.10 a-e).

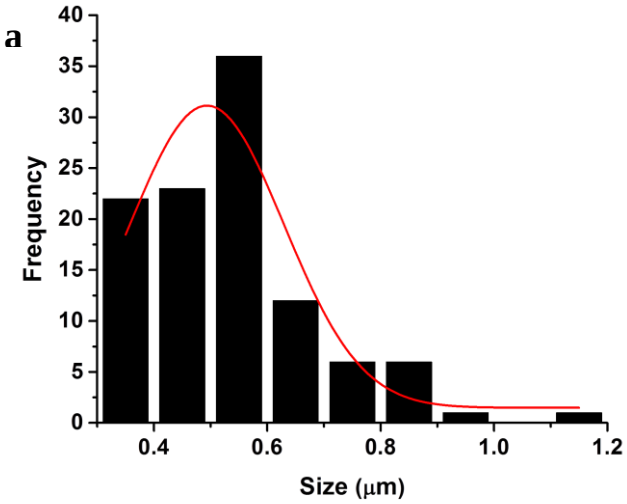

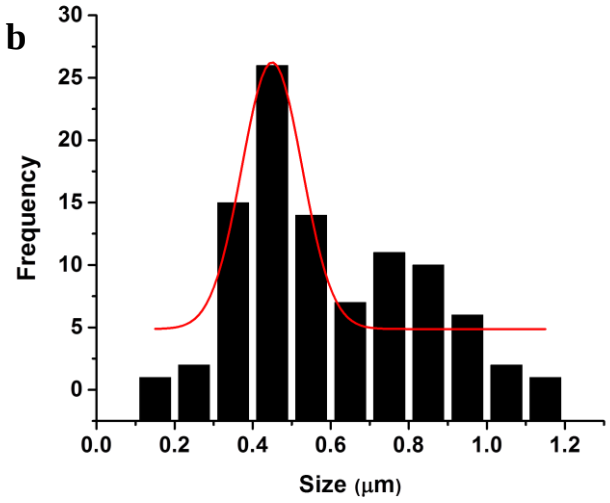

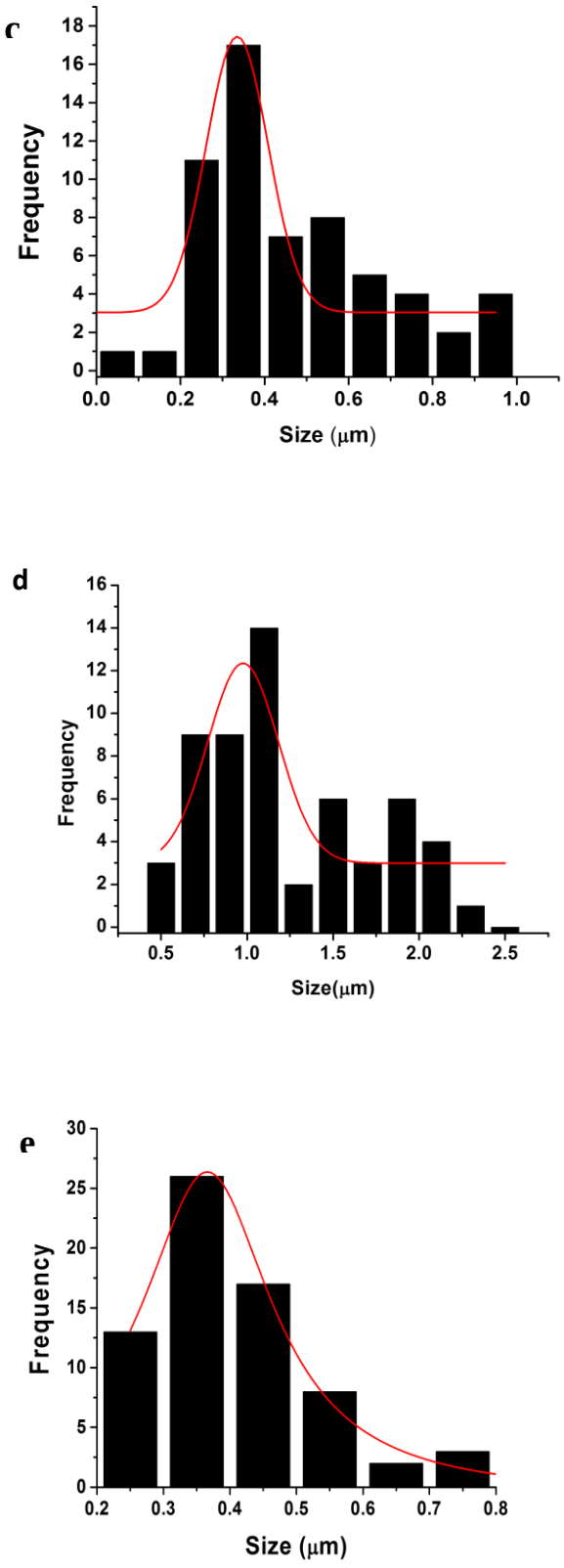

Figure 2.10: Histogram of particles obtained from SEM images (synthesized by reverse micellar route) (a) in absence of flux and presence of flux (b) NaCl, (c) KCl, (d) NaCl-KCl and (e) Na_2SO_4.

It was observed that there is a wide distribution of size ranging from 50 nm to 2 microns (varied with the type of flux that has been used for the synthesis) (Table 2.2).

Table 2.2 **:** Average Particle size obtained from Gaussian fitting of histograms of the particle size distribution for ZnO obtained by decomposition of zinc oxalate (synthesized by reverse micellar route) in presence and absence of flux.

Flux	*Average size (nm)*	*Maximum size (µm)*	*Minimum size (nm)*
No Flux	*490*	*1.15*	*350*
NaCl	*450*	*1.2*	*145*
KCl	*330*	*0.95*	*50*
NaCl-KCl	*980*	*2.3*	*500*
Na_2SO_4	*365*	*0.8*	*230*

The average size observed for these materials was also too large. Thus, based on a wide distribution of size with a large value of average particle size, it can be deciphered that size distribution may not be an influencing parameter on photocatalytic rates. Further, to check if the surface area (an important parameter that influences the photocatalytic rates), has influenced the photocatalytic degradation of RhB, surface area measurements were carried out. The surface area (Table 2.3) was observed to be less than $2m^2/g$ which is very less to have any influence on the photocatalytic rates.

Table 2.3 : BET surface area for ZnO samples obtained by decomposition of zinc oxalate (synthesized via Reverse Micellar route) in the presence and absence of flux

Flux	*Surface Area (m^2/g)*
No Flux	*1.5*
NaCl	*1.4*
KCl	*0.72*
NaCl-KCl	*1.2*
Na_2SO_4	*1.6*

Based on this, it is suggested that the trend observed for the photocatalytic activity of ZnO, synthesized under different flux conditions, is the effect of the nature of the exposed surface and is not influenced by the size and the surface area. The photocatalytic rates were majorly influenced by the nature of flux used during decomposition of the oxalate precursor which played a significant role in determining the degree of preferred orientation for the surfaces of ZnO, as observed from the analysis of texture coefficient.

Computational Studies

To understand the role of flux on the degree of preferred orientation (as observed from the value of texture coefficient) DFT based theoretical studies were carried out. It is known that the relative stability of different ZnO surfaces can be obtained from their surface energy values.[5] A comparison of surface energy values for the pristine surfaces obtained from previous theoretical studies as well as from our work are tabulated in Table 2.4.

Table 2.4: The comparison of surface energies for different ZnO surfaces, The surface energies for the polar surfaces was obtained from the plot of cleavage energy vs 1/D plot as discussed by Meyer and Marx.[8]

Surface	*Method*	$\gamma(J/m^2)$	*Reference*
(0001)	PBE+*U*	4.55*	**This work**
	PBE	3.50	Meyer, Marx[5]
	LDA	4.50	Meyer, Marx[5]
	PW91+*U*	3.71	Tang, Luo[6]
	PW91	3.00	Tang, Luo[6]
	B3LYP	4.00	Harrison[41]
$(10\bar{1}0)$	PBE+*U*	2.33	**This work**
	PBE	1.80	Meyer, Marx[5]
	LDA	2.30	Meyer, Marx[5]
	PW91+*U*	2.15	Tang, Luo[6]
	PW91	1.88	Tang, Luo[6]
	B3LYP	2.13	Harrison[41]
$(11\bar{2}0)$	PBE+*U*	2.37	**This work**
	PBE	1.90	Meyer, Marx[5]
	LDA	2.50	Meyer, Marx[5]
	PW91+*U*	2.21	Tang, Luo[6]
	PW91	1.94	Tang, Luo[6]
	B3LYP	4.10	Harrison[41]
$(10\bar{1}1)$	PBE+*U*	5.85	**This work**

The stability order of pristine ZnO surfaces $(10\bar{1}0)$> $(11\bar{2}0)$> (0001)> $(10\bar{1}1)$ indicates that at ideal vacuum and 0K, $(10\bar{1}0)$ surface would be the preferred surface. This indeed corroborate with a recent study by Shi et al.[42] At cryogenic temperature and ultra-high vacuum conditions the authors exclusively obtained the ZnO $(10\bar{1}0)$ surface. The facet formation may change depending on the growth conditions.

To evaluate the nature of interaction present between the ionic flux and ZnO dimers, we performed the Bader charge analysis for both the non-polar surfaces. From table 2.5, the charges on the Zn and O atoms (both surface and bulk) represents the mixed ionic and

covalent nature of bonding of ZnO. While the charges on Na atom and Cl atom clearly says that the flux is purely ionic in nature as there is no sign of covalent bonding. From the Bader population analysis (Table 2.5) it is clear that the interaction between the ZnO and the flux is purely ionic (i.e. as the ionic charges are completely localized on the Na^+ and Cl^- sites).

Table 2.5 : Bader charge analysis of the optimized flux containing ZnO $10\bar{1}0$- Surface.

Type of the atom	*Bader Charge* $10\bar{1}0$	*Bader Charge* $11\bar{2}0$
Flux affected O atom	-1.342	-1.3465
Flux affected Zn atom	1.228	1.2219
Na	0.99	0.99
Cl	-0.74	-0.76
Bulk O	1.234	-1.2608
Bulk Zn	-1.257	1.2449
Bare surface O atom	-1.2435	-1.2447
Bare surface Zn atom	1.2416	1.2436

Both the Zn and O atoms experience an upward displacement from their relaxed positions (figure 2.11, Table 2.6, figure 2.12).

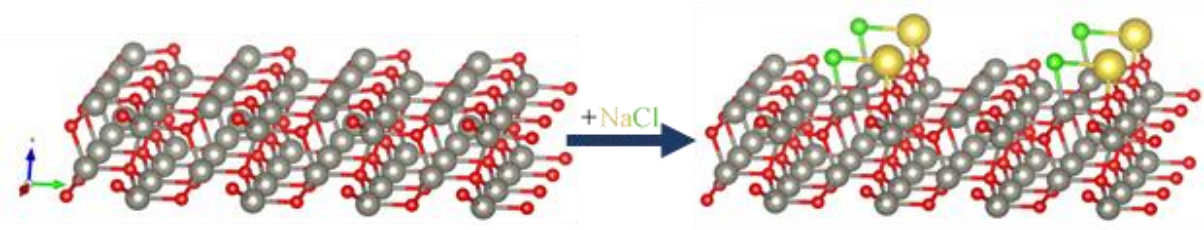

Figure 2.11: Accommodation of NaCl flux by relaxed ZnO $10\bar{1}0$- Surface.

Figure 2.11 schematically showed how the incoming flux is accommodated over the relaxed $10\bar{1}0$ surface. The Cl^- ions are accommodated by one Zn atom while the Na^+ ions are distributed by two O atoms which implies that the distribution of flux is not stoichiometric over surface atoms. The quantitative change of different structural parameters is tabulated in table 2.6.

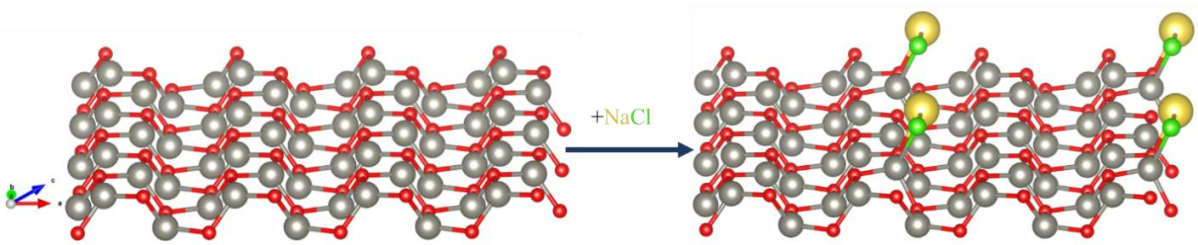

Figure 2.12 : Accommodation of NaCl flux by relaxed ZnO $11\bar{2}0$- Surface.

Figure 2.12 shows the accommodation of the NaCl flux by the ZnO $11\bar{2}0$ surface. It is clear from the figure that there is no non-stoichiometric distribution of the flux over the $11\bar{2}0$ surface as it was seen in the $10\bar{1}0$ surface. Hence it can be concluded that the $11\bar{2}0$ surface is less disturbed by the ionic flux. The disturbance induced by the flux changes the surface energy. The Na^+ ion on $(10\bar{1}0)$ is accommodated by two O atoms on the surface (Na-O distance 2.32±0.01 Å). On the other hand, for $(11\bar{2}0)$-surface there is no such possibility of non-stoichiometric distribution of the flux. Thus, the ionic flux induces more disturbances on $(10\bar{1}0)$-surface compared to the $(11\bar{2}0)$ surface.Table 2.6 quantitatively presents different structural parameters of the flux affected ZnO $10\bar{1}0$ and $11\bar{2}0$ surface. Table 2.6 led us to conclude that $11\bar{2}0$ is less disturbed and hence more stabilized in the presence of ionic flux. Surface energy (Figure 2.13) also reflects the same fact that $(10\bar{1}0)$-surface is more perturbed by the ionic flux.

Table 2.6 : Different structural parameters in the presence and absence of NaCl flux on ZnO $10\bar{1}0$ and $11\bar{2}0$ Surface.

Structural parameter	***Value*** $10\bar{1}0$	***Value*** $11\bar{2}0$
Flux affected surface ZnO distance	1.92 Å	1.95 Å
Bulk ZnO distance	1.93 Å	1.93 Å
Non-affected Surface ZnO distance	1.79 Å	1.81 Å
Na-O distance	2.32±0.01 Å	2.20 Å
Zn-Cl distance	2.25 Å	2.26 Å
Tilt angle (ω) relaxed surface	9.51^0	9.82^0
Tilt angle (ω) for flux affected dimer (figure 2.11)	2.16^0 / 11.48^0	4.15^0

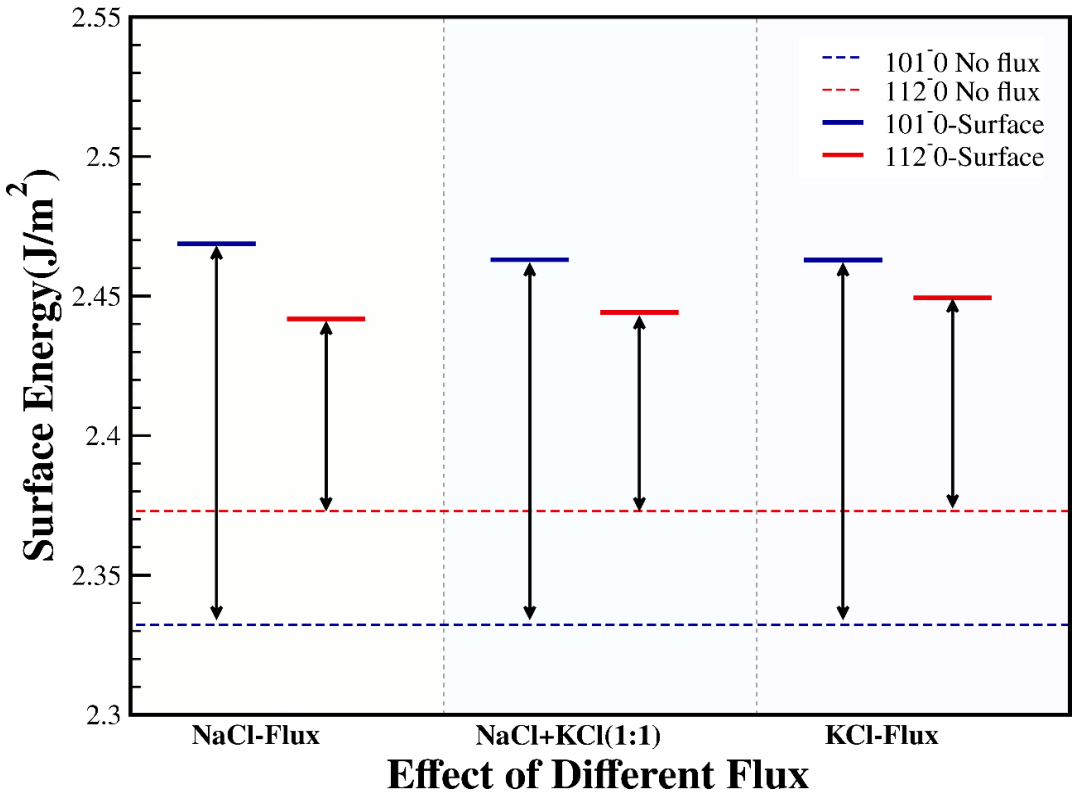

Figure 2.13.:The computed DFT+U surface energies were obtained for the $10\bar{1}0$ & $11\bar{2}0$ surfaces in presence of different ionic flux. In presence of ionic flux (irrespective of its nature) the $11\bar{2}0$ surface gets stabilized over the $10\bar{1}0$ surface and most like to be observed in the experiments and that's what it has been observed in this work.

Thus, from the above-mentioned studies, it was observed that $(11\bar{2}0)$ surfaces of ZnO is stabilized more than the $(10\bar{1}0)$ surface in the presence of ionic flux viz. NaCl, KCl, and 1:1 mixture of NaCl and KCl. This can be correlated to the value of texture coefficient (>1) obtained for $(11\bar{2}0)$ surfaces of ZnO, when the oxide was obtained by thermal decomposition of oxalate precursor in the presence of NaCl, KCl, and 1:1 mixture of NaCl and KCl. From the studies, one can foresee that the presence of ionic species during thermal decomposition of the precursor stabilizes the surface energy of a more destabilized surface. This results in the formation of structures having an increased degree of preferred orientation towards it. Moreover, the value of texture coefficient (an indicator for the degree of preferred orientation), the observed trend in photodegradation of Rhodamine B dye, and the calculation of surface energies corroborated well with each other. The results showcase that the introduction of flux with monovalent anion during the decomposition of the oxalate precursor helped in the growth of the non-polar $(11\bar{2}0)$ plane by overcoming the thermodynamic barrier wherein growth of $(10\bar{1}0)$ surfaces are preferred over $(11\bar{2}0)$ surfaces.

2.5 Conclusions:

Experimental and theoretical studies were carried out to understand the role of flux, introduced during the decomposition of oxalate precursor, in the formation of ZnO structures with a preferred orientation towards a particular plane. In the absence of any flux, the particles were randomly oriented and did not have a preferred orientation for a particular plane, as observed from the value of texture coefficient which was found to be close to 1. The degree of preferred orientation for the $(11\bar{2}0)$ plane was found to increase when the decomposition was carried out in the presence of flux. Theoretical studies reveal that the non-polar $(10\bar{1}0)$ and $(11\bar{2}0)$ surfaces experiences ionic flux completely via electrostatic interactions from the constituent ions of NaCl, KCl, and a mixture of NaCl-KCl. These surfaces get perturbed and change the surface energies and hence the relative faceting behavior. The $(10\bar{1}0)$ surface acts as the most stable surface in the absence of flux. On the other hand, the $(11\bar{2}0)$ surface becomes most stable in the presence of flux. This change in the stability of surfaces is reflected in the increased value of the texture coefficient (>1) for $(11\bar{2}0)$ surface of ZnO synthesized in the presence of these fluxes. Changing the flux from NaCl, KCl, and mixture of NaCl-KCl containing a monovalent anion to Na_2SO_4 changes the morphology to rod shape which was formed from an assembly of particles. This change in morphology is also reflected in the value of the texture coefficient. The influence of the

morphology of the precursor also affected the value of the texture coefficient. The trend observed from the photocatalytic degradation of Rhodamine B correlated with the analysis of the texture coefficient and also reinforced our conclusion that the nature of flux used during decomposition of oxalate precursor played a significant role in determining the degree of preferred orientation for the surfaces of ZnO. The results showcase that the introduction of flux with monovalent anion during the decomposition of the oxalate precursor helped in the growth of non-polar $(11\bar{2}0)$ surfaces by overcoming the thermodynamic barrier wherein growth of $(10\bar{1}0)$ surfaces are preferred over $(11\bar{2}0)$ surfaces. The study gives an understanding of the role of flux/ions/solvents on the degree of preferred orientation of other materials and can be used for the formation of faceted structures of a variety of materials that are synthesized at higher temperatures.

Acknowledgments

I would like to thank Dr. Ehesan Ali and Aritra Mukhopadhyaya for doing computation studies in this work.

This work is published as "**Aditi Vijay**, Aritra Mukhopadhyaya, Vipul Shrivastava, Devanshi Bhardwaj, Ashok K. Ganguli, Md. Ehesan Ali and Sonalika Vaidya*, Understanding the role of ionic flux on the polarity of the exposed surfaces of ZnO, Physical Chemistry Chemical Physics, 2020,22,15427-15436."

2.6 References:

1. Halder, A.; Kundu, P.; Viswanath, B.; Ravishankar, N., Symmetry and shape issues in nanostructure growth. *Journal of Materials Chemistry* **2010,** *20* (23), 4763-4772.
2. Bahl, S.; Suwas, S.; Chatterjee, K., The control of crystallographic texture in the use of magnesium as a resorbable biomaterial. *RSC Advances* **2014,** *4* (99), 55677-55684.
3. Kumar, M.; Kumar, A.; Abhyankar, A. C., Influence of Texture Coefficient on Surface Morphology and Sensing Properties of W-Doped Nanocrystalline Tin Oxide Thin Films. *ACS Applied Materials & Interfaces* **2015,** *7* (6), 3571-3580.
4. Sreeremya, T. S.; Krishnan, A.; Remani, K. C.; Patil, K. R.; Brougham, D. F.; Ghosh, S., Shape-Selective Oriented Cerium Oxide Nanocrystals Permit Assessment of the Effect of the Exposed Facets on Catalytic Activity and Oxygen Storage Capacity. *ACS Applied Materials & Interfaces* **2015,** *7* (16), 8545-8555.
5. Meyer, B.; Marx, D., Density-functional study of the structure and stability of ZnO surfaces. *Physical Review B* **2003,** *67* (3), 035403.
6. Tang, Q.-L.; Luo, Q.-H., Adsorption of CO_2 at ZnO: A Surface Structure Effect from DFT+U Calculations. *The Journal of Physical Chemistry C* **2013,** *117* (44), 22954-22966.
7. Mora-Fonz, D.; Lazauskas, T.; Farrow, M. R.; Catlow, C. R. A.; Woodley, S. M.; Sokol, A. A., Why Are Polar Surfaces of ZnO Stable? *Chemistry of Materials* **2017,** *29* (12), 5306-5320.
8. Huang, M.; Weng, S.; Wang, B.; Hu, J.; Fu, X.; Liu, P., Various Facet Tunable ZnO Crystals by a Scalable Solvothermal Synthesis and Their Facet-Dependent Photocatalytic Activities. *The Journal of Physical Chemistry C* **2014,** *118* (44), 25434-25440.
9. Chang, J.; Ahmed, R.; Wang, H.; Liu, H.; Li, R.; Wang, P.; Waclawik, E. R., ZnO Nanocones with High-Index $\{10\bar{1}1\}$ Facets for Enhanced Energy Conversion Efficiency of Dye-Sensitized Solar Cells. *The Journal of Physical Chemistry C* **2013,** *117* (27), 13836-13844.
10. Tasker, P. W., The stability of ionic crystal surfaces. *Journal of Physics C: Solid State Physics* **1979,** *12* (22), 4977-4984.
11. Garg, N.; Scholl, C.; Mohanty, A.; Jin, R., The role of bromide ions in seeding growth of Au nanorods. *Langmuir* **2010,** *26* (12), 10271-10276.
12. Song, Z.; Zu, R.; Liu, X.; He, L.; Liu, Q., Role of flux on synthesis of poly single crystals of Ce3+ doped yttrium aluminum garnet. *Crystal Research and Technology* **2016**.
13. Liu, J.; Chen, G.; Yu, Y.; Wu, Y.; Zhou, M.; Zhang, W.; Qin, H.; Lv, C.; Fu, W., Controllable and facile synthesis of nearly monodisperse 18-facet indium hydroxide polyhedra. *New Journal of Chemistry* **2015,** *39* (3), 1930-1937.
14. Barik, R.; Mohapatra, M., Solvent mediated surface engineering of α-Fe_2O_3 nanomaterials: facet sensitive energy storage materials. *Crystal Engineering Communication* **2015,** *17* (47), 9203-9215.

15. Noureldine, D.; Anjum, D. H.; Takanabe, K., Flux-assisted synthesis of $SnNb_2O_6$ for tuning photocatalytic properties. *Physical Chemistry Chemical Physics* **2014,** *16* (22), 10762-10769.
16. Shanker, V.; Ganguli, A. K., Comparative study of dielectric properties of $MgNb_2O_6$ prepared by molten salt and ceramic method. *Bulletin of Materials Science* **2003,** *26* (7), 741-744.
17. Nangia, S.; Thirumal, M.; Ganguli, A. K.; Gai, P. L., A New Form of MgTa2O6 obtained by the Molten Salt Method. *Microscopy and Microanalysis* **2002,** *8* (S02), 1414-1415.
18. Xu, C.; Liu, Y.; Xu, G.; Wang, G., Preparation and characterization of CuO nanorods by thermal decomposition of CuC 2 O 4 precursor. *Materials Research Bulletin* **2002,** *37* (14), 2365-2372.
19. Xu, C.; Xu, G.; Wang, G., Preparation and characterization of NiO nanorods by thermal decomposition of NiC_2O_4 precursor. *Journal of materials science* **2003,** *38* (4), 779-782.
20. Jiang, Z.-Y.; Xu, T.; Xie, Z.-X.; Lin, Z.-W.; Zhou, X.; Xu, X.; Huang, R.-B.; Zheng, L.-S., Molten Salt Route toward the Growth of ZnO Nanowires in Unusual Growth Directions. *The Journal of Physical Chemistry B* **2005,** *109* (49), 23269-23273.
21. Ahmad, T.; Vaidya, S.; Sarkar, N.; Ghosh, S.; Ganguli, A. K., Zinc oxalate nanorods: a convenient precursor to uniform nanoparticles of ZnO. *Nanotechnology* **2006,** *17* (5), 1236.
22. Zaidi, Z.; Vaghasiya, K.; Vijay, A.; Sharma, M.; Verma, R. K.; Vaidya, S., Hollow ZnO from assembly of nanoparticles: photocatalytic and antibacterial activity. *Journal of Materials Science* **2018,** *53* (21), 14964-14974.
23. Hohenberg, P.; Kohn, W., Inhomogeneous Electron Gas. *Physical Review* **1964,** *136* (3B), B864-B871.
24. Kohn, W.; Sham, L. J., Self-Consistent Equations Including Exchange and Correlation Effects. *Physical Review* **1965,** *140* (4A), A1133-A1138.
25. Kresse, G.; Furthmüller, J., Efficient iterative schemes for ab initio total-energy calculations using a plane-wave basis set. *Physical Review B* **1996,** *54* (16), 11169-11186.
26. Monkhorst, H. J.; Pack, J. D., Special points for Brillouin-zone integrations. *Physical Review B* **1976,** *13* (12), 5188-5192.
27. Ceperley, D. M.; Alder, B. J., Ground State of the Electron Gas by a Stochastic Method. *Physical Review Letters* **1980,** *45* (7), 566-569.
28. Perdew, J. P.; Zunger, A., Self-interaction correction to density-functional approximations for many-electron systems. *Physical Review B* **1981,** *23* (10), 5048-5079.
29. Perdew, J. P.; Burke, K.; Ernzerhof, M., Generalized Gradient Approximation Made Simple. *Physical Review Letters* **1996,** *77* (18), 3865-3868.
30. Mosey, N. J.; Carter, E. A., Ab initio evaluation of Coulomb and exchange parameters for DFT+U calculations. *Physical Review B* **2007,** *76* (15), 155123.

31. Vaidya, S.; Rastogi, P.; Agarwal, S.; Gupta, S. K.; Ahmad, T.; Antonelli Jr, A. M.; Ramanujachary, K.; Lofland, S.; Ganguli, A. K., Nanospheres, nanocubes, and nanorods of nickel oxalate: control of shape and size by surfactant and solvent. *The Journal of Physical Chemistry C* **2008,** *112* (33), 12610-12615.
32. Qamar, M.; Lofland, S. E.; Ramanujachary, K. V.; Ganguli, A. K., Magnetic and photocatalytic properties of nanocrystalline $ZnMn_2O_4$. *Bulletin of Materials Science* **2009,** *32* (3), 231-237.
33. Ubbelohde, A., The role of diffusion potentials in the growth of ionic crystals. *Discussions of the Faraday Society* **1949,** *5*, 180-182.
34. Niu, W.; Zheng, S.; Wang, D.; Liu, X.; Li, H.; Han, S.; Chen, J.; Tang, Z.; Xu, G., Selective synthesis of single-crystalline rhombic dodecahedral, octahedral, and cubic gold nanocrystals. *Journal of the American Chemical Society* **2008,** *131* (2), 697-703.
35. Zhang, Y.; Sun, S.; Zhang, X.; Tang, L.; Song, X.; Yang, Z., Sulfate-ion-assisted galvanic replacement tuning of silver dendrites to highly branched chains for effective SERS. *Physical Chemistry Chemical Physics* **2014,** *16* (35), 18918-18925.
36. Liu, L.; Gu, X.; Ji, Z.; Zou, W.; Tang, C.; Gao, F.; Dong, L., Anion-assisted synthesis of TiO_2 nanocrystals with tunable crystal forms and crystal facets and their photocatalytic redox activities in organic reactions. *The Journal of Physical Chemistry C* **2013,** *117* (36), 18578-18587.
37. Zhou, K.; Li, Y., Catalysis Based on Nanocrystals with Well-Defined Facets. *Angewandte Chemie International Edition* **2012,** *51* (3), 602-613.
38. Zheng, Z.; Huang, B.; Lu, J.; Qin, X.; Zhang, X.; Dai, Y., Hierarchical TiO_2 Microspheres: Synergetic Effect of {001} and {101} Facets for Enhanced Photocatalytic Activity. *Chemistry – A European Journal* **2011,** *17* (52), 15032-15038.
39. Jiang, J.; Zhao, K.; Xiao, X.; Zhang, L., Synthesis and Facet-Dependent Photoreactivity of BiOCl Single-Crystalline Nanosheets. *Journal of the American Chemical Society* **2012,** *134* (10), 4473-4476.
40. Lizandara-Pueyo, C.; Morant-Miñana, M. C.; Wessig, M.; Krumm, M.; Mecking, S.; Polarz, S., Biomimetic crystallization of anisotropic zinc oxide nanoparticles in the homogeneous phase: shape control by surface additives applied under thermodynamic or kinetic control. *RSC Advances* **2012,** *2* (12), 5298-5306.
41. Wander, A.; Harrison, N. M., The stability of polar oxide surfaces: The interaction of H_2O with ZnO(000$\bar{1}$) and ZnO(000$\bar{1}$). *The Journal of Chemical Physics* **2001,** *115* (5), 2312-2316.
42. Shi, H.; Yuan, H.; Li, Z.; Wang, W.; Li, Z.; Shao, X., Low-Temperature Heterolytic Adsorption of H_2 on ZnO(10$\bar{1}$0) Surface. *The Journal of Physical Chemistry C* **2019,** *123* (21), 13283-13287.

Chapter 3

Tuning the Morphology and Exposed Facets of $SrTiO_3$ Nanostructures for the Photocatalytic Dye Degradation and Hydrogen Evolution

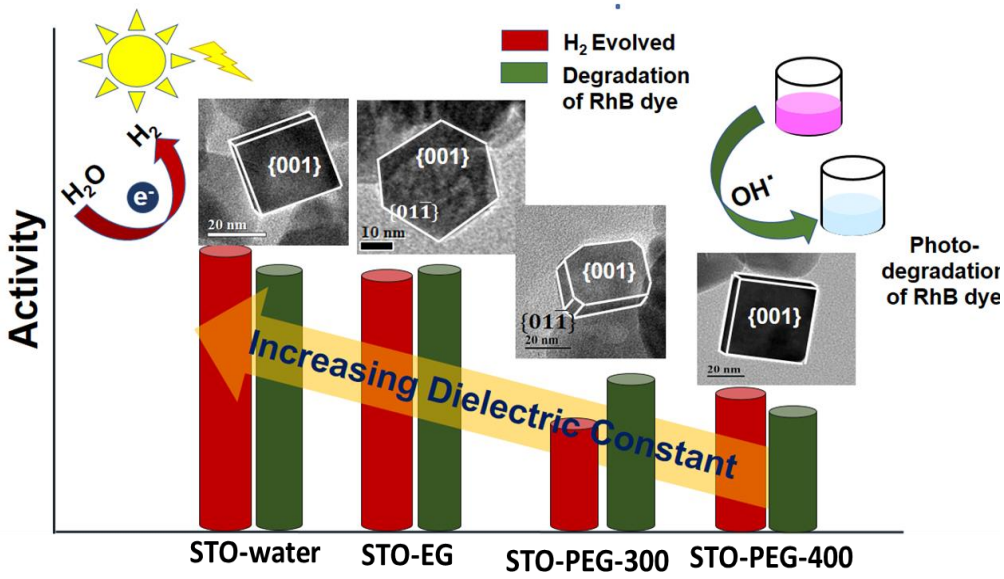

Chapter 3

Tuning the Morphology and Exposed Facets of $SrTiO_3$ Nanostructures for the Photocatalytic Dye Degradation and Hydrogen Evolution

Abstract

This study aims at investigating the role of the dielectric constant of polyols on the size and morphology of $SrTiO_3$ nanostructures and thereby its effect on the photocatalytic performance of the oxide. Among the various available polyols, we have used ethylene glycol (EG), polyethylene glycol-300 (PEG-300), and polyethylene glycol-400 (PEG-400) for our study. The effect of polyols was also compared by taking water as the solvent instead of polyols. Herein, we discuss how, change in the synthetic methodology i.e. change of the solvent, affects the defects, crystallite size, and nature of facet. We observed that the particle size decreased with an increase in the dielectric constant of the solvent (water and polyols). We also observed that the shape (nanocubes with water, nanocuboids with PEG-400, edge truncated nanocuboids with PEG-300, and hexagonal-shaped particles assembled to form a flower-like nanostructure with EG as solvent) and the nature of exposed facets were also affected by the dielectric constant of the solvent. The top exposed facet of the synthesized $SrTiO_3$ nanostructures was observed to be [001], (for $SrTiO_3$ nanostructures synthesized using different solvents) with $[01\bar{1}]$ facet, observed for sample synthesized using EG and PEG-300 as the solvent. The effect of size and shape on their photocatalytic performance (both photodegradation of Rhodamine B (RhB) and hydrogen evolution) was also evaluated.

Keywords: Polyols, morphology, facets, Photocatalysis, hydrogen evolution.

3.1 Introduction:

In recent years, photocatalytic water splitting has gained much attraction due to its potential application in the field of hydrogen energy production by solar energy conversion. This process utilizes natural sources i.e. solar energy and water for the production of hydrogen which is considered a clean source of energy. Morphology [1-2], crystallinity and crystal structure, and the formation of heterostructures[3] are a few important parameters that play a major role in tuning the photocatalytic properties of the materials. By changing these parameters, the efficiency for separation of photogenerated charge carrier can be enhanced which improves the photocatalytic behavior of the material. Various efforts are being put into this field to form nanostructures by the introduction of structure-directing agents (organic ligands, ions, etc.) during synthesis. It has been reported by Liao et.al that the shape and size of TiO_2 nanoparticles can be controlled by variation of surfactant during the synthesis which affected the photocatalytic property of the material[4].

Among various materials, semiconductor-based photocatalysts mainly metal oxides proved to be suitable candidates for water splitting because of their stability, light absorption, charge transfer, and excited-state lifetime properties. There are several reports in the literature on metal oxide-based photocatalysts such as TiO_2[5-6], $SrTiO_3$[7], Ta_2O_5[8], etc. Among all the binary or ternary metal oxides, perovskite-based metal oxides proved to be unique photocatalysts because of their interesting photophysical properties[9]. Among various perovskite, $SrTiO_3$ has been extensively studied for photocatalytic activity[10-11]. Several attempts have been made to improve the photocatalytic properties of $SrTiO_3$. For instance, photocatalytic properties of $SrTiO_3$ nanostructures were shown to enhance by doping of metal ions at both, A and B sites[12-13], by the formation of assembled mesoporous structure[14], by introducing plasmonic nanoparticles with the oxide[15], by tuning the facets[16], or by the creation of oxygen vacancies[17].

In this chapter, we discuss the effect of change in the dielectric constant of polyols on the size and morphology of $SrTiO_3$ nanostructures. We also discuss how, change in the synthetic methodology affects the defects, crystallite size, and nature of facet. The effect of size and shape on their photocatalytic performance (both photodegradation of RhB and hydrogen evolution) was also evaluated. To the best of our knowledge, there has been only one report on the photocatalytic performance of $SrTiO_3$, synthesized with titanium triethanolamine complex as the

titanium source and by varying the nature of polyalcohols (ethylene glycol (EG), Diethylene glycol (DEG), trimethylene glycol (TMG)). The authors observed that $SrTiO_3$ synthesized using water/EG mixture as solvent exhibited maximum hydrogen evolution[18]. In our studies, we have not used any other complexing agent like triethanolamine as there is a possibility that these complexing agents have either synergistic or anti-synergistic effects on the size, shape and faceting behavior which would be difficult to ascertain. Keeping these arguments in our mind, we used only polyalcohols as the solvent (without any other complexing agents) to establish their role on various parameters affecting the photocatalytic behavior of $SrTiO_3$ nanostructures.

3.2 Experimental:

3.2.1: Materials and Methods:

Strontium nitrate ($Sr(NO_3)_2$, 99%], Ethylene glycol (EG) (99%), Polyethylene glycol (PEG)-400 (99%), Methanol (ACS grade), sodium sulphate (99%) were purchased from Merck. Polyethylene glycol (PEG)-300 was purchased from TCI. Titanium isopropoxide (97%) and sodium sulfite (98%) were purchased from Sigma-Aldrich.

$SrTiO_3$ with different morphologies was prepared by using the solvothermal method. For the synthesis, 1.48 mL of titanium isopropoxide was added to water (30 mL). To this, we added 1.058 g of strontium nitrate followed by a dropwise addition of 5 mL of 5 M NaOH solution to obtain suspension of white precipitates. The volume of the final mixture was maintained at 35 mL. The reaction mixture was then sealed in a 50 mL Teflon-lined stainless steel vessel and kept in an oven at 180^o C for 24 h. The resultant precipitates were washed several times with distilled water and absolute ethanol and dried in an oven at 80^oC for 8h. To study the effect of polyols on the morphology of $SrTiO_3$, the methodology for the synthesis was the same with water being replaced by EG, PEG-300, and PEG-400 as the solvent. A schematic illustrating the methodology adopted for the synthesis is shown in figure 3.1. For convenience, we refer to the sample as STO1, STO2, STO3 and STO4 for $SrTiO_3$ synthesized using water, EG, PEG-300, and PEG-400 as the solvent respectively.

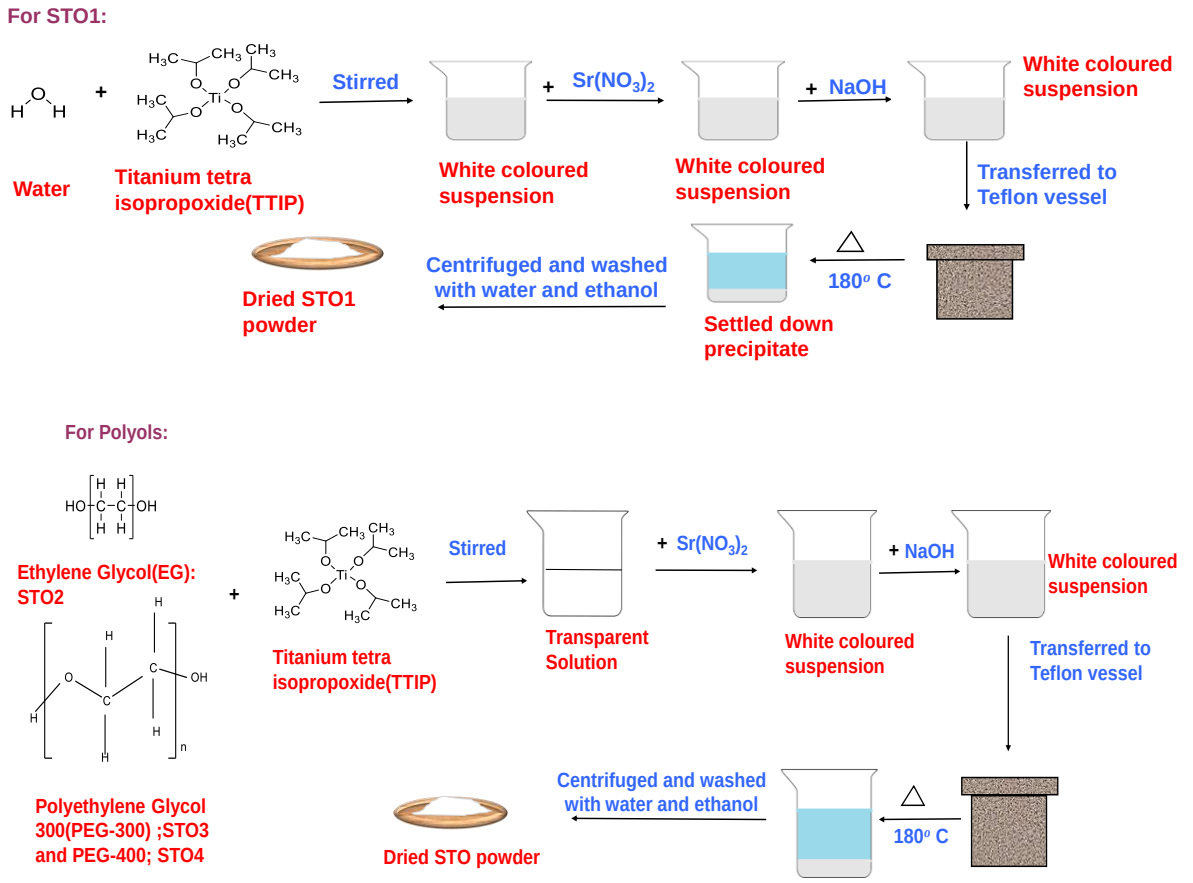

Figure 3.1: Schematic illustrating the synthetic methodology adopted for the synthesis of $SrTiO_3$ nanostructures.

3.2.2: Characterization:

The crystal structure and the phase purity of $SrTiO_3$ samples were characterized using Eco D8 Advance Bruker PXRD with a Cu-Kα radiation source (λ= 0.15406 nm). The instrument was operated at 40 kV and 25 mA at a scanning step of 0.02 in the 2θ range of 10–80 degrees. Crystallite size was calculated using Topas v5 software by loading the structure file corresponding to strontium titanate. Transmission electron microscope studies (TEM) studies were carried out on JEOL, JEM-2100 operated at an accelerating voltage of 200 kV. The samples were prepared by dispersing the powder samples in ethanol and drop-casting on a

carbon-coated copper grid. FESEM studies were carried out on a HITACHI SU8010 Scanning Electron Microscope. The samples were mounted on a carbon tape and coated with Pt. Raman studies were carried out using WI Tec's Raman microscope, alpha 300 R. The samples for Raman studies were prepared by drop-casting the dispersion of the oxides, prepared in ethanol, onto a silicon wafer. FTIR-ATR studies were done using, Bruker VERTEX70. Diffuse reflectance spectra of the solid samples were recorded on UV–visible spectrophotometer Shimadzu UV-2600, which was operated in a solid-state mode in the wavelength range of 200–800 nm with barium sulfate as the reference. The bandgap of the $SrTiO_3$ nanostructures was calculated using to Kubleka-Munk (K-M) equation. Nitrogen adsorption-desorption isotherms were obtained with Quanta Chrome Model Q2, and the specific surface area was determined using the multi-point BET method. Photoluminescence and time-resolved photoluminescence studies were carried out on Horiba's TCSPC at the excitation wavelength of 357 nm. Decay curves in the time-resolved photoluminescence spectra were fitted with a double exponential decay equation:

$$y = A_1 e^{(-x/\tau_1)} + A_2 e^{(-x/\tau_2)} + y_0 \qquad (3.1)$$

The average lifetime of the samples was calculated using the following equation:

$$\tau = \frac{\sum_{i=1}^{n} A_i \tau_i^2}{\sum_{i=1}^{n} A_i \tau_i} \qquad (3.2)$$

Transient photocurrent response measurement was performed on Metrohm Multi Autolab using a three-electrode electrochemical workstation with 350 W Xe lamp as a source of irradiation at 0.7 V vs. Ag/AgCl. For preparing the working electrode, 15 mg of STO samples were dispersed (through ultra-sonication for 1 h) in 0.5 mL of isopropyl alcohol containing 10µL of Nafion resin solution. The dispersed samples were deposited on a cleaned FTO substrate having an area of 1 cm^2 and dried for further use. The sample coated on FTO substrate was taken as a working electrode, 3M Ag/AgCl was taken as the reference electrode, and platinum wire was used as a counter electrode. All measurements were carried out in a 50 mL vessel containing 0.5M Na_2SO_4 as an electrolyte, saturated with Argon for 30 minutes.

3.2.3 Photocatalytic activity:

3.2.3.1. Dye Degradation:

For the photocatalytic degradation of Rhodamine B (RhB), 25 mg of the catalyst was dispersed in 25 mL of 8 μM (RhB) dye solution and the mixture was irradiated with UV light, using a medium pressure Hg lamp (250 W). The dye solution was kept in dark for 30 minutes to observe the adsorption capacity of the catalyst used. 1 mL of the sample was taken out from the solution at an interval of 30 minutes. The photodegradation of RhB dye was evaluated from the reduction in the intensity of the absorption band of RhB. The percentage of dye degradation was calculated according to the equation given below:

$$Degradation\,\% = \frac{C_o - C_n}{C_o} \times 100 \qquad (3.3)$$

where C_o represents the initial concentration of the RhB dye and C_n denotes the concentration of the dye at a different time interval.

3.2.3.2 Photocatalytic evaluation of hydrogen gas:

Photocatalytic reactions for hydrogen evolution from water were conducted in a quartz reactor of capacity 140 mL with top irradiation. 40 mg of the sample was dispersed into 0.05 M Na_2SO_3 aqueous solution (40 mL) through ultra-sonication. After sonication, the solution was purged with Ar gas for 30 minutes, to remove dissolved oxygen from the solution. The mixture was irradiated with a 250 W medium pressure Mercury Vapor lamp and the catalytic performance was checked for 5h. 1 mL of the gas sample was taken out at an interval of one hour from the reactor and injected into GC through the side injection method. The amount of H_2 gas was determined by using an offline thermal conductivity detector in gas chromatography (GC, Perkin Elmer Clarus 680).

Apparent quantum yield (AQY) for hydrogen evolution gas was calculated using equation 3.4.

$$AQY = \frac{2nN_A hc}{PS\lambda t} \times 100 \qquad (3.4)$$

Where, n is the amount of hydrogen evolved after 5 hours of reaction; N_A is Avogadro's constant (6.022×10^{23} mol^{-1}); h is Planck's constant (6.63×10^{-34} Js); c is the speed of the light (3×10^{10} cm s^{-1}); P is the power density of the incident light measured using Ray virtual radiation actinometer, Newport, Model 91150V (11.83×10^{-3} Wcm^{-2}); S is the irradiation area (12.6 cm^2); λ is the representative wavelength of the incident light (using radiation spectrum of the lamp, 368 nm (368×10^{-7} cm)) and t is the time duration of incident light (18000 s).

3.3. Results and discussion:

Figure 3.2a shows the PXRD pattern of the $SrTiO_3$ obtained after solvothermal treatment. All the reflection planes could be indexed to the cubic unit cell (JCPDS card no.00-035-0734) having a space group, $Pm\bar{3}m$. No impurity peaks were observed in any of the samples. The crystallite size, calculated using Topas v5, for all the samples is tabulated in Table 3.1. From figure 3.2b, it is observed that the average crystallite size increases with the change in the solvent from water to PEG-400, varying in their dielectric constant (used as a solvent for the synthesis of the $SrTiO_3$).

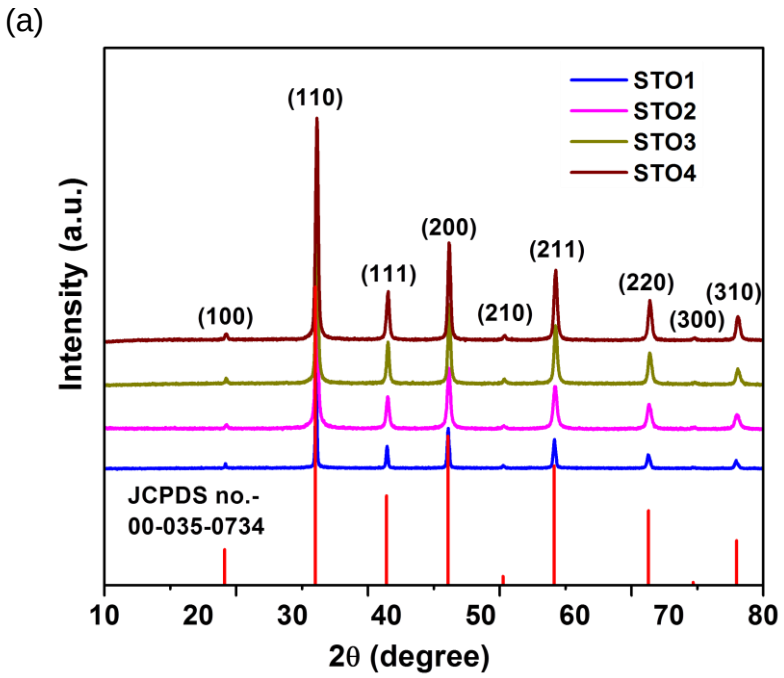

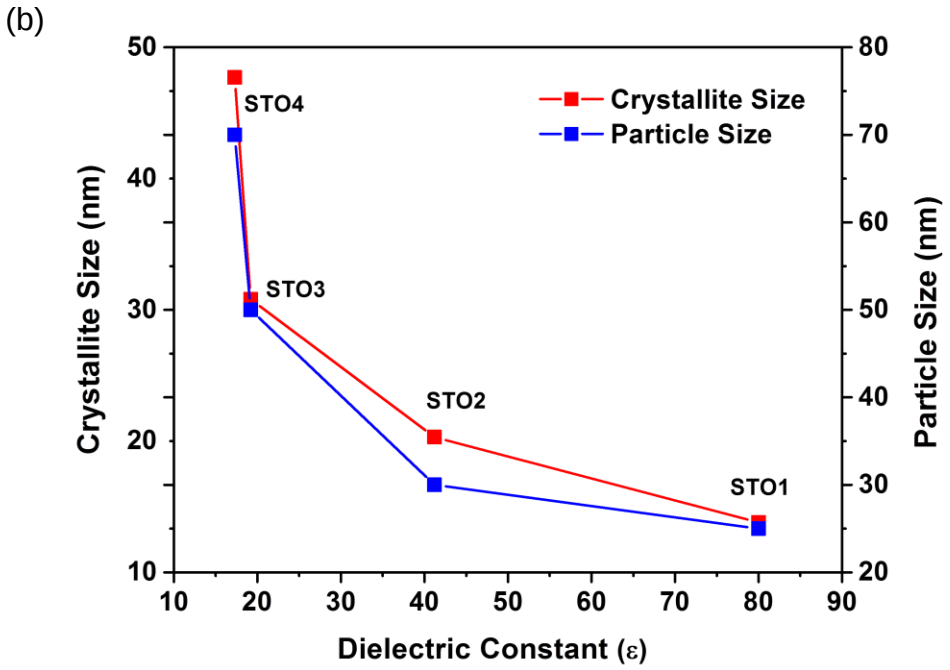

Figure 3.2 : (a) PXRD plot of $SrTiO_3$ synthesized using water (STO1), EG (STO2), PEG-300 (STO3), and PEG-400 (STO4). (b) Plot showing the variation of crystallite and particle size with the dielectric constant of the solvents.

Table 3.1: The average crystallite size was obtained from PXRD data, bandgap, and BET surface area of the $SrTiO_3$ nanostructures.

Samples	Crystallite size (nm)	Band Gap (direct) (eV)	BET Surface Area (m^2/g)
STO1	14	3.6	54
STO2	20	3.7	49
STO3	31	3.3	27
STO4	48	3.5	17

To check the effect of the dielectric constant on the size of the particles, TEM studies were carried out on synthesized $SrTiO_3$ nanostructures. Nanocubes with a size of ~25 nm and sharp boundaries were formed for STO1 (figure 3.3a). On changing the solvent to EG (STO2), flower-like nanostructures, formed from the assembly of hexagonal-shaped particles of size ~30 nm, were observed (figure 3.3b). When a higher chain length of the polyols, viz PEG-300 and PEG-400, were used as a solvent, edge-truncated nanocuboids and nanocuboids with sharp boundaries were formed respectively. The size of these nanostructures ranged from 30-70 nm for STO3 (figure 3.3c) and 40-100 nm for STO4 (figure 3.3 d).

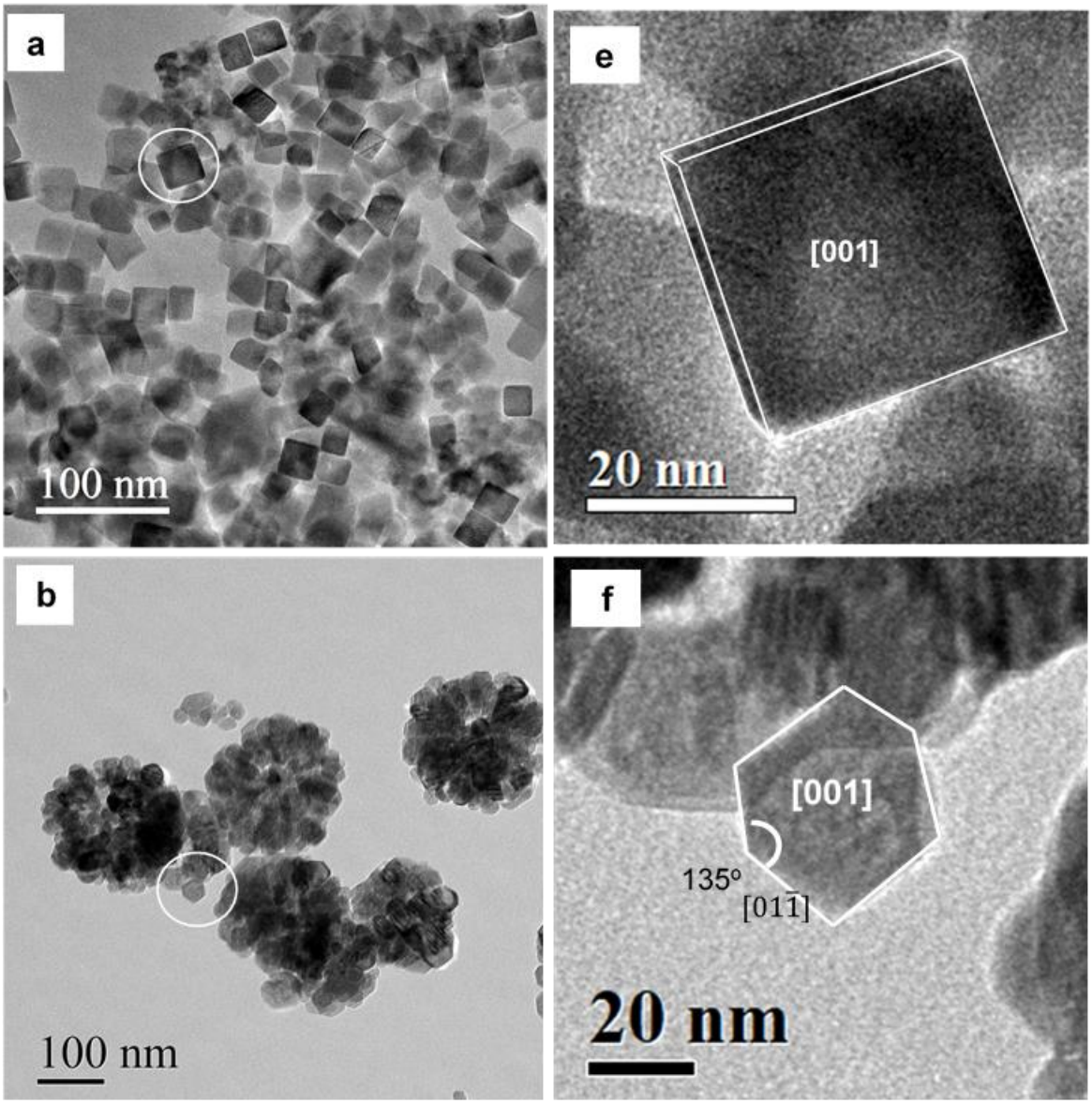

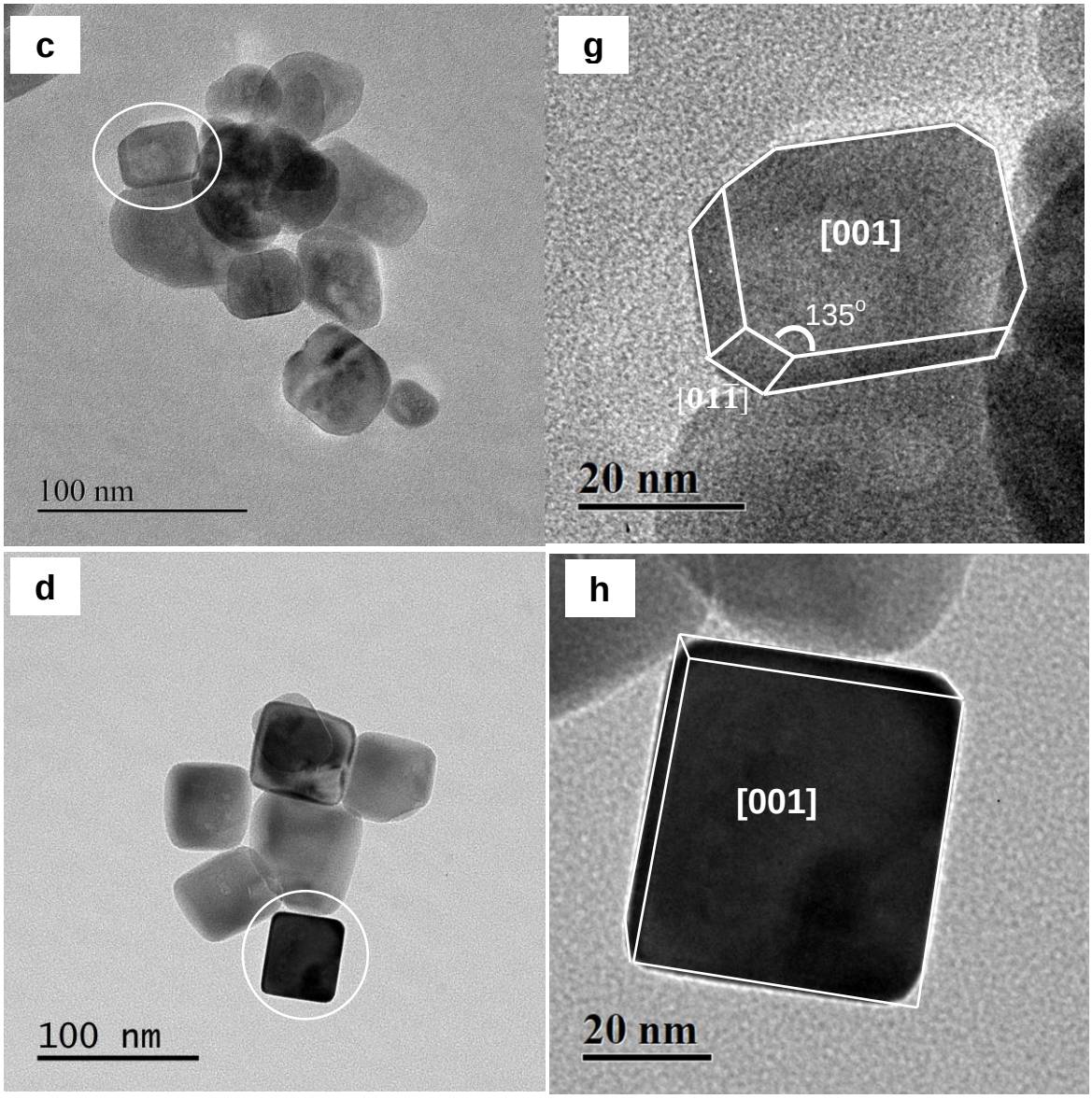

Figure 3.3: TEM images of $SrTiO_3$ and the corresponding enlarged image of a particle showing the nature of exposed facet synthesized using (a, e) water (STO1), (b, f) EG (STO2), (c, g) PEG-300 (STO3) and (d, h) PEG-400 (STO4).

With water as the solvent, cubes having a size of ~ 25 nm were obtained (figure 3.4(a)). On changing the solvents from water to polyols viz. EG, PEG-300, and PEG-400, the shape changed from clusters formed from small nanoparticles (STO2, figure 3.4(b)) to large cuboids (STO3 and STO4, figure 3.4(c) and 3.4(d) respectively).

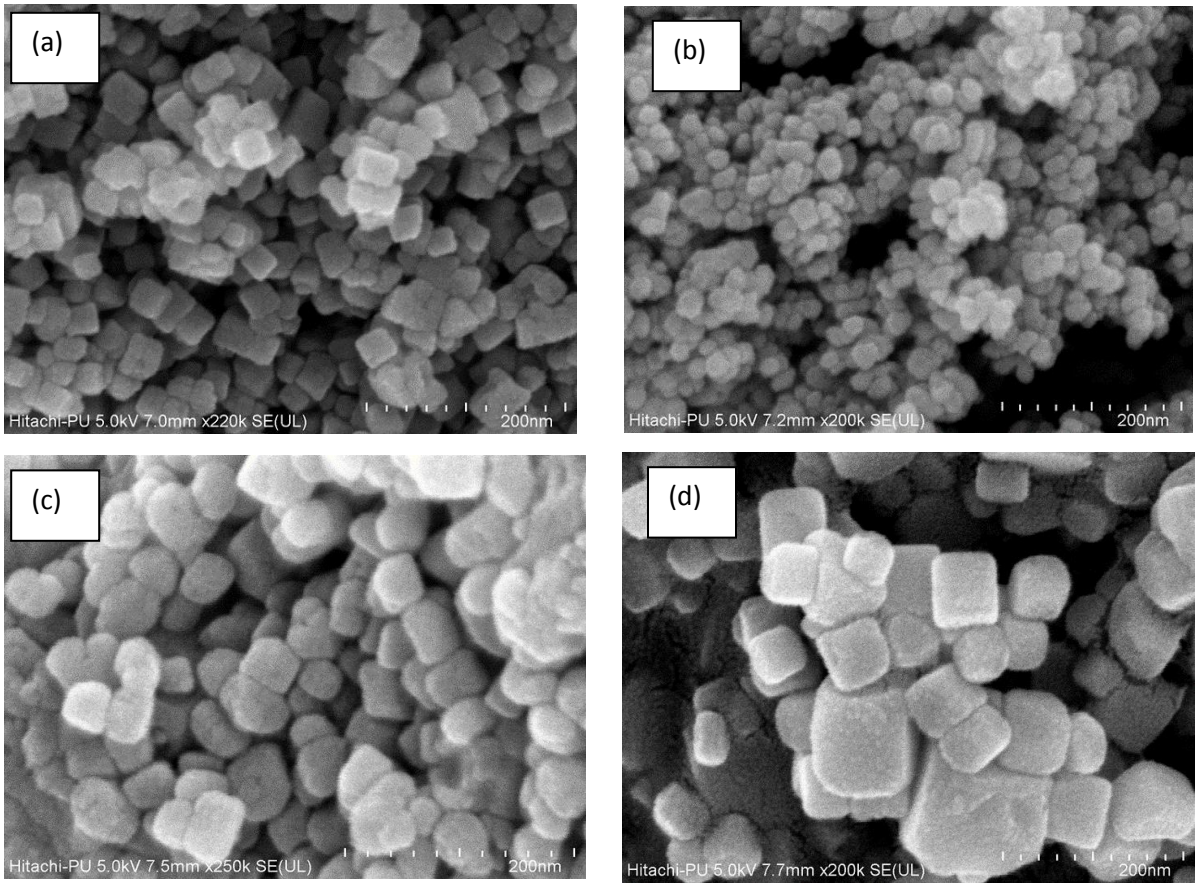

Figure 3.4: FESEM images of (a) STO1, (b) STO2, (c) STO3 and (d) STO4.

It was observed that there was a decrease in both crystallite size (obtained from XRD) and particle size (obtained using TEM) with an increase in the dielectric constant of the polyols (figure 3.2b). It is to be noted that the dielectric constant[19] for water is 80, EG: 41.2, PEG-300: 19.2, and PEG-400: 17.3. Such effect was also observed by Wu et.al [20] that the solvent with the lowest dielectric constant resulted in the formation of nanostructures with the largest crystallite size. This effect was attributed to the fact that the low dielectric constant of the solvent results in lower solubility of solid metal oxide (due to a decrease in the solvation energy) i.e. higher degree of supersaturation. As a result, a large number of nuclei are formed, that is, more nucleation sites for the growth of particles. These nuclei are bound by the glycol and polyols having a terminating –OH group, which enables them to interact with each other to form assembled structures. It has been reported[21] that the time required for the formation of these assembled structures is more in ethylene glycol as compared to that in polyethylene glycols. This enables larger time for the growth of the assembled structures through the process of Ostwald ripening

(as the total time for the reaction is the same in all the systems) in the case of polyethylene glycols, resulting in the formation of larger crystallite size. We observed that with ethylene glycol (EG) as the solvent, flower-shaped clusters were formed from the assembly of hexagonal-shaped nanoparticles. Such assembly was also observed by Changming et.al. [21] wherein flower-shaped clusters of iron oxide were formed with EG as the solvent. A schematic diagram illustrating the mechanism of formation of $SrTiO_3$ nanostructures in presence of different polyols and water is shown in figure 3.5.

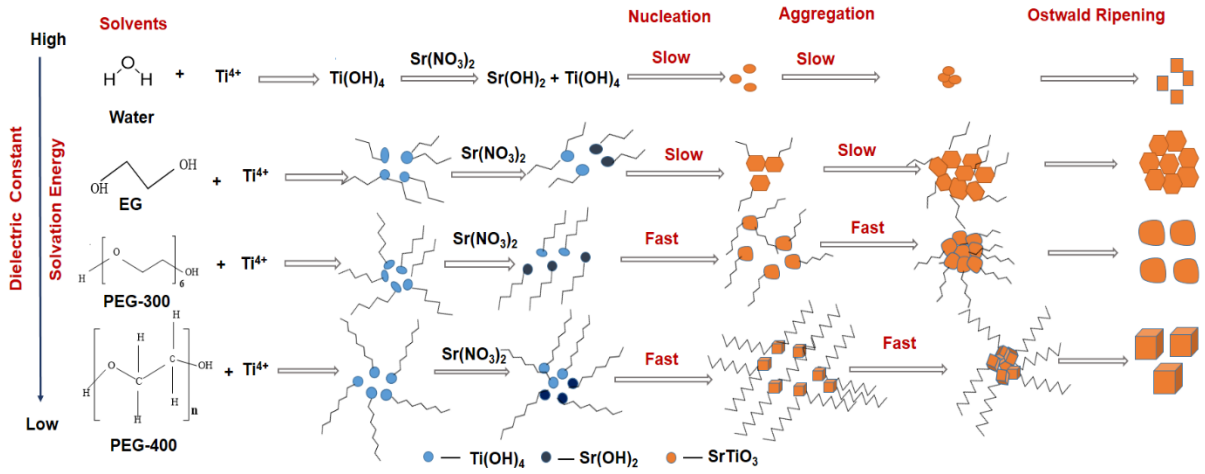

Figure 3.5: Schematic diagram illustrating the mechanism of formation of $SrTiO_3$ nanostructures in presence of different solvents.

The nature of exposed facets is one of the important factors that govern photocatalytic reactions. For this, we analyzed the nanostructures for the nature of exposed facets using HRTEM. Lattice fringes corresponding to (110) plane of cubic $SrTiO_3$, having an interplanar spacing of 2.7 Å, were observed in the HRTEM for STO1-STO4 (figure 3.6-3.9).

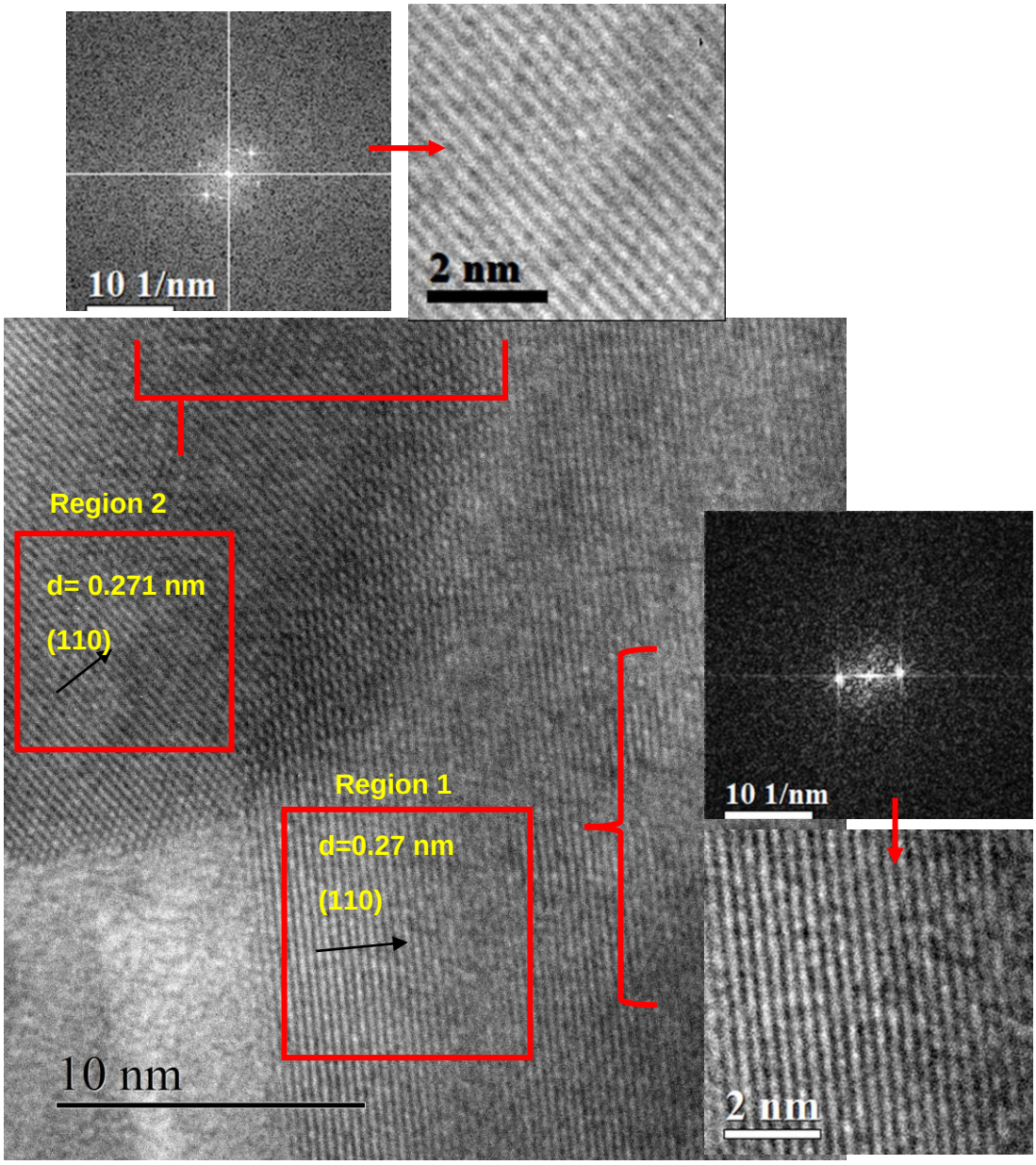

Figure 3.6: HRTEM images of STO1. The insets show reduced FFT and corresponding IFFT of the reduced FFT for a region marked in red.

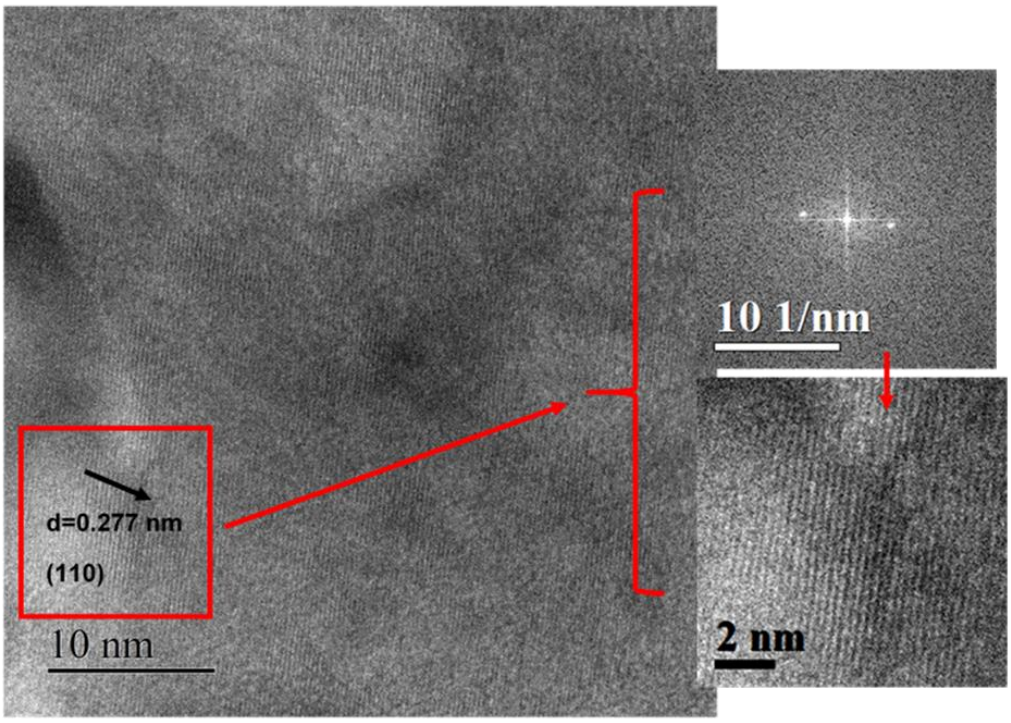

Figure 3.7: HRTEM images of STO2. The insets show reduced FFT and corresponding IFFT of the reduced FFT for a region marked in red.

.

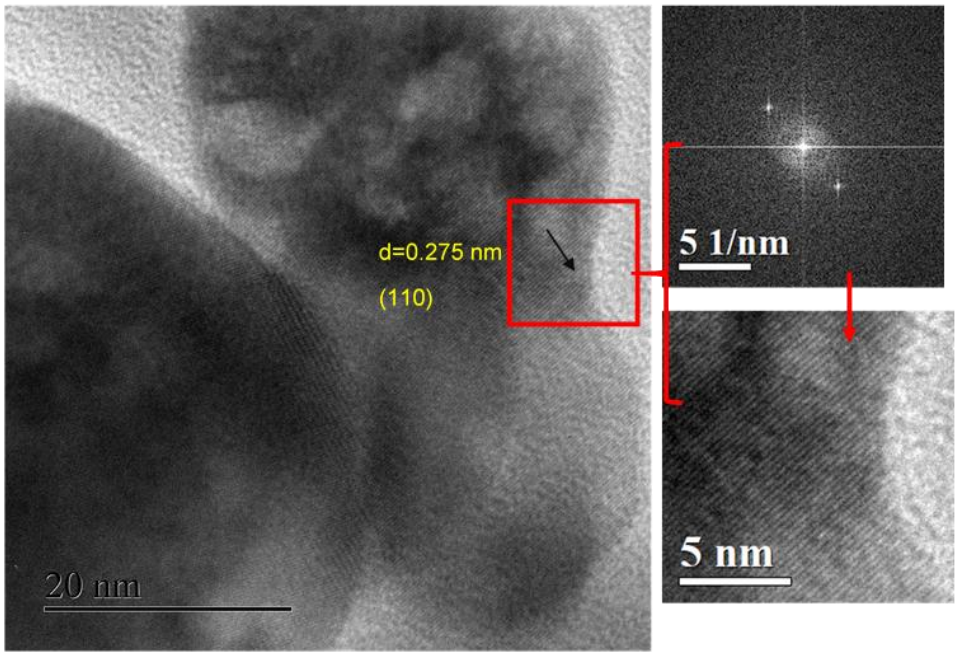

Figure 3.8: HRTEM images of STO3. The insets show reduced FFT and corresponding IFFT of the reduced FFT for a region marked in red.

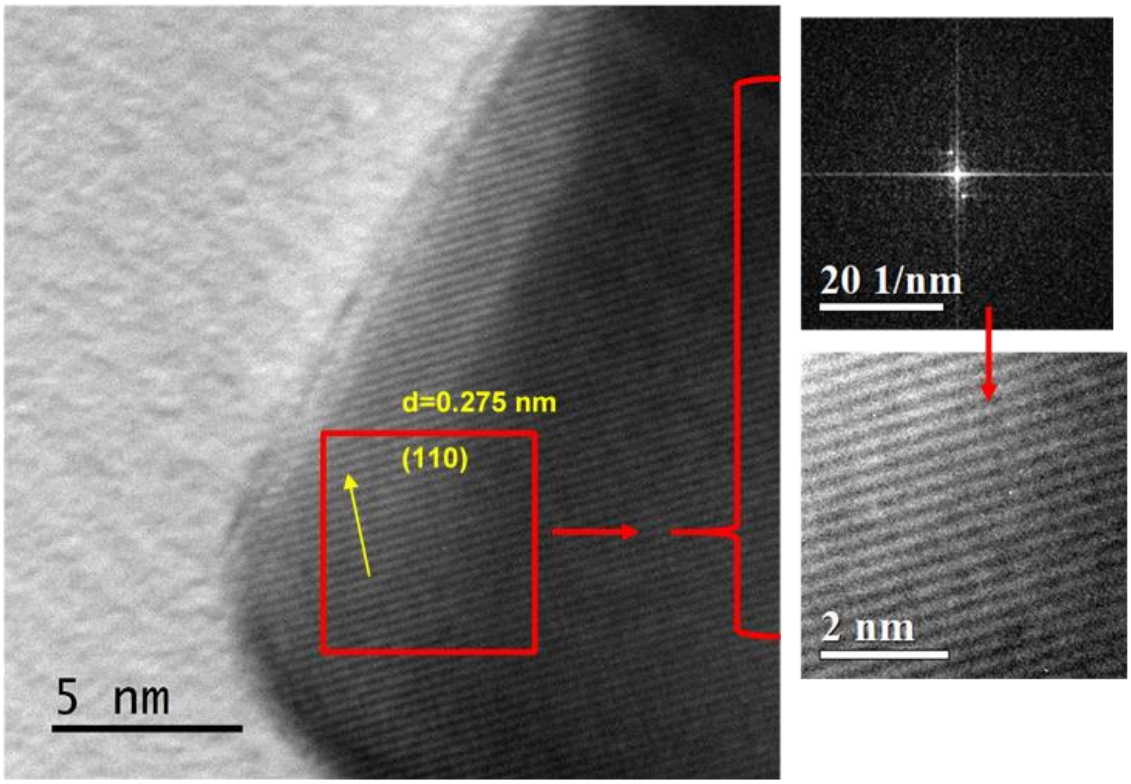

Figure 3.9: HRTEM images of STO4. The insets show reduced FFT and corresponding IFFT of the reduced FFT for a region marked in red.

This (110) plane was perpendicular to the <001> direction, suggesting that the top exposed facet of STO1-STO4 nanostructure to be [001], as shown in figure 3.3 e-h. This facet, [001], is significant in governing the photo-reduction reactions [22]. Apart from [001], we also observed $[01\bar{1}]$ facet in STO2 (figure 3.3 f) and STO3 (figure 3.3 h), which was calculated from the angle between the facets according to the equation given below;

$$cos\theta = \frac{h_1h_2 + k_1k_2 + l_1l_2}{\sqrt{h_1^2 + k_1^2 + l_1^2}\sqrt{h_2^2 + k_2^2 + l_2^2}} \qquad (3.5)$$

where ($h_1k_1l_1$) are the miller indices of facet1 and ($h_2k_2l_2$) are the miller indices of facet 2. *Cos* θ is the angle between the facets ($h_1k_1l_1$) and ($h_2k_2l_2$).

The dielectric constant of the solvent gives a measure of its polarity. The higher the value of the dielectric constant, the more polar is the solvent. Solvent molecules tend to preferentially adsorb on specific facets, altering the energy barrier that is required for the growth of crystalline material with specific facets exposed on the surface. The surface energy of the facets can be altered by changing the polarity of the solvent, which plays an influential role in the adsorption of the molecules on the surface, thereby controlling the nature of exposed facets. The effect of solvents on the crystal morphology of various organic crystals has been studied by Lahav et.al.[23] wherein in one example they have shown that the morphology of the crystals of α- rhamnose monohydrate could be tuned from bipyramidal to pyramidal by changing the solvent from water to a mixture of water and methanol. In another example, Barik et.al.[24] have shown that changing the concentration of ethylene glycol, resulted in the formation of α-Fe_2O_3 nanostructures with preferred facets. Thus, in our system, the solvent molecules (glycols in this case), surrounded the initial nuclei, and the nature of aggregates formed thereafter could have been the result of the preferred interaction of the solvent molecule for a particular facet over another.

Raman studies for STO1-STO4 nanostructures show the presence of both first and second-order bands at 114, 182, 550, and 805 cm^{-1} corresponding to E_g, TO2, TO4, and LO4 modes respectively (figure 3.10). Among these E_g, TO2 and TO4 modes are first-order Raman scattering. It has been reported that, as per the selection rule, for $SrTiO_3$ crystallizing in a cubic unit cell, first-order bands are not allowed[25]. However, for nanostructures, these bands are observed because of the lowering of symmetry which may arise as a result of the presence of impurity atom at the nanoscopic level or local tetragonal structure that destroys the inversion symmetry[26]. There may be frozen dipole moments present at the surface which may penetrate the crystals, thereby destroying the inversion symmetry. This destruction of the inversion symmetry may give rise to the local tetragonal structure. The Eg mode arises as a result of a break in the inversion symmetry of the crystal due to the presence of frozen dipole moments at the surface. The TO2 and TO4 modes are associated with O-Ti-O bonding [26]. These first-order modes were more pronounced in the Raman scattering with STO3 and STO4, indicating the presence of defects in these materials.

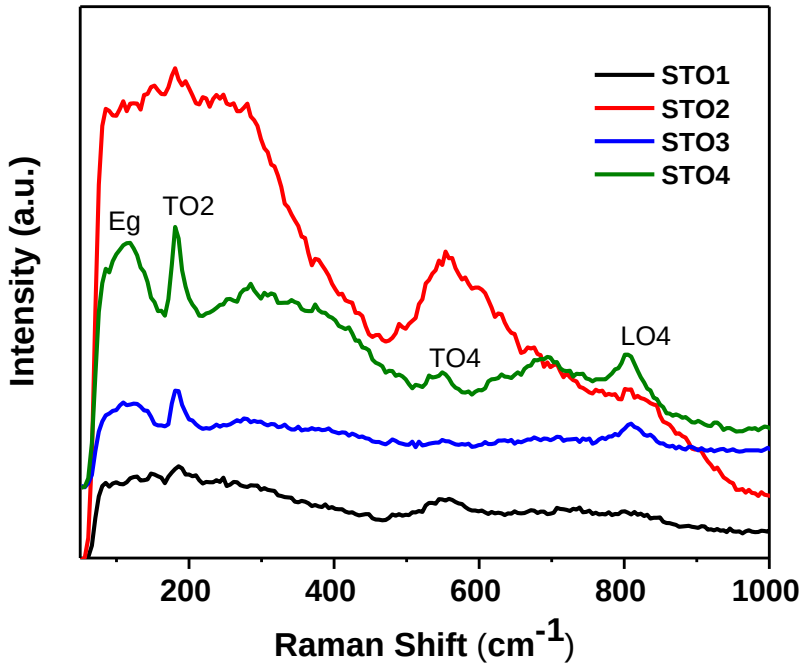

Figure 3.10 : Raman Spectra of $SrTiO_3$ nanostructures synthesized using water (STO1), EG (STO2), PEG-300 (STO3), and PEG-400 (STO4).

Figure 3.11 shows the ATR-FTIR spectra of the $SrTiO_3$ nanostructures, synthesized using different solvents. H-O-H bending and stretching vibration of adsorbed water were observed at 1630 cm^{-1} and 3200-3400 cm^{-1} respectively (figure 3.11(a)). ATR-FTIR with a spectral resolution in the region of 400-800 cm^{-1} is shown in figure 3.11(b). The presence of Ti-O-Ti bending at 418 cm^{-1}, Sr-O stretching at 618 cm^{-1} and Ti-O stretching at 548 cm^{-1} could be observed in the FTIR spectra.

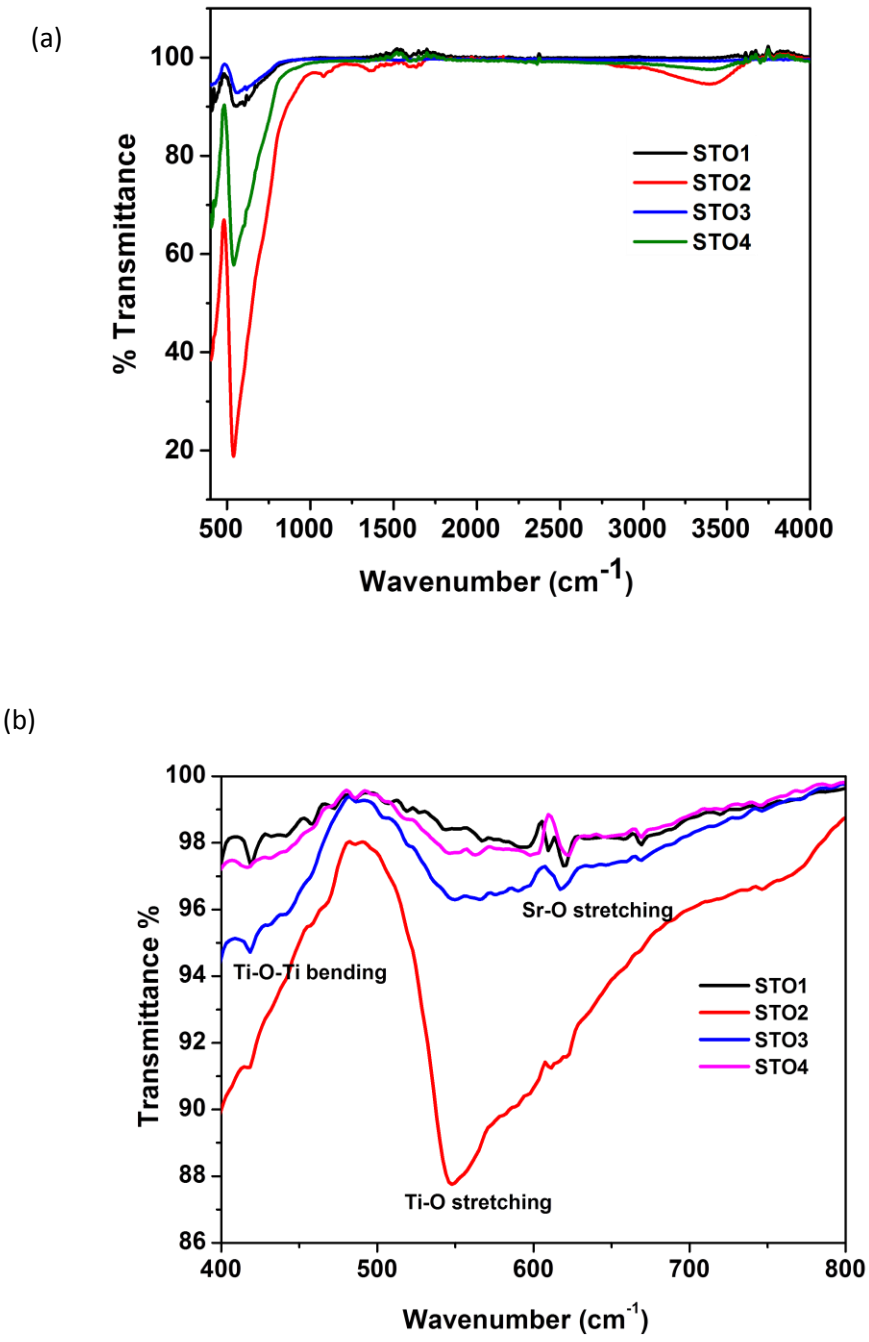

Figure 3.11: ATR-FTIR spectra of the $SrTiO_3$ nanostructures synthesized using water (STO1), EG (STO2), PEG-300 (STO3), and PEG-400 (STO4) in the spectral resolution (a) 400-4000 cm^{-1} and (b) 400-800 cm^{-1}.

To measure the bandgap for the synthesized $SrTiO_3$ nanostructures, optical properties of these were measured using UV-Visible diffuse reflectance spectroscopy (DRS). UV-visible absorption spectra and Tauc plot are shown in figures 3.12 a and b respectively. The Tauc equation used for calculating the bandgap of $SrTiO_3$ is given in equation 3.6.

$$(\alpha h\upsilon)^{\frac{1}{n}} = C\left(h\upsilon - E_g\right) \qquad (3.6)$$

where α is absorption coefficient; E_g is the bandgap of the material; n denotes the nature of transition (n = ½ for direct transition and n = 2 for indirect transition).

The bulk bandgap of the $SrTiO_3$ semiconductor[27] is reported to be 3.3 eV. We observed an increase in the value of direct bandgap value for STO1-STO4 from 3.3 to 3.7 eV (Table 3.1). An increase in the value of the bandgap in comparison to that reported for bulk $SrTiO_3$ can be attributed to the quantum size effect. Such effect was also observed by Townsend et al.[27], wherein they observed that the bandgap of $SrTiO_3$ nanoparticles synthesized using different methodologies (resulting in variation of the size of the $SrTiO_3$), was greater than that of the bulk $SrTiO_3$. The authors attributed this to the quantum size effect. The value of the bandgap also suggests that $SrTiO_3$ would be photoactive in the UV region of the solar spectrum.

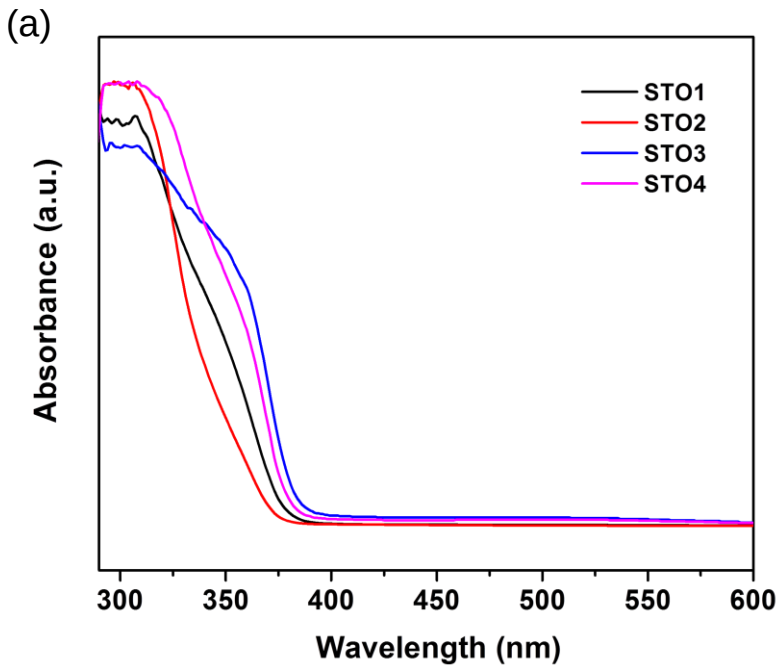

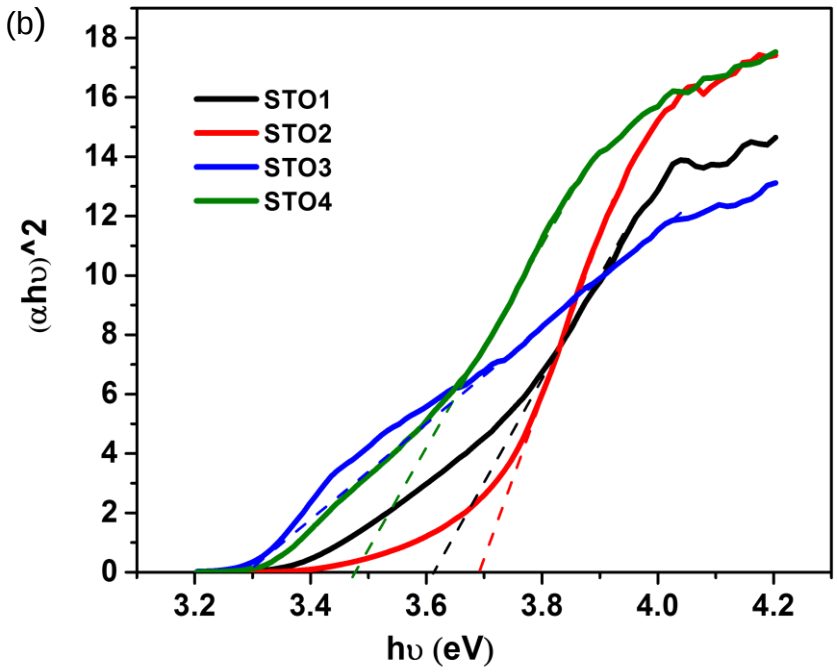

Figure 3.12 : (a) UV-Visible absorbance and (b) Tauc Plot for calculating the direct bandgap of STO1-STO4.

It has been known that size, surface area, electron-hole recombination, and nature of facets have a strong influence on the photocatalytic properties of the material. Smaller particle size and the high surface area offer a large number of active sites to influence the catalytic efficiency[28]. The crystallite size affects the reactions that occur at the surface because particles having smaller crystallite sizes have a larger external surface which provides a higher number of active sites. This enhances the reaction taking place above the active site for particles having smaller crystallite sizes than the particles having larger crystallite sizes.

To see the effect of surface area and electron-hole recombination, both BET and photoluminescence studies were carried out. BET studies for all the samples (STO1-STO4) showed Type IV adsorption-desorption isotherm with H3 hysteresis loop, a characteristic of the mesoporous structure (figure 3.13(a-d)). The surface area is summarized in Table 3.1. We observed a higher value of the surface area for nanostructures synthesized using water and EG as the solvent whereas the surface area was observed to be quite low for nanostructures synthesized with PEG-300 and PEG-400 as the solvent.

(a)

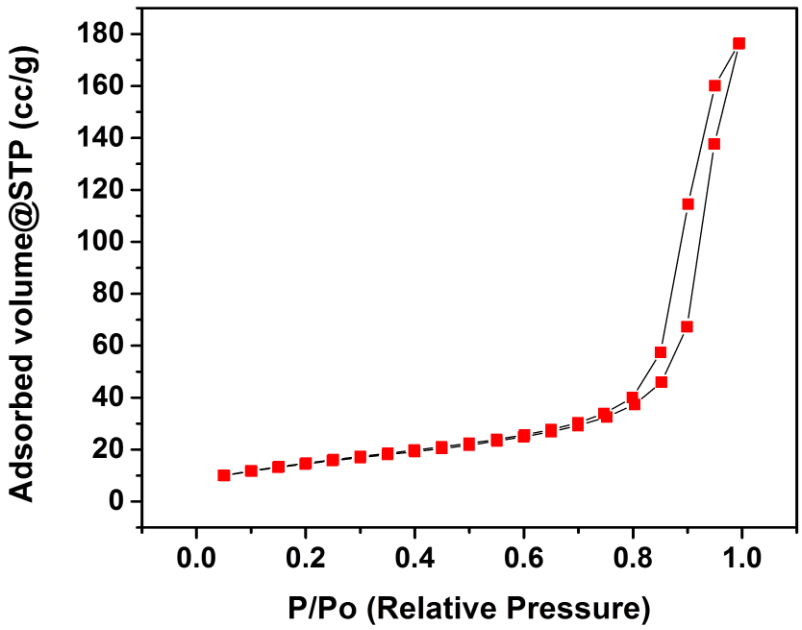
Adsorbed volume@STP (cc/g)
180
160
140
120
100
80
60
40
20
0
0.0
0.2
0.4
0.6
0.8
1.0
P/Po (Relative Pressure)

(b)

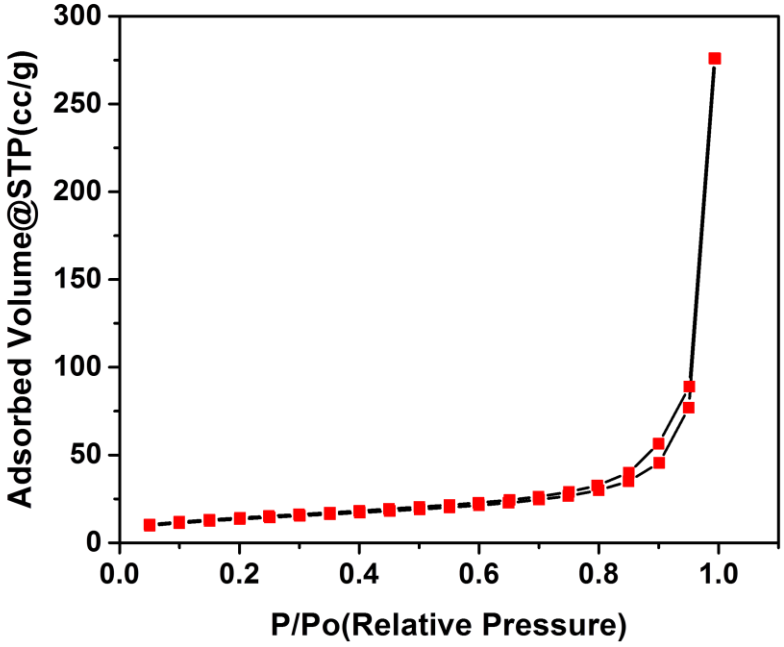
Adsorbed Volume@STP(cc/g)
300
250
200
150
100
50
0
0.0
0.2
0.4
0.6
0.8
1.0
P/Po(Relative Pressure)

(c)

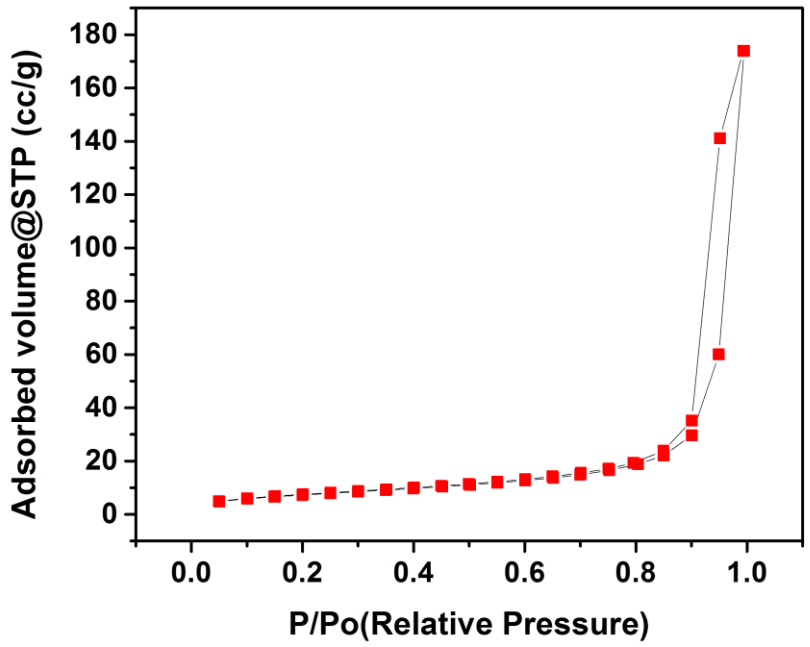

(d)

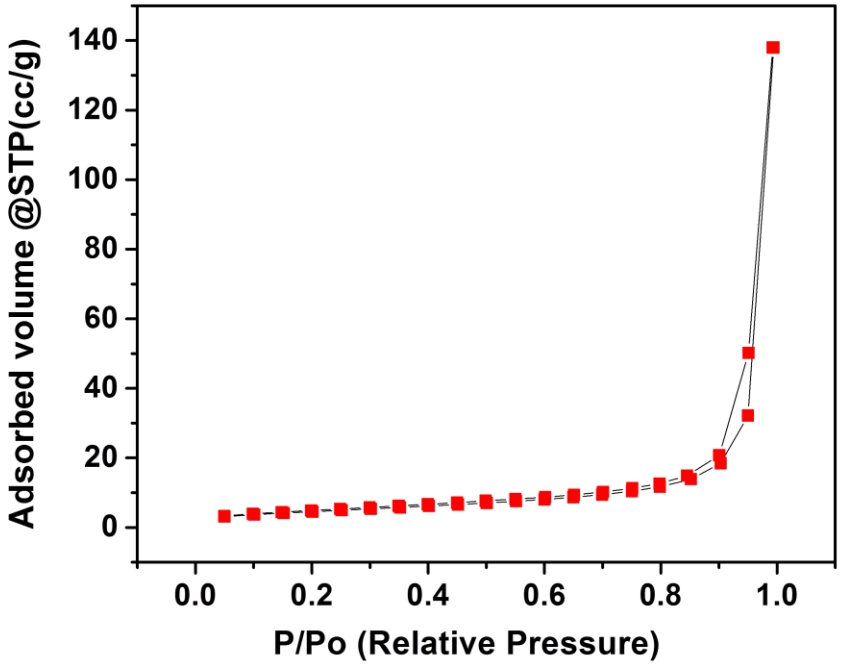

Figure 3.13: Adsorption-desorption isotherms for (a) STO1, (b) STO2, (c) STO3 and (d) STO4.

Photoluminescence studies were carried out to investigate the separation behavior of excitons and the presence of defects. In our studies (Figure 3.14(a)), we observed emissions in the violet-blue region. The spectra show maxima at 432 nm, two peaks at 410 nm, and 452 nm (when deconvoluted) (Figure 3.14(b)). This emission in the violet-blue region is attributed to the shallow and surface defects present in the samples[29]. Observations from PL studies were in agreement with Raman studies. In Raman studies, first-order bands were more pronounced for STO3 and STO4. In PL studies, the intensity of the emission in the violet-blue region for STO3 and STO4 was more than that observed for STO1 and STO2. The emission in the violet-blue region indicates the recombination of electrons and holes at an intermediate state which lies above the valence band that may be generated because of distorted clusters or oxygen vacancies[30]. The lower intensity of emission peak would mean lesser recombination of electrons and holes indicating that a larger number of electrons are available at the surface to participate in Hydrogen Evolution Reaction (HER) and electrons and holes for photodegradation of RhB.

(a)

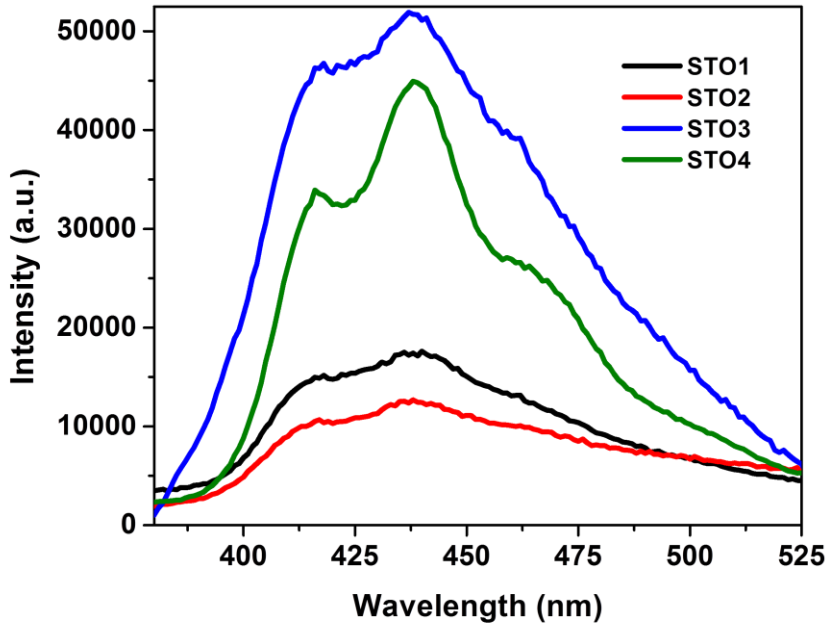

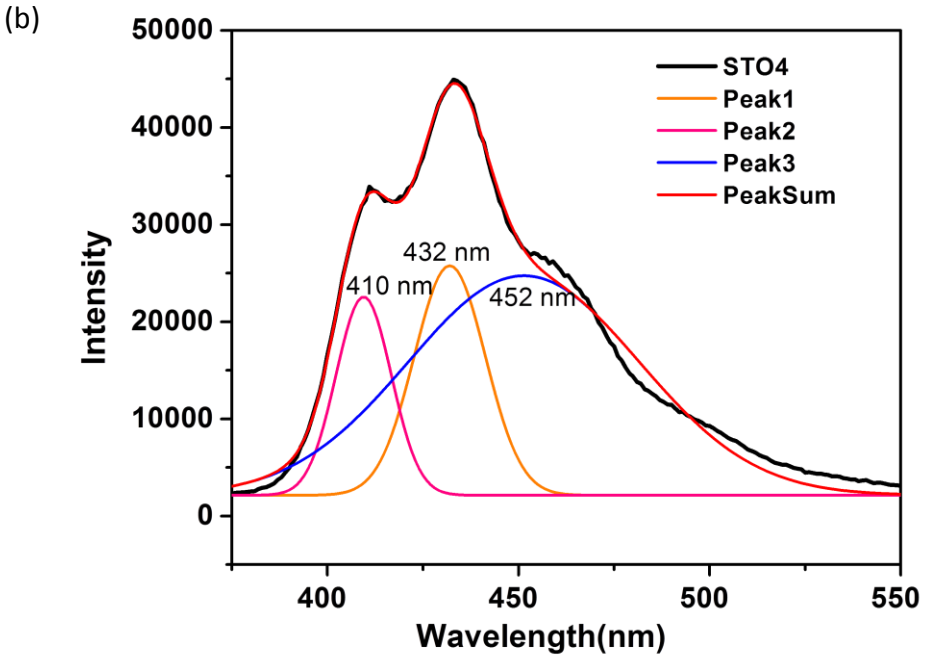

Figure 3.14 : (a)Photoluminescence spectra of $SrTiO_3$ nanostructures synthesized using water (STO1), EG (STO2), PEG-300 (STO3), and PEG-400 (STO4).(b) De-convoluted Photoluminescence spectra for STO4.

The transfer of photogenerated charge carrier was checked using Time-resolved photoluminescence spectra. Figure 3.15 (a-d) shows decay curves and their fit obtained for sample STO1-STO4. The values of the excited-state lifetime, obtained by fitting the decay curves with the double exponential decay equation (equation 3.1) are given in Table 3.2. No significant changes in the value of decay time were observed within the error limits.

(a)

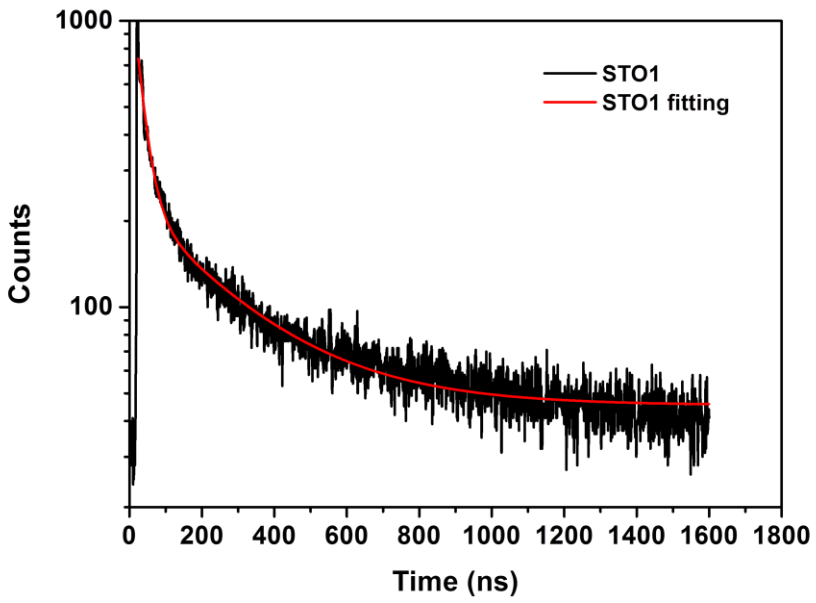
1000
100
Counts
0
200
400
600
800
1000
1200
1400
1600
1800
Time (ns)
STO1
STO1 fitting

(b)

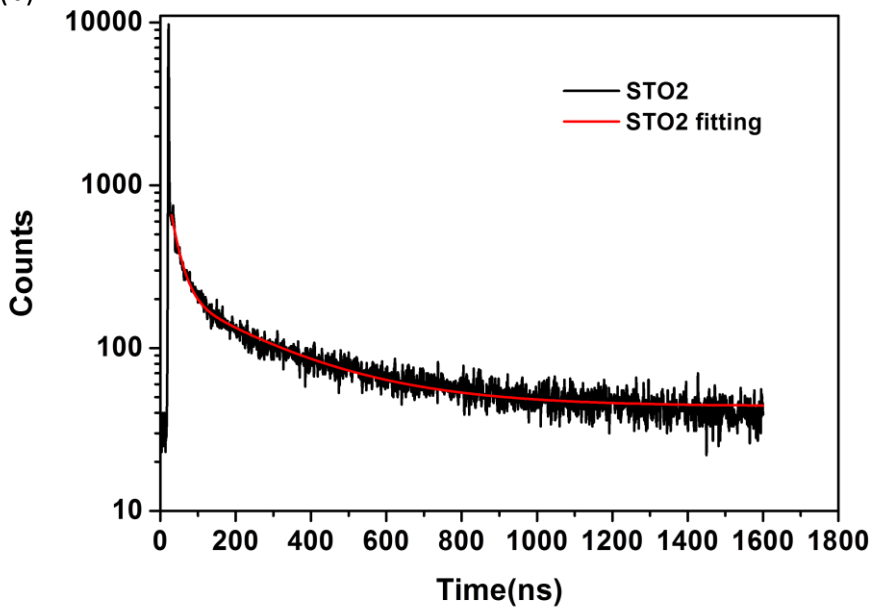
10000
1000
100
10
Counts
0
200
400
600
800
1000
1200
1400
1600
1800
Time(ns)
STO2
STO2 fitting

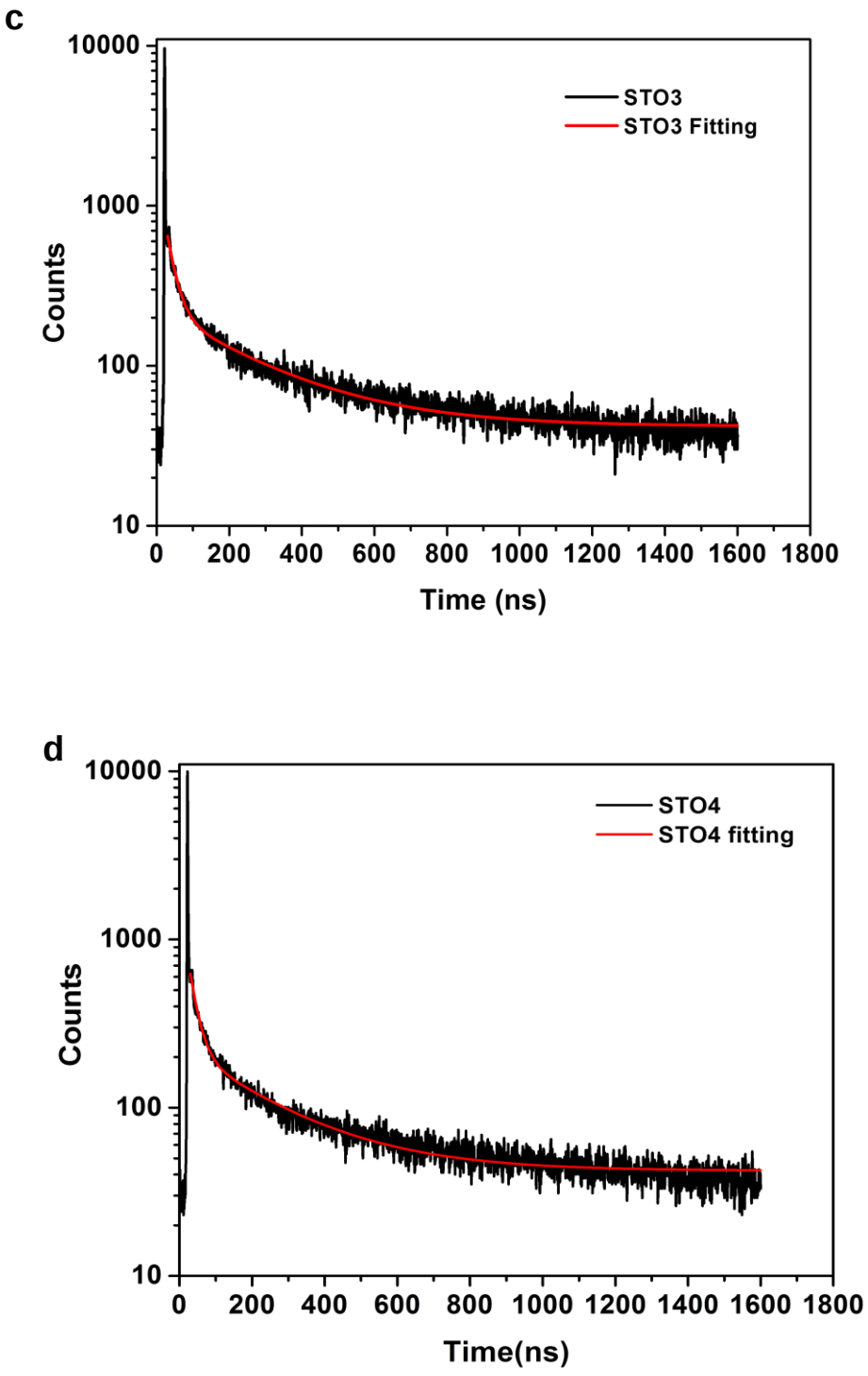

Figure 3.15: Decay curves with fitting obtained from Time-resolved photoluminescence study for (a) STO1, (b) STO2, (c) STO3, and (d) STO4.

Table 3.2: Parameters obtained after exponential fitting of the decay curves for STO1-STO4.

Sample	A_1	τ_1(ns)	A_2	τ2(ns)	Average Lifetime(ns) Using equation 3.2
STO1	1350	25.9±0.2	192.4	262.5±6.4	165.7
STO2	1500	24.6±0.2	188.9	266.3±6.2	164.1
STO3	1537	23.8±0.5	189.2	262.7±6.3	161.4
STO4	1502	23.5±0.5	181.62	261.7±4.4	160.1

Further, transient photocurrent measurements were carried out to obtain information about the photocurrent response and photocurrent gain of the catalysts. The photocurrent measurement performance of the sample from STO1-STO4 is shown in figure 3.16. It was observed that the photocurrent density was found to follow the order: STO4>STO3>STO2>STO1 (figure 3.16). The observed trend is per the increasing order observed for the size of the nanostructures. It has been reported [27-31] that with a decrease in the particle size, the photocurrent density decreases. We also observed a similar trend of the photocurrent density with size. However, to check the efficacy of the catalyst in presence of light, we calculated photocurrent gain (defined as a number of charge carriers circulated per incident photon), I_{photo}/I_{dark}. The photocurrent gain was observed to be highest for STO1 and found in order of STO1>STO2>STO3>STO4 (Table 3.3). The enhancement in the value of photocurrent gain showcases that the catalysts are more efficient when irradiated with light. Such effect was also observed by Behera et al.[32], wherein they attributed the increased photocatalytic performance of Ag-SnS to the enhancement of the photocurrent gain.

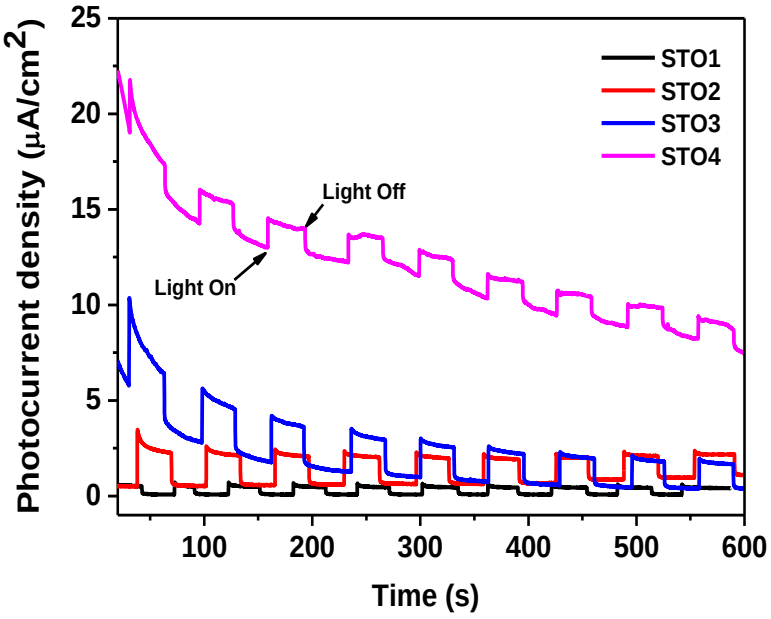

Figure 3.16: Transient photocurrent response measurement for STO1-STO4.

Table 3.3: Photoresponse and photocurrent gain calculated from transient photocurrent studies

Sample	I (μA)	I_{on}(μA)	△ I = I_{on}-I_{off} (μA)	Photocurrent Gain = $\frac{\Delta I}{I_{off}}$
STO1	0.072	0.69	0.63	8.72
STO2	0.519	2.59	2.07	3.9
STO3	2.78	5.61	2.83	1.01
STO4	14.2	16	1.8	0.12

Photocatalytic dye degradation:

The efficiency of the $SrTiO_3$ nanostructures for Photocatalysis was checked with the degradation of RhB dye under UV irradiation. Changes in the concentration of the RhB dye with time were observed using the UV-Visible spectrophotometer and are shown in figure 3.17a. It was observed that samples synthesized using water (STO1) and EG (STO2) as a solvent, have similar degradation efficiency of around 70%. When the photodegradation was carried out using $SrTiO_3$ synthesized using PEG-300 (STO3) and PEG-400 (STO4), the efficiency was found to decrease to 51% and 41% respectively.

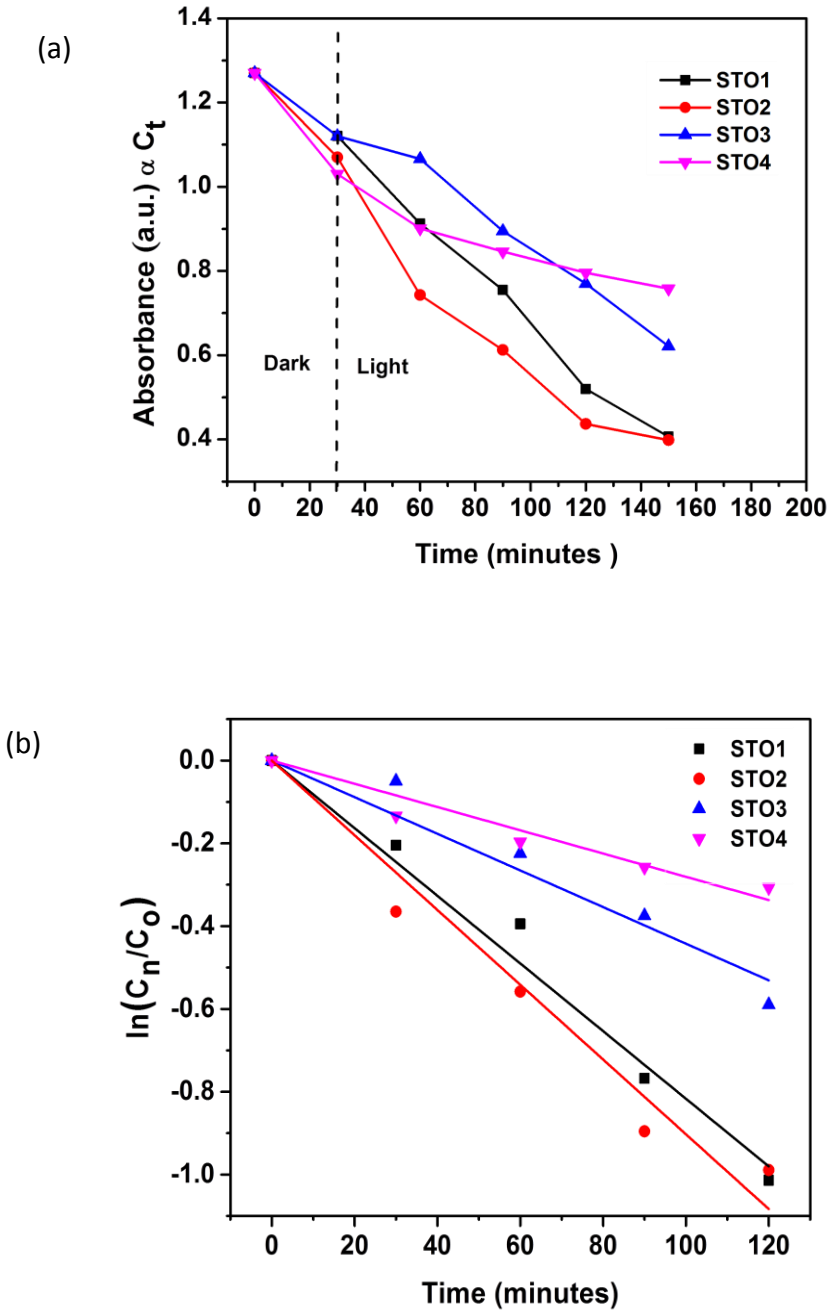

Figure 3.17: (a) Photodegradation of Rhodamine B dye using $SrTiO_3$ nanostructures (STO1-STO4) as photocatalyst. (b) Plot showing pseudo-first-order kinetics for the photocatalytic reaction using $SrTiO_3$ nanostructures (STO1-STO4).

The degradation of the dye followed pseudounimolecular order and the rate constant was calculated using first-order equation (equation 3.7):

$$\ln\left(\frac{C_n}{C_0}\right) = -kt \qquad (3.7)$$

where C_o is the concentration of dye at time t=0 and C_n represents the concentration of dye at time t.

The slope obtained upon linear fitting of the plot $\ln(C_n/C_0)$ vs t equals the pseudo-first-order rate constant, k (figure 3.17b). The pseudo rate constant and surface area normalized rate constant obtained for different samples is summarized in Table 3.4. The rate constant was found to be similar for both STO1 and STO2 and the order of rate constant was observed to be STO2 ~ STO1 > STO3 > STO4.

Table 3.4: The pseudo-unimolecular first-order rate constant, and surface area normalized rate constant for photocatalytic degradation of RhB dye using $SrTiO_3$ as photocatalyst.

Sample	**Rate Constant, $k/10^{-3}$ (min^{-1})**	**Normalized Rate Constant, 10^{-3} (g/m^2 min)**
STO1	8.17	0.15
STO2	9.03	0.18
STO3	4.42	0.16
STO4	2.81	0.16

Though the rate of photodegradation of RhB dye is similar for both STO1 and STO2, there is a slight increase in the photocatalytic rate constant, observed, for STO2 in comparison to that for STO1. This can be attributed to the fact that in the degradation of the dye using Photocatalysis, electrons move from the valence band to the conduction band of the catalyst (in presence of light). This creates a positive hole in the valence band. Electrons (present in the conduction band) participate in the formation of superoxide anion (O_2^{2-}), by reacting with the oxygen adsorbed at the surface of the photocatalyst. This superoxide anion further reacts with water to form hydroxyl radicals. Also, holes present at the valence band react with water to form hydroxyl radicals. Both hydroxyl radicals, produced at the valence and conduction band, participate in degradation of the dye. In the case of $SrTiO_3$, [001] facet has been reported to be significant in governing the photo-reduction reactions (involving electrons)[22] whereas $[01\bar{1}]$

facet is known to participate in photo-oxidation reactions (involving holes)[22]. Thus, for photodegradation of RhB dye both the facets have active participation, attributing to a slight high performance of STO2, having both kinds of facets, as also observed from the normalized rate constant (Table 3.4). Such observation of normalized rate constant on photocatalytic activity, to correlate the effect of exposed facets, was also demonstrated by Liu et.al[33].

Photocatalytic Hydrogen evolution

The amount of hydrogen evolved using $SrTiO_3$ nanostructures from 0.05M aqueous solution of Na_2SO_3 under 250 W medium pressure mercury vapor lamp is shown in figure 3.18.

The observed H_2 evolution varies with the size of the nanoparticles formed with different solvents following the order STO1>STO2>STO4>STO3. We observed that around 2.5 times more hydrogen is generated with STO1 as the catalyst when compared with that generated using STO3 and around 1.7 times that generated with STO4 as the catalyst. Apparent quantum yield was calculated using equation 4. The quantum yield obtained has been tabulated in Table 3.5. STO1 shows the highest apparent quantum yield among all the nanostructures.

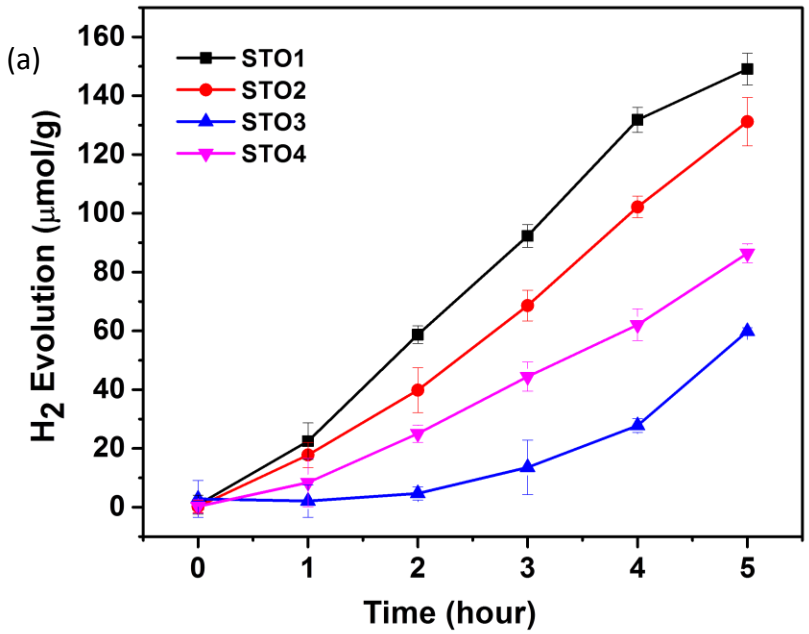

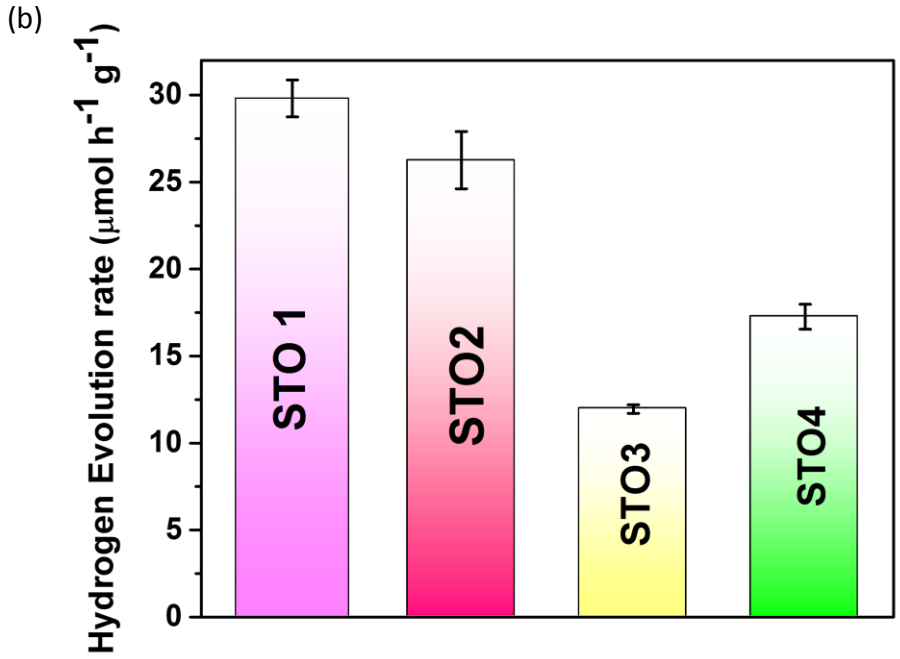

Figure 3.18: (a) Plot showing the amount of Hydrogen Evolution per gram of the catalyst (STO1-STO4) and (b) the rate of Hydrogen Evolution per gram of the catalyst using $SrTiO_3$ nanostructures (STO1-STO4) as photocatalyst under UV irradiation.

There have been many reports in the literature wherein $SrTiO_3$ and its composites with other metal oxides have been used for photocatalytic hydrogen generation[16,34,35,36,37,38, 39, 40, 41, 42, 43]. However, in these reports, the light source and scavengers used are different from our studies, with metal co-catalyst being used in several reports. We have carried out our study with Na_2SO_3 as an electron donor or hole scavenger which acts as per the following mechanism [44]:

On irradiation with UV light: $SO_3^{2-} + h\nu \longrightarrow SO_3^{2-*}$

oxidation: $SO_3^{2-*} + 2OH^- \longrightarrow SO_4^{2-} + H_2O + 2e^-$

reduction: $2H_2O + 2e^- \longrightarrow H_2 + 2OH^-$

overall: $SO_3^{2-} + H_2O + h\nu \longrightarrow SO_4^{2-} + H_2$

We chose Na_2SO_3 as the hole scavenger as the byproduct of this scavenger is sulfate ion (non-hazardous to the environment). With methanol, the byproduct is formaldehyde [45], an organic

product, which if not isolated can be hazardous to the environment. The study was carried out in absence of a metal co-catalyst to see the direct influence of the nature of facets on the photocatalytic performance of STO1-STO4.

Table 3.5: Apparent quantum yield for hydrogen evolution using STO1-STO4 as photocatalyst.

Sample	n (Amount of hydrogen gas evolved after 5 h of the reaction) (mol)	Apparent Quantum Yield (AQY) (%)
STO1	5.8×10^{-6}	0.14
STO2	5.24×10^{-6}	0.13
STO3	2.39×10^{-6}	0.06
STO4	3.45×10^{-6}	0.08

Based on the above observations of crystallite/particle size, nature of exposed facets, surface area, presence of defects, recombination of photo-generated electrons and hole pair, and photocurrent response of the catalysts, it could be deciphered that maximum surface area, lowest crystallite/particle size, low recombination of photo-generated electron and hole pair, high photocurrent response of the catalyst (I_{photo}/I_{dark}) and presence of [001] as the only exposed facet could be the reason for observing the high photocatalytic performance of STO1 towards hydrogen evolution reaction. Thus, with STO1, all factors affecting photocatalytic behavior were favorable. For STO2, though the surface area was high, crystallite/particle size was less, and recombination of photo-generated electrons and hole pair was also less, a decrease in the photocatalytic efficiency towards HER was observed (when compared with STO1). This possibly could be attributed to the presence of $[01\bar{1}]$ facets along with [001] facet and the low response of the current for the catalyst in presence of light compared to STO1. The $[01\bar{1}]$ facet is known to participate in photo-oxidation reactions [22]. The photocatalytic hydrogen evolution was found to decrease for STO3 and STO4, even though the exposed facet in both the cases was [001], possibly because of low surface area, large crystallite/particle size, high recombination of photo-generated electron and hole pair arising due to presence of defects (observed from Raman

studies), and low photocurrent response. These parameters could have been dominating factors in governing the photocatalytic performance of the catalyst over the other parameter, that is the nature of the exposed facet. Another interesting observation was that the photocatalytic performance (towards HER) of STO3 was found to be less than that of STO4, possibly due to the presence of $[01\bar{1}]$ facet in STO3.

To check the stability of the catalyst after photocatalytic reactions, PXRD and TEM studies were carried out on samples obtained after completing the photocatalytic reactions. No change in the structure and morphology of STO1-STO4 was observed, from the PXRD (figure 3.19) and TEM studies (figure 3.20 a-d), respectively, indicating that the catalysts are stable after the photocatalytic reactions.

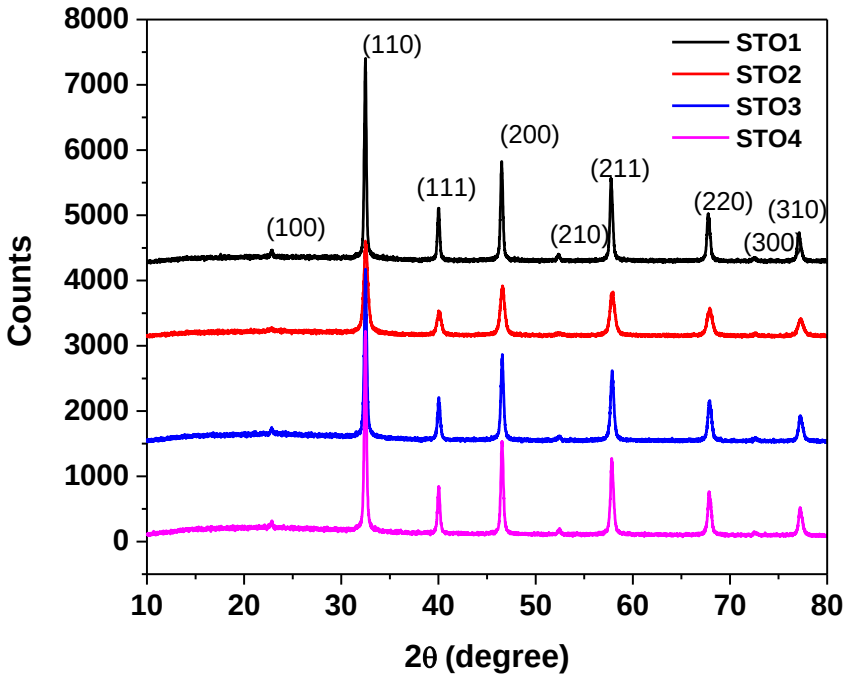

Figure 3.19: PXRD plot of $SrTiO_3$ obtained after photocatalytic reactions for STO1-STO4.

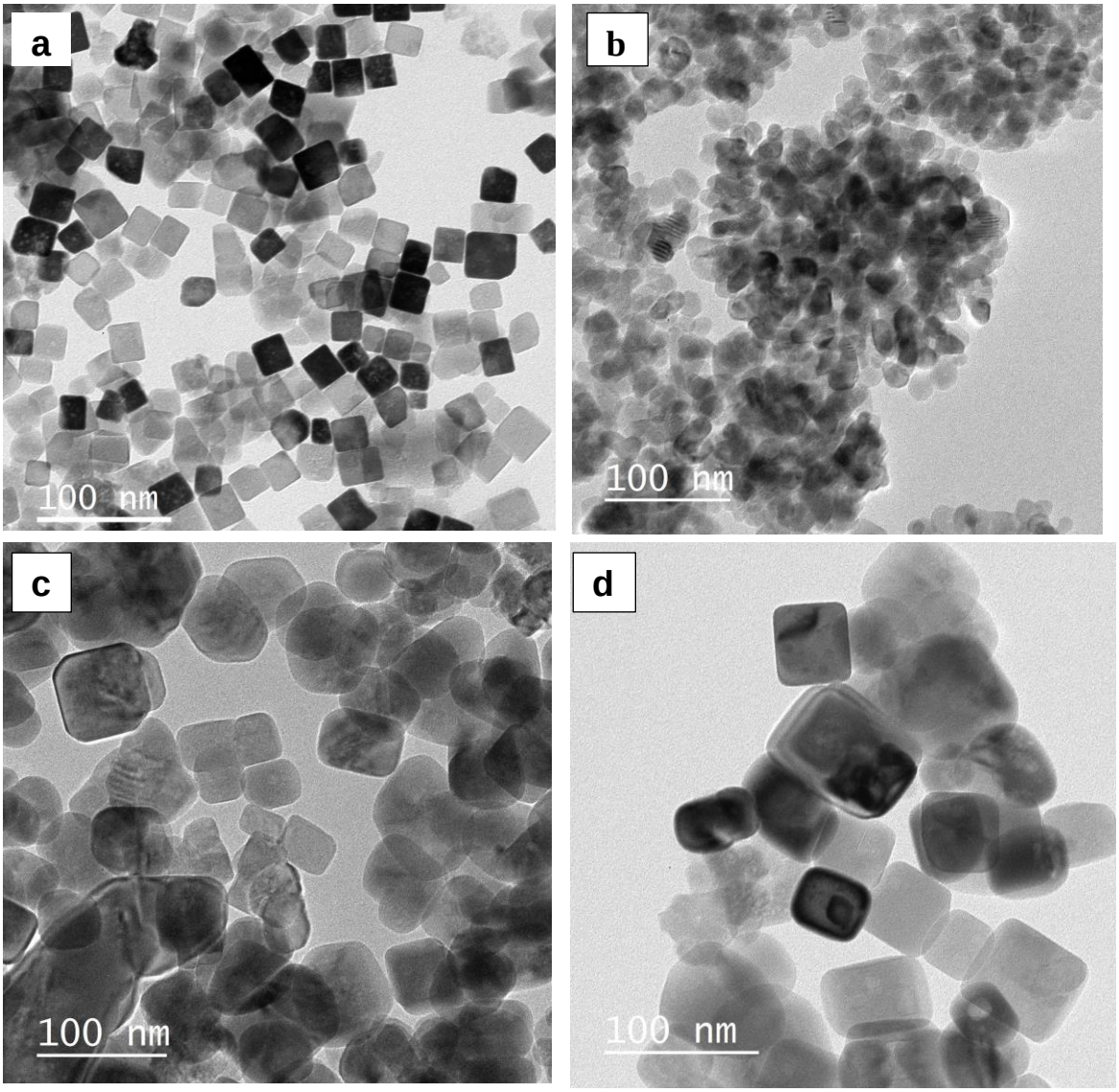

Figure 3.20: TEM images of $SrTiO_3$ obtained after photocatalytic reactions for (a) STO1, (b) STO2, (c) STO3 and (d) STO4.

Thus, the use of glycols as solvents helped in tuning the nature of facets. Apart from tuning the nature of facets, the glycols played an important role in tuning other parameters affecting the photocatalytic behavior of the oxides which includes surface area, crystallite size, and defects.

3.4 Conclusions:

This work shows that the dielectric constant of different polyols, acting as a solvent, played a significant role in the size, shape, nature of facets, and defects in $SrTiO_3$ nanostructures. We observed nanocubes, hexagonal-shaped particles assembled to form flower-like structures, and edge-truncated nanocuboids and nanocuboids with sharp boundaries, using different solvents viz. water, Ethylene Glycol (EG), and Polyethylene Glycol (PEG-300, PEG-400) respectively. Thus, based on our observation, we inferred that the synergistic effect of having maximum surface area, lowest crystallite/particle size, low recombination of photo-generated electron and hole pair, a large value of $I_{photo}/I_{dark,}$ and presence of [001] as the only exposed facet could be the reason for observing the high photocatalytic performance of STO1 nanostructures towards hydrogen evolution reaction. The presence of the $[01\bar{1}]$ facet was found to decrease the photocatalytic hydrogen evolution performance of the catalyst whereas for photodegradation of RhB dye both the facets have active participation. Thus, the role of the dielectric constant of the solvent, with a focus specifically on polyols and water as the solvent, discussed here could add to the field of understanding about their role on various parameters affecting the photocatalytic behavior of $SrTiO_3$ nanostructures. We feel that such establishments are important to synthesize materials with improved performances. Though, the studies about the role of solvent in altering the surface energy and thereby the formation of facets and the assembling behavior of nanostructures could add to the overall understanding of the growth process.

Acknowledgement

Aditi Vijay and Sonalika Vaidya*, Tuning the Morphology and Exposed Facets of SrTiO3 Nanostructures for Photocatalytic Dye Degradation and Hydrogen Evolution, ACS Applied Nanomaterials. 2021, 4, 4, 3406–3415.

3.5 References:

1. Ma, Y.; Lv, C.; Hou, J.; Yuan, S.; Wang, Y.; Xu, P.; Gao, G.; Shi, J., 3D Hollow Hierarchical Structures Based on 1D BiOCl Nanorods Intersected with 2D Bi_2 WO_6 Nanosheets for Efficient Photocatalysis Under Visible Light. *Nanomaterials (Basel, Switzerland)* **2019,** *9* (3), 322.
2. Yin, X.-L.; Li, L.-L.; Jiang, J.-H.; Du, X.-X.; Pang, D.-H.; Yang, J.; Li, Z.-J.; Wang, Y.-X.; Li, X.-Y.; Li, D.-C.; Dou, J.-M., Noble-metal-free $Zn_{0.5}Cd_{0.5}S$@MoS_2 core@shell heterostructures for visible-light-driven H_2 evolution with enhanced efficiency and stability. *Chemical Engineering Journal* **2019,** *375*, 121970.
3. Dou, M.-Y.; Han, S.-R.; Du, X.-X.; Pang, D.-H.; Li, L.-L., Well-defined FeP/CdS heterostructure construction with the assistance of amine for the efficient H_2 evolution under visible light irradiation. *International Journal of Hydrogen Energy* **2020,** *45* (56), 32039-32049.
4. Liao, D. L.; Liao, B. Q., Shape, size and photocatalytic activity control of TiO2 nanoparticles with surfactants. *Journal of Photochemistry and Photobiology A: Chemistry* **2007,** *187* (2), 363-369.
5. Ni, M.; Leung, M. K. H.; Leung, D. Y. C.; Sumathy, K., A review and recent developments in photocatalytic water-splitting using TiO_2 for hydrogen production. *Renewable & Sustainable Energy Reviews* **2007,** *11* (3), 401-425.
6. Zou, Z.; Ye, J.; Sayama, K.; Arakawa, H., Direct splitting of water under visible light irradiation with an oxide semiconductor photocatalyst. *Nature* **2001,** *414* (6864), 625-627.
7. Domen, K.; Kudo, A.; Onishi, T., Mechanism of photocatalytic decomposition of water into H_2 and O_2 over NiO-$SrTiO_3$. *Journal of Catalysis* **1986,** *102* (1), 92-98.
8. Sreethawong, T.; Ngamsinlapasathian, S.; Suzuki, Y.; Yoshikawa, S., Nanocrystalline mesoporous Ta_2O_5-based photocatalysts prepared by surfactant-assisted templating sol–gel process for photocatalytic H_2 evolution. *Journal of Molecular Catalysis A: Chemical* **2005,** *235* (1), 1-11.
9. Bhalla, A. S.; Guo, R.; Roy, R., The perovskite structure – a review of its role in ceramic science and technology. *Materials Research Innovations* **2000,** *4* (1), 3-26.
10. Jia, Q.; Iwase, A.; Kudo, A., $BiVO_4$-Ru/$SrTiO_3$:Rh composite Z-scheme photocatalyst for solar water splitting. *Chemical Science* **2014,** *5* (4), 1513-1519.
11. Sayama, K.; Mukasa, K.; Abe, R.; Abe, Y.; Arakawa, H., Stoichiometric water splitting into H_2 and O_2 using a mixture of two different photocatalysts and an IO_3^-/I^- shuttle redox mediator under visible light irradiation. *Chemical Communications* **2001,** (23), 2416-2417.
12. Wang, D.; Ye, J.; Kako, T.; Kimura, T., Photophysical and Photocatalytic Properties of $SrTiO_3$ Doped with Cr Cations on Different Sites. *The Journal of Physical Chemistry B* **2006,** *110* (32), 15824-15830.

13. Hou, D.; Hu, X.; Ho, W.; Hu, P.; Huang, Y., Facile fabrication of porous Cr-doped $SrTiO_3$ nanotubes by electrospinning and their enhanced visible-light-driven photocatalytic properties. *Journal of Materials Chemistry A* **2015,** *3* (7), 3935-3943.
14. Kayaalp, B. E.; Lee, Y. J.; Kornowski, A.; Gross, S.; D'Arienzo, M.; Mascotto, S., Cooperative assembly synthesis of mesoporous $SrTiO_3$ with enhanced photocatalytic properties. *RSC Advances* **2016,** *6* (93), 90401-90409.
15. Wan, S.; Chen, M.; Ou, M.; Zhong, Q., Plasmonic Ag nanoparticles decorated $SrTiO_3$ nanocubes for enhanced photocatalytic CO_2 reduction and H_2 evolution under visible light irradiation. *Journal of CO_2 Utilization* **2019,** *33*, 357-364.
16. Hsieh, P.-L.; Naresh, G.; Huang, Y.-S.; Tsao, C.-W.; Hsu, Y.-J.; Chen, L.-J.; Huang, M. H., Shape-Tunable $SrTiO_3$ Crystals Revealing Facet-Dependent Optical and Photocatalytic Properties. *The Journal of Physical Chemistry C* **2019,** *123* (22), 13664-13671.
17. Tan, H.; Zhao, Z.; Zhu, W.-b.; Coker, E. N.; Li, B.; Zheng, M.; Yu, W.; Fan, H.; Sun, Z., Oxygen Vacancy Enhanced Photocatalytic Activity of Pervoskite $SrTiO_3$. *ACS Applied Material & Interfaces* **2014,** *6* (21), 19184-19190.
18. Kimijima, T.; Kanie, K.; Nakaya, M.; Muramatsu, A., Solvothermal synthesis of $SrTiO_3$ nanoparticles precisely controlled in surface crystal planes and their photocatalytic activity. *Applied Catalysis B: Environmental* **2014,** *144*, 462-467.
19. Sengwa, R. J.; Kaur, K.; Chaudhary, R., Dielectric properties of low molecular weight poly(ethylene glycol)s. *Polymer International* **2000,** *49* (6), 599-608.
20. Wu, J.; Lü, X.; Zhang, L.; Huang, F.; Xu, F., Dielectric Constant Controlled Solvothermal Synthesis of a TiO_2 Photocatalyst with Tunable Crystallinity: A Strategy for Solvent Selection. *European Journal of Inorganic Chemistry* **2009,** *2009* (19), 2789-2795.
21. Cheng, C.; Xu, F.; Gu, H., Facile synthesis and morphology evolution of magnetic iron oxide nanoparticles in different polyol processes. *New Journal of Chemistry* **2011,** *35* (5), 1072-1079.
22. Mu, L.; Zhao, Y.; Li, A.; Wang, S.; Wang, Z.; Yang, J.; Wang, Y.; Liu, T.; Chen, R.; Zhu, J.; Fan, F.; Li, R.; Li, C., Enhancing charge separation on high symmetry $SrTiO_3$ exposed with anisotropic facets for photocatalytic water splitting. *Energy & Environmental Science* **2016,** *9* (7), 2463-2469.
23. Lahav, M.; Leiserowitz, L., The effect of solvent on crystal growth and morphology. *Chemical Engineering Science* **2001,** *56* (7), 2245-2253.
24. Barik, R.; Mohapatra, M., Solvent mediated surface engineering of α-Fe_2O_3 nanomaterials: facet sensitive energy storage materials. *CrystEngComm* **2015,** *17* (47), 9203-9215.
25. Nilsen, W. G.; Skinner, J. G., Raman Spectrum of Strontium Titanate. *Journal of Chemical Physics* **1968,** *48* (5), 2240-2248.

26. Banerjee, S.; Kim, D.-I.; Robinson, R. D.; Herman, I. P.; Mao, Y.; Wong, S. S., Observation of Fano asymmetry in Raman spectra of $SrTiO_3$ and $Ca_xSr_{1-x}TiO_3$ perovskite nanocubes. *Applied Physics Letters* **2006,** *89* (22), 223130.
27. Townsend, T. K.; Browning, N. D.; Osterloh, F. E., Nanoscale Strontium Titanate Photocatalysts for Overall Water Splitting. *ACS Nano* **2012,** *6* (8), 7420-7426.
28. Li, X.; Li, Q.; Wang, L., The effects of $NaNbO_3$ particle size on the photocatalytic activity for 2-propanol photodegradation. *Physical Chemistry Chemical Physics* **2013,** *15* (34), 14282-14289.
29. Longo, V. M.; Figueiredo, A. T. d.; Lázaro, S. d.; Gurgel, M. F.; Costa, M. G. S.; Paiva-Santos, C. O.; Varela, J. A.; Longo, E.; Mastelaro, V. R.; Vicente, F. S. D.; Hernandes, A. C.; Franco, R. W. A., Structural conditions that leads to photoluminescence emission in $SrTiO_3$: An experimental and theoretical approach. *Journal of Applied Physics* **2008,** *104* (2), 023515.
30. Souza, A. E.; Santos, G. T. A.; Barra, B. C.; Macedo, W. D.; Teixeira, S. R.; Santos, C. M.; Senos, A. M. O. R.; Amaral, L.; Longo, E., Photoluminescence of SrTiO3: Influence of Particle Size and Morphology. *Crystal Growth & Design* **2012,** *12* (11), 5671-5679.
31. Macounová, K. M.; Nebel, R.; Klusáčková, M.; Klementová, M.; Krtil, P., Selectivity Control of the Photo-Catalytic Water Oxidation on $SrTiO_3$ Nanocubes via Surface Dimensionality. *ACS Applied Material & Interfaces* **2019,** *11* (18), 16506-16516.
32. Behera, C.; Ghosh, S. P.; Kar, J. P.; Samal, S. L., Facile synthesis and enhanced photocatalytic activity of Ag–SnS nanocomposites. *New Journal of Chemistry* **2020,** *44* (27), 11684-11693.
33. Liu, B.; Ning, L.; Zhao, H.; Zhang, C.; Yang, H.; Liu, S., Visible-light photocatalysis in Cu_2Se nanowires with exposed {111} facets and charge separation between (111) and (-1-1-1) polar surfaces. *Physical Chemistry Chemical Physics* **2015,** *17* (20), 13280-13289.
34. Ng, J.; Xu, S.; Zhang, X.; Yang, H. Y.; Sun, D. D., Hybridized Nanowires and Cubes: A Novel Architecture of a Heterojunctioned $TiO_2/SrTiO_3$ Thin Film for Efficient Water Splitting. *Advanced Functional Materials* **2010,** *20* (24), 4287-4294.
35. Zhou, D.; Zhai, P.; Hu, G.; Yang, J., Upconversion luminescence and enhanced photocatalytic hydrogen production for Er^{3+} doped $SrTiO_3$ nanopaeticles. *Chemical Physics Letters* **2018,** *711*, 77-80.
36. Yin, X.-L.; Li, L.-L.; Li, D.-C.; Wei, D.-H.; Hu, C.-C.; Dou, J.-M., Room temperature synthesis of $CdS/SrTiO_3$ nanodots-on-nanocubes for efficient photocatalytic H_2 evolution from water. *Journal of Colloid and Interface Science* **2019,** *536*, 694-700.
37. Puangpetch, T.; Sreethawong, T.; Yoshikawa, S.; Chavadej, S., Hydrogen production from photocatalytic water splitting over mesoporous-assembled $SrTiO_3$ nanocrystal-based photocatalysts. *Journal of Molecular Catalysis A: Chemical* **2009,** *312* (1), 97-106.

38. Ha, M. N.; Zhu, F.; Liu, Z.; Wang, L.; Liu, L.; Lu, G.; Zhao, Z., Morphology-controlled synthesis of $SrTiO_3/TiO_2$ heterostructures and their photocatalytic performance for water splitting. *RSC Advances* **2016,** *6* (25), 21111-21118.

39. Han, J.; Dai, F.; Liu, Y.; Zhao, R.; Wang, L.; Feng, S., Synthesis of $CdSe/SrTiO_3$ nanocomposites with enhanced photocatalytic hydrogen production activity. *Applied Surface Science* **2019,** *467-468*, 1033-1039.

40. Bui, D.-N.; Mu, J.; Wang, L.; Kang, S.-Z.; Li, X., Preparation of Cu-loaded $SrTiO_3$ nanoparticles and their photocatalytic activity for hydrogen evolution from methanol aqueous solution. *Applied Surface Science* **2013,** *274*, 328-333.

41. Han, S.; Yu, L.; Zhang, H.; Chu, Z.; Chen, X.; Xi, H.; Long, J., Gold Plasmon-Enhanced Solar Hydrogen Production over $SrTiO_3/TiO_2$ Heterostructures. *ChemCatChem* **2019,** *11* (24), 6203-6207.

42. Liu, Y.; Wang, Z.; Wang, W.; An, X.; Mi, S.; Tang, J.; Huang, W., Sandwich $SrTiO_3/TiO_2$/H-Titanate nanofiber composite photocatalysts for efficient photocatalytic hydrogen evolution. *Applied Surface Science* **2014,** *315*, 314-322.

43. Wei, Y.; Wang, J.; Yu, R.; Wan, J.; Wang, D., Constructing $SrTiO_3$–TiO_2 Heterogeneous Hollow Multi-shelled Structures for Enhanced Solar Water Splitting. *Angewandte Chemie International Edition* **2019,** *58* (5), 1422-1426.

44. Huang, C.; Linkous, C. A.; Adebiyi, O.; T-Raissi, A., Hydrogen Production via Photolytic Oxidation of Aqueous Sodium Sulfite Solutions. *Environmental Science & Technology* **2010,** *44* (13), 5283-5288.

45. Schneider, J.; Bahnemann, D. W., Undesired Role of Sacrificial Reagents in Photocatalysis. *Journal of Physical Chemistry Letters* **2013,** *4* (20), 3479-3483.

Chapter 4

Role of oriented assemblies of $SrTiO_3$ along (200) plane in enhancing Photocatalytic hydrogen evolution activity

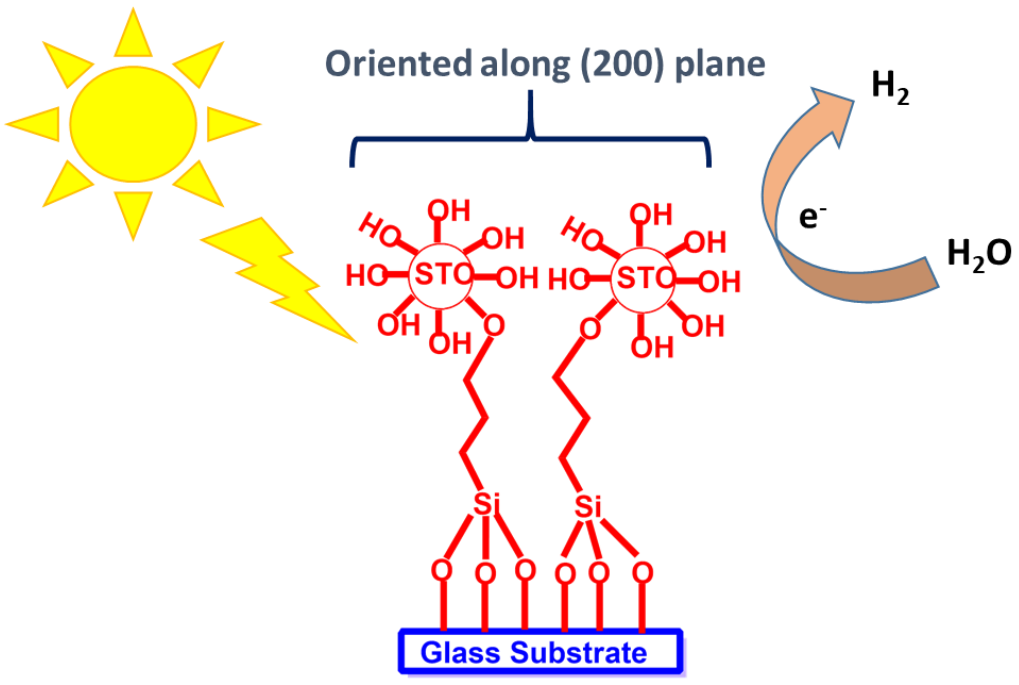

Chapter 4

Role of oriented assemblies of $SrTiO_3$ along (200) plane in enhancing Photocatalytic hydrogen evolution activity

Abstract

This study aims to see the effect of oriented assemblies of $SrTiO_3$ on photocatalytic hydrogen evolution. We have successfully synthesized the $SrTiO_3$ through the hydrothermal method and its structure and phase purity was checked through PXRD. Assemblies of the $SrTiO_3$ on the glass plate were formed by coating $SrTiO_3$ on IPTMS (3-iodopropyl-trimethoxy silane) functionalized glass substrate through an ultrasonication process. These assemblies on glass substrate were characterized using PXRD and FESEM. It was observed that the orientation of uniform assemblies of $SrTiO_3$ was along the (200) plane. Photocatalytic hydrogen evolution reaction was checked on these assemblies. The observed photocatalytic hydrogen evolution rate is found to be in accordance with a highly oriented sample along the (200) plane.

4.1. Introduction:

A surge in the world's population led to the exhaustion of fossil fuels and growth in environmental pollution. Therefore, the development of a clean and green source of energy is considered an effective method to tackle energy and environmental issues. In this regard, Hydrogen Energy can be considered an alternative source of energy as it is environmentally friendly and can be produced using renewable resources of energy. In recent past years, Photocatalytic water-splitting has emerged as an effective technique to produce hydrogen from water and solar energy using semiconductor material[1-2]. Understanding the mechanism behind photocatalytic reactions and developing a highly effective catalyst for photocatalytic hydrogen production is a key to advancing photocatalysis. So far, many efforts have been made to increase the separation of photoinduced charge carriers for improving the catalyst's efficiency, including size reduction[3], morphology, exposed facets control, etc. In addition to the above-mentioned approaches of modifying the physical properties, it was observed that studies on altering the crystallographic orientation of a semiconductor photocatalyst have been carried out to establish a relation between the photocatalytic properties and surface atomic structures[4, 5].

In this concern, crystallographically oriented nanomaterial and thin films have been synthesized. Orientation induced photochemical reduction on TiO_2 rutile surfaces which are preferentially grown along (100), (110), (101), (111), and (001) plane[6]. The authors observed that films grown along the (001) plane are found to be the most active for photoreduction. Guoqiang Li et. al[7] reported the catalytic activity of WO_3 thin films grown on (001), (110), and (111) oriented $LaAlO_3$ substrates. The photocatalytic RhB dye degradation on WO_3 thin films was found to be dependent on crystallographic orientation and follows the order (111) > (110) > (001). The authors also calculated the surface energy of oriented thin films and observed the surface energy follows the order (111) > (110) > (001) which is in accordance with the photocatalytic activity. In another report[8], the authors have grown $NaNbO_3$ single-crystal films grown on $LaAlO_3$ with preferred orientation along (100), (110), and (111) crystal planes .The photocatalytic dye degradation of Rhodamine B (RhB) was studies under the xenon lamp, the degradation of the dye was observed to be maximum in the case of the films oriented along (111) crystal plane which was found to be correlative with the generation of $^{\cdot}OH$ radical. Chenning Zhang et al.[9] reported that the photocatalytic degradation of methyl orange dye activity was improved in (001) oriented Nb-doped TiO_2 compared with random thick films and particles. In addition to

photocatalytic activity, Photoelectrochemical activity is also found to be enhanced in [010]-orientated $BiVO_4$ due to an increase in photoinduced charge separation[10].

It has been known that $SrTiO_3$ is one of the promising candidates for photocatalytic water splitting under uv-light as it has a wide bandgap of around 3.2 eV. It has been reported that the photocatalytic activity of $SrTiO_3$ could be enhanced by doping with metal cations or by defect engineering. Different morphologies of $SrTiO_3$ were synthesized such as nanocubes[11], dodecahedron[12], flower[13], and star-like shape[14] for improving photocatalytic water splitting. Moreover, the dependence of exposed crystal facets of $SrTiO_3$ on photocatalytic activity was also established. Bin Wang et. al.[15] showed that the {001} facet of $SrTiO_3$ was found to be active for photoreduction whereas the {023} facet was active for photo-oxidation reaction. In another report, Wu et. al[16] observed that photocatalytic oxidation activity was found to be higher in {110} facet exposed $SrTiO_3$ was higher when compared with {001}. Also in a previous report of ours[17], we observed higher photocatalytic hydrogen evolution activity for $SrTiO_3$ having [100] exposed facet. Mingyi Zhang et. al[18] studied the silver (Ag^+) photoreduction on (100), (110), and (111) oriented $SrTiO_3$ single crystals. They have observed that (100) oriented single crystals showed high activity for photo-reduction of silver than (110) oriented $SrTiO_3$ single crystals. Jennifer L. Giocondi et al[19] reported that the (110) surface of $SrTiO_3$ showed more photoanodic properties than (100). Thus, from the previous reports, we have concluded that the photocatalytic properties of $SrTiO_3$ are strongly affected by the presence of exposed facets.

Keeping the above factors (crystallographic orientation and exposed facets) in consideration, in this chapter we have synthesized oriented assemblies of cubic shaped $SrTiO_3$ nanostructures on the glass substrate. Here, we have used IPTMS (3-idopropyl-trimethoxy silane) as a linker between the glass substrate and $SrTiO_3$ for creating oriented assemblies. We observed higher hydrogen evolution activity on the assemblies of $SrTiO_3$ oriented along the (200) plane. To the best of our knowledge, there is no report on the use of oriented assemblies of $SrTiO_3$ nanostructures on the glass substrate for photocatalytic hydrogen evolution activity.

4.2. Experimental:

4.2.1 Materials and Methods:

Strontium nitrate [($Sr(NO_3)_2$), 99%], Methanol (ACS grade), Toluene (≥ 99.9 %,) Ethanol (> 99%) and Sodium hydroxide [(NaOH) (≥ 97%)] were purchased from Merck. Sodium sulfide flakes were purchased from CDH fine chemicals. Titanium tetraisopropoxide (TTIP) (97%), (3-iodopropyl)trimethoxysilane (≥95%) (IPTMS) and sodium sulfite (98%) were purchased from Sigma-Aldrich.

Synthesis of $SrTiO_3$ nanostructures

Strontium Titanate, $SrTiO_3$ was synthesized using the hydrothermal process as reported previously[17] wherein water was taken as a solvent during the synthesis. For the synthesis of oriented assemblies of $SrTiO_3$ on the glass substrate, different methods were adopted as discussed below.

Functionalization of Glass Substrate

The procedure was followed as reported in the literature. [20] The glass substrate (size 2 cm X 1.5 cm) were washed with HCl (35%) followed by deionized water (DI water) and isopropanol. These were dried with nitrogen gas. For functionalization of the glass substrate, the dried substrates were immersed in a 5 mL solution of toluene containing 98µL of IPTMS. The solution containing the glass substrate was refluxed at 70 ^oC under a nitrogen atmosphere. The functionalized glass substrates were washed with toluene to remove excess IPTMS.

Functionalization of $SrTiO_3$ nanostructures

For functionalization of $SrTiO_3$, 30 mg of $SrTiO_3$ nanostructures were dispersed in 30 mL of ethanol solution containing 587µL of IPTMS. This dispersion containing the nanostructures was stirred for 24 h at 40ºC. The particles were then centrifuged and washed with ethanol and dried at 60 C.

Assembling $SrTiO_3$ on a glass substrate

The methodology was followed as reported in the literature[20] with some modifications. 5mg of $SrTiO_3$ powder (functionalized/non-functionalized) was dispersed in 5 mL toluene using

ultrasonication for 3 hours. Glass substrate (functionalized/non-functionalized) was immersed in the above dispersion. The system was sonicated in an ultrasonicated for around 10 minutes. The glass substrate with $SrTiO_3$ deposited over was then immersed in Toluene and sonicated for 10s, to remove extra material on the substrate. The STO coated glass substrates were then dried by flushing using a nitrogen gun.

Four different conditions were used for depositing $SrTiO_3$ on the glass substrate. These have been discussed as follows:

STO-F1: In this, both $SrTiO_3$ powder used for the formation of assembly and the glass substrate were functionalized with IPTMS.

STO-F2: In this, the glass substrate was functionalized with IPTMS while $SrTiO_3$ powder that was used for the formation of the assembly was not functionalized.

STO-F3: In this, $SrTiO_3$ powder that was used for the formation of the assembly was functionalized with IPTMS while the glass substrate was not functionalized.

STO-F4: In this, neither the glass substrate nor $SrTiO_3$ powder that was used for the formation of the assembly was functionalized with IPTMS.

4.2.2. Characterization:

The phase purity of synthesized $SrTiO_3$ and the orientation of $SrTiO_3$ powder on the glass substrate (STO-F1-STO-F4) was checked using powder X-ray diffraction (PXRD, Bruker D8 Advance Eco) with Cu Kα as an X-ray source (λ = 0.15406 nm). The PXRD instrument was operated at 40 kV and 25 mA at scanning steps of 0.0103 in the 2θ range of 10−80° and the duration of the scan was 36 minutes.

Field Emission Scanning Electron Microscopy (FESEM) studies were carried out on JEOL JSM-7610FPlus. Raman study was carried out on WI Tec's Raman microscope, α 300 R. Transmission electron microscope studies (TEM) studies were carried out on JEOL, JEM-2100 operated at an accelerating voltage of 200 kV. The samples were prepared by dispersing the powder samples in ethanol and drop-casting on a carbon-coated copper grid. XPS (X-Ray Photoelectron Spectroscopy) studies were carried out on Thermo Scientific's K-alpha X-ray Photoelectron Spectrometer (XPS) System. The sample for XPS analysis was prepared by

depositing a thick paste of the oxide (prepared in ethanol) onto a glass slide. The deposited oxide was dried and used for XPS analysis. Diffuse Reflectance Spectra were collected on a UV–visible spectrophotometer, Shimadzu UV-2600, in a wavelength range of 200-800 nm. Kubelka-Munk's (K-M) equation was used to calculate the bandgap of the materials from the reflectance spectra. Photoluminescence spectra were obtained from Horiba's TCSPC at an excitation wavelength of 350 nm.

4.2.3 Photocatalytic Hydrogen Evolution Reaction (HER):

A top irradiation quartz reactor of capacity 140 mL was used for the photocatalytic reaction for the hydrogen evolution. In a typical experiment, the assemblies of particles on a glass substrate were immersed in a 40 mL aqueous solution containing 0.35M Na_2SO_3. The study was carried out in absence of any metal co-catalyst to see the direct influence of the oriented assembly of $SrTiO_3$ on the photocatalytic performance. The solution was purged with N_2 gas for 30 minutes to eliminate the dissolved oxygen. A 450W Xe lamp was used as a source of light. The photon flux of the Xe lamp was obtained from Ray virtual radiation actinometer, Newport, Model 91150V. The gas component from the reactor was analyzed using gas chromatography (GC, Perkin Elmer Clarus 680) with a thermal conductivity detector at an interval of 1 h. The apparent quantum efficiency was calculated using the equation given below:

$$AQY = \frac{2nN_A hc}{PS\lambda t} \times 100 \qquad (4.1)$$

where n is the amount of hydrogen evolved; N_A is Avogadro's constant (6.022×10^{23} mol^{-1}); h is Planck's constant (6.63×10^{-34} J s); c is the speed of the light (3×10^{10} cm/s); P is the power density of the incident light (181×10^{-3} W/cm^2); S is the irradiation area (12.6 cm^2); λ is the representative wavelength of the incident light (using the radiation spectrum of the lamp, 390 nm (390×10^{-7} cm)); and t is the time duration of the incident light (18000 s).

4.3 Results and Discussion:

As synthesized $SrTiO_3$ nanostructures

PXRD studies of $SrTiO_3$ nanostructures (figure 4.1) showed the formation of a pure phase wherein all the reflection planes could be indexed to the cubic unit cell (JCPDS card no.00-035-0734) having space group, $Pm\bar{3}m$. TEM studies of $SrTiO_3$ nanostructures show nanocubes

having a size of ~50-80 nm were formed (figure 4.2). These nanocubes were further used for the formation of assemblies on a glass substrate under different conditions.

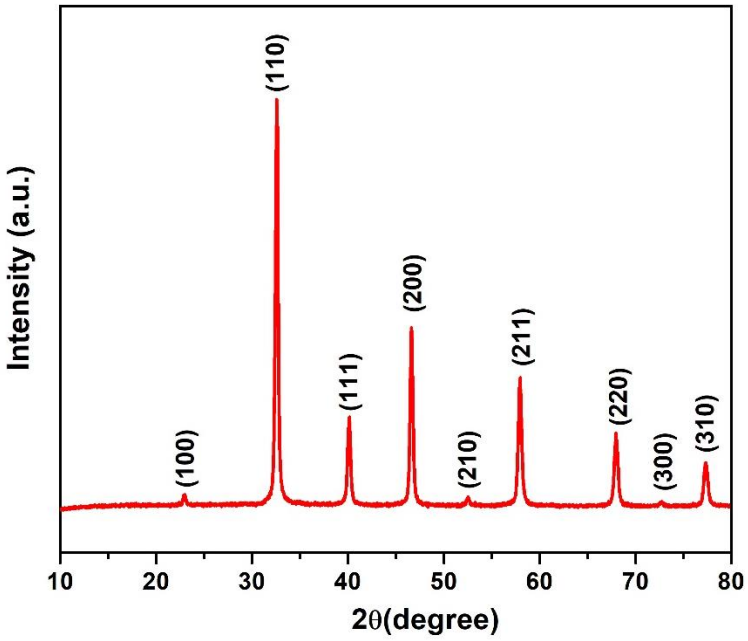

Figure 4.1: PXRD of the $SrTiO_3$ nanostructures

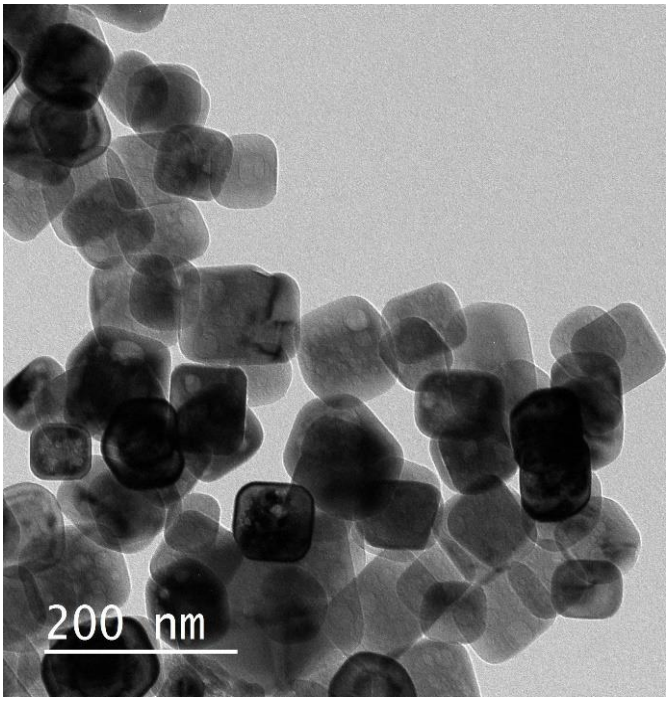

Figure 4.2: TEM image of $SrTiO_3$ nanostructures

The high-resolution spectra of $SrTiO_3$ are shown in figure 4.3 a-c. Peaks at binding energy: 132.4 eV and 134.1 eV were observed for Sr (3d) spectra (figure 4.3 a) which could be assigned to Sr $3d_{5/2}$ and Sr $3d_{3/2}$ respectively. The difference in the energy between the splitting (between $3d_{5/2}$ and $3d_{3/2}$) was observed to be 1.76 eV which is consistent with the literature[21]. The fitting of the high resolution spectra of Ti (2p) (figure 4.3 b) indicated the presence of Ti^{3+} (456.8 ($2p_{3/2}$) and 462.3 eV ($2p_{1/2}$); difference 5.5 eV) along with Ti^{4+} (457.8 ($2p_{3/2}$) and 463.7 eV ($2p_{1/2}$); difference 5.9 eV). Figure 4.3 c shows high–resolution O1s spectra for the oxide which was fitted in two Gaussian peaks at binding energy at 528.9 and 530.5 eV. The peaks at 528.9 eV can be attributed to the Metal –oxygen bond i.e. the presence of O^{2-} ions in the crystal structure whereas the peak at 530.5 was related to the presence of defect arising due to oxygen vacancy in $SrTiO_3$. The presence of vacancy can also be correlated to the fact that Ti^{3+} is observed along with Ti^{4+} which can arise only due to oxygen vacancies in the sample. Thus the presence of peak corresponding to oxygen vacancy along with Ti^{3+} confirms the presence of oxygen vacancy in the lattice[22].

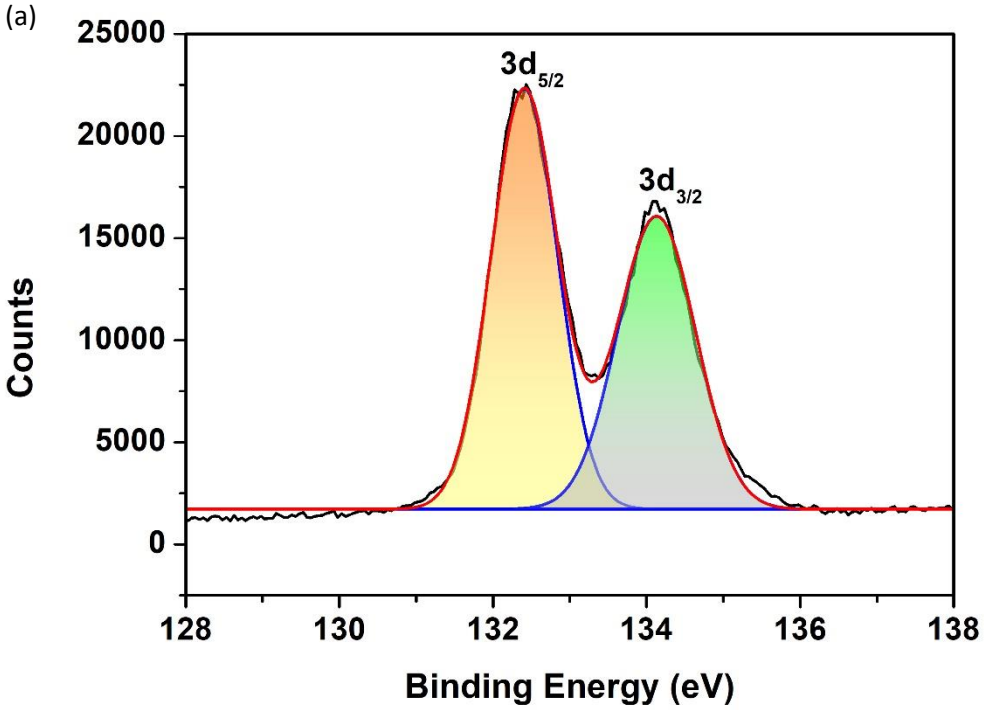

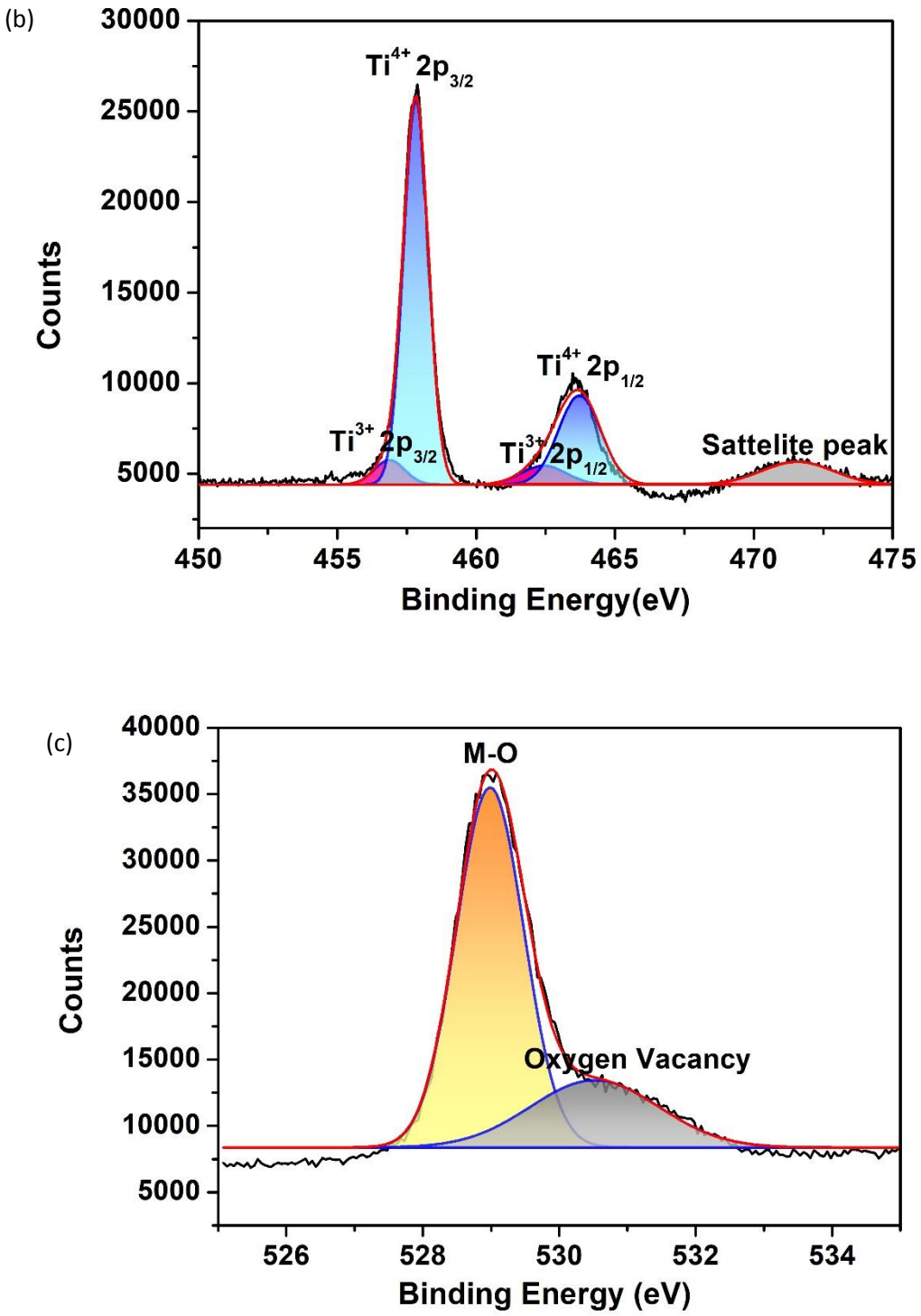

Figure 4.3: XPS spectra of SrTiO3 nanostructures showcasing elemental scan of (a) Strontium (Sr 3d), (b) Titanium, (Ti 2p) and (c) Oxygen, O(1s).

Assemblies of $SrTiO_3$ nanocubes on the glass substrate

To see the effect of assemblies on the orientation of the nanostructures on the glass substrate, XRD studies were carried out on STO-F1-STO-F4 (figure 4.4 a-d). Three peaks corresponding to the (100), (110) and (200) planes were observed for STO-F1 and STO-F2 whereas two peaks corresponding to the (110) and (200) planes were observed for STO-F3 and STO-F4. It was observed that the intensity of the (200) plane was higher than that of the (110) plane for STO-F2 which was different from the conventional pattern of intensity wherein the intensity of the (110) plane is higher than (200) plane. The higher intensity of the (200) plane in STO-F2 suggests the orientation of the film along the (200) plane.

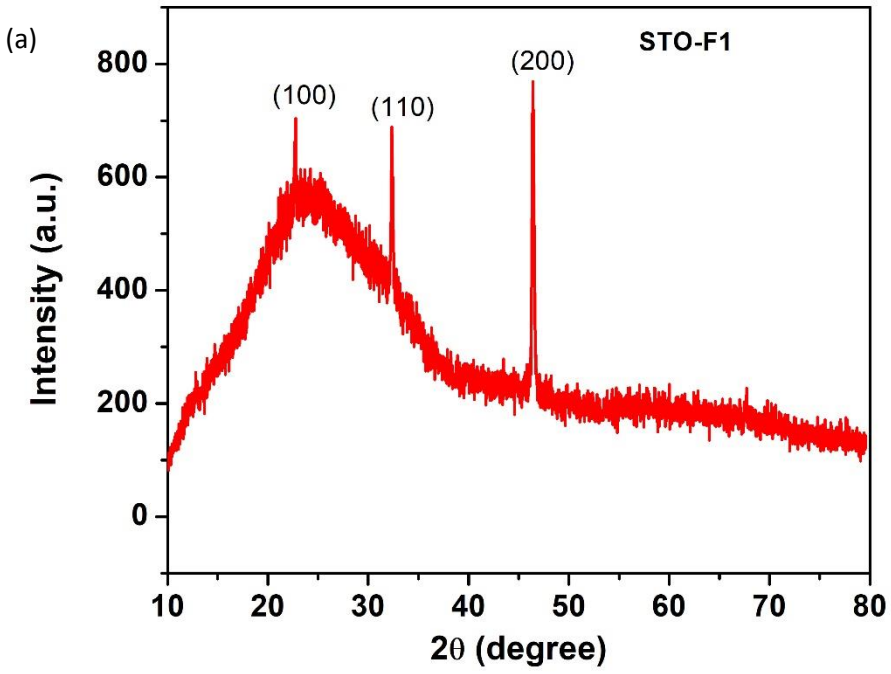

(c)

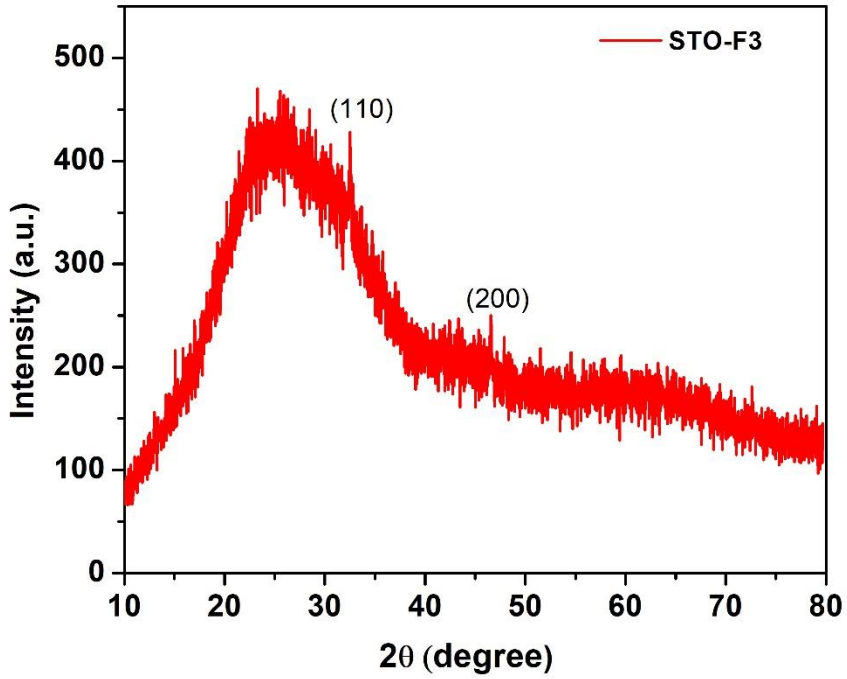
STO-F3
(110)
(200)
Intensity (a.u.)
2θ (degree)
0
100
200
300
400
500
10
20
30
40
50
60
70
80

(b)

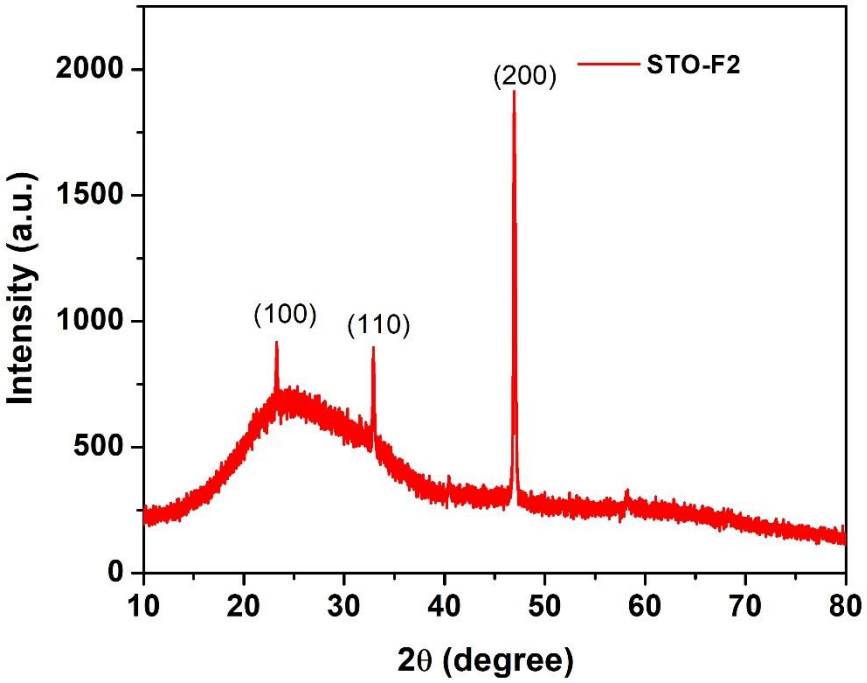
STO-F2
(200)
(100)
(110)
Intensity (a.u.)
2θ (degree)
0
500
1000
1500
2000
10
20
30
40
50
60
70
80

(d)

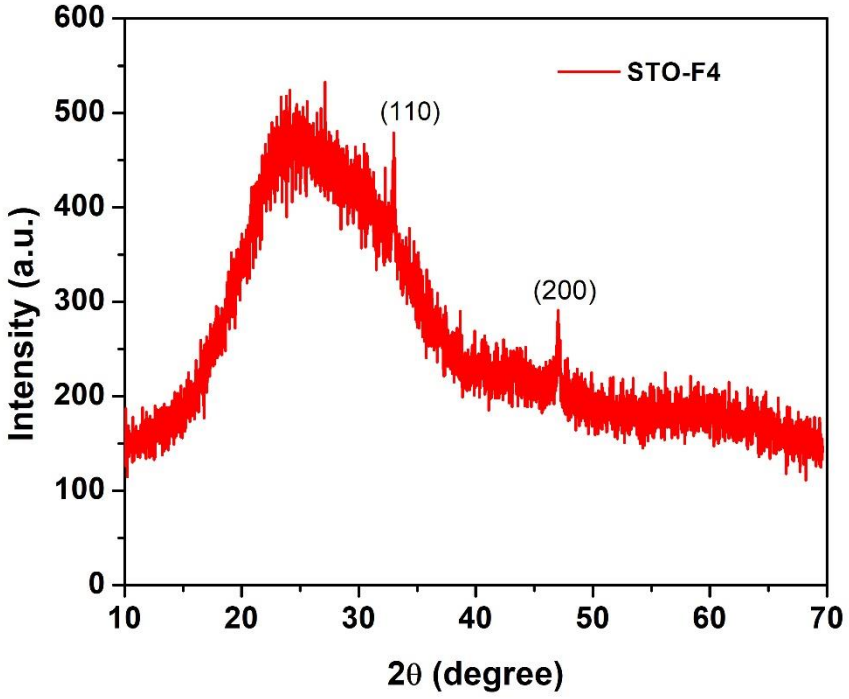

Figure 4.4 (a-d): PXRD pattern of assemblies of $SrTiO_3$ nanostructures on the glass substrate.

To see the nature of assemblies of $SrTiO_3$ nanocubes on glass substrate for STO-F1-STO-F4, FESEM studies were carried out (figure 4.5a-d). At lower magnification, we observed a uniform distribution of the $SrTiO_3$ nanocubes with the maximum degree of coverage on the glass substrate for STO-F2 which was fabricated by deposition of the non-functionalized nanocubes over IPTMS-functionalized glass substrate (figure 4.5b). Further, a closer look at the assembly (inset in figure 4.5 b) showed that there was no cluster or agglomeration during the formation of the assembly. Monolayer kinds of deposition of particles that did not lay over each other were observed. This uniform and monolayer kind of assembly were not observed for STO-F1 (figure 4.5a), STO-F3 (figure 4.5c) and STO-F4 (figure 4.5d), though the coverage of nanocubes was more for STO-F3 and STO-F4 amongst the three kinds of assemblies. The particles were agglomerated in STO-F1, STO-F3 and STO-F4.

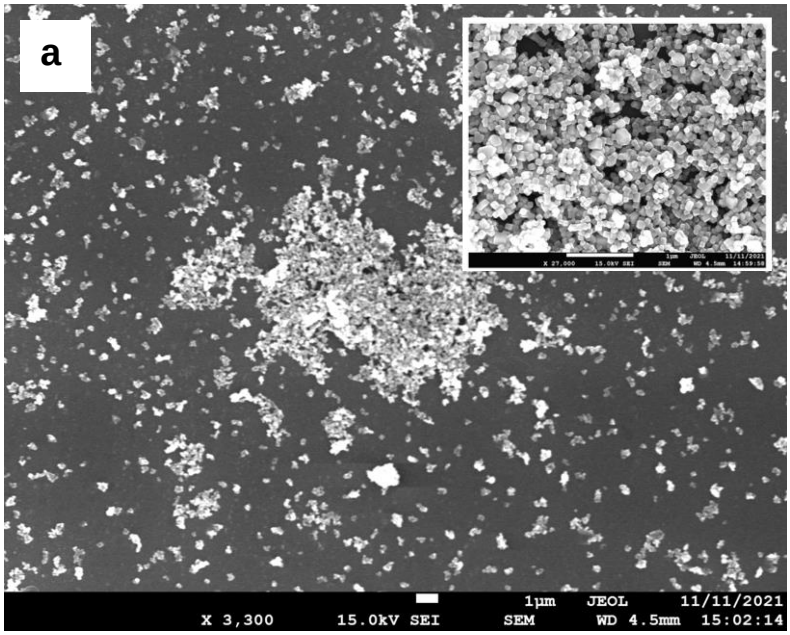
a
X 3,300 15.0kV SEI SEM 1µm JEOL WD 4.5mm 11/11/2021 15:02:14

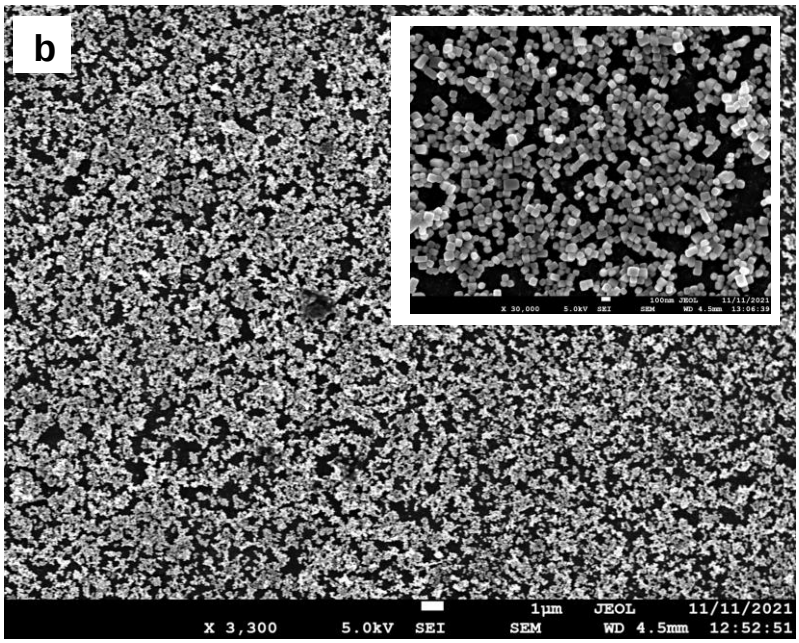
b
X 3,300 5.0kV SEI SEM 1µm JEOL WD 4.5mm 11/11/2021 12:52:51

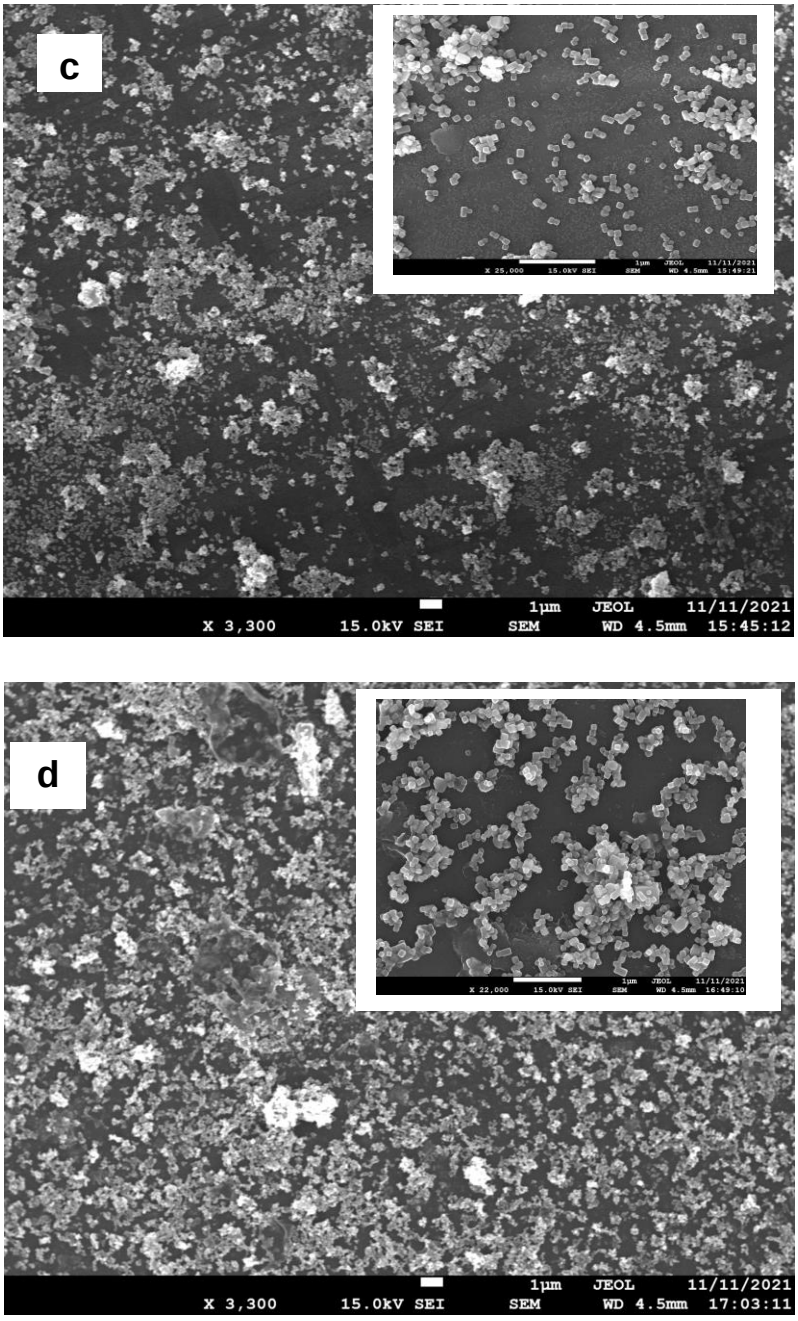

Figure 4.5 (a-d): FESEM images of (a) STO-F1, (b) STO-F2, (c) STO-F3, (d) STO-F4, inset shows images at higher resolution.

Figure 4.6 (a) and (b) show attachment of IPTMS to $SrTiO_3$ nanocubes and glass substrate respectively. A schematic showcasing a plausible mechanism for the formation of assemblies of $SrTiO_3$ on the glass substrate for STO-F1 to STO-F4 is shown in figure 4.6 (c-f). It was observed

that the non-functionalized $SrTiO_3$ with IPTMS helped in maximum coverage of the nanocubes over the substrate (as observed for STO-F2 and STO-F4). Agglomeration of particles in STO-F1 and STO-F3 could be explained by the fact that the oxide nanostructures were functionalized with IPTMS, which could have resulted in an interaction of the deposited nanostructures with other functionalized nanostructures, resulting in the agglomerated cluster. The agglomeration in STO-F4, wherein particles was not functionalized, could be due to the effect of evaporation of the solvent after deposition.

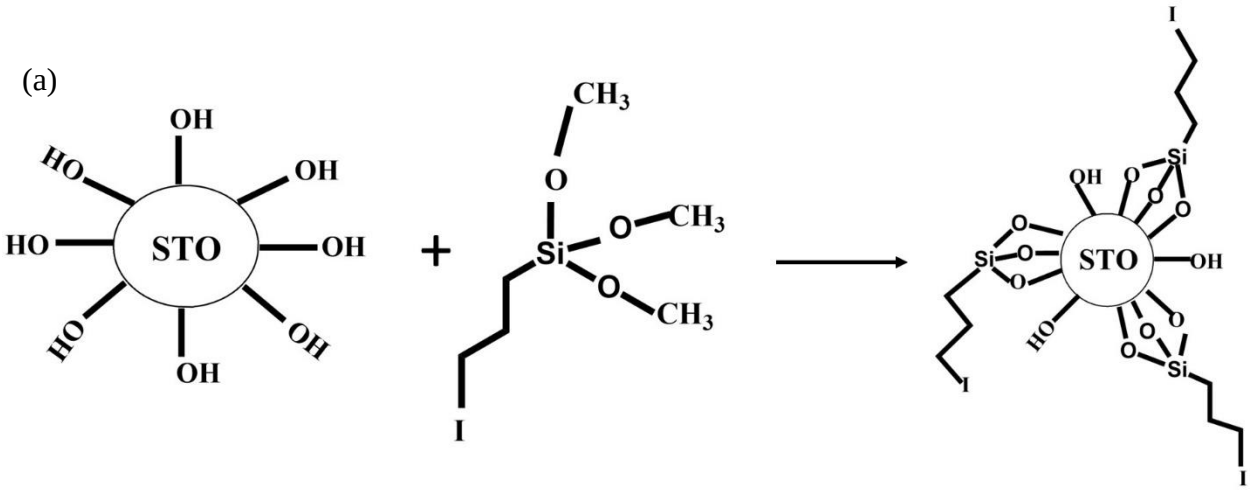

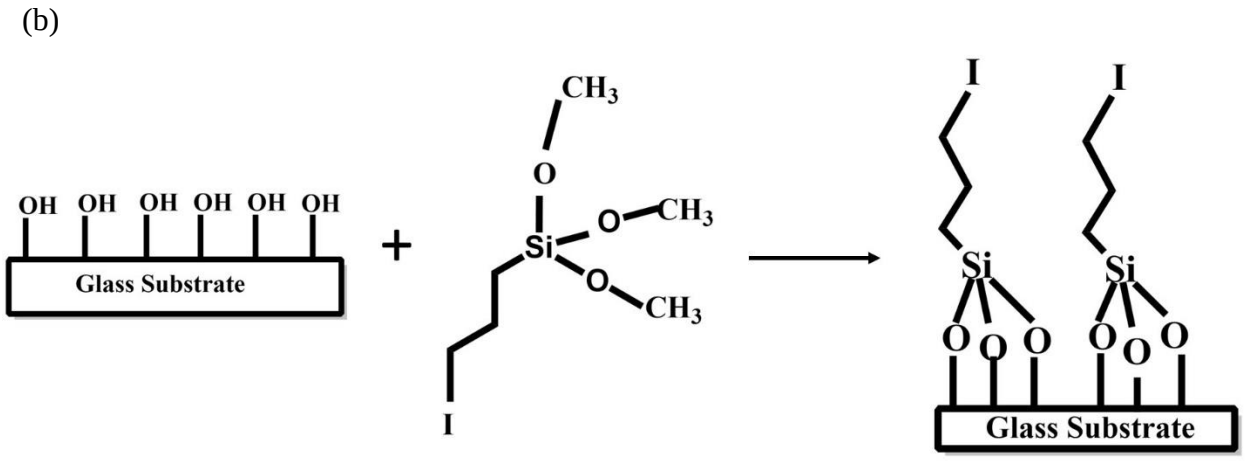

(c)

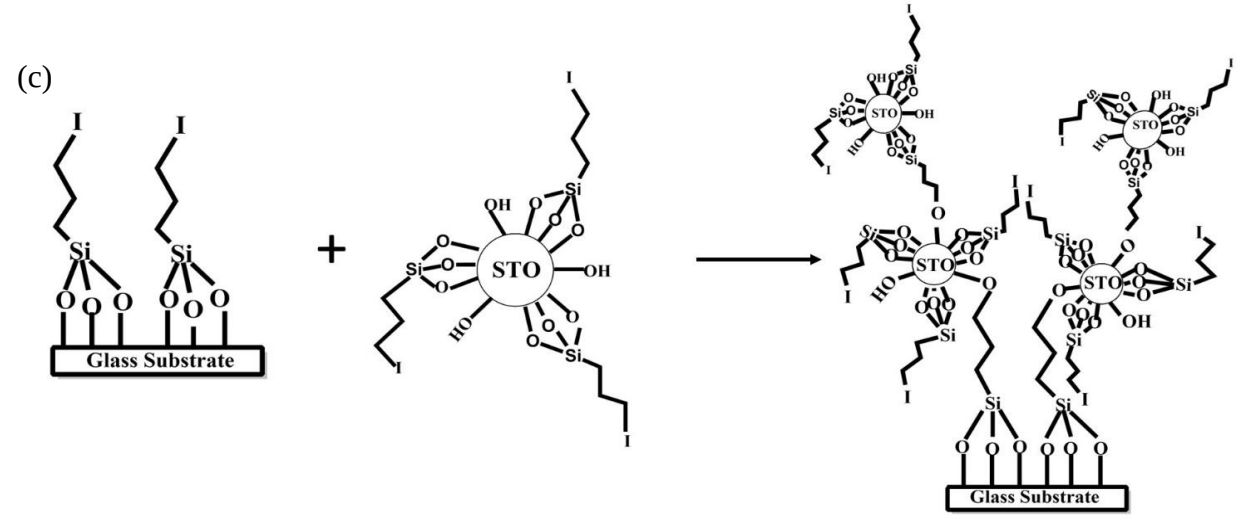
Glass Substrate
STO
Glass Substrate

(d

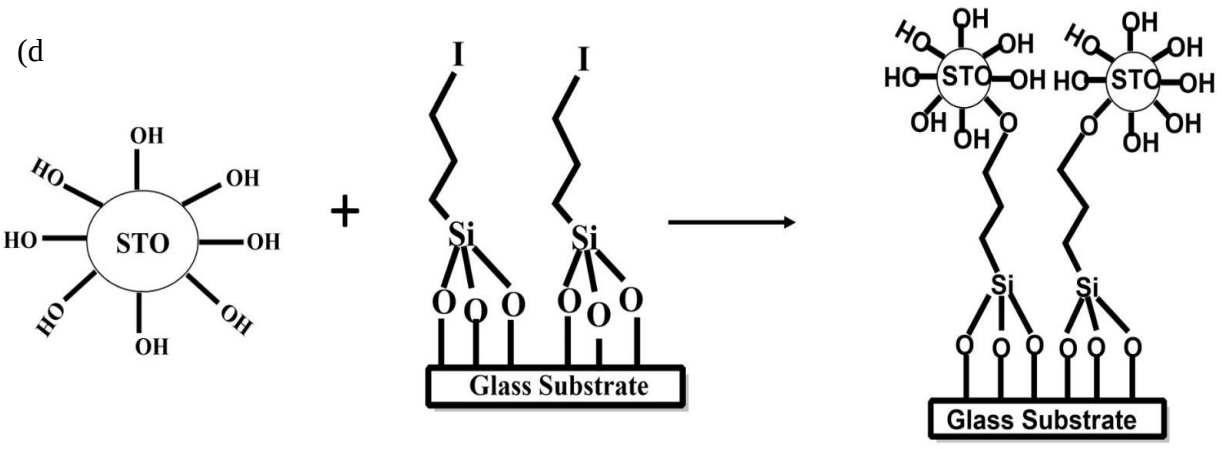
STO
Glass Substrate
STO
Glass Substrate

(e)

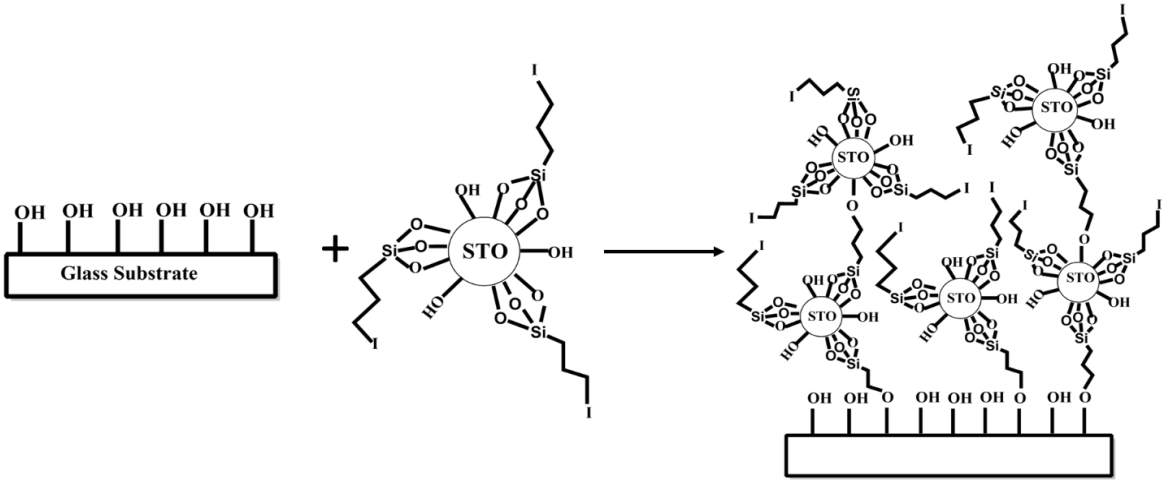
Glass Substrate
STO

(f)

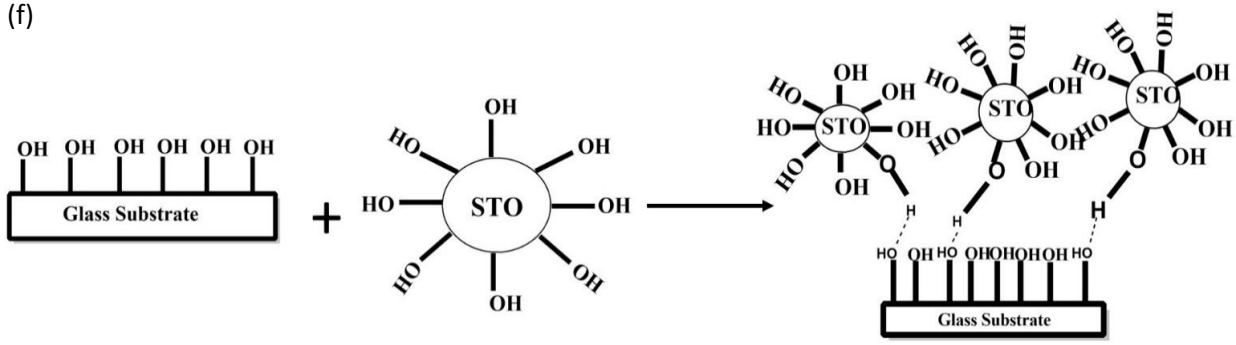

Figure 4.6: Schematic representation of the formation of assemblies of SrTiO3 nanocubes on the glass substrate under different conditions, (a) attachment of ITMPS to SrTiO3 nanocubes, (b) attachment of ITMPS to a glass substrate, (c) STO-F1, (d) STO-F2, (e) STO-F3, (f) STO-F4.

Optical properties were measured on oriented assemblies of $SrTiO_3$ of STO-F1-STO-F4 using UV-Visible diffuse reflectance spectroscopy (DRS). UV-visible absorption spectra and Tauc plot are shown in figures 4.7 a and b respectively. The bandgap of these STO1-STO4 was calculated using the equation given below:

$$(\alpha h\upsilon)^{\frac{1}{n}} = C\left(h\upsilon - E_g\right) \qquad (4.2)$$

where α is the absorption coefficient; E_g is the bandgap of the material; n denotes the nature of transition (n = ½ for direct transition and n = 2 for indirect transition). From figure 4.7 b, no change in the bandgap was observed. The bandgap of STO-F1-STO-F4 was calculated to be 3.6 eV which is the same for all four samples, indicating that the assemblies are active under the UV region of the solar spectrum.

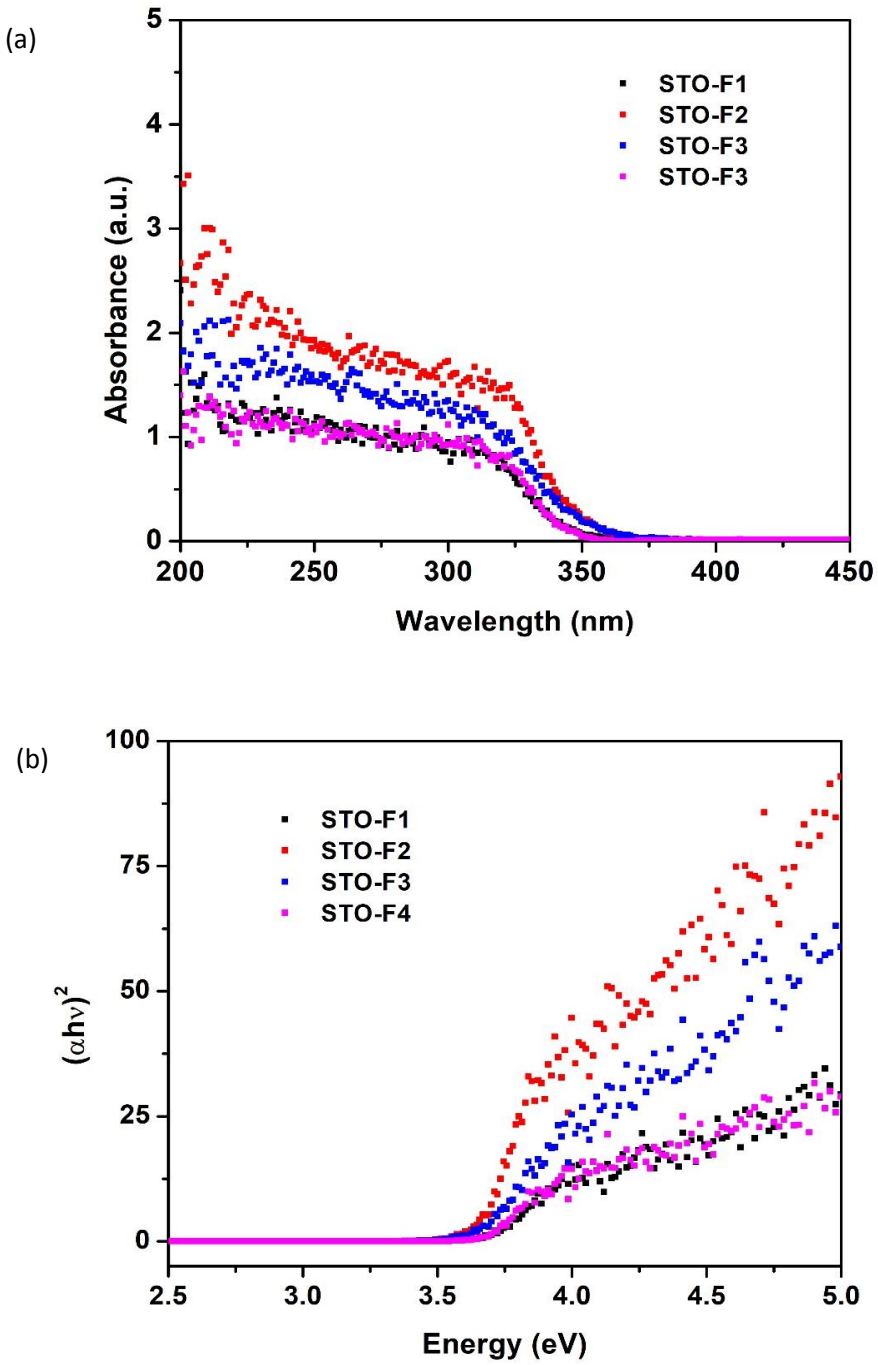

Figure 4.7: (a) UV-visible absorption spectra and (b) Tauc plot of assemblies of $SrTiO_3$ nanocubes on the glass substrate, STO-F1-STO-F4.

Raman Studies on samples STO-F1-STO-F4 were done to check the effect of orientated assembly of $SrTiO_3$ nanostructures on phase structure. We did not observe any change in Raman spectra of four of the samples (STO-F1-STO-F4) as shown in figure 4.8.

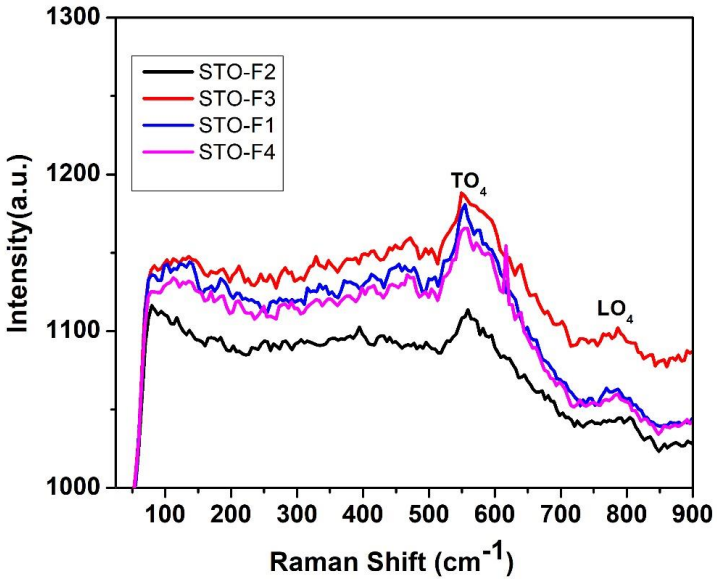

Figure 4.8: Raman Spectra of assemblies of $SrTiO_3$ nanocubes on the glass substrate, STO-F1-STO-F4.

Photoluminescence studies were performed on STO-F1-STO-F4 samples (Figure 4.9). The lower intensity of photoluminescence emission was observed for STO-F2 which suggests lower recombination of electrons and holes involved in the radiative transition.

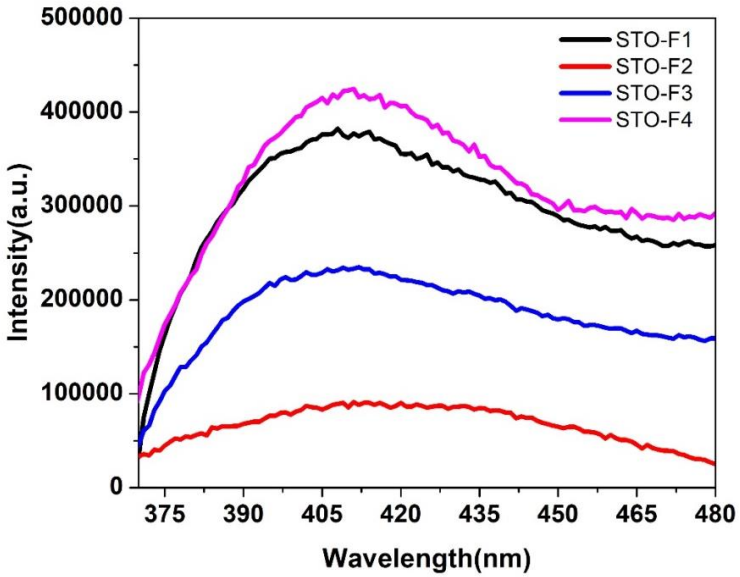

Figure 4.9: Photoluminescence spectra of assemblies of $SrTiO_3$ nanostructures (STO-F1, STO-F2, STO-F3, and STO-F4).

Photocatalytic Hydrogen Evolution Study

To see the influence of the orientation of the assembly of $SrTiO_3$ nanocubes, formed on a glass substrate (STO-F1-STO-F4), on the photocatalytic hydrogen evolution activity, the amount of hydrogen evolved from an aqueous solution containing 0.35M Na_2SO_3 (used as hole-scavenger) under 450 W Xenon lamp was measured. No H_2 gas was evolved in the absence of light. Temporal hydrogen evolution under light is shown in Figure 4.10. The apparent quantum yield was calculated using equation 4.1 and is tabulated in Table 4.1.

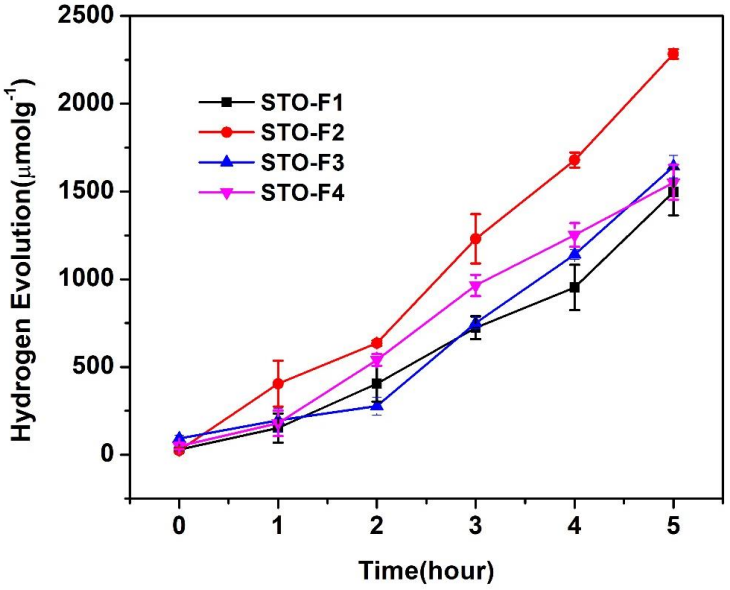

Figure 4.10: Photocatalytic hydrogen evolution by assemblies of $SrTiO_3$ nanostructures (STO-F1, STO-F2, STO-F3, and STO-F4).

Table 4.1**:** Apparent quantum yield for hydrogen evolution using the oriented assembly of $SrTiO_3$ nanoparticles on a glass plate (STO-F1- STO-F4).

Sample	n (Amount of hydrogen gas evolved after 5 h of the reaction) (mol)	Apparent Quantum Yield (AQY) (%)
STO-F1	1.497×10^{-6}	0.0022
STO-F2	2.283×10^{-6}	0.0034
STO-F3	1.643×10^{-6}	0.0024
STO-F4	1.551×10^{-6}	0.0023

It was observed that the hydrogen evolution activity of STO-F2 (Figure 4.10) was highest amongst the four kinds of assembly viz. STO-F1, STO-F2, STO-F3, and STO-F4. The rate of hydrogen evolution reaction was observed to follow the order STO-F2>STO-F3>STO-F1 ≈STO-F4 with a maximum rate of 457 $\mu molg^{-1}h^{-1}$ for STO-F2. STO-F2 was shown to have a high degree of preferred orientation of particles for the (200) plane. To ensure whether the enhanced activity was due to preferred orientation or local ordered arrangement of particles on the glass substrate, GISAXS studies were carried out on all the samples.

(a

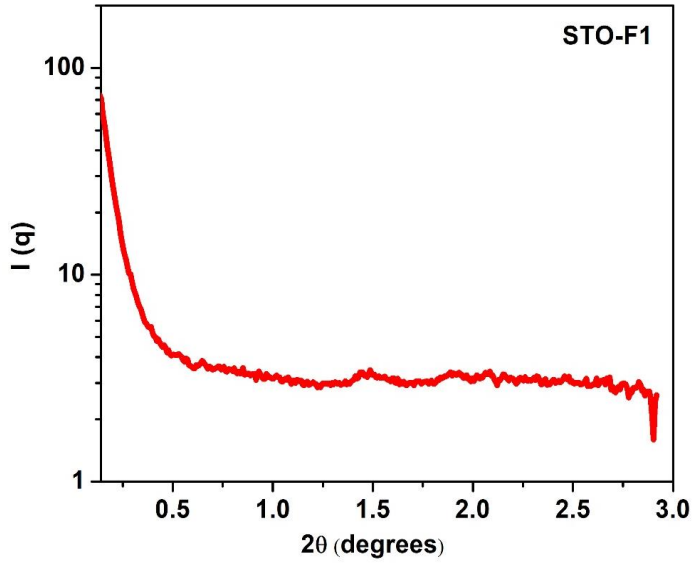

(b

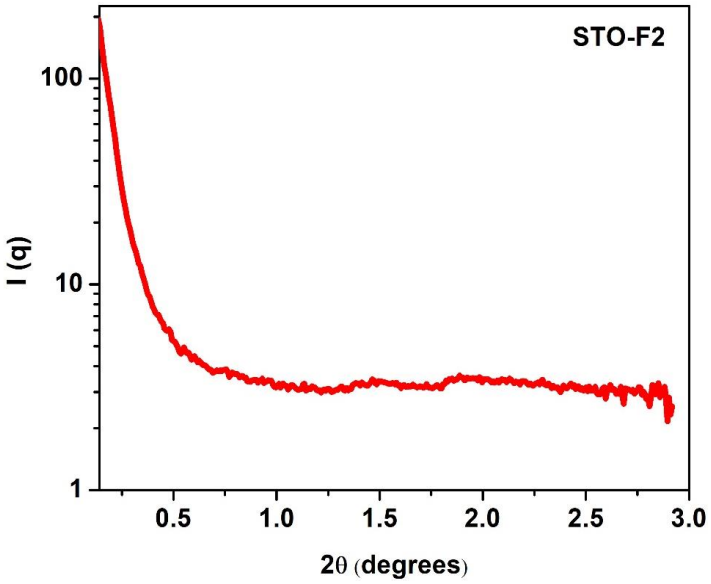

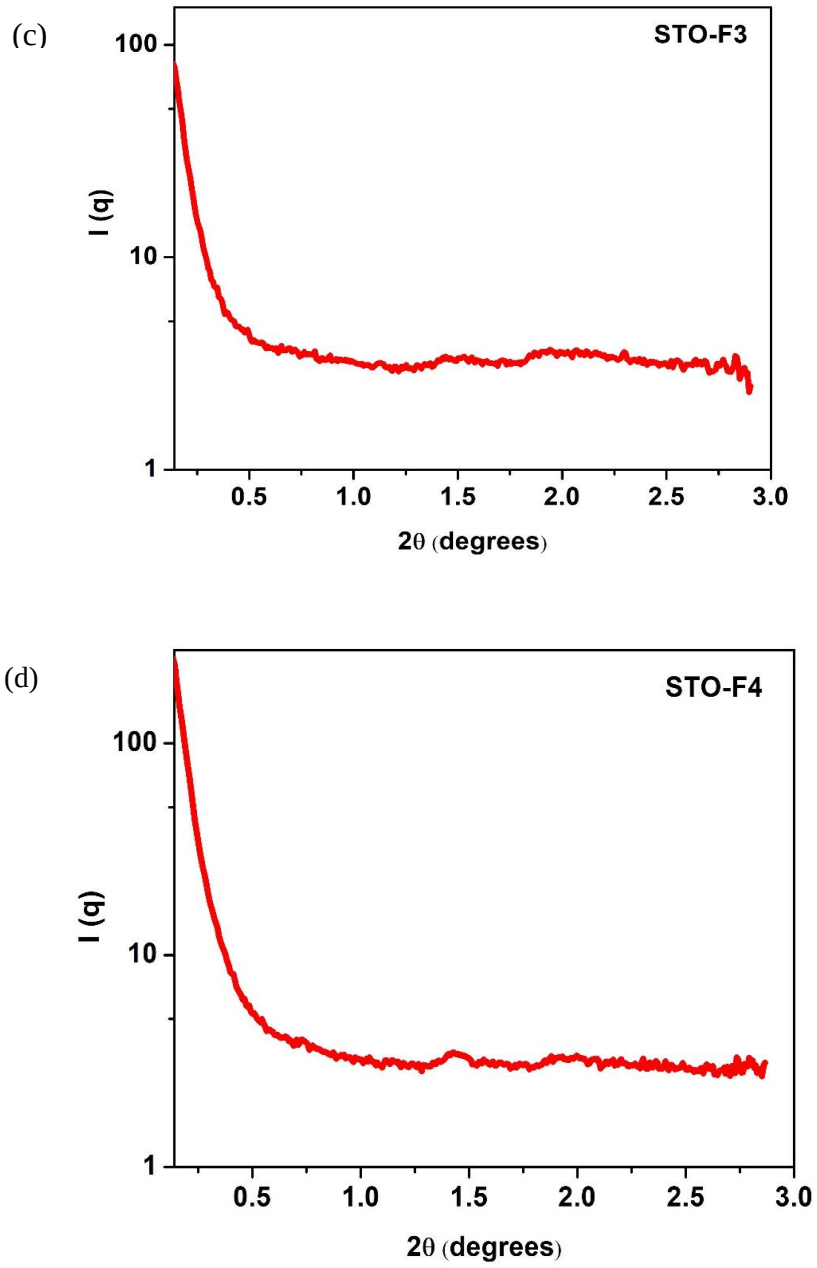

Figure 4.11 : GISAXS intensity profile for samples (a) STO-F1, (b) STO-F2, (c) STO-F3, (d) STO-F4.

From the graph (figure 4.11 a-d), no local ordering of particles was seen on these assemblies of $SrTiO_3$ on a glass substrate. Thus, it can be concluded that the (200) orientation of $SrTiO_3$ (in STO-F2) plays an important role in the catalytic activity. In addition to the (200) orientation of the particles in STO-F2, the deposition of particles over a glass substrate is quite dense and uniform (figure 4.5b). So it is likely that there is a large number of particles having (200) as the

preferred orientation present in the assembly over the glass substrate, which could have resulted in enhanced photocatalytic activity of STO-F2.

To check the stability of the catalyst after photocatalytic reactions, XRD studies were carried out on STO-F2 obtained after completing the photocatalytic reactions. No change in the structure and the preferred orientation for the (200) plane was observed for STO-F2 from the XRD (figure 4.12) indicating that the oriented assemblies of STO-F2 are stable after the photocatalytic reactions.

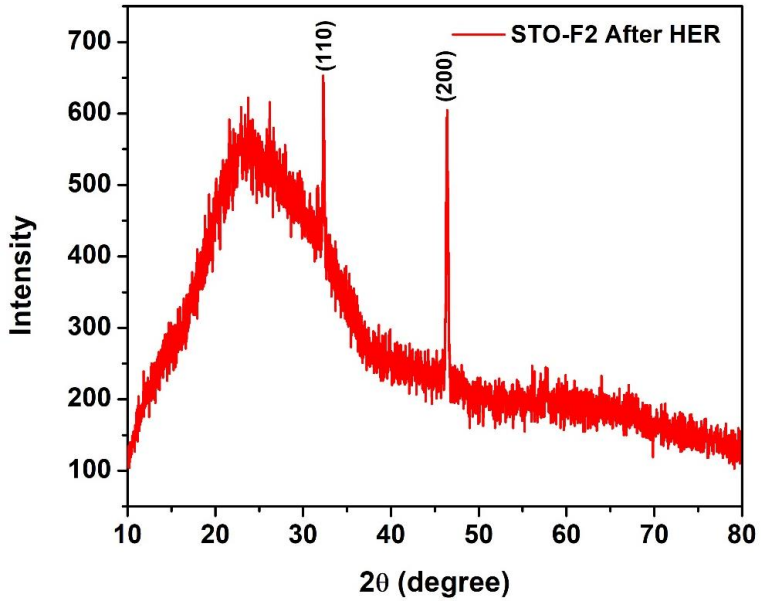

Figure 4.12: PXRD pattern of STO-F2 after photocatalytic hydrogen evolution.

Thus, from the trend observed in the photocatalytic hydrogen evolution activity, we could see a clear dependence of photocatalytic activity on crystal plane orientation. The photocatalytic hydrogen evolution is enhanced with (200) crystal plane orientation. Thus, in our study, both the (200) plane crystal orientation and high surface coverage of $SrTiO_3$ nanostructures on the glass substrate resulted in enhanced photocatalytic hydrogen evolution activity of the STO-F2. The higher photocatalytic performance of STO-F2 was also supported by photoluminescence studies. Hence, the proper choice of crystal orientation could play an important role in designing the highly efficient catalyst for photocatalytic HER.

4.4 Conclusion:

We have synthesized assemblies of $SrTiO_3$ nanostructures on the glass substrate under different conditions where IPTMS was used as a linker between $SrTiO_3$ nanostructures and glass substrate. The orientation of $SrTiO_3$ nanostructures along the (200) plane was observed to be higher in STO-F2 where only glass substrate was functionalized with IPTMS. From the FESEM study, a uniform layer with high coverage of $SrTiO_3$ nanostructures on the glass substrate was observed for STO-F2 as compared to other samples. Mechanism of the formation of assemblies $SrTiO_3$ nanostructures for STO-F1–STO-F2 were also explained based on IPTMS linkage with the glass substrate and with $SrTiO_3$ nanostructures. The photocatalytic hydrogen evolution activity was observed to be highest in STO-F2 (457 $\mu molg^{-1}h^{-1}$). Results of photocatalyst hydrogen evolution can be explained based on the orientation of $SrTiO_3$ nanostructures along the (200) plane for STO-F2. Photoluminescence spectra show lower recombination of photogenerated charge carriers in STO-F2 involved in the radiative process. Thus, our work demonstrates the role of oriented assemblies along any preferred crystal plane in enhancing photocatalytic hydrogen activity.

Acknowledgement

We would like to acknowledge Prof. Santanu Pal for performing GISAXS studies in this work.

4.5 References:

1. Maeda, K., Photocatalytic water splitting using semiconductor particles: History and recent developments. *Journal of Photochemistry and Photobiology C: Photochemistry Reviews* **2011,** *12* (4), 237-268.
2. Maeda, K.; Teramura, K.; Lu, D.; Takata, T.; Saito, N.; Inoue, Y.; Domen, K., Photocatalyst releasing hydrogen from water. *Nature* **2006,** *440* (7082), 295.
3. Tong, H.; Ouyang, S.; Bi, Y.; Umezawa, N.; Oshikiri, M.; Ye, J., Nano-photocatalytic Materials: Possibilities and Challenges. *Advanced Materials* **2012,** *24* (2), 229-251.
4. Yang, H. G.; Sun, C. H.; Qiao, S. Z.; Zou, J.; Liu, G.; Smith, S. C.; Cheng, H. M.; Lu, G. Q., Anatase TiO_2 single crystals with a large percentage of reactive facets. *Nature* **2008,** *453* (7195), 638-641.
5. Ohsawa, T.; Lyubinetsky, I.; Du, Y.; Henderson, M. A.; Shutthanandan, V.; Chambers, S. A., Crystallographic dependence of visible-light photoactivity in epitaxial $TiO_{2-x}N_x$ anatase and rutile. *Physical Review B* **2009,** *79* (8), 085401.
6. Morris Hotsenpiller, P. A.; Bolt, J. D.; Farneth, W. E.; Lowekamp, J. B.; Rohrer, G. S., Orientation Dependence of Photochemical Reactions on TiO_2 Surfaces. *The Journal of Physical Chemistry B* **1998,** *102* (17), 3216-3226.
7. Li, G.; Varga, T.; Yan, P.; Wang, Z.; Wang, C.; Chambers, S. A.; Du, Y., Crystallographic dependence of photocatalytic activity of WO3 thin films prepared by molecular beam epitaxy. *Physical Chemistry Chemical Physics* **2015,** *17* (23), 15119-15123.
8. Li, G.; Yi, Z.; Bai, Y.; Zhang, W.; Zhang, H., Anisotropy in photocatalytic oxidization activity of NaNbO3 photocatalyst. *Dalton Transactions* **2012,** *41* (34), 10194-10198.
9. Zhang, C.; Uchikoshi, T.; Ishigaki, T., Effect of crystalline orientation on photocatalytic performance for Nb-doped TiO2 nanoparticles. *Advanced Powder Technology* **2021,** *32* (11), 4149-4154.
10. Li, D.; Liu, Y.; Shi, W.; Shao, C.; Wang, S.; Ding, C.; Liu, T.; Fan, F.; Shi, J.; Li, C., Crystallographic-Orientation-Dependent Charge Separation of BiVO4 for Solar Water Oxidation. *ACS Energy Letters* **2019,** *4* (4), 825-831.
11. Macounová, K. M.; Nebel, R.; Klusáčková, M.; Klementová, M.; Krtil, P., Selectivity Control of the Photo-Catalytic Water Oxidation on SrTiO3 Nanocubes via Surface Dimensionality. *ACS Applied Materials & Interfaces* **2019,** *11* (18), 16506-16516.
12. Hsieh, P.-L.; Naresh, G.; Huang, Y.-S.; Tsao, C.-W.; Hsu, Y.-J.; Chen, L.-J.; Huang, M. H., Shape-Tunable $SrTiO_3$ Crystals Revealing Facet-Dependent Optical and Photocatalytic Properties. *The Journal of Physical Chemistry C* **2019,** *123* (22), 13664-13671.

13. Wu, Z.; Zhang, Y.; Wang, X.; Zou, Z., Ag@SrTiO3 nanocomposite for super photocatalytic degradation of organic dye and catalytic reduction of 4-nitrophenol. *New Journal of Chemistry* **2017,** *41* (13), 5678-5687.

14. Zhou, M.; Chen, J.; Zhang, Y.; Jiang, M.; Xu, S.; Liang, Q.; Li, Z., Shape-controlled synthesis of golf-like, star-like, urchin-like and flower-like SrTiO3 for highly efficient photocatalytic degradation and H2 production. *Journal of Alloys and Compounds* **2020,** *817*, 152796.

15. Wang, B.; Shen, S.; Guo, L., Surface Reconstruction of Facet-Functionalized SrTiO3 Nanocrystals for Photocatalytic Hydrogen Evolution. *ChemCatChem* **2016,** *8* (4), 798-804.

16. Wu, X.; Wang, X.; Li, J.; Zhang, G., Boosting molecular oxygen activation of SrTiO3 by engineering exposed facets for highly efficient photocatalytic oxidation. *Journal of Materials Chemistry A* **2017,** *5* (45), 23822-23830.

17. Vijay, A.; Vaidya, S., Tuning the Morphology and Exposed Facets of SrTiO3 Nanostructures for Photocatalytic Dye Degradation and Hydrogen Evolution. *ACS Applied Nano Materials* **2021,** *4* (4), 3406-3415.

18. Zhang, M.; Salvador, P. A.; Rohrer, G. S., Influence of pH and Surface Orientation on the Photochemical Reactivity of SrTiO3. *ACS Applied Materials & Interfaces* **2020,** *12* (20), 23617-23626.

19. Giocondi, J. L.; Rohrer, G. S., Structure Se nsitivity of Photochemical Oxidation and Reduction Reactions on SrTiO3 Surfaces. *Journal of the American Ceramic Society* **2003,** *86* (7), 1182-1189.

20. Ma, G.; Takata, T.; Katayama, M.; Zhang, F.; Moriya, Y.; Takanabe, K.; Kubota, J.; Domen, K., Semiconductor monolayer assemblies with oriented crystal faces. *CrystEngComm* **2012,** *14* (1), 59-62.

21. Sosulnikov, M. I.; Teterin, Y. A., X-ray photoelectron studies of Ca, Sr and Ba and their oxides and carbonates. *Journal of Electron Spectroscopy and Related Phenomena* **1992,** *59* (2), 111-126.

22. Panomsuwan, G.; Saito, N., Effect of Oxygen Partial Pressure on Crystal Structure, Oxygen Vacancy, and Surface Morphology of Epitaxial SrTiO3 Thin Films Grown by Ion Beam Sputter Deposition. *Oxygen* **2021,** *1* (1).

Chapter 5

Relating Structure, Property, and Activity of nanostructured $SrTiO_3$ and $SrO-(SrTiO_3)_n$ (n= 1 and 2) for Photocatalytic Hydrogen Evolution

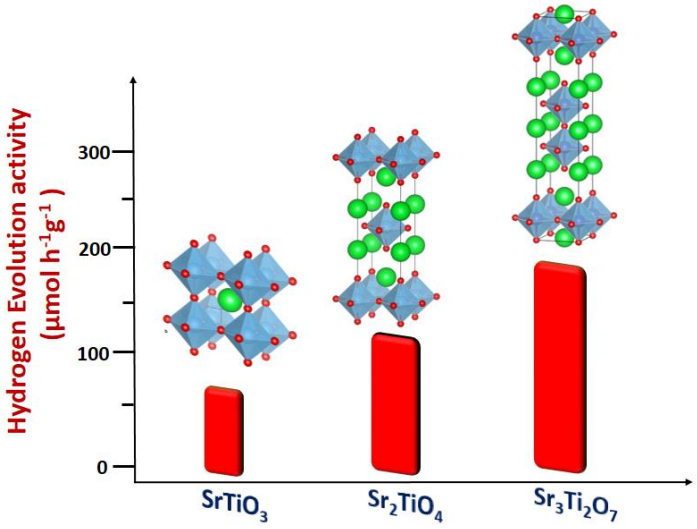

Role of crystal structure on hydrogen evolution efficiency in perovskite oxides

Chapter 5

Relating Structure, Property, and Activity of nanostructured $SrTiO_3$ and $SrO-(SrTiO_3)_n$ (n= 1 and 2) for Photocatalytic Hydrogen Evolution

Abstract

This study focuses on relating the structure with their properties and activity and carries out a comparative study amongst the three members of the Sr-Ti-O system for photocatalytic hydrogen evolution. The three oxides focused on in this study are based on perovskite structure viz. $SrTiO_3$ and $SrO-(SrTiO_3)_n$ (n= 1 and 2). We have successfully synthesized these three oxides through a methodology that combined the polymeric citrate precursor method with the hydrothermal method. Their crystal structure, morphology, and optical properties (absorption, and photoluminescence) were systematically explored. $SrTiO_3$ belonged to a class of cubic perovskite while Sr_2TiO_4 (n=1) and $Sr_3Ti_2O_7$ (n=2) belonged to layered Ruddlesden-Popper based perovskite oxides. We observed cube-shaped morphology for nanostructured $SrTiO_3$ and layered morphology for Ruddlesden-Popper based oxides, Sr_2TiO_4 and $Sr_3Ti_2O_7$. The photocatalytic hydrogen evolution performance of these nanostructured oxides was investigated. Amongst the three nanostructured oxides, the maximum amount of hydrogen was evolved with $Sr_3Ti_2O_7$ as the photocatalyst. These results were supported by photoluminescence, time-resolved photoluminescence, and Photoelectrochemical study.

Keywords: Ruddlesden-Popper; perovskite; Photocatalysis; hydrogen evolution

5.1 Introduction :

Production of hydrogen energy via the utilization of solar energy is a sustainable and effective solution for the world's energy crisis and environmental problems. In this regard, photocatalytic splitting of water into H_2 and O_2 over a semiconducting catalyst has been recognized as an effective strategy to develop a sustainable energy structure[1-2]. The efficiency of photocatalytic reaction can be enhanced by modulating several factors such as crystal structure[3], electronic structure[4] (i.e. position of the conduction band and valence band edge), the presence of vacancies (anion or cation)[5] and controlling the morphology [6-7].

Over the past few decades, several semiconductor oxides such as TiO_2, ZnO, $AgGaO_2$, and $BiVO_4$ have been discovered as efficient catalysts for photocatalytic hydrogen evolution[8-14]. Among all the developed photocatalysts, perovskite structure i.e. ABO_3 has gained much popularity because of its composition which can be easily modulated at A and B sites[15-17] Among the various perovskite semiconductor oxides, $SrTiO_3$ is widely studied as a photocatalyst[18-20] for its outstanding structural stability and compositional flexibility. Ruddlesden Popper-based layered perovskite, having a general formula as $AO\text{-}(ABO_3)_n$, (which can be also written as $(A_{n+1}BO_{3n+1})$ or $A'_2[A_{n-1}B_nO_{3n+1}]$) have attracted much attention in the field of photocatalytic water splitting due to their physical properties which can be modified by intercalation, and ion-exchange. [21-22] These structures consist of a large number of active sites such as the B site and the AO layer site to facilitate the reaction. Several metal ions can be doped[23, 24] at the A and B sites in these structures which modulates the bandgap of the oxide towards the visible region thereby enhancing their photocatalytic activity.

Figure 5.1 shows the crystal structure of $SrTiO_3$ and $SrO\text{-}(SrTiO_3)_n$ (n= 1 and 2). $SrTiO_3$ belongs to the class of perovskite having a cubic structure that is composed of cornered shared TiO_6 octahedra with Sr, present in the holes formed from the cuboctahedron symmetry. When n =1 and 2, the structure belongs to a class of oxide known as Ruddlesden-Popper phases. The two-lower symmetry 2D-Ruddlesden-Popper oxides, Sr_2TiO_4 (n=1) and $Sr_3Ti_2O_7$ (n=2) have body-centered tetragonal symmetry. These structures are composed of stacking of *n*$SrTiO_3$ perovskite layers separated by SrO rock-salt type layer as shown in figure 5.1.

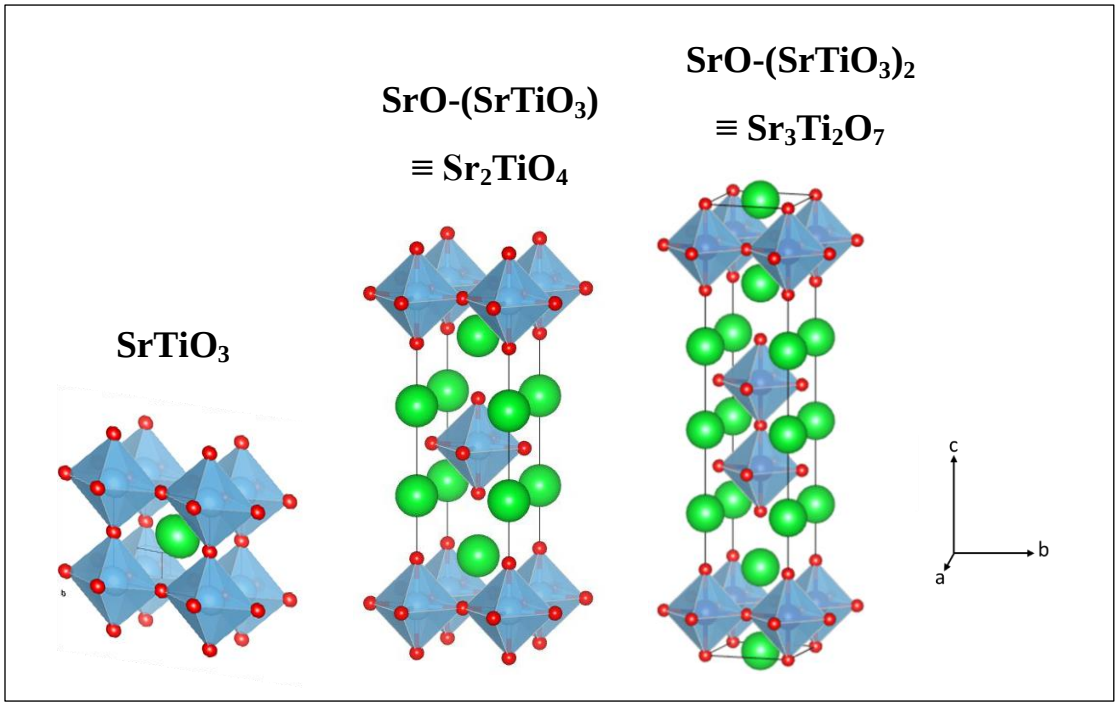

Figure 5.1: Schematic showcasing crystal structure of $SrTiO_3$, $SrO-(SrTiO_3)_n$ for n = 1 (Sr_2TiO_4), and n = 2 ($Sr_3Ti_2O_7$).

Here, we have discussed a comparative study on the performance of nanostructured $SrTiO_3$ and $SrO-(SrTiO_3)_n$ viz. Sr_2TiO_4 (n=1) and $Sr_3Ti_2O_7$ (n= 2) towards photocatalytic hydrogen evolution reaction. Out of these three perovskite oxides, Sr_2TiO_4 and $Sr_3Ti_2O_7$ belong to *I4/mmm*, tetragonal symmetry whereas $SrTiO_3$ belongs to, the $Pm\bar{3}m$ space group. The photocatalytic property of these nanostructured oxides is investigated through hydrogen evolution reaction under UV–visible light irradiation. Photoluminescence, Time-resolved photoluminescence, and Photoelectrochemical studies have been carried out to see the role of the perovskite structure in influencing photocatalytic activity. To the best of our knowledge, there are no reports on a comparative study of the three kinds of structures on photocatalytic hydrogen evolution performance. However, there is one report[25] where the ratio of Sr/Ti in $SrTiO_3$ was varied and their photocatalytic HER was studied for different ratios from 1.00 to 1.25. Photocatalytic hydrogen evolution activity of these three perovskite oxides has been studied separately[23, 26-27]. In this study, we have tried to highlight that the choice of structure (crystallographic), amongst the cubic and layered perovskite (showcased here with the Sr-Ti-O system), could be an efficient

way for the development of a catalyst for hydrogen evolution reaction with improved performance.

5.2 Experimental:

5.2.1 Materials and Methods:

Strontium nitrate [($Sr(NO_3)_2$), 99%], ethylene glycol (EG) (99%), methanol (ACS grade), citric acid anhydrous (98%), and sodium sulfate (99%) were purchased from Merck. Sodium sulfide flakes were purchased from CDH fine chemicals. Titanium tetraisopropoxide (TTIP) (97%) and sodium sulfite (98%) were purchased from Sigma-Aldrich.

For the synthesis of $SrTiO_3$, TTIP (12 mmol) was added to a mixture of ethylene glycol (25 mL) and methanol (10 mL). To this aqueous solution containing citric acid in 5 mL water and solid $Sr(NO_3)_2$, (12 mmol) were added. The amount of citric acid taken was equivalent to that of TTIP. The resultant mixture was heated at 130°C for 4 hours to form a single-phase transparent solution. Afterward, the pH of this was adjusted to 13 by adding 5 M NaOH (5 mL). The resulting solution was transferred into a Teflon vessel followed by hydrothermal treatment at 200ºC for 48 h. After the Teflon vessel was cooled down to room temperature, the obtained gel was vacuum dried at 200℃ for 16 h. The products were washed several times with glacial acetic acid (to remove carbonate present as an impurity in the sample), deionized (DI) water, and ethanol, and then dried overnight at 70°C. $SrTiO_3$ was finally synthesized by calcining the dried powder at 750°C for 5 h.

For the synthesis of Sr_2TiO_4 and $Sr_3Ti_2O_7$, the exact procedure was followed as for $SrTiO_3$ except for the ratio of Sr and Ti precursor and heating temperature. For Sr_2TiO_4, the ratio of Sr and Ti precursor was kept to be 2:1(12 mmol of $Sr(NO_3)_2$ and 6 mmol of TTIP) and calcined first at 650 ºC and then at 1000ºC for 12 h whereas, for $Sr_3Ti_2O_7$, the ratio was kept to be 3:2 (9 mmol of $Sr(NO_3)_2$ and 6 mmol of TTIP) and calcined first at 650 ºC and then at 950 ºC for 6 h.

5.2.2 Characterization:

Phase identification and crystal structure of the samples were analyzed using powder X-ray diffraction (PXRD, Bruker D8 Advance Eco) with Cu Kα as an X-ray source (λ = 0.15406 nm). The step size of 0.02 with a time of 0.3 s/step was used for data collection. Crystallite size

(Scherrer) was calculated using TOPAS v5 software by using the peak positioned at a two-theta value of 32.5^o, 31.4^o, and 46.6^o for $SrTiO_3$, Sr_2TiO_4, and $Sr_3Ti_2O_7$ respectively. To obtain information about the morphology of the sample, transmission electron microscopy studies were carried out on a JEOL, JEM-2100 Transmission Electron Microscope (TEM), used at an operating voltage of 200 kV. The samples for the TEM study were prepared by dispersing the powder samples in ethanol and drop-casting them on a carbon-coated copper grid. Raman study was carried out on WI Tec's Raman microscope, α 300 R. The studies were carried out on powder samples taken on a glass slide. Diffuse Reflectance Spectra were collected on a UV–visible spectrophotometer, Shimadzu UV-2600, in a wavelength range of 200-800 nm with barium sulfate as the reference material. Kubelka-Munk's (K-M) equation was used to calculate the bandgap of the materials from the reflectance spectra. XPS (X-Ray Photoelectron Spectroscopy) studies were carried out on Thermo Scientific's K-alpha X-ray Photoelectron Spectrometer (XPS) System with the following settings: 0.05eV Step, 1s time per step, and 5 cycles, Source Al k-alpha-1486eV. The surface area of the samples was determined using Nitrogen adsorption-desorption isotherms with Quanta Chrome Model Q2. Photoluminescence and Time-resolved photoluminescence spectra were obtained from Horiba's TCSPC (Time Correlation Single Photon Counting) at an excitation wavelength of 380 nm and 340 nm respectively. Time-resolved photoluminescence decay curves were fitted by using a double logarithmic decay equation which is given below:

$$y = A_1 e^{(-x/\tau_1)} + A_2 e^{(-x/\tau_2)} + y_0 \quad (5.1)$$

The average lifetime was obtained from the equation given below:

$$\tau = \frac{\sum_{i=1}^{n} A_i \tau_i^2}{\sum_{i=1}^{n} A_i \tau_i} \quad (5.2)$$

Photocatalytic Hydrogen Evolution Reaction (HER) and Photoelectrochemical studies

A top irradiation quartz reactor of capacity 140 mL was used for the photocatalytic reaction for the hydrogen evolution. In a typical experiment, 40 mg of the catalyst was dispersed in a 40 mL aqueous solution containing 0.35M Na_2SO_3 and 0.25M Na_2S through ultrasonication. The study was carried out in absence of any metal co-catalyst to see the direct influence of the nature

of the crystal structure on the photocatalytic performance of Sr-Ti-O based oxides. The solution was purged with N_2 gas for 30 minutes to eliminate the dissolved oxygen. A 450W Xe lamp was used as a source of light. The photon flux of the Xe lamp was obtained from Ray virtual radiation actinometer, Newport, Model 91150V. The gas components from the reactor were analyzed using gas chromatography (GC, Perkin Elmer Clarus 680) with a thermal conductivity detector at an interval of 1 h. The apparent quantum efficiency was calculated using the equation given below:

$$AQY = \frac{2nN_A hc}{PS\lambda t} \times 100 \qquad (5.3)$$

where n is the amount of hydrogen evolved; N_A is Avogadro's constant (6.022×10^{23} mol^{-1}); h is Planck's constant (6.63×10^{-34} J s); c is the speed of the light (3×10^{10} cm/s); P is the power density of the incident light (181×10^{-3} W/cm^2); S is the irradiation area (12.6 cm^2); λ is the representative wavelength of the incident light (using the radiation spectrum of the lamp, 390 nm (390×10^{-7} cm)); and t is the time duration of the incident light (18000 s).

Photoelectrochemical studies were performed on a PGSTAT-30 (Autolab) electrochemical workstation using a standard three-electrode system consisting of Ag/AgCl (3M KCl) as the reference electrode, platinum wire as the counter electrode, and Sr-Ti-O samples deposited on a glass substrate coated with fluorine-doped tin oxide (FTO) as the working electrode. For the synthesis of the working electrode, the catalyst was drop cast on a glass substrate coated with FTO having a surface area of 1 cm × 1 cm. For the preparation of the catalyst ink, 10 mg of the catalyst was dispersed in 200μL of isopropyl alcohol containing 10μL of Nafion resin solution through the ultra-sonication method. Here, 0.1 M Na_2SO_4 (pH= 7) was taken as an electrolyte, saturated with Argon for 30 minutes to remove dissolved oxygen. A 350 W Xe lamp was used as the source of irradiation. LSV (linear sweep voltammetry) curves were obtained in the range from 0 to -1 V vs Ag/AgCl at a scan rate of 10 mV/s under the light. Electrochemical impedance spectroscopy (EIS) was carried out at -0.35 V vs Ag/AgCl in the frequency range from 0.1 Hz to 100 kHz under the light.

5.3 Results & Discussion:

The Powder X-ray diffraction (PXRD) pattern of the as-prepared nanostructured oxides is shown in Figure 5.2. No impurity peaks were observed in the PXRD pattern indicating the formation of

a single phase. The pattern for the perovskite $SrTiO_3$ was indexed based on cubic symmetry (PDF 00-035-0734, space group, $Pm\bar{3}m$.). The other two Ruddlesden-Popper layered structures, Sr_2TiO_4 (n = 1) and $Sr_3Ti_2O_7$ (n = 2) were indexed based on tetragonal symmetry having space group, I4/mmm (JCPDF 00-039-1471 and JCPDF 01-078-2479 respectively). The crystallite size for all the three oxides viz. $SrTiO_3$, Sr_2TiO_4, and $Sr_3Ti_2O_7$ were found to be 63 nm, 39 nm, and 42 nm respectively.

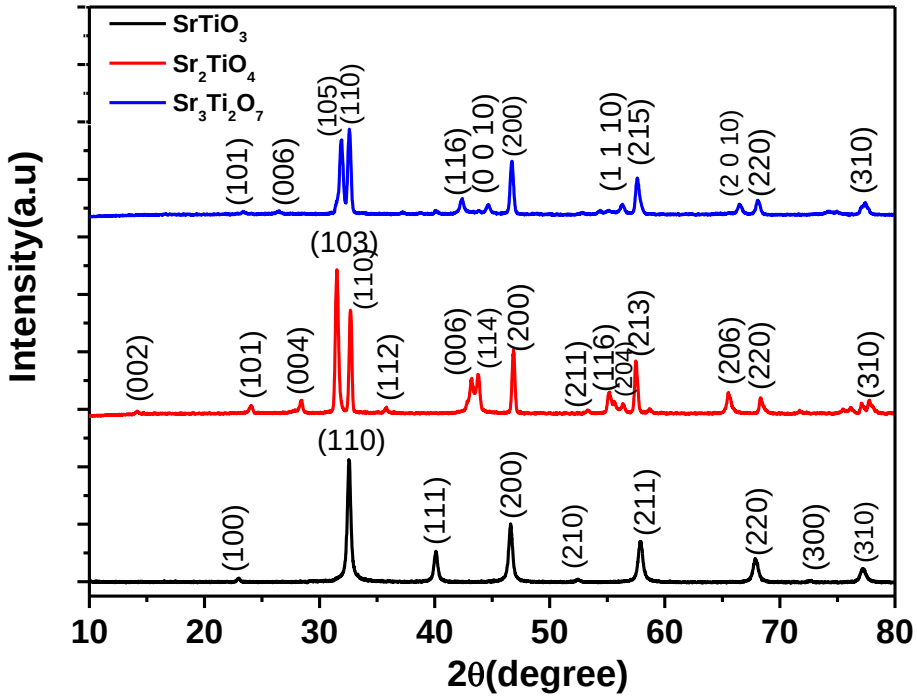

Figure 5.2: PXRD pattern for $SrTiO_3$, Sr_2TiO_4, and $Sr_3Ti_2O_7$

Raman spectra of the three nanostructured oxides i.e. $SrTiO_3$, Sr_2TiO_4, and $Sr_3Ti_2O_7$ are shown in figure 5.3. The Raman spectra obtained for the perovskite $SrTiO_3$ matched well with the previous reports[28-29]. The spectra consist of a low-frequency band present at 77 cm^{-1} which were assigned to doubly degenerate modes. E_g and second order Raman bands were also observed between 200-400 cm^{-1} and 600-800 cm^{-1}. No first-order bands were observed in the Raman Spectra, as expected for the cubic structure. It has been previously reported[30] that there are four Raman active modes, A_{1g}, and E_g, observed for layered Ruddlesden–Popper oxide with n=1, Sr_2TiO_4. The Raman bands present at 121, 203, 182, and 571cm^{-1} were assigned to E_g, A_{1g}, E_u, and A_{1g} modes respectively (figure 5.3). The broader band observed between 400-450 cm^{-1} and around

700 cm^{-1} indicates the presence of a second-order band or defect-induced excitations which may originate at the oxygen sublattice. According to the report by Nilsen et al.[28] second-order Raman scattering are due to the creation and destruction of two phonons which can originate from anywhere in the Brillouin zone. The authors observed a second-order band or overtone for $SrTiO_3$ at 369cm^{-1} which was attributed to the combination of various bands including the TO_4-TA, TO_4 -TO_l, and $2TO_2$ band whereas the band at 684 cm^{-1} was assigned to the $2TO_3$ overtone. Raman Spectra of $Sr_3Ti_2O_7$ (Figure 5.3) show bands at 178, 198, 274, 500, and 633 cm^{-1} which can be assigned to A_{1g}, E_g, E_g, A_{1g}, and A_{1g} modes respectively which was consistent with the previous report[31]. A defect-induced excitation was also observed at 92 cm^{-1}. The band corresponding to the A_{1g} mode was observed to be more intense in both Sr_2TiO_4 and $Sr_3Ti_2O_7$, which could be due to symmetric stretching of oxygen lattice. [32]

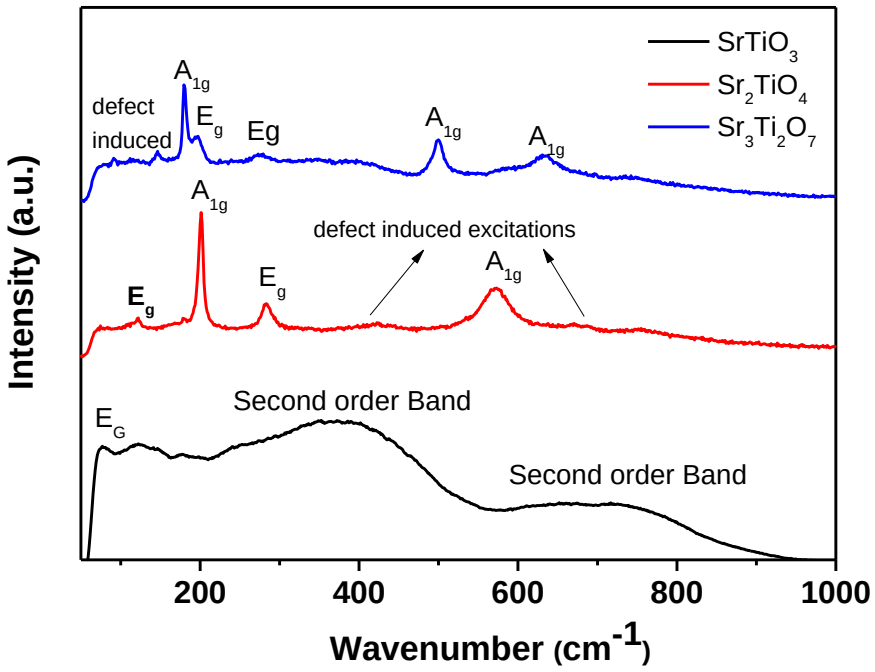

Figure 5.3: Raman Spectra of $SrTiO_3$, Sr_2TiO_4, and $Sr_3Ti_2O_7$

The high resolution XPS spectra of strontium (Sr(3d), figure 5.4 a-c), oxygen (O(1s), figure 5.5a-c) and titanium, (Ti(2p), figure 5.6 a-c), was obtained for $SrTiO_3$ Sr_2TiO_4 and $Sr_3Ti_2O_7$. Peaks at binding energy 133.7 eV (135.5 eV), 133.9 eV (135.5 eV) and 133.6 eV (135.4 eV) were observed for Sr $3d_{5/2}$ ($3d_{3/2}$) spectra of $SrTiO_3$ (figure 5.4a), Sr_2TiO_4 (figure 5.4b) and $Sr_3Ti_2O_7$ (figure 5.4c) respectively.

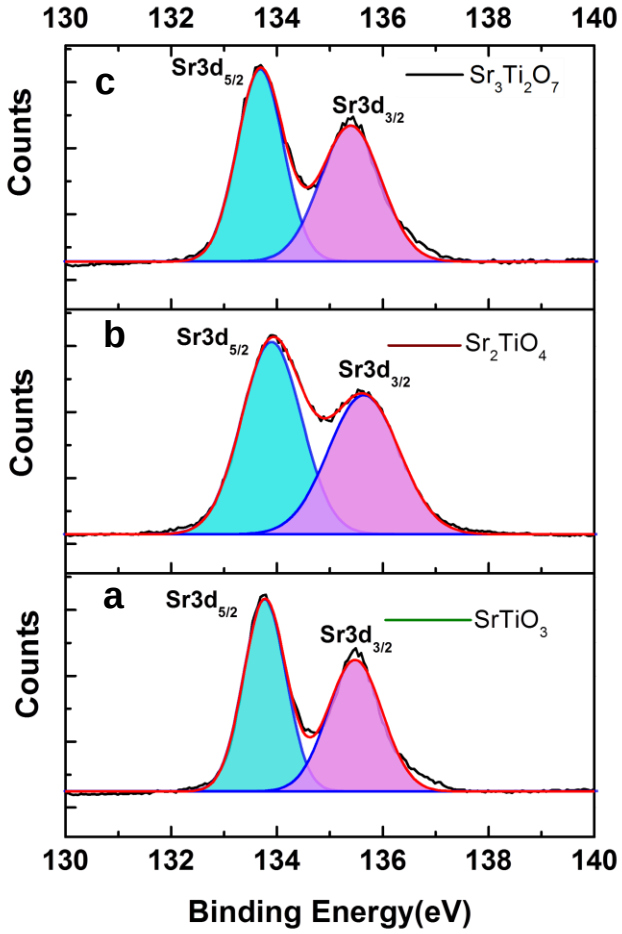

Figure 5.4: High Resolution Sr (3d) XPS spectra of (a) $SrTiO_3$, (b) Sr_2TiO_4, and (c) $Sr_3Ti_2O_7$.

Figure 5.5 a-c shows high–resolution O1s spectra for $SrTiO_3$, Sr_2TiO_4, and $Sr_3Ti_2O_7$. The peaks were fitted with two Gaussian peaks having binding energy at 529.7 and 531.2 eV for $SrTiO_3$, 529.3 and 531.4 eV for Sr_2TiO_4, and 529.8 and 531.77 eV for $Sr_3Ti_2O_7$. The peaks at lower energy can be attributed to the metal-oxygen bond i.e. the presence of O^{2-} ions in the crystal structure whereas the peak at higher energy can be related to the oxygen vacancies.

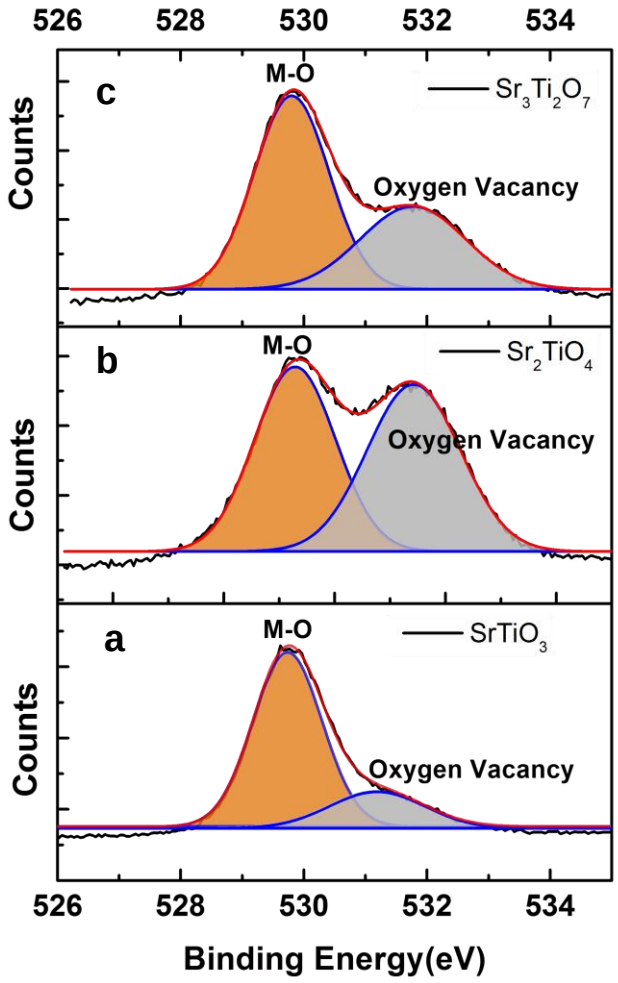

Figure 5.5: High Resolution O (1s) XPS spectra of (a) $SrTiO_3$, (b) Sr_2TiO_4, and (c) $Sr_3Ti_2O_7$.

Figure 5.6 a-c shows high-resolution spectra of Ti(2p) for $SrTiO_3$, Sr_2TiO_4, and $Sr_3Ti_2O_7$ respectively. Presence of Ti^{3+} was observed along with Ti^{4+} ion after fitting of the peaks. Peaks centered at 458.3 eV (464.2 eV), 458.1 eV (453.8 eV) and 458.5 eV (464.1 eV) were observed for Ti^{4+} $2p_{3/2}$ ($2p_{1/2}$) spectra of $SrTiO_3$ Sr_2TiO_4 and $Sr_3Ti_2O_7$ respectively. Ti^{3+} $2p_{3/2}$ ($2p_{1/2}$) spectra of $SrTiO_3$ Sr_2TiO_4 and $Sr_3Ti_2O_7$ was observed at 456.4 eV (462.8 eV), 456.8 eV (462.1 eV) and 456.6 eV (461.9 eV) respectively. Thus the presence of peaks corresponding to Ti^{3+} also confirms the presence of oxygen vacancy in the lattice. Based on the area under the peak, the order for the ratio of oxygen vacancies: M-O and Ti^{3+}: Ti^{4+} was found to be Sr_2TiO_4 > $Sr_3Ti_2O_7$ > $SrTiO_3$.

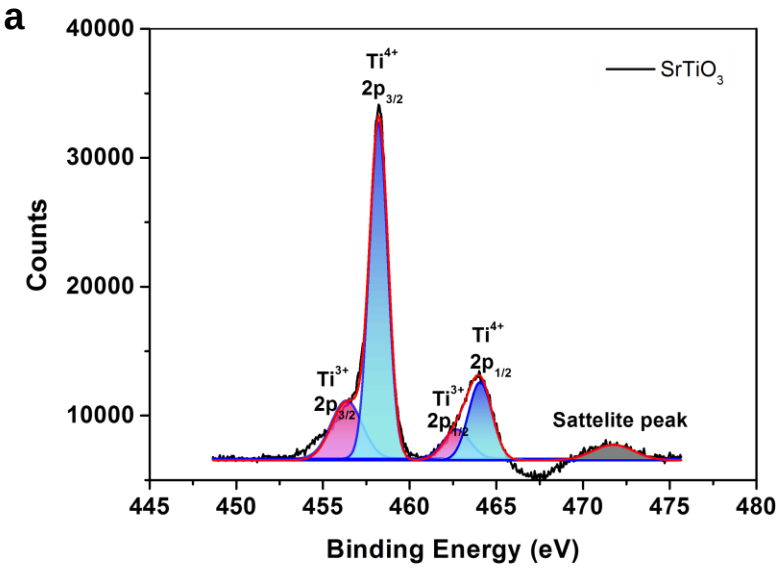
a
40000
30000
20000
10000
Counts
445
450
455
460
465
470
475
480
Binding Energy (eV)
SrTiO3
Ti4+ 2p3/2
Ti3+ 2p3/2
Ti3+ 2p1/2
Ti4+ 2p1/2
Sattelite peak

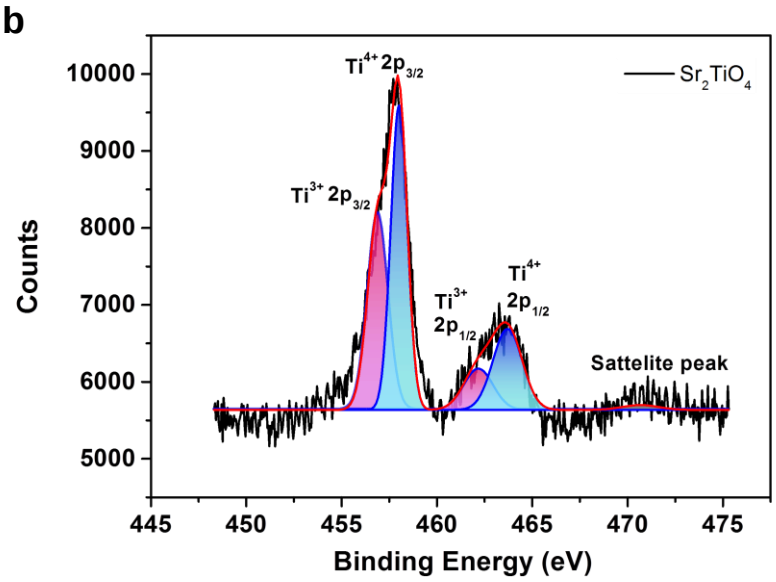
b
10000
9000
8000
7000
6000
5000
Counts
445
450
455
460
465
470
475
Binding Energy (eV)
Sr2TiO4
Ti4+ 2p3/2
Ti3+ 2p3/2
Ti3+ 2p1/2
Ti4+ 2p1/2
Sattelite peak

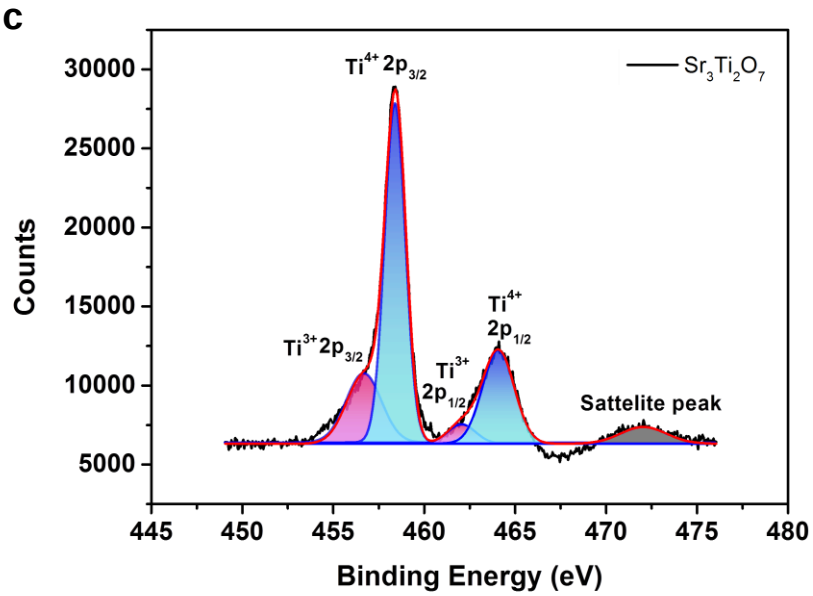

Figure 5.6: High Resolution Ti (2p) XPS spectra of (a) $SrTiO_3$, (b) Sr_2TiO_4, and (c) $Sr_3Ti_2O_7$.

TEM studies for $SrTiO_3$ showed nanocubes having a size of 80-100 nm (figure 5.7a). HRTEM image (figure 5.7 b) shows lattice fringes with a spacing of 0.281 nm, corresponding to the (110) plane. A rectangular sheet-like morphology was observed for both Ruddlesden-Popper based oxides i.e. Sr_2TiO_4 (figure 5.7c) and $Sr_3Ti_2O_7$ (Figure 5.7e). The size along one dimension of these sheets was observed to be ~250 nm and ~350 nm for Sr_2TiO_4 and $Sr_3Ti_2O_7$ respectively. The lattice fringes corresponding to a spacing of 0.276 nm for Sr_2TiO_4 (figure 5.7 d) and 0.273 nm for $Sr_3Ti_2O_7$ (figure 5.7f) were observed which corresponded to the (110) plane. BET surface area of all the samples viz. $SrTiO_3$, Sr_2TiO_4, and $Sr_3Ti_2O_7$ were observed to be 15 m^2/g, 6.2 m^2/g, and 14 m^2/g respectively.

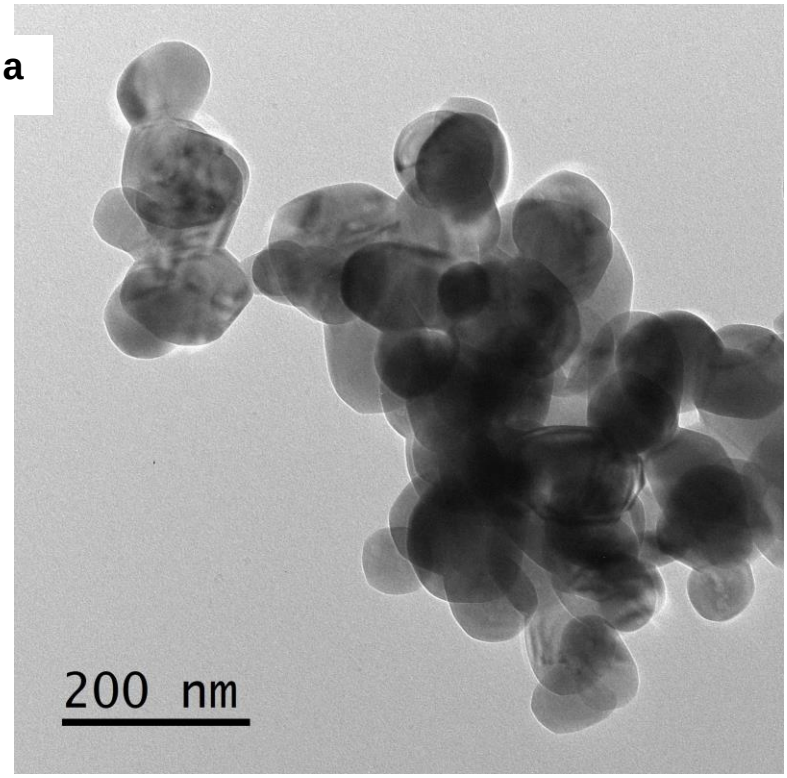
a
200 nm

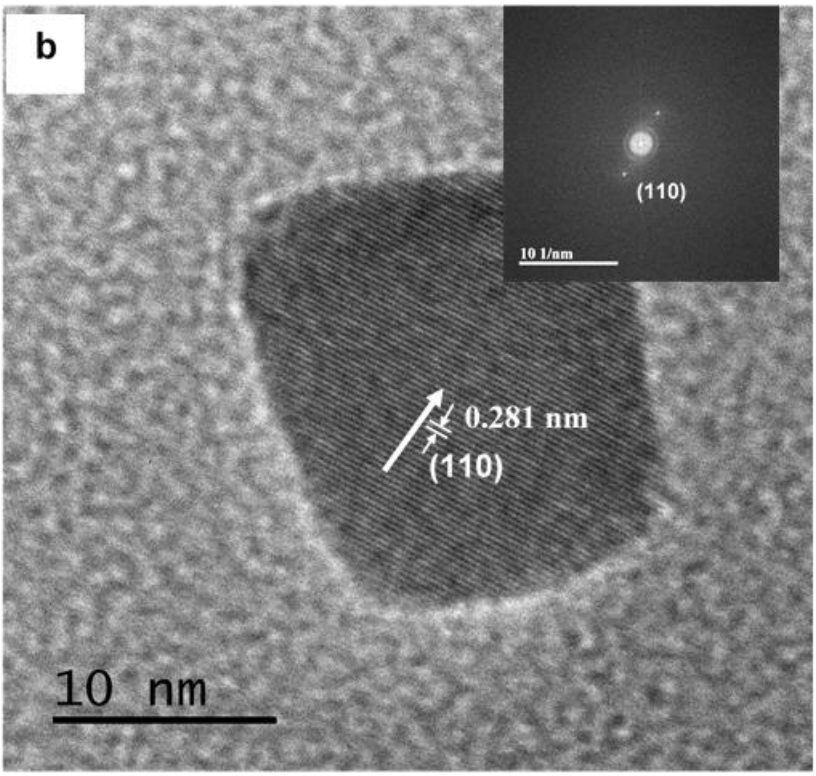
b
(110)
10 1/nm
0.281 nm
(110)
10 nm

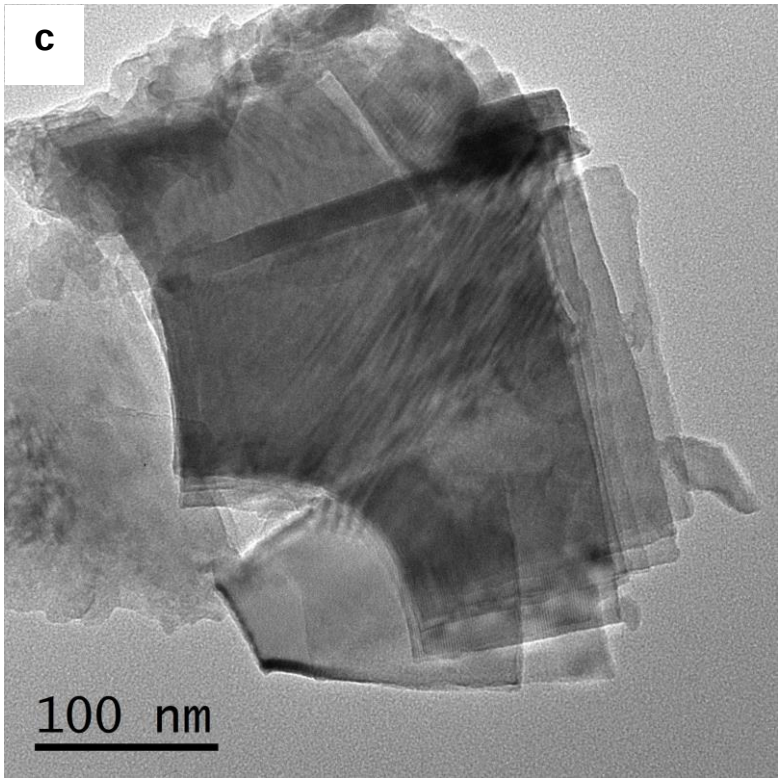
c
100 nm

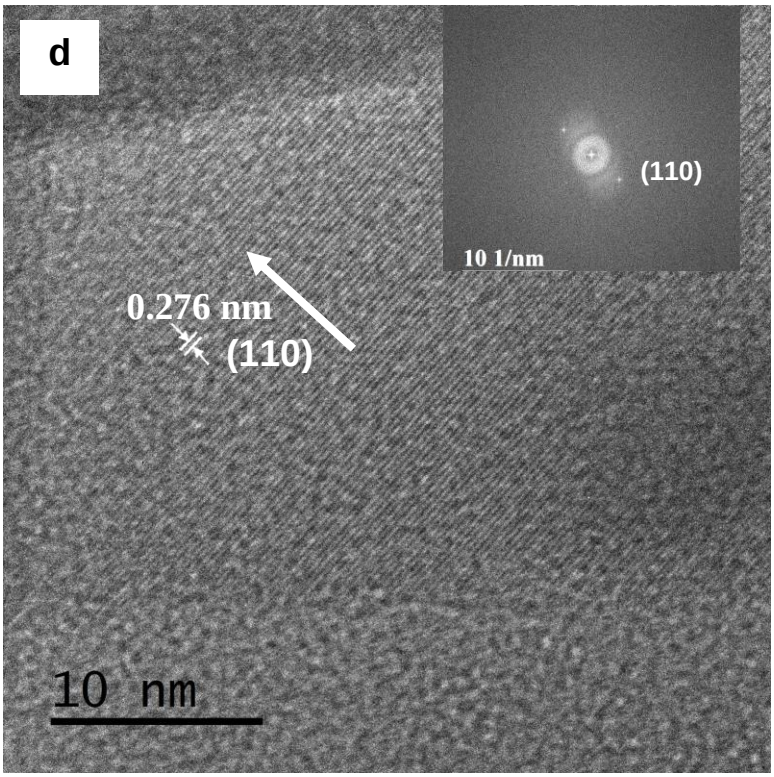
d
(110)
10 1/nm
0.276 nm
(110)
10 nm

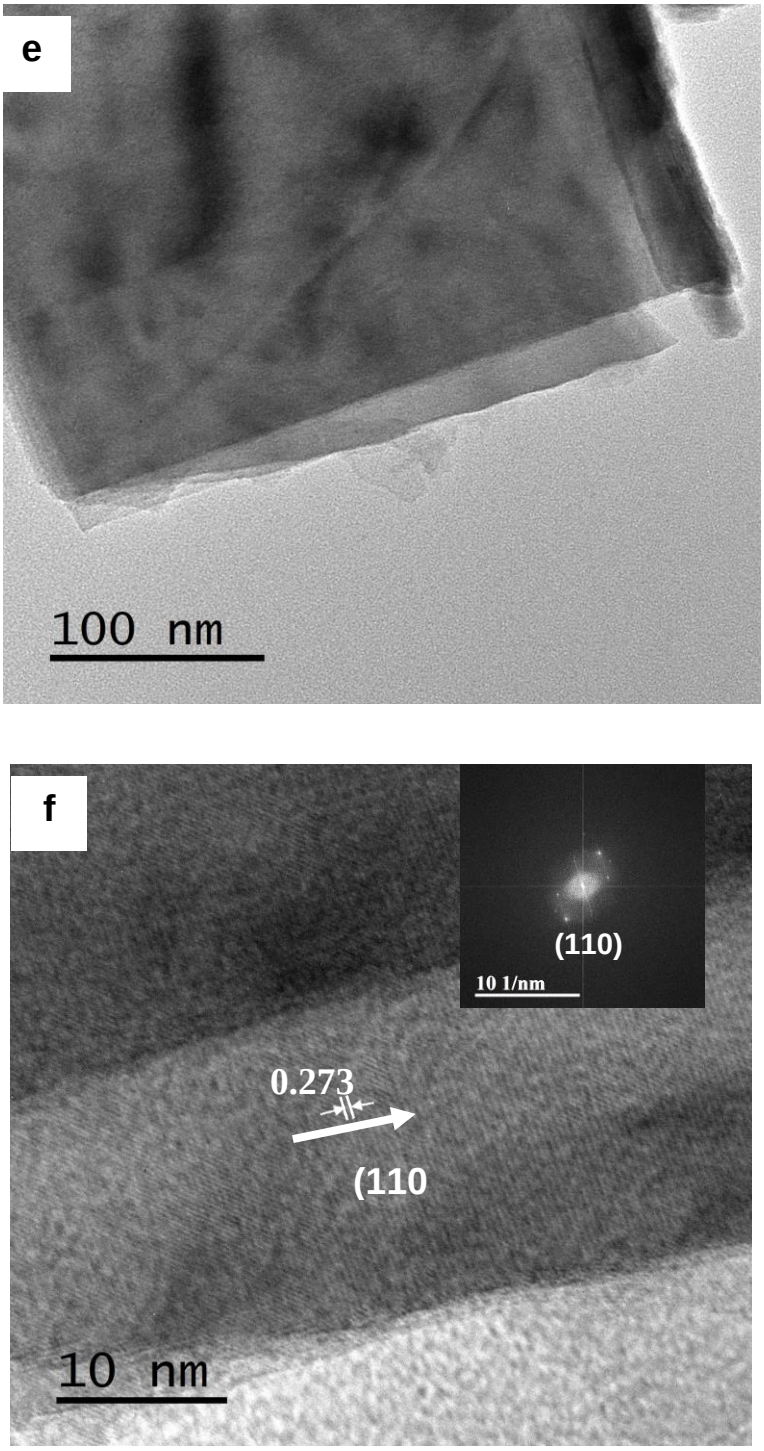

Figure 5.7: TEM images of (a) $SrTiO_3$, (c) Sr_2TiO_4, and (e) $Sr_3Ti_2O_7$. HRTEM images of (b) $SrTiO_3$, (d) Sr_2TiO_4, and (f) $Sr_3Ti_2O_7$. Inset shows corresponding reduced FFT of HRTEM image.

The bandgap of the oxides was calculated using the Tauc equation (equation 5.4).

$$(\alpha h\upsilon)^{\frac{1}{n}} = C(h\upsilon - E_g) \qquad (5.4)$$

where E_g is the bandgap of the semiconductor materials; h is Planck's constant, υ is the frequency of the light, α is the absorption coefficient; n represents the type of transition (n = ½ stands for direct transition whereas n = 2 is used for indirect transition). It is known that the oxides viz. $SrTiO_3$, Sr_2TiO_4, and $Sr_3Ti_2O_7$ possess indirect bandgap[33]. The indirect bandgap of the nanostructured $SrTiO_3$ Sr_2TiO_4 and $Sr_3Ti_2O_7$ was found to be 3.26 eV, 3.16 eV, and 3.11 eV respectively (figure 5.8). A small change in the bandgap with a change in the value of 'n' in $SrO-(SrTiO_3)_n$ was observed, which was consistent with the report by Chen et.al[34] wherein the authors also observed, through theoretical calculations, that the bandgap is affected by a small value with a slight change in the value of 'n' (n concerning $AO(ABO_3)_n$) in Mn-based Ruddlesden Popper based perovskite.

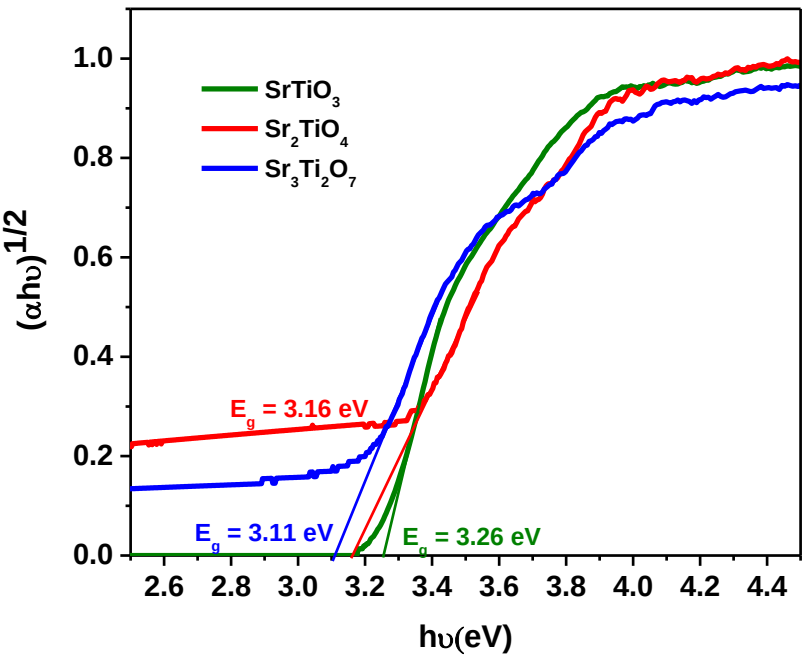

Figure 5.8: Tauc plot for $SrTiO_3$, Sr_2TiO_4, and $Sr_3Ti_2O_7$.

To calculate the band energy positions, XPS Valence Band spectra were recorded for $SrTiO_3$, Sr_2TiO_4, and $Sr_3Ti_2O_7$ (figure 5.9 a-c). The position of the valence band maxima was observed to be 2.01, 1.47, and 1.16 eV for $SrTiO_3$, Sr_2TiO_4, and $Sr_3Ti_2O_7$ respectively.

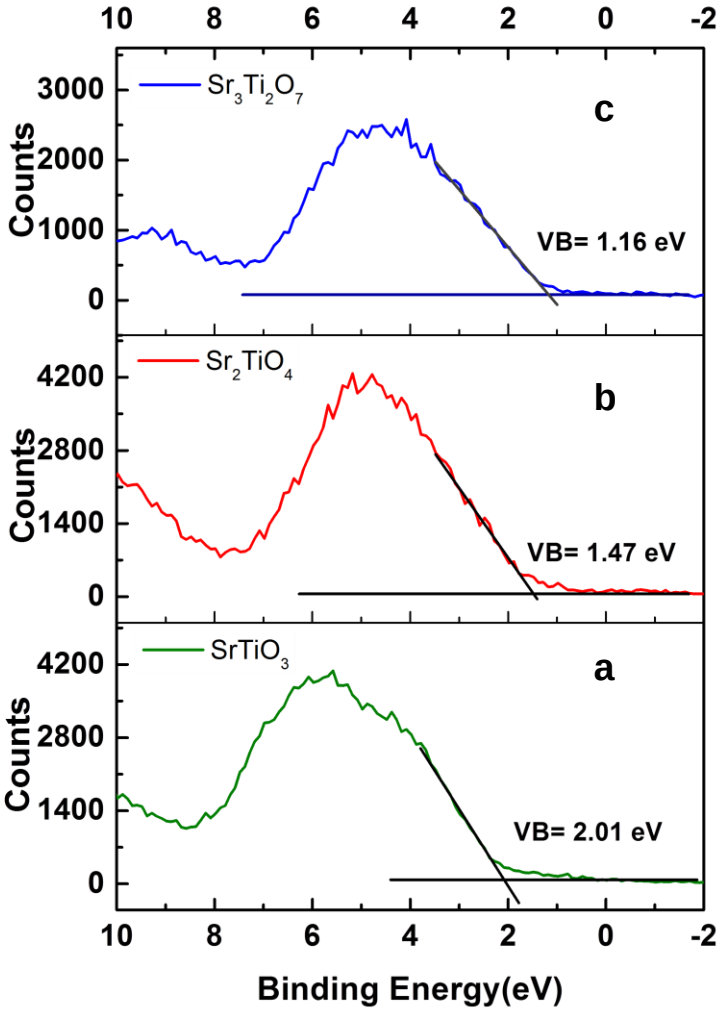

Figure 5.9: XPS Valence Band Spectra of (a) $SrTiO_3$, (b) Sr_2TiO_4 and (c) $Sr_3Ti_2O_7$.

From the value of the bandgap obtained from the Tauc's plot and valence band maxima obtained from valence band spectra using XPS, the conduction band minima for $SrTiO_3$, Sr_2TiO_4, and $Sr_3Ti_2O_7$ were found to be -1.25, -1.69, and -1.95 eV (figure 5.10). The conduction band positions for Sr_2TiO_4 and $Sr_3Ti_2O_7$ were observed to be more negative than $SrTiO_3$ indicating

that the Ruddlesden-Popper phases are likely to exhibit superior catalytic activity towards hydrogen evolution than $SrTiO_3$.[35]

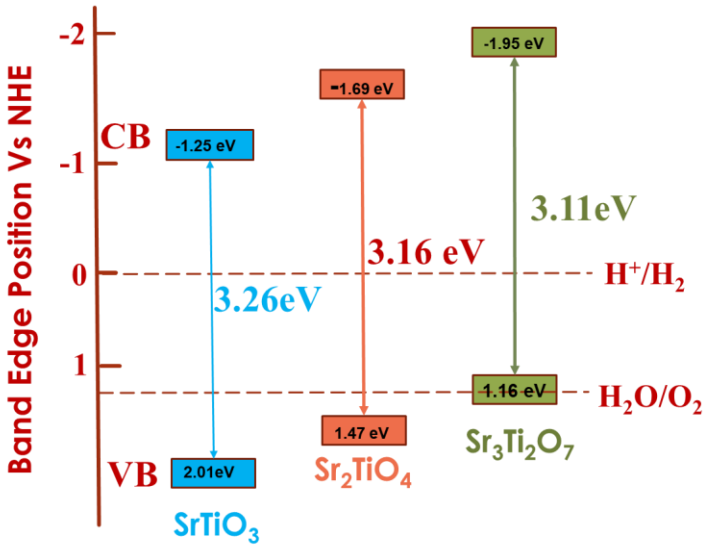

Figure 5.10: Schematic showcasing Energy diagram for $SrTiO_3$, Sr_2TiO_4, and $Sr_3Ti_2O_7$.

Photocatalytic H_2 Evolution:

The photocatalytic hydrogen evolution of nanostructured $SrTiO_3$ and $SrO(SrTiO_3)_n$ (n=1and 2) was studied by observing the amount of hydrogen evolved from an aqueous solution containing 0.25 M Na_2S and 0.35M Na_2SO_3 (used as hole-scavenger). The study was carried out in absence of any metal co-catalyst to see the direct influence of the nature of the crystal structure on the photocatalytic performance of Sr-Ti-O based perovskite and Ruddlesden-Popper based oxides. At first, the experiments were carried out in dark conditions. No H_2 gas was observed in the absence of light. Temporal hydrogen evolution under light is shown in Figures 5.11 a and 5.11 b. It was observed that the amount of H_2 evolved follows the order $Sr_3Ti_2O_7$> Sr_2TiO_4> $SrTiO_3$. Apparent quantum yield was calculated using equation 5.3. The quantum yield obtained has been tabulated in Table 5.1. The recyclability test was performed on $Sr_3Ti_2O_7$ (exhibiting the evolution of the highest amount of hydrogen amongst the three oxides) to check its reusability. The recyclability test was examined for 12 h and each experimental cycle was carried out for 4 h (Figure 5.11c). The oxide was centrifuged and washed with water between each cycle. A slight decrease in the rate of H_2 evolution was observed for three cycles.

a

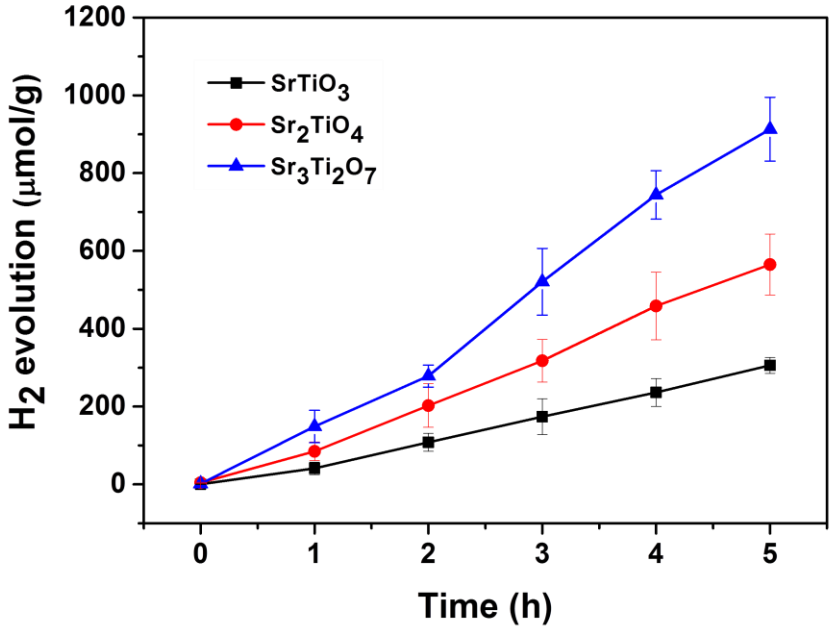
1200
1000
800
600
400
200
0
H2 evolution (μmol/g)
SrTiO3
Sr2TiO4
Sr3Ti2O7
0
1
2
3
4
5
Time (h)

b

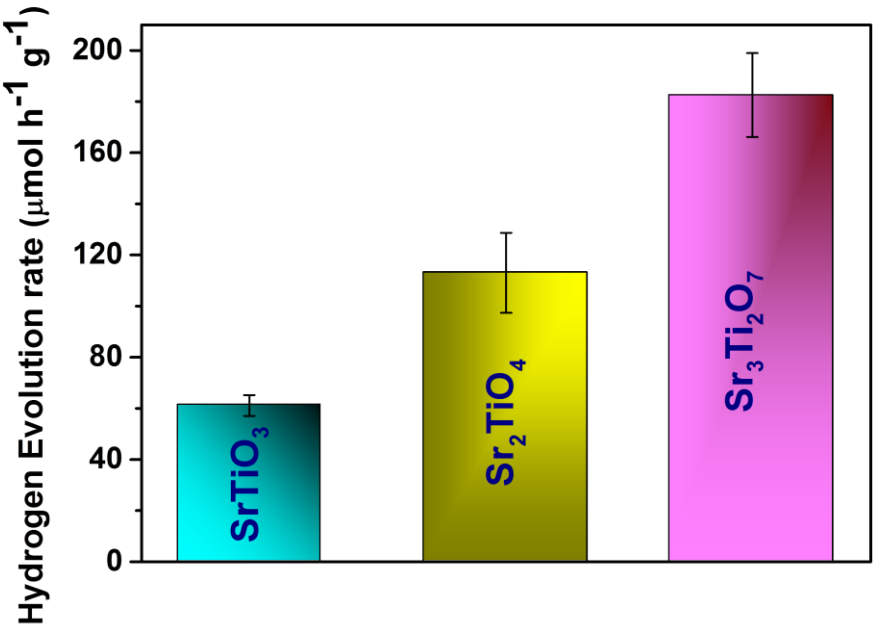
200
160
120
80
40
0
Hydrogen Evolution rate (μmol h-1 g-1)
SrTiO3
Sr2TiO4
Sr3Ti2O7

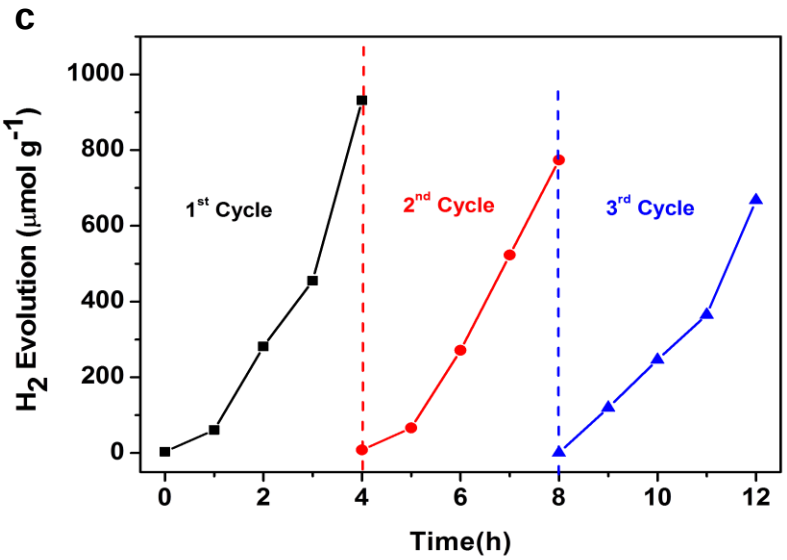

Figure 5.11: (a) Plot showing the amount of Hydrogen evolved per gram of the nanostructured catalyst ($SrTiO_3$, Sr_2TiO_4, and $Sr_3Ti_2O_7$), (b) the rate of Hydrogen Evolution per gram of the catalyst using nanostructures of $SrTiO_3$, Sr_2TiO_4, and $Sr_3Ti_2O_7$ as photocatalysts and (c) Recyclability test of $Sr_3Ti_2O_7$ for three consecutive cycles.

Table 5.1**:** Apparent quantum yield for hydrogen evolution using $SrTiO_3$, Sr_2TiO_4, and $Sr_3Ti_2O_7$ nanostructures as photocatalysts.

Sample	**n (Amount of hydrogen gas evolved after 5 h of the reaction) (mol)**	**Apparent Quantum Yield (AQY) (%)**
$SrTiO_3$	12.2×10^{-6}	0.018
Sr_2TiO_4 ($SrO(SrTiO_3)$)	22.6×10^{-6}	0.030
$Sr_3Ti_2O_7$ ($SrO(SrTiO_3)_2$)	36.5×10^{-6}	0.058

The stability of the catalyst was checked after the recyclability test of 12 h through PXRD (Figure 5.12). It was observed that the crystal structure of the catalyst remained unchanged after reusability. No additional peaks corresponding to any impurity were observed suggesting that the oxide was stable after 12h.

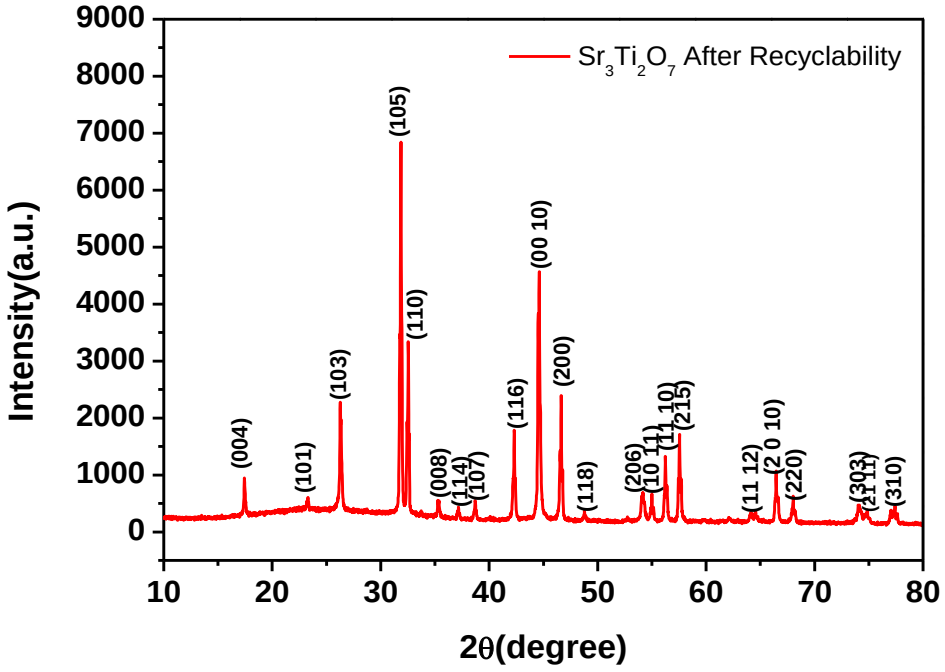

Figure 5.12: PXRD pattern of $Sr_3Ti_2O_7$ after performing recyclability studies

To ascertain the reason for the observed trend for the photocatalytic hydrogen evolution, photoluminescence (PL) and time-resolved photoluminescence studies were carried out for the three oxides. Figure 5.13 shows photoluminescence spectra for all the samples. Here, the samples were excited at a wavelength of 380 nm, and the emission spectra were recorded in the range of 395-700 nm. All the samples showed PL emission in the violet-blue region with a peak centered at 414 nm and 436 nm.

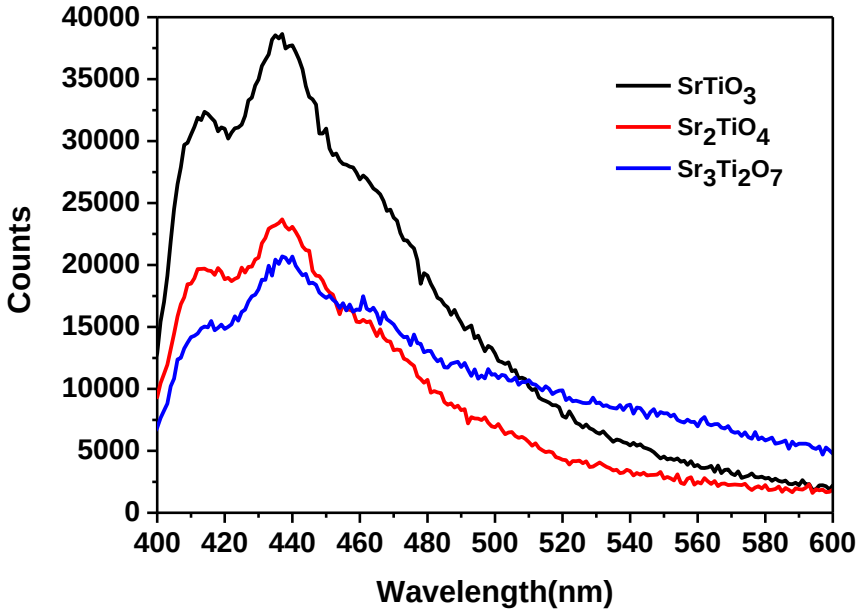

Figure 5.13: Photoluminescence Spectra of $SrTiO_3$, Sr_2TiO_4, and $Sr_3Ti_2O_7$.

It has been reported[36] that the photoluminescence for $SrTiO_3$ based oxides arises mostly due to recombination of the electrons and holes that are trapped in the intermediate states (present within the bandgap). These intermediate states arise as a result of distortion, oxygen vacancies, etc. It has also been reported[36] that the emission in the violet-blue region occurs due to the presence of a surface or shallow defects which may arise due to oxygen vacancies. Oxygen vacancies are also known to affect the catalytic behavior of oxides[5, 37]. The presence of a controlled concentration of defects (oxygen vacancies) is known to increase the photocatalytic efficiency of $SrTiO_3$ towards hydrogen evolution[38]. The oxygen vacancies act as electron donors which either result in an increased charge transport or a shift in the Fermi level towards conduction band[38]. Such a phenomenon is likely to improve the charge separation behavior of the oxide. In our studies, the presence of defects/oxygen vacancies was also confirmed by Raman, and XPS studies**.** In addition to the presence of defects, it was also observed that the PL emission, corresponding to the defect, decreased in the following order $SrTiO_3$ > Sr_2TiO_4 > $Sr_3Ti_2O_7$. With the same excitation energy and no significant changes in the optical bandgap of the oxides, the decrease in the PL emission can be related to a decrease in the recombination of electron and hole pairs giving rise to radiative emission. To further investigate the lifetime of

photo-induced charge carriers, Time-resolved Photoluminescence decay spectra were recorded. The data were fitted using equation 5.1 and the average lifetime (τ_{avg}) was calculated using equation 5.2. Figure 5.14a-c shows the second exponential decay fit of the time-resolved PL of the three oxides. The parameters obtained after fitting are listed in Table 5.2. The average lifetime was found to follow the order $Sr_3Ti_2O_7 > Sr_2TiO_4 > SrTiO_3$, for the Sr-Ti-O system.

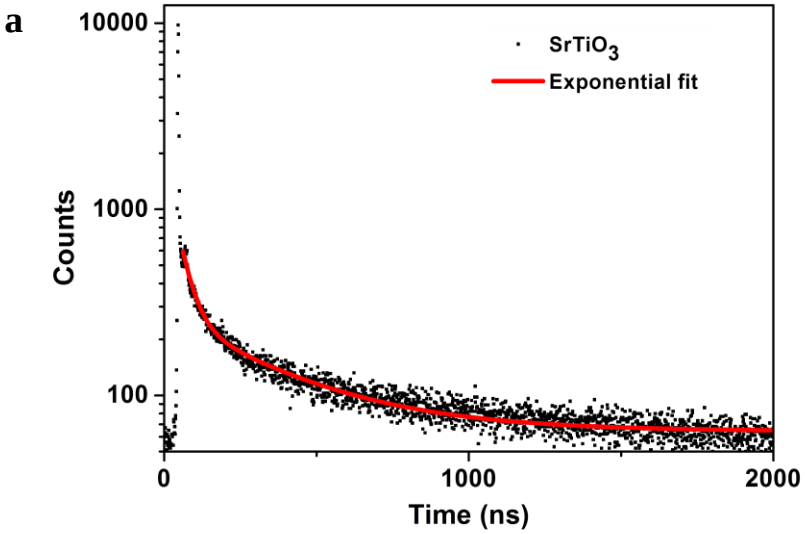

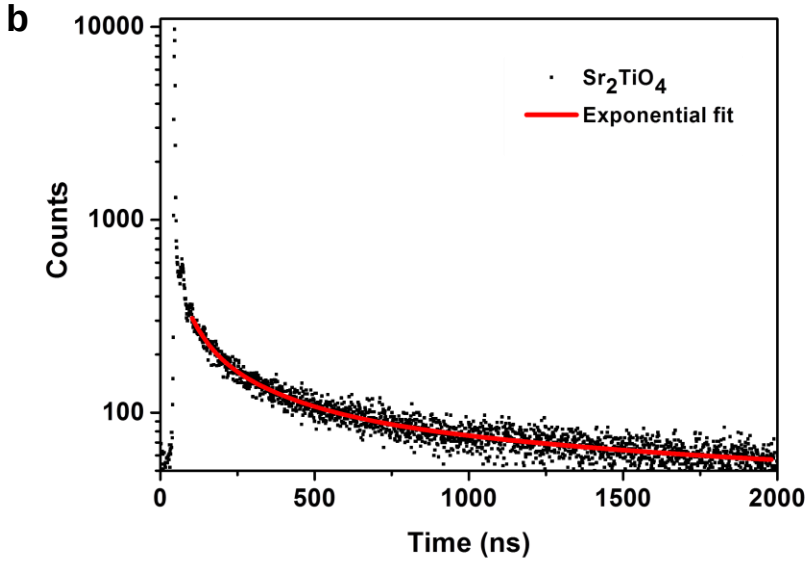

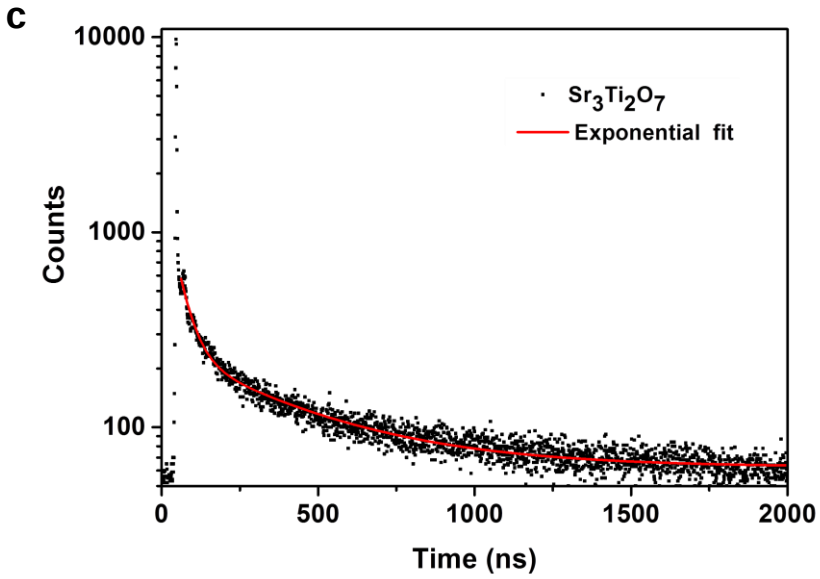

Figure 5.14: Time-Resolved Photoluminescence decay of (a) $SrTiO_3$, (b) Sr_2TiO_4 and (c) $Sr_3Ti_2O_7$.

Table 5.2: Parameters obtained after exponential fitting of the decay curves for $SrTiO_3$, Sr_2TiO_4, and $Sr_3Ti_2O_7$.

Sample	**A_1**	**τ_1(ns)**	**A_2**	**τ2(ns)**	**Average Lifetime τ_{avg} (ns)**
$SrTiO_3$	1800	37.7±1.0	213	351±8.6	202
Sr_2TiO_4	1646	38±1.2	198	367±8.8	215
$Sr_3Ti_2O_7$	1619	40.3±1	194	392±10	230

From the values obtained for τ_{avg}(ns), it can be concluded that the recombination of photo-induced charge carriers is delayed for Ruddlesden-Popper based oxides (Sr_2TiO_4 and $Sr_3Ti_2O_7$) than $SrTiO_3$. The longer lifetime implies that a large number of photo-induced electrons could reach the surface of the catalysts which would be captured by the H^+ ion. Thus, the longer lifetime of the photo-induced charge carriers for $Sr_3Ti_2O_7$ further supports the increased photocatalytic properties of $Sr_3Ti_2O_7$. The presence of interlayers (SrO layer in our study) results in a reduction in the recombination of photogenerated charge carriers by separation of the electrons and holes thereby enhancing the photocatalytic water splitting reaction.[39]

Further to evaluate the charge transfer behavior of the three oxides in presence of light, Photoelectrochemical studies were carried out. The photocurrent density (figure 5.15 a) was found to be maximum for $Sr_3Ti_2O_7$. The onset potential was observed to be ~ -0.40 V vs. Ag/AgCl, which is nearly the same for all three samples. The overpotential for hydrogen evolution reaction (HER) for the three oxides was evaluated from the current-voltage curve at -0.1mA/cm^2 vs Ag/AgCl. (figure 5.15b). The overpotential was found to follow the order $SrTiO_3$ > Sr_2TiO_4 > $Sr_3Ti_2O_7$, for the Sr-Ti-O system. Figure 5.15 c shows Nyquist plots for the three oxides. Based on R_{ct} (charge transfer resistance), R_s (solution resistance), and a constant phase element with impedance, which is related to the angular frequency of the applied potential, ω (using equation 5.5),

$$Z = \frac{Z_0}{(i\omega)^n} \tag{5.5}$$

where Z_0 is a constant, and the value of n ranges as follows: $0 < n < 1$, $i = \sqrt{-1}$, the curve was fit to an equivalent circuit, shown in the inset of figure 5.15 c. The parameters obtained after the fitting are tabulated in Table 5.3.

Table 5.3: Parameters obtained after fitting the Nyquist plot

Sample	R_{ct} (kΩ)	R_s (Ω)	CPE (μmho)	T
$SrTiO_3$	20.6	36.5	16.0	0.940
Sr_2TiO_4	14.5	28.4	12.5	0.973
$Sr_3Ti_2O_7$	12.3	26.5	12.1	0.974

The charge transfer resistance originating as a result of the ionic and electronic resistance across the electrode-electrolyte interface, R_{ct}, was observed to follow the order: $Sr_3Ti_2O_7$< Sr_2TiO_4< $SrTiO_3$. Mott-Schottky studies in presence of light (figure 5.15 d) were carried out to calculate charge carrier density using the following equation:

$$\frac{1}{C^2} = \frac{2}{\varepsilon\varepsilon_0 A^2\ e\ N_d}\left(V - V_{fb} - \frac{k_B T}{e}\right) \qquad (5.6)$$

where C is the interfacial capacitance, ε is the dielectric constant of the material (250, 38, and 50 for $SrTiO_3$ Sr_2TiO_4 and $Sr_3Ti_2O_7$ respectively)[40], ε_0 is the permittivity of vacuum (8.854×10^{-12} F m^{-1}), e is the fundamental charge (1.602×10^{-19} C), A is the area of the electrode ($1cm^2$), N_d is the charge carrier density, V is the applied potential, k_B is Boltzmann's constant, and T is the temperature. The positive slope of the plot suggests the n-type semiconducting behavior of the oxides. n-type behavior in $SrTiO_3$ arises due to the presence of oxygen vacancies.[41-42] The charge carrier density, N_d was calculated from the slope using equation 5.7.

$$Slope\ = \frac{2}{\varepsilon\varepsilon_o\ e \times N_d} \ldots. \qquad (5.7)$$

The slope was observed to be 1.07×10^{10} $F^{-2}cm^4V^{-1}$, 0.88×10^{10} $F^{-2}cm^4V^{-1}$ and 0.87×10^{10} $F^{-2}cm^4V^{-1}$ for $SrTiO_3$ Sr_2TiO_4 and $Sr_3Ti_2O_7$ respectively. Thus, N_d was calculated to be 5.3×10^{19} cm^{-3}, 4.2×10^{20} cm^{-3} and $3.2\ \times10^{20}$ cm^{-3} for $SrTiO_3$ Sr_2TiO_4 and $Sr_3Ti_2O_7$ respectively. The charge carrier density was found to be in the following order: Sr_2TiO_4 ≈ $Sr_3Ti_2O_7$ > $SrTiO_3$ consistent with the photocatalytic performance of the oxide.

a

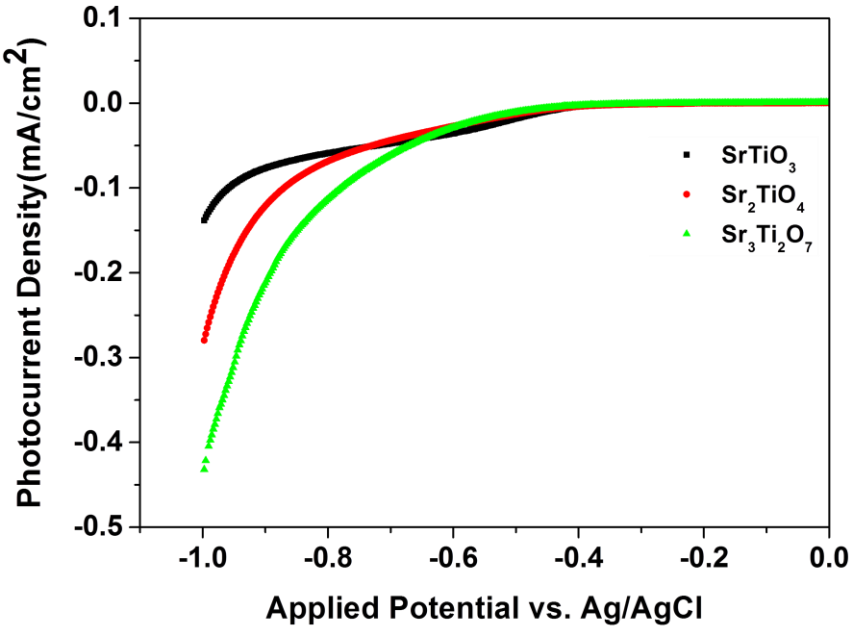
Photocurrent Density(mA/cm2)
0.1
0.0
-0.1
-0.2
-0.3
-0.4
-0.5
-1.0
-0.8
-0.6
-0.4
-0.2
0.0
Applied Potential vs. Ag/AgCl
SrTiO3
Sr2TiO4
Sr3Ti2O7

c

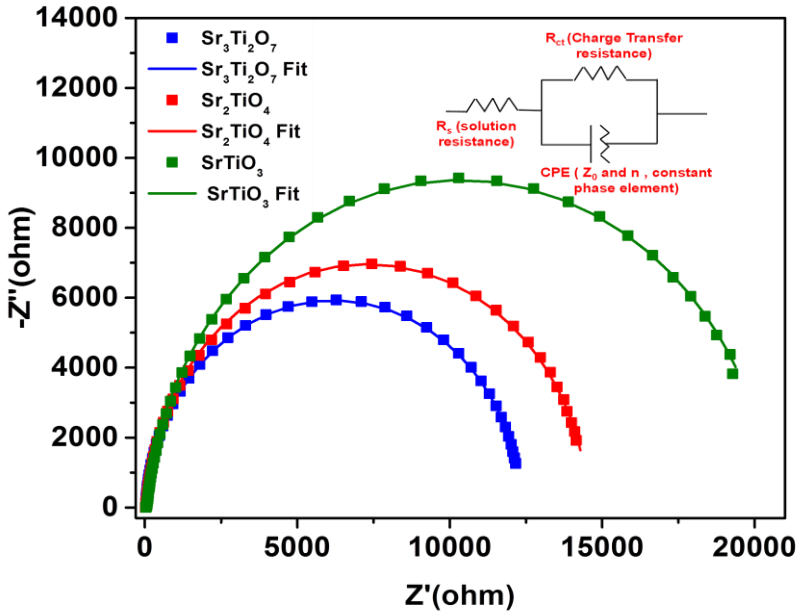
-Z''(ohm)
14000
12000
10000
8000
6000
4000
2000
0
0
5000
10000
15000
20000
Z'(ohm)
Sr3Ti2O7
Sr3Ti2O7 Fit
Sr2TiO4
Sr2TiO4 Fit
SrTiO3
SrTiO3 Fit
Rct (Charge Transfer resistance)
Rs (solution resistance)
CPE (Z0 and n , constant phase element)

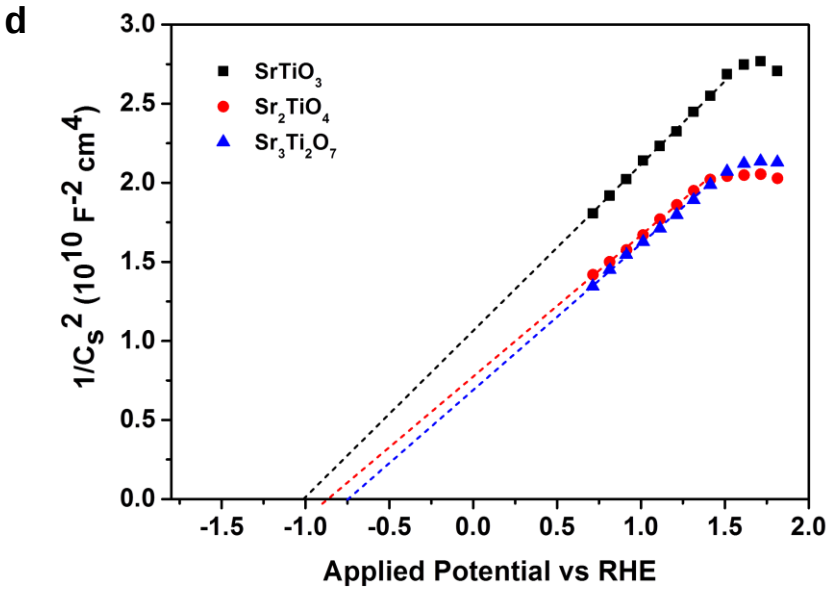

Figure 5.15: (a) Photocurrent density, (b) Overpotential (c) Nyquist plot and (d) Mott-Schottky plot for $SrTiO_3$, Sr_2TiO_4, and $Sr_3Ti_2O_7$.

Thus, from the trend observed for the photocatalytic hydrogen evolution, there are few interesting observations. The photocatalytic hydrogen evolution increased with the introduction of the SrO layer i.e. when comparing $SrTiO_3$ with Sr_2TiO_4 ($SrO(SrTiO_3)$). SrO layer in Ruddlesden-Popper based layered perovskite[43] is responsible for the dissociation of water. The oxygen site (apical oxygen) in $SrTiO_3$ of Ruddlesden-Popper based layered perovskite favors the adsorption of hydrogen enabling its recombination with other adsorbed hydrogen to form H_2. Wei et.al. [44] also observed that insertion of the SrO layer in $SrTaO_2N$ to form Sr_2TaO_3N (a Ruddlesden-Popper based oxynitride) resulted in the improved photocatalytic performance of the oxynitride. *Second*, with the increase in the $SrTiO_3$ perovskite unit in Ruddlesden-Popper based layered perovskite i.e. on comparing Sr_2TiO_4 and $Sr_3Ti_2O_7$, the photocatalytic activity was found to increase for $Sr_3Ti_2O_7$. For photocatalytic water splitting, the active sites in Ruddlesden-Popper based layered perovskite are the B-site cations (Ti in Sr-Ti-O based systems), and AO layers (SrO layer in Sr-Ti-O based systems), and defects arising due to oxygen vacancies. This arrangement of layers is known to suppress the charge carrier recombination, as evident from

time-resolved photoluminescence studies, and promote charge carrier transfer, as evident from a decrease in charge carrier resistance.

Based on the study, it is also to be noted there are two important synergistic factors that affect the photocatalytic behavior of the oxides: (a) crystal structure and the arrangement of atoms, and (b) the presence of defects (oxygen vacancies). Thus, synergism in the role of the SrO layer and the $SrTiO_3$ perovskite unit along with the layered morphology, low crystallite size, and presence of defects (oxygen vacancies), is presumed to have resulted in improved photocatalytic performance for Ruddlesden-Popper based layered perovskite. This improved performance was evident from reduced overpotential, low charge transfer resistance, and high charge carrier density for Ruddlesden-Popper based layered perovskite. Hence, proper choice of the crystal structure from a series could result in attaining the desired factors required for designing of efficient catalyst for photocatalytic HER.

5.4 Conclusions:

We have successfully synthesized three members of the Sr-Ti-O system viz. $SrTiO_3$, Sr_2TiO_4, and $Sr_3Ti_2O_7$ using a combination of polymeric citrate precursor and hydrothermal method. $SrTiO_3$ was observed to crystallize in cubic structure and possessed cube-like morphology. Sr_2TiO_4 and $Sr_3Ti_2O_7$ were found to crystallize in the tetragonal crystal structure. Sheet-like morphology was observed for these two oxides. We have demonstrated photocatalytic hydrogen evolution activity for these three nanostructured oxides. All three structures were found to be active photocatalysts under a full range of light irradiation and in absence of any co-catalyst. We observed that the nanocubes of $SrTiO_3$ (perovskite cubic crystal structure were less active for photocatalytic HER than layered Sr_2TiO_4, and $Sr_3Ti_2O_7$ (tetragonal, Ruddlesden-popper structure). Synergism of many factors which included the presence of SrO layer, $SrTiO_3$ unit, layered morphology, low crystallite size, and defects are attributed to the observed photocatalytic performance of the Ruddlesden-popper structure in comparison to cubic perovskite $SrTiO_3$. Thus, the findings in our study highlight the influence of the Ruddlesden-Popper crystal structure on the hydrogen evolution efficiency of perovskite oxides. The study opens a strategic approach based on choosing the crystal structure while designing highly efficient catalysts.

Acknowledgement

This work is published as "**Aditi Vijay**, Kadambari Bairagi, Sonalika Vaidya*Relating Structure, Property and Activity of nanostructured SrTiO3 and SrO-(SrTiO3) n (n= 1 and 2) for Photocatalytic Hydrogen Evolution. (accepted in Material Advances)"

5.5 References:

1. Maeda, K.; Teramura, K.; Lu, D.; Takata, T.; Saito, N.; Inoue, Y.; Domen, K., Photocatalyst releasing hydrogen from water. *Nature* **2006,** *440* (7082), 295.
2. Tong, H.; Ouyang, S.; Bi, Y.; Umezawa, N.; Oshikiri, M.; Ye, J., Nano-photocatalytic Materials: Possibilities and Challenges. *Advanced Materials* **2012,** *24* (2), 229-251.
3. Li, Y.-F.; Liu, Z.-P.; Liu, L.; Gao, W., Mechanism and Activity of Photocatalytic Oxygen Evolution on Titania Anatase in Aqueous Surroundings. *Journal of the American Chemical Society* **2010,** *132* (37), 13008-13015.
4. Ouyang, S.; Ye, J., β-$AgAl_{1-x}Ga_xO_2$ Solid-Solution Photocatalysts: Continuous Modulation of Electronic Structure toward High-Performance Visible-Light Photoactivity. *Journal of the American Chemical Society* **2011,** *133* (20), 7757-7763.
5. Kumar, A.; Krishnan, V., Vacancy Engineering in Semiconductor Photocatalysts: Implications in Hydrogen Evolution and Nitrogen Fixation Applications. *Advanced Functional Materials* **2021,** *31* (28), 2009807.
6. Flores, N. M.; Pal, U.; Galeazzi, R.; Sandoval, A., Effects of morphology, surface area, and defect content on the photocatalytic dye degradation performance of ZnO nanostructures. *RSC Advances* **2014,** *4* (77), 41099-41110.
7. Zhang, L.; Xu, T.; Zhao, X.; Zhu, Y., Controllable synthesis of Bi_2MoO_6 and effect of morphology and variation in local structure on photocatalytic activities. *Applied Catalysis B: Environmental* **2010,** *98* (3), 138-146.
8. Liu, Y.; Huang, B.; Dai, Y.; Zhang, X.; Qin, X.; Jiang, M.; Whangbo, M.-H., Selective ethanol formation from photocatalytic reduction of carbon dioxide in water with $BiVO_4$ photocatalyst. *Catalysis Communications* **2009,** *11* (3), 210-213.
9. Ouyang, S.; Kikugawa, N.; Chen, D.; Zou, Z.; Ye, J., A Systematical Study on Photocatalytic Properties of $AgMO_2$ (M = Al, Ga, In): Effects of Chemical Compositions, Crystal Structures, and Electronic Structures. *Journal of Physical Chemistry C* **2009,** *113* (4), 1560-1566.
10. Kandiel, T. A.; Feldhoff, A.; Robben, L.; Dillert, R.; Bahnemann, D. W., Tailored Titanium Dioxide Nanomaterials: Anatase Nanoparticles and Brookite Nanorods as Highly Active Photocatalysts. *Chemistry of Materials* **2010,** *22* (6), 2050-2060.
11. Li, T.; Cai, H.; Li, C.; Liu, X.; Huang, F., Rocksalt-Zincblende–Wurtzite Mixed-Phase ZnO Crystals With High Activity as Photocatalysts for Visible-Light-Driven Water Splitting. *Frontiers in Chemistry* **2020,** *8*, 351.
12. Chen, S.; Huang, D.; Xu, P.; Xue, W.; Lei, L.; Cheng, M.; Wang, R.; Liu, X.; Deng, R., Semiconductor-based photocatalysts for photocatalytic and photoelectrochemical water splitting: will we stop with photocorrosion? *J. Mater. Chem. A* **2020,** *8* (5), 2286-2322.

13. Cai, J.; Cao, A.; Wang, Z.; Lu, S.; Jiang, Z.; Dong, X.-Y.; Li, X.; Zang, S.-Q., Surface oxygen vacancies promoted Pt redispersion to single-atoms for enhanced photocatalytic hydrogen evolution. *Journal of Material Chemistry A* **2021,** *9* (24), 13890-13897.

14. Kumar, S.; Kumar, A.; Kumar, A.; Krishnan, V., Nanoscale zinc oxide based heterojunctions as visible light active photocatalysts for hydrogen energy and environmental remediation. *Catalysis Reviews* **2020,** *62* (3), 346-405.

15. Mai, H.; Chen, D.; Tachibana, Y.; Suzuki, H.; Abe, R.; Caruso, R. A., Developing sustainable, high-performance perovskites in photocatalysis: design strategies and applications. *Chemical Society Reviews* **2021,** *50* (24), 13692-13729.

16. Zhang, G.; Liu, G.; Wang, L.; Irvine, J. T. S., Inorganic perovskite photocatalysts for solar energy utilization. *Chemical Society Reviews* **2016,** *45* (21), 5951-5984.

17. Kumar, A.; Kumar, A.; Krishnan, V., Perovskite Oxide Based Materials for Energy and Environment-Oriented Photocatalysis. *ACS Catalysis* **2020,** *10* (17), 10253-10315.

18. Kimijima, T.; Kanie, K.; Nakaya, M.; Muramatsu, A., Solvothermal synthesis of $SrTiO_3$ nanoparticles precisely controlled in surface crystal planes and their photocatalytic activity. *Applied Catalysis B: Environmental* **2014,** *144*, 462-467.

19. Hsieh, P.-L.; Naresh, G.; Huang, Y.-S.; Tsao, C.-W.; Hsu, Y.-J.; Chen, L.-J.; Huang, M. H., Shape-Tunable $SrTiO_3$ Crystals Revealing Facet-Dependent Optical and Photocatalytic Properties. *The Journal of Physical Chemistry C* **2019,** *123* (22), 13664-13671.

20. Vijay, A.; Vaidya, S., Tuning the Morphology and Exposed Facets of $SrTiO_3$ Nanostructures for Photocatalytic Dye Degradation and Hydrogen Evolution. *ACS Applied Nano Materials* **2021,** *4* (4), 3406-3415.

21. Oshima, T.; Yokoi, T.; Eguchi, M.; Maeda, K., Synthesis and photocatalytic activity of $K_2CaNaNb_3O_{10}$, a new Ruddlesden–Popper phase layered perovskite. *Dalton Trans.* **2017,** *46* (32), 10594-10601.

22. Shimizu, K.-i.; Tsuji, Y.; Hatamachi, T.; Toda, K.; Kodama, T.; Sato, M.; Kitayama, Y., Photocatalytic water splitting on hydrated layered perovskite tantalate $A_2SrTa_2O_7{\cdot}nH_2O$ (A = H, K, and Rb). *Physical Chemistry Chemical Physics* **2004,** *6* (5), 1064-1069.

23. Sun, X.; Xie, Y.; Wu, F.; Chen, H.; Lv, M.; Ni, S.; Liu, G.; Xu, X., Photocatalytic Hydrogen Production over Chromium Doped Layered Perovskite Sr_2TiO_4. *Inorganic Chemistry* **2015,** *54* (15), 7445-7453.

24. Zhang, H.; Ni, S.; Mi, Y.; Xu, X., Ruddlesden-Popper compound Sr_2TiO_4 co-doped with La and Fe for efficient photocatalytic hydrogen production. *Journal of Catalysis* **2018,** *359*, 112-121.

25. Yamada, K.; Suzuki, H.; Abe, R.; Saeki, A., Complex Photoconductivity Reveals How the Nonstoichiometric Sr/Ti Affects the Charge Dynamics of a $SrTiO_3$ Photocatalyst. *Journal of Physical Chemistry Letters* **2019,** *10* (8), 1986-1991.

26. Jeong, H.; Kim, T.; Kim, D.; Kim, K., Hydrogen production by the photocatalytic overall water splitting on $NiO/Sr_3Ti_2O_7$: Effect of preparation method. *International Journal of Hydrogen Energy* **2006,** *31* (9), 1142-1146.

27. Liu, Y.; Xie, L.; Li, Y.; Yang, R.; Qu, J.; Li, Y.; Li, X., Synthesis and high photocatalytic hydrogen production of $SrTiO_3$ nanoparticles from water splitting under UV irradiation. *Journal of Power Sources* **2008,** *183* (2), 701-707.

28. Nilsen, W. G.; Skinner, J. G., Raman Spectrum of Strontium Titanate. *Journal of Chemical Physics* **1968,** *48* (5), 2240-2248.

29. Banerjee, S.; Kim, D.-I.; Robinson, R. D.; Herman, I. P.; Mao, Y.; Wong, S. S., Observation of Fano asymmetry in Raman spectra of $SrTiO_3$ and $Ca_xSr_{1-x}TiO_3$ perovskite nanocubes. *Applied Physics Letters* **2006,** *89* (22), 223130.

30. Viennois, R.; Hermet, P.; Machon, D.; Koza, M. M.; Bourgogne, D.; Fraisse, B.; Petrović, A. P.; Maurin, D., Stability and Lattice Dynamics of Ruddlesden–Popper Tetragonal Sr_2TiO_4. *Journal of Physical Chemistry C* **2020,** *124* (51), 27882-27893.

31. Dias, A.; Viegas, J. I.; Moreira, R. L., Synthesis and μ-Raman scattering of Ruddlesden-Popper ceramics $Sr_3Ti_2O_7$, $SrLa_2Al_2O_7$ and $Sr_2LaAlTiO_7$. *Journal of Alloys and Compounds* **2017,** *725*, 77-83.

32. Kamba, S.; Samoukhina, P.; Kadlec, F.; Pokorný, J.; Petzelt, J.; Reaney, I. M.; Wise, P. L., Composition dependence of the lattice vibrations in $Sr_{n+1}Ti_nO_{3n+1}$ Ruddlesden–Popper homologous series. *Journal of the European Ceramic Society* **2003,** *23* (14), 2639-2645.

33. Lee, C.-H.; Podraza, N. J.; Zhu, Y.; Berger, R. F.; Shen, S.; Sestak, M.; Collins, R. W.; Kourkoutis, L. F.; Mundy, J. A.; Wang, H.; Mao, Q.; Xi, X.; Brillson, L. J.; Neaton, J. B.; Muller, D. A.; Schlom, D. G., Effect of reduced dimensionality on the optical band gap of $SrTiO_3$. *Applied Physics Letters* **2013,** *102* (12), 122901.

34. Chen, A.; Zhang, X.; Zhang, Z.; Yao, S.; Zhou, Z., Band engineering of two-dimensional Ruddlesden–Popper perovskites for solar utilization: the relationship between chemical components and electronic properties. *Journal of Material Chemistry A* **2019,** *7* (18), 11530-11536.

35. Chen, H.; Xu, X., Ruddlesden-Popper compounds in the double-perovskite family $Sr_2FeTaO_6(SrO)_n$ (n=0, 1 and 2) and their photocatalytic properties. *Applied Catalysis B: Environmental* **2017,** *206*, 35-43.

36. Souza, A. E.; Santos, G. T. A.; Barra, B. C.; Macedo, W. D.; Teixeira, S. R.; Santos, C. M.; Senos, A. M. O. R.; Amaral, L.; Longo, E., Photoluminescence of $SrTiO_3$: Influence of Particle Size and Morphology. *Crystal Growth & Design* **2012,** *12* (11), 5671-5679.

37. Zheng, T.; Sang, W.; He, Z.; Wei, Q.; Chen, B.; Li, H.; Cao, C.; Huang, R.; Yan, X.; Pan, B.; Zhou, S.; Zeng, J., Conductive Tungsten Oxide Nanosheets for Highly Efficient Hydrogen Evolution. *Nano Letters* **2017,** *17* (12), 7968-7973.

38. Tan, H.; Zhao, Z.; Zhu, W.-b.; Coker, E. N.; Li, B.; Zheng, M.; Yu, W.; Fan, H.; Sun, Z., Oxygen Vacancy Enhanced Photocatalytic Activity of Pervoskite $SrTiO_3$. *ACS Applied Material & Interfaces* **2014,** *6* (21), 19184-19190.

39. Liang, Z.; Tang, K.; Shao, Q.; Li, G.; Zeng, S.; Zheng, H., Synthesis, crystal structure, and photocatalytic activity of a new two-layer Ruddlesden–Popper phase, $Li_2CaTa_2O_7$. *Journal of Solid State Chemistry* **2008,** *181* (4), 964-970.

40. Kwestroo, W.; Paping, H. A. M., The Systems BaO-SrO-TiO2, BaO-CaO-TiO_2, and SrO-CaO-TiO_2. *Journal of the American Ceramic Society* **1959,** *42* (6), 292-299.

41. Calvani, P.; Capizzi, M.; Donato, F.; Lupi, S.; Maselli, P.; Peschiaroli, D., Observation of a midinfrared band in $SrTiO_{3-y}$. *Physical Review B* **1993,** *47* (14), 8917-8922.

42. Tufte, O. N.; Chapman, P. W., Electron Mobility in Semiconducting Strontium Titanate. *Physical Review* **1967,** *155* (3), 796-802.

43. Zhu, Y.; Tahini, H. A.; Hu, Z.; Dai, J.; Chen, Y.; Sun, H.; Zhou, W.; Liu, M.; Smith, S. C.; Wang, H.; Shao, Z., Unusual synergistic effect in layered Ruddlesden−Popper oxide enables ultrafast hydrogen evolution. *Nature Communications* **2019,** *10* (1), 149.

44. Wei, S.; Xu, X., Boosting photocatalytic water oxidation reactions over strontium tantalum oxynitride by structural laminations. *Applied Catalysis B: Environmental* **2018,** *228*, 10-18.

Chapter 6

Role of crystal structure and electrical polarization of an electrocatalyst in enhancing Oxygen Evolution performance: Bi-Fe-O system as a case study

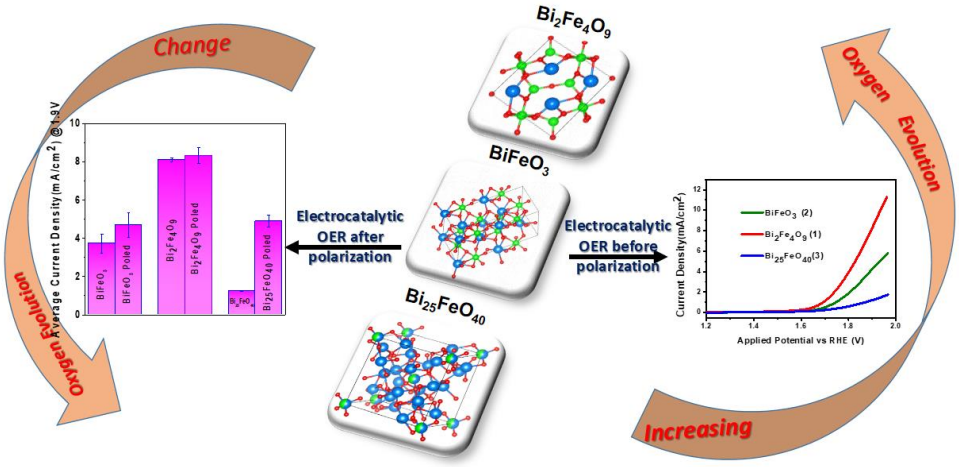

Chapter 6

Role of crystal structure and electrical polarization of an electrocatalyst in enhancing Oxygen Evolution performance: Bi-Fe-O system as a case study

Abstract

This work aims to give an insight into the influence of crystal structure (for a system containing the same elements but crystallizing in different structures) and the effect of electrical polarization on these oxides on the performance of oxygen evolution reaction (OER). We have tried to highlight this influence by taking the Bi-Fe-O system for the study. Herein, we have synthesized three structures of the Bi-Fe-O system viz. $BiFeO_3$ (perovskite structure), $Bi_2Fe_4O_9$ (mullite structure), and $Bi_{25}FeO_{40}$ (sillenite structure) as an example to establish the relation. These oxides were characterized by Rietveld refinement for structure and scanning electron microscopy (SEM) for morphology. Their optical and magnetic properties were also investigated. Systematic studies were carried out with both as-synthesized and electrically polarized oxides for their performance towards OER. We observed that the order for OER activity (using non-polarized catalyst) of the three stable structures synthesized was $Bi_2Fe_4O_9$ > $BiFeO_3$> $Bi_{25}FeO_{40}$, which was attributed to the presence of $Fe_{(oct)}$-O-$Fe_{(td)}$ linkages in $Bi_2Fe_4O_9$. While the current density of $Bi_2Fe_4O_9$ and $BiFeO_3$ remained unchanged after poling, that of $Bi_{25}FeO_{40}$ increased by four-fold. From the study, we have demonstrated that proper choice of the crystal structure and utilization of electrical polarization can be effective strategies to manipulate the surfaces of an electrocatalytic material.

Keywords: $BiFeO_3$; $Bi_2Fe_4O_9$; $Bi_{25}FeO_{40}$; crystal structure; electrical polarization; oxygen evolution reaction

6.1 Introduction:

Electrocatalytic splitting of water involves an oxygen evolution reaction (OER) taking place at the anode and a hydrogen evolution reaction (HER) at the cathode. Amongst these, electrochemical oxygen evolution reaction (OER) is considered to be a rate-limiting step in the overall reaction process as it involves a four-electron transfer and requires a higher overpotential to complete reaction [1-2]. In the past several years, many attempts have been made to minimize the overpotential and enhance the efficiency of the water oxidation reaction [3-7]. Several transition metals (Ni, Fe, Co, Mn) oxides/hydroxides [3, 8-14] have been developed to replace the noble metal catalyst which is expensive and less abundant in the earth's crust. The efficiency of the electrocatalytic OER is affected by various parameters of the catalyst, viz. electronic [15], crystal structure [16-17], phase structure [18-19], morphology [20-21], oxidation state [22], orientation, etc. Amongst these, the crystal structure of inorganic materials is proven to be one of the important parameters in changing the catalytic performance as it influences changes in the arrangement of atoms and thereby their electronic structure [23-24].

Recently, it has also been discovered that there occurs further enhancement in the molecular adsorption and desorption at the surface of ferroelectric catalysts [25-26] due to the surface charge. Thus, these surface reactions may provide an efficient way to increase the electrocatalytic water splitting (i.e., HER and OER). Kushwaha *et.al* [27] showed that polarizing a ferroelectric catalyst $Bi_{0.5}Na_{0.5}TiO_3$ led to changes in the flat band potential which increases the catalytic activity towards OER. Similarly, Li *et.al* [28] demonstrated that applying polarization by a corona poling technique on $Bi_4Ti_3O_{12}\cdot(BiCoO_3)_2$ resulted in an enhancement in the OER activity. Electrically polarizing a semiconducting or insulating catalyst could be an effective way to increase its efficiency towards an electrocatalytic water-splitting reaction. In this study, we have explored the influence of crystal structure (for a system containing the same elements but crystallizing in different structures, by talking the Bi-Fe-O system as an example) and the effect of electrical polarization on these oxides on their oxygen evolution performance. To the best of our knowledge, the effect of the crystal structure of three different phases of the Bi-Fe-O system viz. $BiFeO_3$, $Bi_2Fe_4O_9$, and $Bi_{25}FeO_{40}$ and the role of electric polarization on these oxides (both kind ferroelectric and non-ferroelectric), on the oxygen evolution performance, discussed here, has not been carried out so far. $BiFeO_3$, crystallizing in perovskite structure (space group *R*3*c*), is a multiferroic oxide (figure 6.1a). $Bi_2Fe_4O_9$ possesses the mullite structure (space group *Pbam*) (figure 6.1b) whereas $Bi_{25}FeO_{40}$ crystallizes in the sillenite structure (space group I*23*) (figure 6.1c). From

our study, we have demonstrated that the choice of crystal structure within different sets of oxides in a ternary system (showcased here with the Bi-Fe-O system as an example) could be an efficient way for the development of a highly active catalyst for oxygen evolution reaction. In addition to the crystal structure, we have also demonstrated that electrically polarizing the oxides, enhances the electrocatalytic activity.

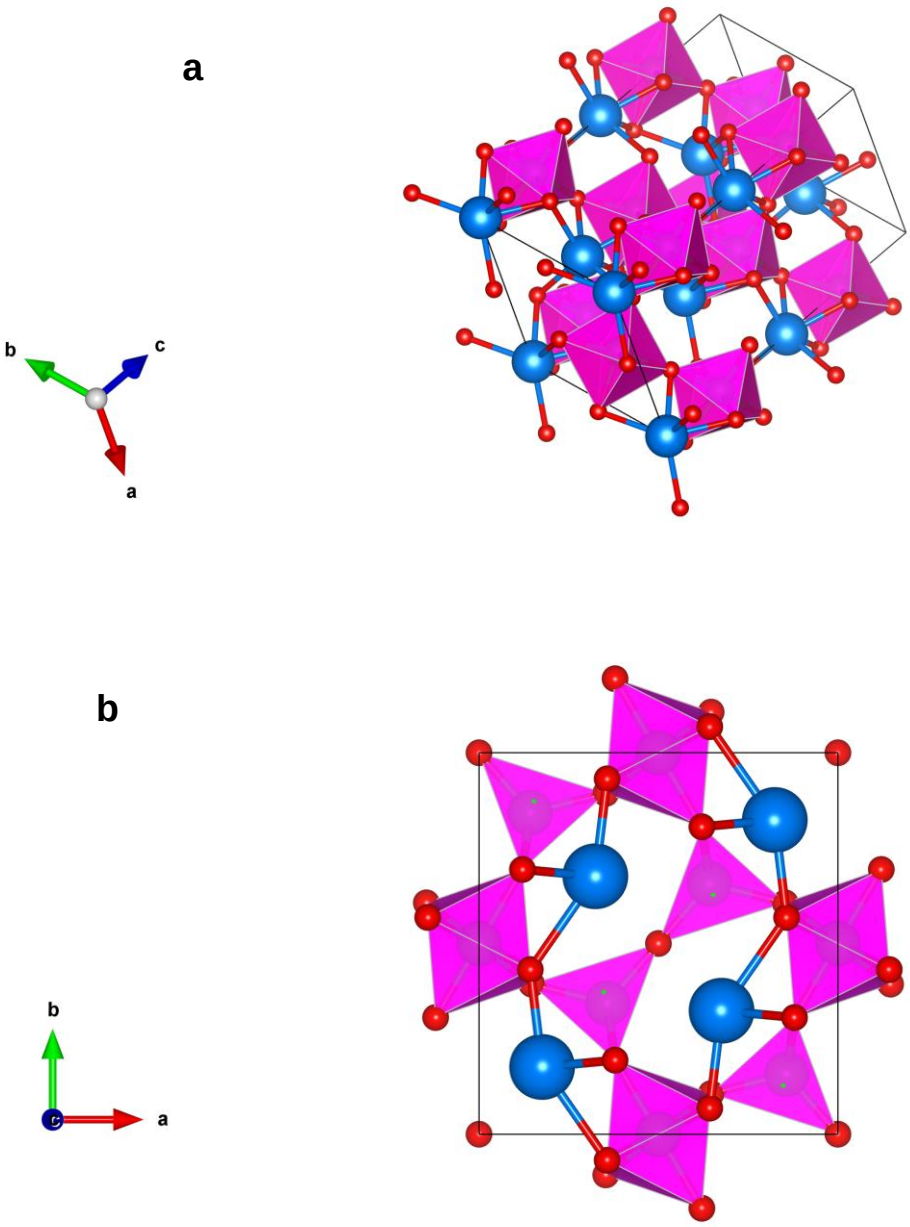

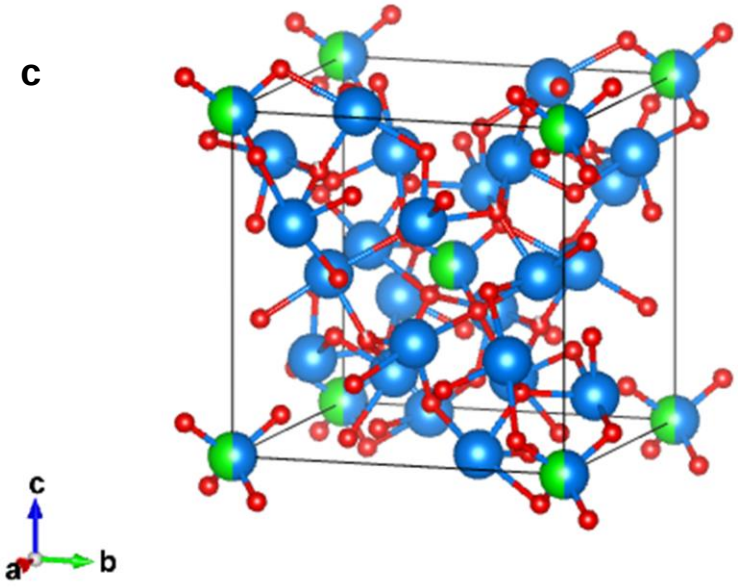

Figure 6.1: Unit cell structures of (a) $BiFeO_3$, (b) $Bi_2Fe_4O_9$ and (c) $Bi_{25}FeO_{40}$. (Blue, Green, and Red color is used for depicting Bi, Fe, and O atom respectively. FeO_6 octahedron and FeO_4 tetrahedron is depicted by pink color)

6.2 Materials and Method:

6.2.1 Materials used:

Bismuth nitrate pentahydrate ($Bi(NO_3)_3.5H_2O$ (99%)), iron nitrate nonahydrate ($Fe(NO_3)_3.9H_2O$ (99%)), and Nafion resin solution were purchased from Sigma Aldrich. Sodium hydroxide pellets (NaOH), potassium hydroxide pellets (KOH), and nitric acid were purchased from Merck.

6.2.2 Material Synthesis:

Bi-Fe-O-based oxides were synthesized by the hydrothermal method. In a typical synthesis, bismuth nitrate was dissolved in a mixture containing 1 mL conc. nitric acid and 6.5 mL water, which was followed by the addition of iron nitrate. To synthesize three stable phases of the Bi-Fe-O system viz. $BiFeO_3$, $Bi_2Fe_4O_9$, and $Bi_{25}FeO_{40}$, the ratio of Bi to Fe were varied along with a combination of NaOH and KOH. For the synthesis of $BiFeO_3$, the ratio of Bi to Fe was maintained at 1:1 whereas, for $Bi_2Fe_4O_9$ and $Bi_{25}FeO_{40}$, the ratio was maintained to be 1:2 and 25:1 respectively. To the clear, transparent solution containing Bi^{3+} and Fe^{3+}, 2M KOH solution (for $BiFeO_3$ and $Bi_2Fe_4O_9$) or 2M NaOH solution (for $Bi_{25}FeO_{40}$) were added

under constant stirring. The pH of the solution was maintained at 13 during the addition of hydroxide. After complete precipitation, the precipitates were washed with deionized (DI) water to remove NO_3^- and K^+/Na^+ ions. The precipitates were mixed with 40mL of 12M KOH (for $BiFeO_3$) or 14M NaOH (for $Bi_2Fe_4O_9$ and $Bi_{25}FeO_{40}$) under constant stirring for half an hour. The suspension was transferred to a Teflon-lined hydrothermal vessel and kept in an oven at 180° C for 12 h. The products formed were washed with DI water followed by ethanol. They were dried in an oven at 70° C. For $BiFeO_3$, only KOH was used, both as the precipitating agent and as the solvent added to the hydrothermal vessel during heating. For $Bi_2Fe_4O_9$, KOH was used as the precipitating agent whereas NaOH was used as the solvent during heating under hydrothermal conditions. For $Bi_{25}FeO_{40}$, NaOH was used, both as the precipitating agent and as the solvent added during heating under hydrothermal conditions. For $BiFeO_3$ and $Bi_2Fe_4O_9$, the precipitates obtained after heating the reactant mixture under hydrothermal conditions were washed and dried. $Bi_{25}FeO_{40}$ was formed after calcining the precipitate at 700° C for 12 h.

6.2.3 Characterization:

6.2.3.1 Material Characterization

The crystalline phase of the oxides was investigated by powder x-ray diffraction using a Bruker D8 Advance Eco diffractometer with a Cu-K$\boldsymbol{\alpha}$ X-ray source, operated at 25mA, and 40 kV, at a scan speed of 3 s/step and a step size of 0.0183°. Rietveld refinement studies were carried out with TOPAS v5 software using a structure file with a space group of $R3c$ (No. 161) for $BiFeO_3$, *Pbam* (No. 55) for $Bi_2Fe_4O_9$, and $I23$ (No. 197) for $Bi_{25}FeO_{40}$. A tenth-order Chebyshev polynomial of the first kind was used to model the background. Simulation of the peak profile was carried out with the Thompson-Cox-Hastings pseudo-Voigt function. The cell parameters, scaling factor, background fitting, amorphous phase, and the occupancy factor for all the atoms were refined. The refined atomic coordinates were used to draw unit cell structures for the oxides, using Vesta software.

The morphology of the samples was investigated with a JEOL JSM-1T300 scanning electron microscope (SEM). Diffuse reflectance spectroscopy was carried out on a Shimadzu UV-2600 spectrometer with $BaSO_4$ as the reference. X-ray photoelectron spectroscopy was performed on PHI 5000 Versa Prob II, FEI Inc with the following settings: pass setting of 23.5 eV, 0.025eV/0.05eV Step, 50 ms time per step and 10 cycles, Source Al k-alpha-1486eV, Dual-beam Neut. Magnetic properties of the Bi-Fe-O samples were studied with a

Quantum Design Physical Property Measurement System (PPMS) in the temperature range of 5–300 K with an applied field of up to 10000 Oe. Post OER characterization (PXRD and FESEM) were carried out on the electrode prepared on a graphite strip containing the catalyst with Nafion resin. FESEM studies were carried out on JEOL JSM-7610F Plus.

6.2.3.2 Electrochemical Testing :

All the electrochemical measurements were carried out on a Metrohm Multi Autolab three-electrode electrochemical workstation. The samples were used to coat a graphite strip which served as the working electrode. 10 mg of Bi-Fe-O samples were dispersed in 1 mL of isopropyl alcohol (IPA) containing 20µL of Nafion resin solution through ultra-sonication for 1 h. The dispersed samples were deposited on a cleaned graphite strip having an area of 0.5 cm^2 which was dried for further use. The load mass density on the graphite substrate was 4 mg/cm^2, 3mg/cm^2, and 10 mg/cm^2 for $BiFeO_3$, $Bi_2Fe_4O_9$ and $Bi_{25}FeO_{40}$ respectively. 3M Ag/AgCl was taken as the reference electrode, and platinum wire was used as the counter electrode. All measurements were carried out in a 50 mL vessel containing 0.1M KOH as the electrolyte. The electrolyte solution was saturated with argon for 30 min before the study. Linear sweep voltammetry (LSV) was performed at a scan rate of 10 mVs^{-1}. The measurements were carried out twice. The mean of the two current densities is reported. Long term stability of the catalysts was carried out using Chronoamperometric studies at an applied potential of 1.5 V vs. RHE. The electrochemical impedance spectra (EIS) were measured over the frequency range of 0.01 to 100,000 Hz at an applied potential of 1.5V V/s RHE.

The flat-band potential V_{fb} of the oxides was calculated with the Mott-Schottky equation:

$$\frac{1}{C^2} = \frac{2}{\varepsilon\varepsilon_0 A^2\ e\ N_d}\left(V - V_{fb} - \frac{k_B T}{e}\right) \quad (6.1)$$

where C is the interfacial capacitance, ε is the dielectric constant, ε_0 is the permittivity of vacuum, e is the fundamental charge, A is the area of the electrode, N_d is the charge carrier density, V is the applied potential, k_B is Boltzmann's constant, and T is the temperature.

The Rotating Ring-Disk Electrode (RRDE) method was used to measure the faradaic efficiency (FE) for OER, using equation 6.2 [29]. N_2 gas was purged in the experimental cell, containing 0.1M KOH solution, for 30 minutes before the experiment. The gas was also purged during the entire experiment. 5 µL of the ink, containing the catalyst and Nafion resin solution, was drop cast on the surface of the glassy carbon (GC) disk of the electrode. The Pt ring of the electrode was held at -0.546 V vs Ag/AgCl (0.4 V vs RHE) throughout the

experiment. The disk electrode was scanned in the potential range of 0 to +1 V. The rotation speed of the RRDE electrode was maintained at 1600 rpm throughout the measurement.

$$FE = \frac{I_R\, n_D}{I_D\, n_R\, N} \qquad (6.2)$$

where I_R is current at the ring electrode, I_D is current at disk electrode, number of electrons transferred at the disk, $n_D = 4$ (number of electrons generated due to oxygen evolution), and number of electrons transferred at the ring, $n_R = 2$ (number of electrons used during reduction of oxygen), current collection efficiency, N = 0.249 (theoretical value reported for RRDE manufactured by Metrohm)

6.2.3.3 Poling method:

The samples were electrically polarized with a corona poling unit, manufactured by Milman Thin Film Systems Pvt. Ltd. A voltage of 40 kV was applied at the point electrode and 2 kV was applied on the mesh grid for 30 minutes. The sample-coated graphite strip was placed below the mesh grid. The distance between the sample holder and the point electrode was maintained at 2 cm. The poling process was conducted at room temperature.

6.3 Results and discussion:

From the Rietveld refinement of powder x-ray diffraction data, it was observed that the Bi-Fe-O phases (figure 6.2a-c) crystallized in their expected space groups. The degree of crystallinity was found to be 99.4%, 98.7%, and 99.99% for $BiFeO_3$, $Bi_2Fe_4O_9$, and $Bi_{25}FeO_{40}$ respectively. No impurity phase was observed in $BiFeO_3$, while 1.5% of $BiFeO_3$ and 2.6% of Bi_2O_3 were observed with $Bi_2Fe_4O_9$ and $Bi_{25}FeO_{40}$ respectively. The refined lattice parameters, atomic position, and atomic occupancy has been tabulated in Table 6.1. The ratio of Bi: Fe, observed after refinement, in $BiFeO_3$, $Bi_2Fe_4O_9$, and $Bi_{25}FeO_{40}$ was 1:1, 1:2.2, and 25.3:1 which is consistent within the accuracy of the refinement with the loaded ratio.

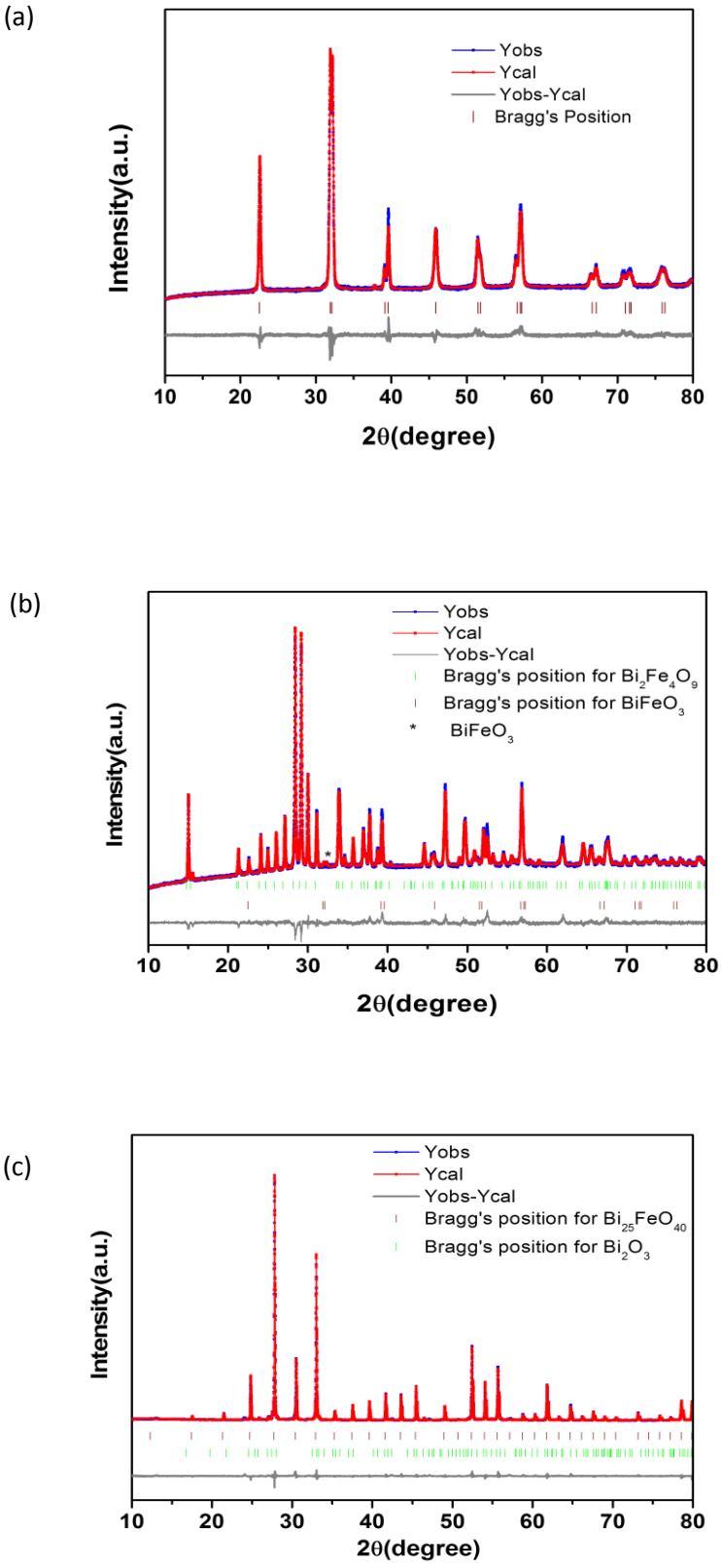

Figure 6.2: Observed, calculated, and difference plot of (a) $BiFeO_3$, (b) $Bi_2Fe_4O_9$, and (c) $Bi_{25}FeO_{40}$ as obtained by Rietveld refinement of powder X-ray data.

Table 6.1: Parameters obtained after Rietveld refinement of $BiFeO_3$, $Bi_2Fe_4O_9$, and $Bi_{25}FeO_{40}$

Parameters	**$BiFeO_3$**	**$Bi_2Fe_4O_9$**	**$Bi_{25}FeO_{40}$**
Space Group	*R*3*c*	*Pbam*	*I*23
Phase Purity	(i) Crystalline: 99.4% (ii)Amorphous: 0.6%	(i) Crystalline: 98.7% *Impurity: 1.48% ($BiFeO_3$) (ii)Amorphous: 1.28%	(i) Crystalline: 99.99% *Impurity: 2.58% (Bi_2O_3) (ii) Amorphous: 0.01%
Lattice Parameters (Å)	**a** = 5.58397(10) **b** = 13.8656(3)	**a** = 7.96778(11) **b** = 8.45458(12) **c** = 6.00858(10)	**a** = 10.19023(3)
Cell Volume ($Å^3$)	374.416(16)	404.763(11)	1058.162(10)
Atomic Position Parameters	**Bi:** **x** = 0.00000 **y** = 0.00000 **z** = 0.00309	**Bi:** **x**= 0.17584 **y**= 0.17625 **z**= 0.00000	**Bi(1):** **x** = 0.17658 **y** = 0.31779 **z** = 0.01357
			Bi(2): **x** = 0.00000 **y** = 0.00000 **z** = 0.00000
	Fe: **x** = 0.0000 **y** = 0.0000 **z** = 0.22637	**Fe(1):** **x**= 0.50000 **y** = 0.00000 **z** = 0.26395	**Fe:** **x** = 0.00000 **y** = 0.00000 **z** = 0.00000
		Fe(2): **x** = 0.35771 **y** = 0.34315 **z** = 0.50000	
	O: **x** = 0.44122 **y** = 0.00093 **z** = 0.96265	**O(1):** **x** = 0.00000 **y** = 0.00000 **z** = 0.50000	**O(1):** **x** = 0.69589 **y** = 0.69589 **z** = 0.69589
		O(2): **x** = 0.37908 **y** = 0.19408 **z** = 0.26563	**O(2):** **x** = 0.63730 **y** = 0.77346 **z** = 0.99253
		O(3): **x** = 0.14679 **y** = 0.39341 **z** = 0.50000	**O(3):** **x** = 0.89133 **y** = 0.89133 **z** = 0.89133
		O(4): **x** = 0.14300 **y** = 0.43167 **z** = 0.00000	
R_{wp}	5.80	3.94	7.84
GOF	1.62	1.74	2.13

Figure 6.3a-c shows SEM images for $BiFeO_3$, $Bi_2Fe_4O_9$ and $Bi_{25}FeO_{40}$ respectively. Flower-like clusters formed from the assembly of cuboids (~ 5-10 µm) were observed for $BiFeO_3$ (figure 6.3a). Square-shaped plates with a size of 2 µm were formed for $Bi_2Fe_4O_9$ (figure 6.3b), while cubes (~ 800 nm) were observed for $Bi_{25}FeO_{40}$ (figure 6.3c). To further investigate the morphology of the building blocks of these clusters, TEM analysis was done on these oxides. TEM image of $BiFeO_3$ (Figure 6.4a) shows the presence of a spherical-shaped cluster of size ~4 µm. HRTEM studies on the $BiFeO_3$ (Figure 6.4b) show lattice fringes corresponding to the (101) plane. Figure 6.4c shows square plates like morphology for $Bi_2Fe_4O_9$. HRTEM images show lattice fringes (figure 6.4d) corresponding to the (120) plane. Figure 6.4e shows the TEM image of $Bi_{25}FeO_{40}$, with some rectangular and irregular-shaped structures having a size ~1 µm. HRTEM image (figure 6.4f) shows the lattice plane corresponding to the (220) plane.

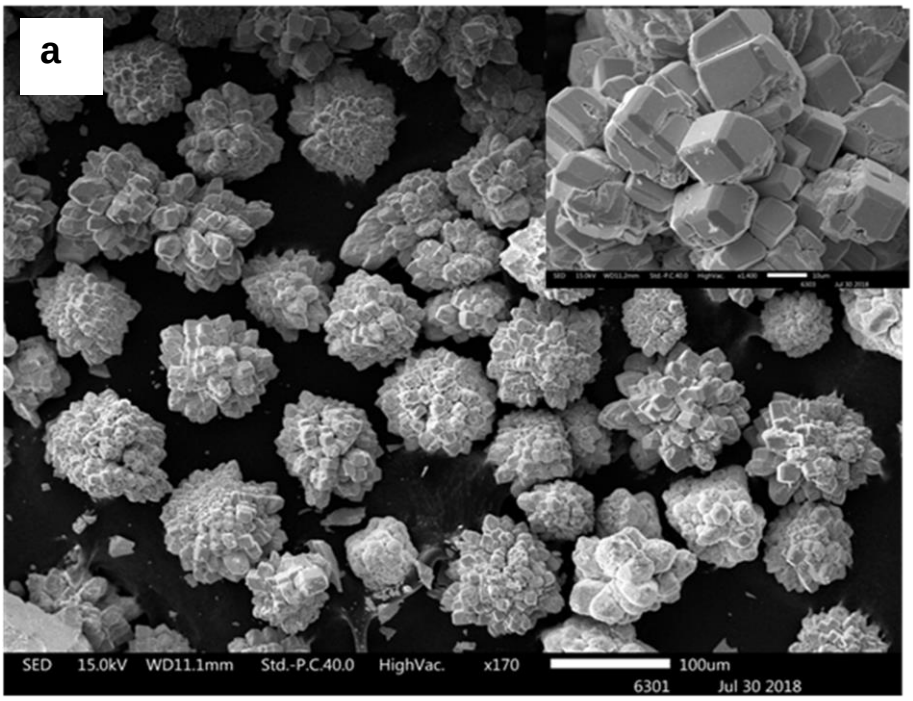

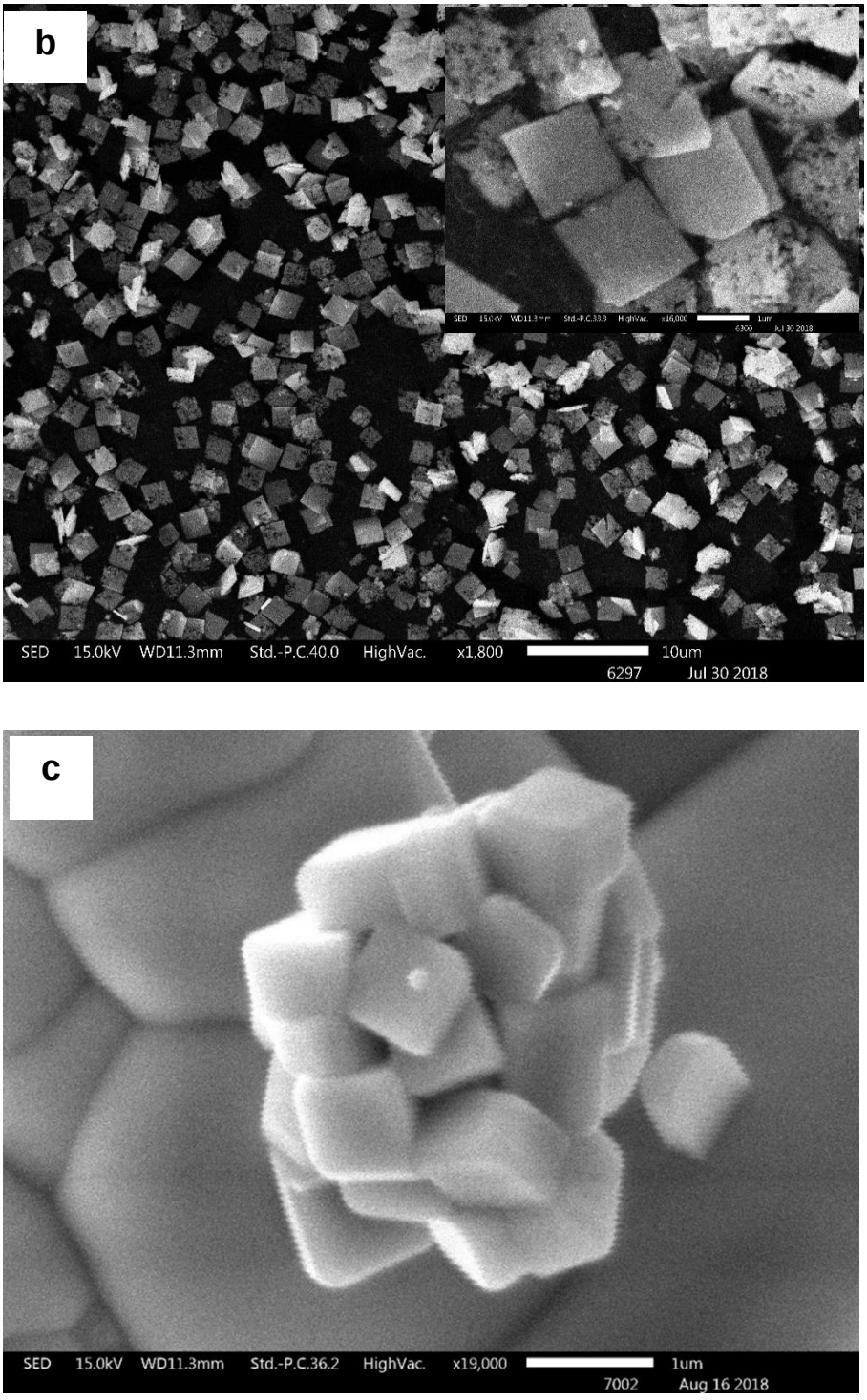

Figure 6.3: SEM images of (a) $BiFeO_3$, (b) $Bi_2Fe_4O_9$ and (c) $Bi_{25}FeO_{40}$

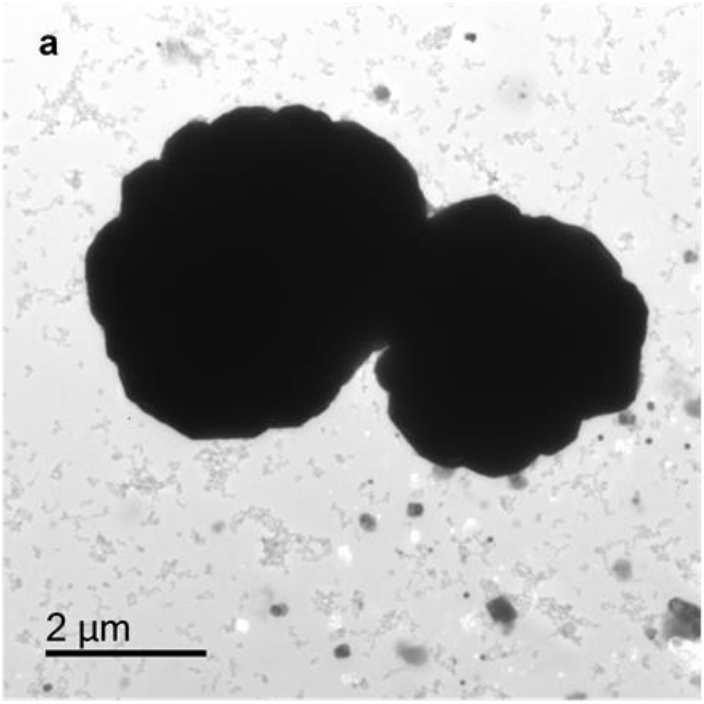
a
2 µm

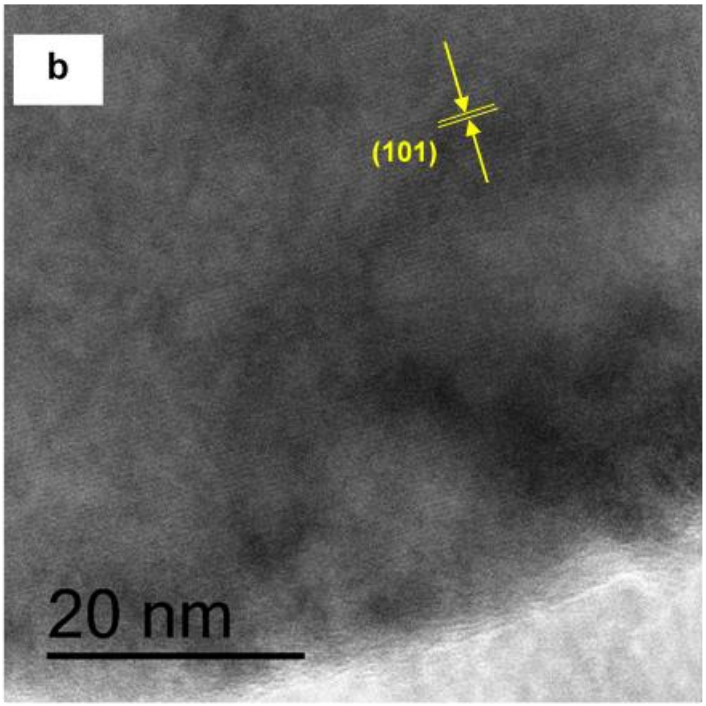
b
(101)
20 nm

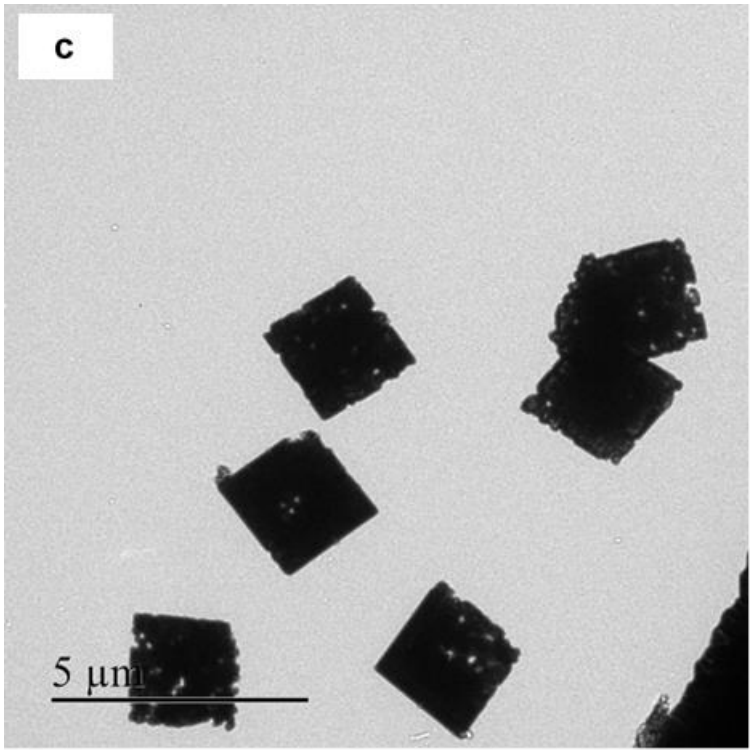
c
5 μm

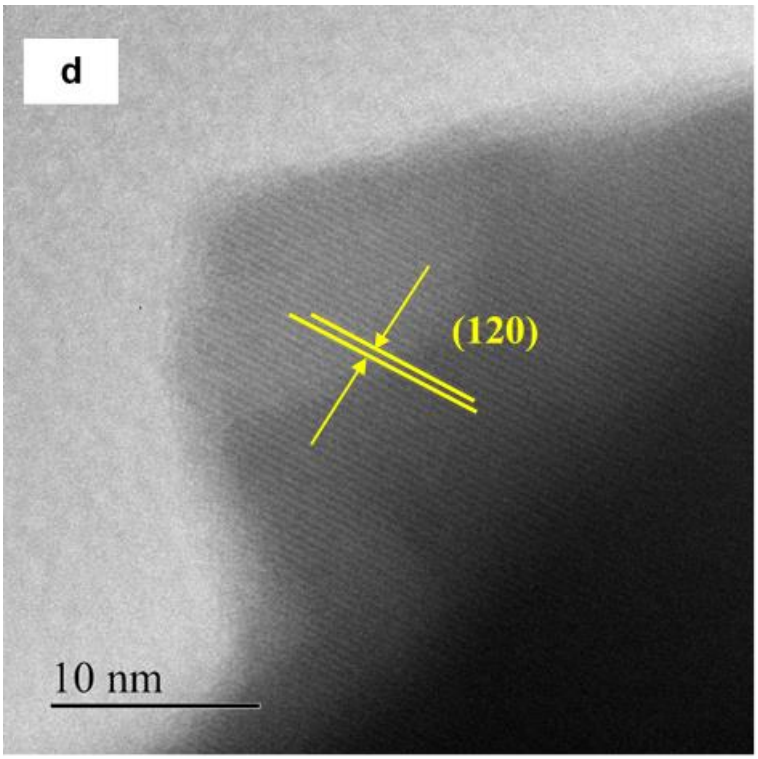
d
(120)
10 nm

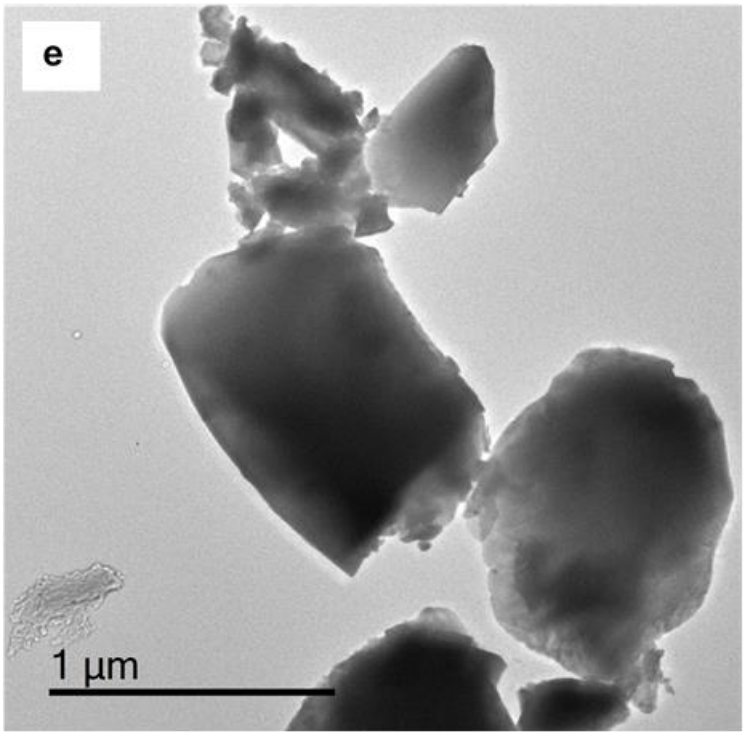

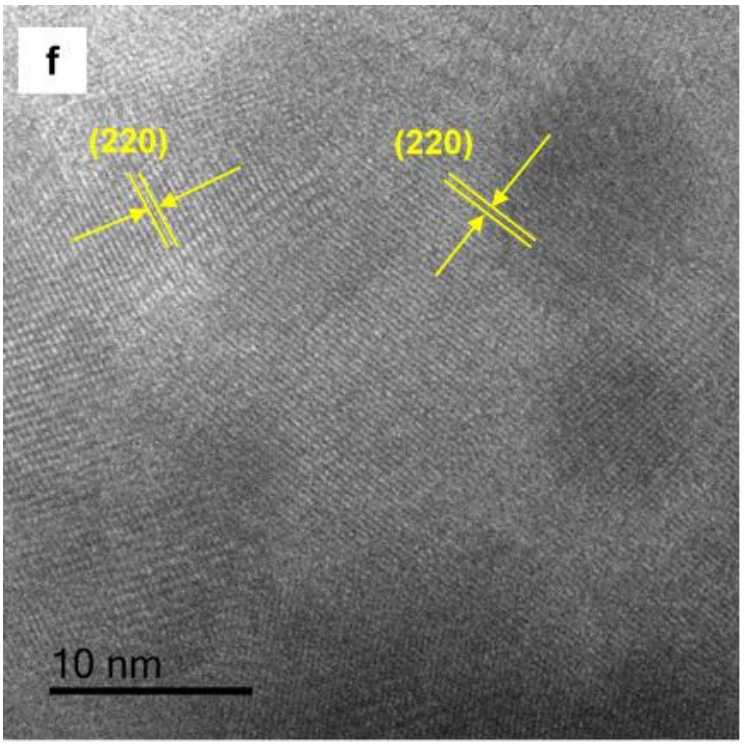

Figure 6.4: TEM images (a) $BiFeO_3$, (c) $Bi_2Fe_4O_9$ and (e) $Bi_{25}FeO_{40}$. HRTEM images (b) $BiFeO_3$, (d) $Bi_2Fe_4O_9$ and (f) $Bi_{25}FeO_{40}$.

The diffuse reflectance spectra were recorded for the oxides (figure 6.5) to investigate the optical properties. The absorption coefficient α was calculated from the reflectance *R* using equation 6.3 and 6.4.

$$\alpha = \frac{(1-R)^2}{2R}. \tag{6.3}$$

α is related to the band energy gap via the Tauc equation:

$$\alpha h\upsilon = K\,(h\upsilon - E_g)^{1/n} \tag{6.4}$$

where *h* is Planck's constant, ν is the frequency of the electromagnetic radiation, E_g is the optical band gap, *K* is an energy-independent constant, and *n* is a constant exponent. The value of *n* depends on the type of transition (*n* = 2 for direct transition and *n* = 0.5 for indirect transition). The bandgap of the Bi-Fe-O samples was calculated to be 1.94 eV, 2.24 eV, and 2.54 eV for $BiFeO_3$, $Bi_2Fe_4O_9$, and $Bi_{25}FeO_{40}$ respectively.

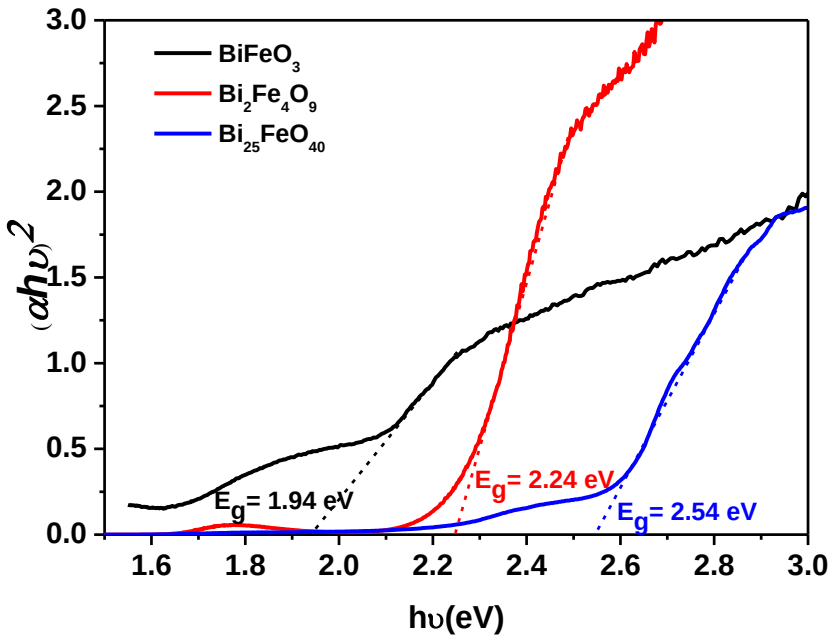

Figure 6.5: Tauc Plot for calculating the direct bandgap of $BiFeO_3$, $Bi_2Fe_4O_9$, and $Bi_{25}FeO_{40}$.

XPS analysis on the synthesized $BiFeO_3$, $Bi_2Fe_4O_9$, and $Bi_{25}FeO_{40}$ powders are shown in figure 6.6-6.8 . Figure 6.6a shows the survey spectrum of $BiFeO_3$ wherein peaks corresponding to Bi, Fe, and O could be observed. High-resolution spectra for these elements are shown in figure 6.6b-d. Peaks at 158.6 eV and 163.9 eV corresponding to $4f_{7/2}$ and $4f_{5/2}$,

respectively were observed in high-resolution spectra for Bi^{3+} (figure 6.6b). In Fe2p core-level spectra (Figure 6c), peaks at 710.2 eV and 723.3 eV, corresponding to (Fe^{3+}) $2p_{3/2}$ and $2p_{1/2}$, respectively were observed. Figure 6.6d shows O1s spectra having a peak at 529.5 eV arising due to lattice oxygen. For $Bi_2Fe_4O_9$, peaks corresponding to Bi, Fe, and O were observed in the survey scan (figure 6.7a). Peaks at 158.8 eV and 164.1 eV were observed in the high-resolution spectra of Bi, corresponding to $4f_{7/2}$ and $4f_{5/2}$, of Bi^{3+} respectively (figure 6.7b). Peaks for (Fe^{3+}) $2p_{3/2}$ and $2p_{1/2}$ were observed at 710 eV and 723.9 eV respectively (figure 6.7c). Figure 6.7 d shows O1s spectra having a peak at 529.7 eV arising due to lattice oxygen. The survey scan of $Bi_{25}FeO_{40}$ is shown in figure 6.8a. Peaks corresponding to $4f_{7/2}$ and $4f_{5/2}$, of Bi^{3+} were observed at 158.5 eV and 163.8 eV respectively (figure 6.8b). A very small peak, merged in the background (due to low concentration of Fe in the sample), centered at 709.3 eV was observed for (Fe^{3+}) $2p_{3/2}$ (figure 6.8c). Figure 6.8d shows O1s spectra having a peak at 529.4 eV arising due to lattice oxygen.

Figure 6.9a shows the magnetic hysteresis loops at 5 K. Both $BiFeO_3$ and $Bi_2Fe_4O_9$ are antiferromagnets with reasonably large Neel temperatures (643 K and ~260 K, respectively) [30-31]. The loops are presumably due to some unpaired surface spins and in the case of $BiFeO_3$, spin canting also. This can also be seen in magnetization data (Figure 6.9b) where the two phases show that the magnetization slowly increases and then become constant with lowering the temperature. In contrast, the dilution of the magnetic cation in $Bi_{25}FeO_{40}$ leads to paramagnetism even at low temperatures. The magnetic susceptibility χ of the sillenite phase was fit to a modified Curie law given by

$$\chi = \chi_0 + \frac{C'}{T} \qquad (6.5)$$

where χ_0 is a temperature-independent susceptibility and C' the Curie constant. The fit (inset, Figure 6.9b) gives C'=4.48 emu K/mol, which corresponds to an effective moment of 5.98 Bohr magnetons for Fe^{3+}, in good agreement with the expected value of 5.92 Bohr magnetons.

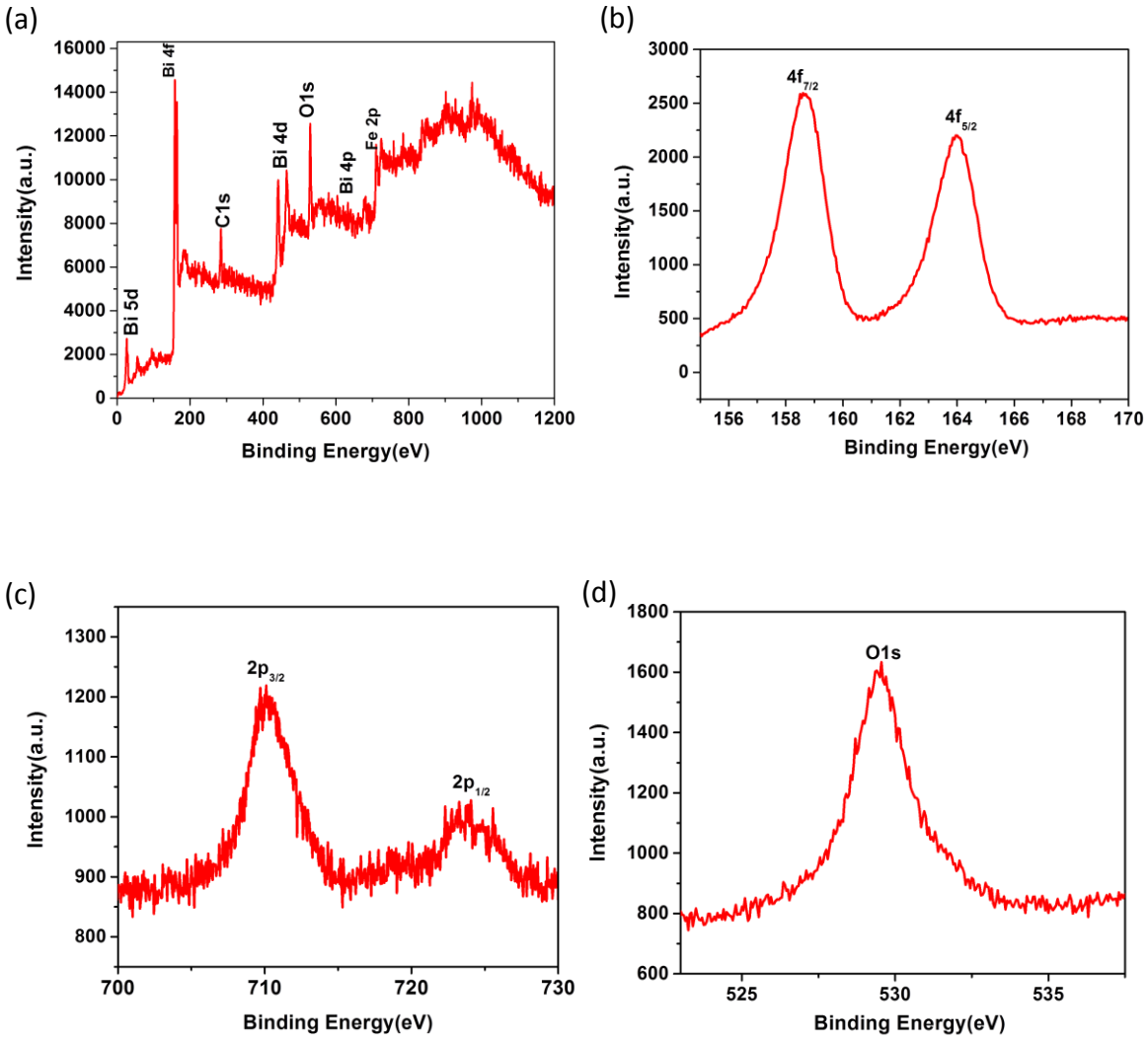

Figure 6.6: XPS spectra of $BiFeO_3$ showcasing (a) Survey scan, Elemental scan of (b) Bismuth, (c) Iron, and (d) Oxygen.

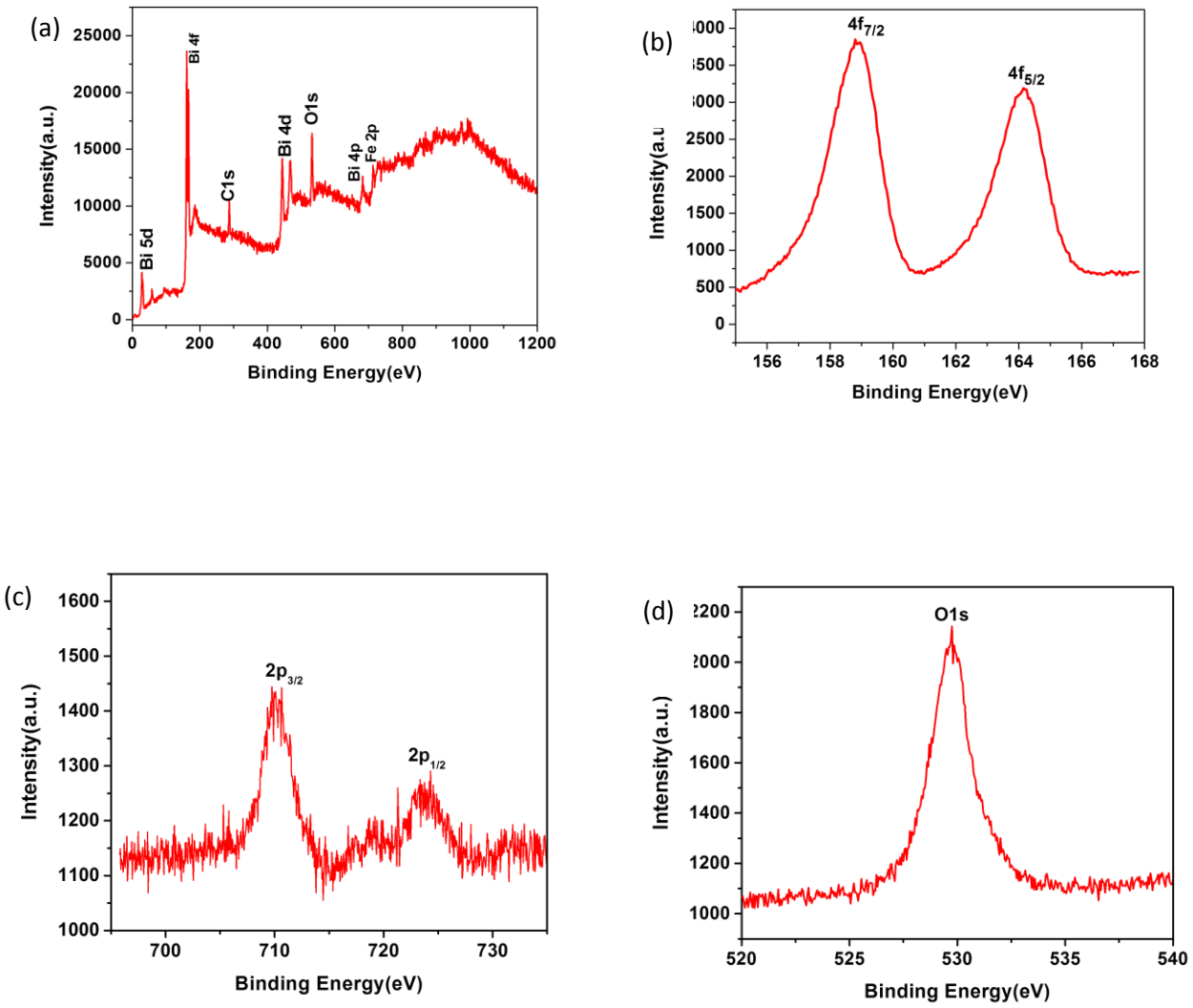

Figure 6.7: XPS spectra of $Bi_2Fe_4O_9$ showcasing (a) Survey scan, Elemental scan of (b) Bismuth, (c) Iron, and (d) Oxygen.

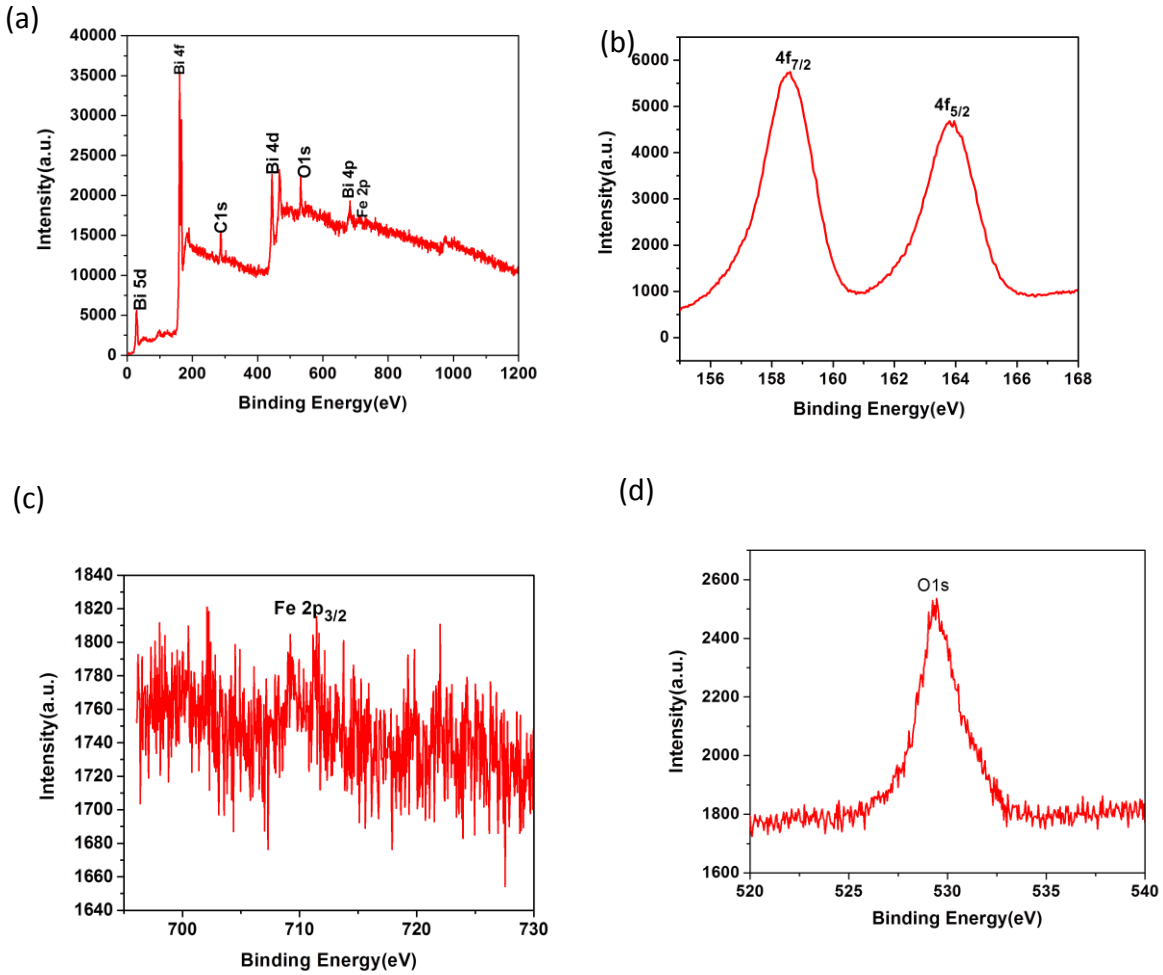

Figure 6.8: XPS spectra of $Bi_{25}FeO_{40}$ showcasing (a) Survey scan, Elemental scan of (b) Bismuth, (c) Iron, and (d) Oxygen

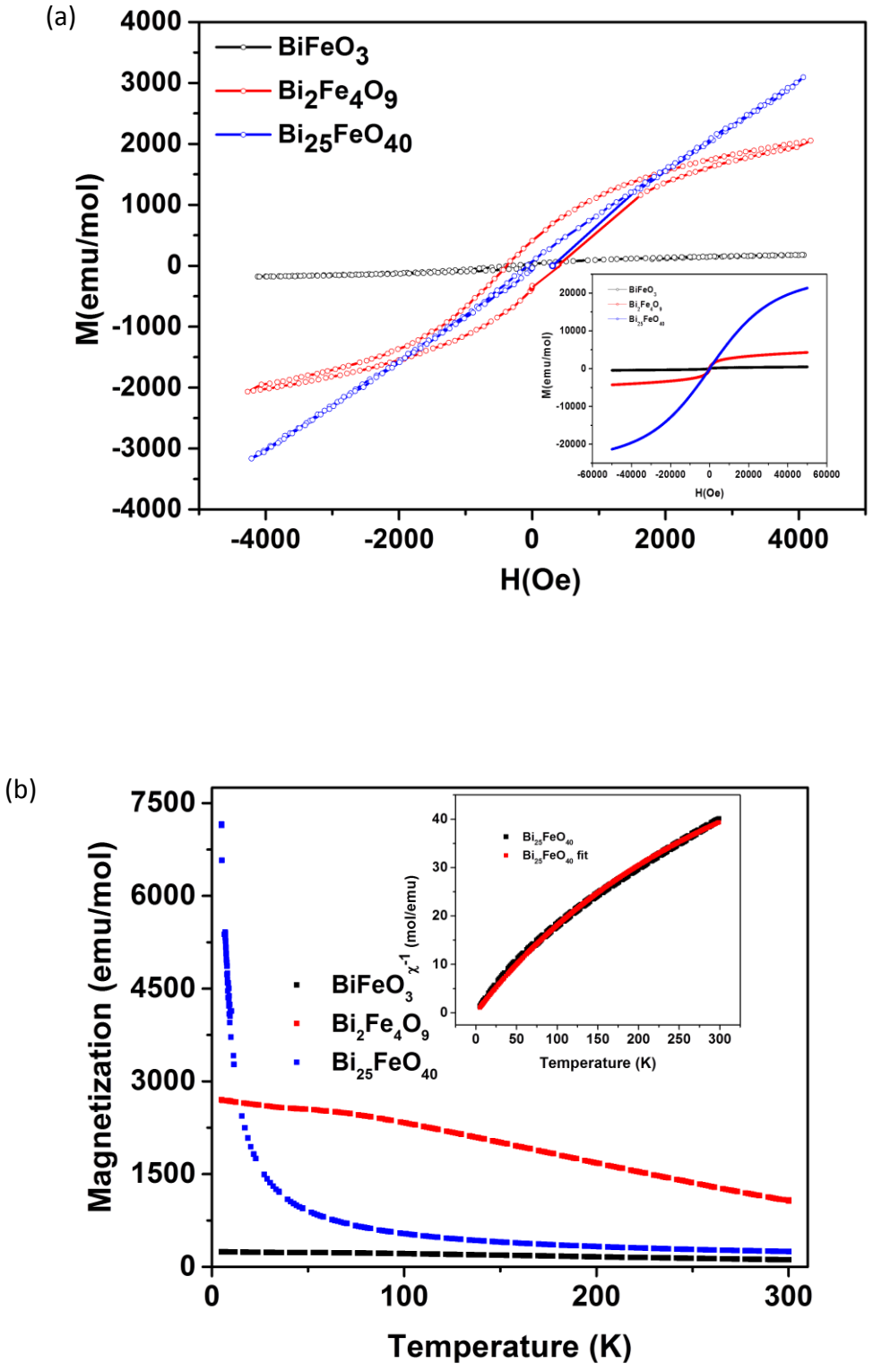

Figure 6.9: (a) Magnetic hysteresis loops at 5 K. The inset shows the high-field behavior. (b) Temperature dependence of the magnetization at 10 kOe. The inset shows the variation of inverse susceptibility with temperature for $Bi_{25}FeO_{40}$ and the corresponding fit to the modified Curie law.

Oxygen Evolution Performance of the oxides

Electrochemical water oxidation activity of the Bi-Fe-O systems was studied under two different conditions. In the first method, as-synthesized oxides were used to fabricate the electrodes whereas, in the second, the prepared working electrode was polarized by the corona poling technique before testing.

As-prepared working electrode

Electrochemical water oxidation activity of as-prepared samples (figure 6.10) yielded average current densities at 1.9 V vs RHE (scan rate: 10 mV/s) of 3.7, 8.1, and 1.2 mA/cm^2 for $BiFeO_3$, $Bi_2Fe_4O_{9,}$ and $Bi_{25}FeO_{40}$ respectively. To check the effect of scan rate on the trend observed for the performance of the oxides towards OER, LSV studies were also carried out at 2 and 5 mV/s (figure 6.11 a-c). It was observed that though the current densities decreased with a decrease in the scan rate, the trend of the three oxides towards OER was unaffected. The overpotential for the three oxides was calculated at 1 mA/cm^2 and was found to be 515 mV, 460 mV, and 640 mV for $BiFeO_3$, $Bi_2Fe_4O_{9,}$ and $Bi_{25}FeO_{40}$ respectively.

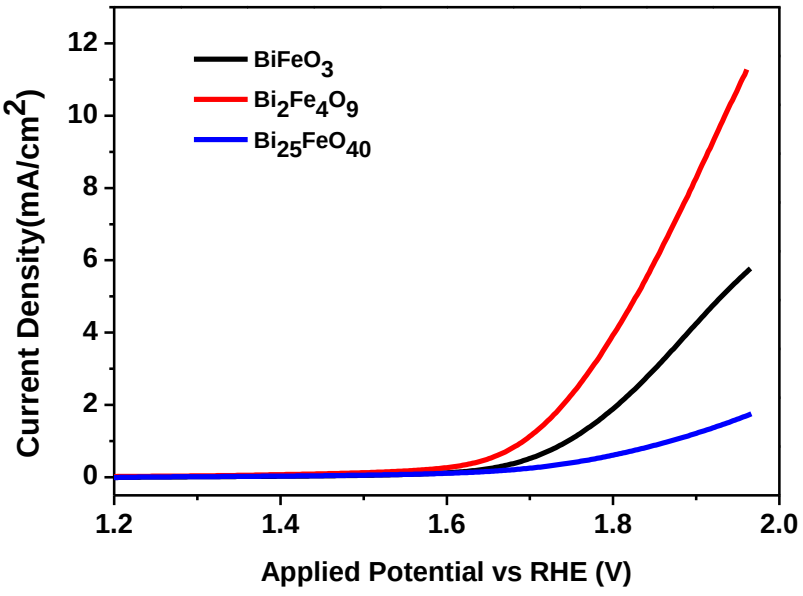

Figure 6.10: OER performance of $BiFeO_3$, $Bi_2Fe_4O_{9,}$ and $Bi_{25}FeO_{40}$.

(a)

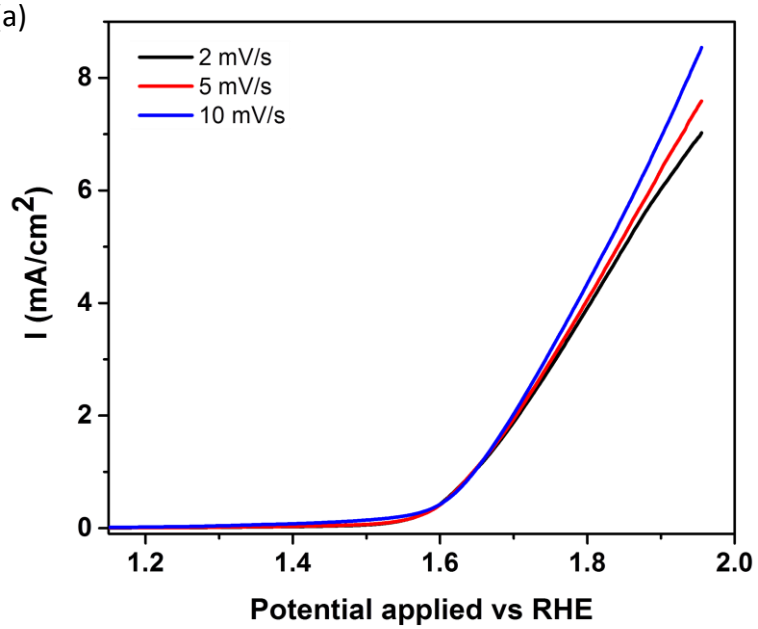
2 mV/s
5 mV/s
10 mV/s
I (mA/cm2)
0
2
4
6
8
1.2
1.4
1.6
1.8
2.0
Potential applied vs RHE

(b)

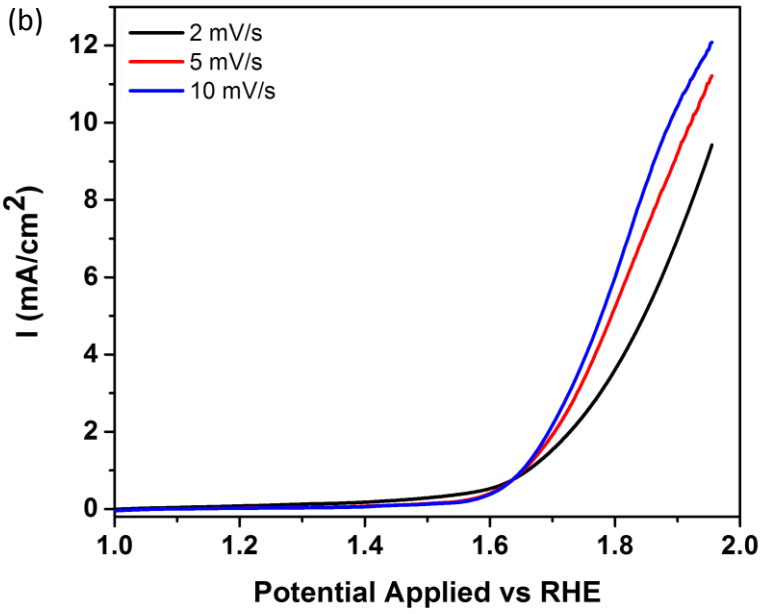
2 mV/s
5 mV/s
10 mV/s
I (mA/cm2)
0
2
4
6
8
10
12
1.0
1.2
1.4
1.6
1.8
2.0
Potential Applied vs RHE

(c)

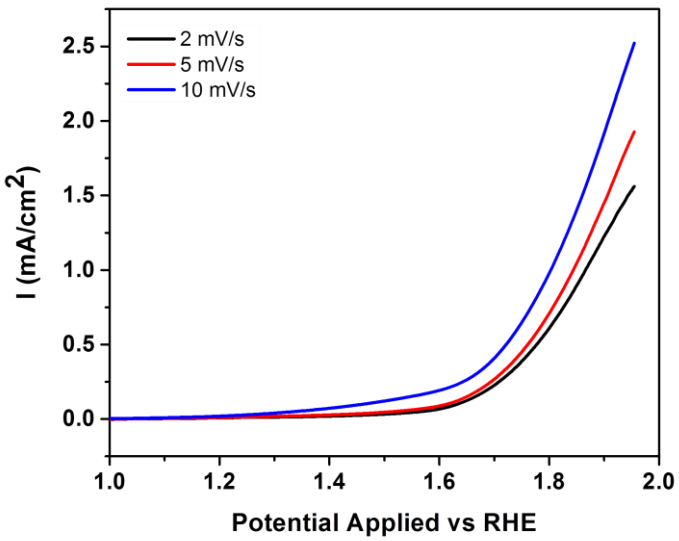

Figure 6.11: LSV curves of (a) $BiFeO_3$, (b) $Bi_2Fe_4O_9$ and (c) $Bi_{25}FeO_{40}$ catalyst at different scan rates (2, 5 and 10 mV/s).

Electrochemical impedance studies were carried out to investigate charge transfer. Figure 6.12 shows the Nyquist plot for the oxides. The curve was fit to an equivalent circuit (inset of figure 6.12) based on the charge transfer resistance R_{ct}, solution resistance $R_{s,}$ and a constant phase element with impedance

$$Z = \frac{Z_0}{(i\omega)^n} \tag{6.5}$$

where Z_0 is a constant, $0 < n < 1$, $i = \sqrt{-1}$, and ω is the angular frequency of the applied potential (Table 6.2).

Table 6.2: Parameters obtained from Nyquist plot (figure 6.12)

Sample	**R_{ct} (Ω)**	**R_s (Ω)**	**Z_o(CPE)**	**n (CPE)**	**C_{dl} (μF/cm^2)**
$BiFeO_3$	1820	3.5	375	0.82	174
$Bi_2Fe_4O_9$	603	3.90	775	0.79	454
$Bi_{25}FeO_{40}$	4160	3.94	522	0.78	286

R_{ct}, which originates from the ionic and electronic resistance across the electrode-electrolyte interface was found to be minimum for $Bi_2Fe_4O_9$ followed by $BiFeO_3$ and $Bi_{25}FeO_{40}$. The double-layer capacitance is calculated using the following equation:

$$C_{dl} = \frac{\left(\frac{Z_0}{Rs^{n-1}}\right)^{1/n}}{S} \tag{6.6}$$

where S is the area of the external surface of the electrode (0.5 cm^2)

It was observed that the order of the value for C_{dl} was $Bi_2Fe_4O_9$> $Bi_{25}FeO_{40}$>$BiFeO_3$(table 6.2). It has been reported [28] that the C_{dl} is directly proportional to electrochemical active surface area (ECSA). Thus, a higher value of C_{dl} (ECSA) can relate to a higher value of current density since ECSA is a measure of the number of electrochemically active sites per unit area.

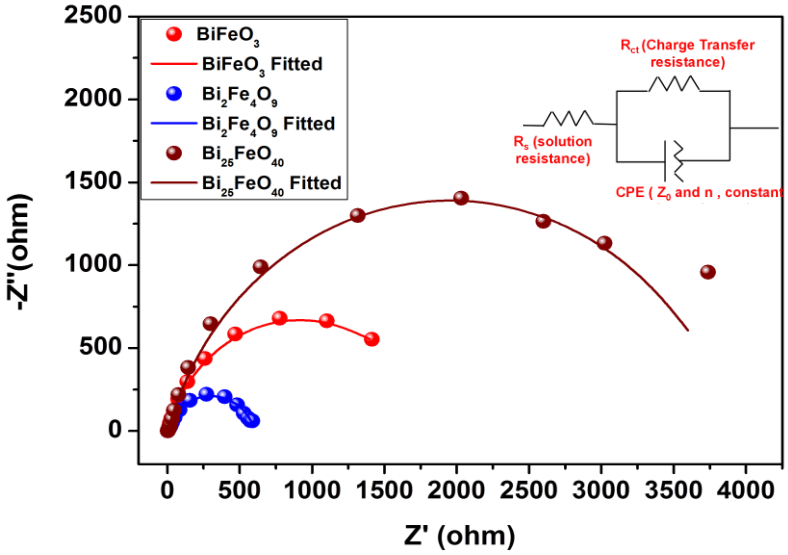

Figure 6.12: Nyquist plot for the oxides $BiFeO_3$, $Bi_2Fe_4O_9$, and $Bi_{25}FeO_{40}$ respectively.

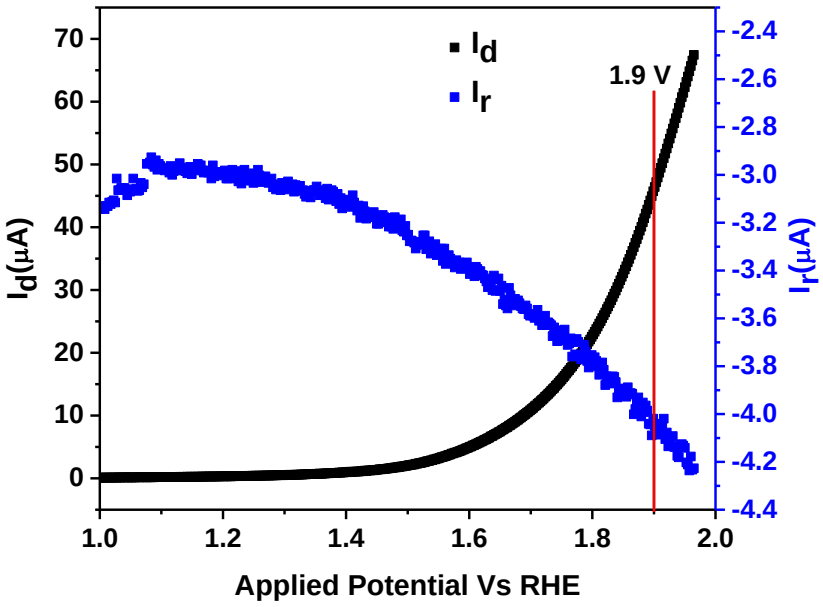

Figure 6.13: OER at the $Bi_2Fe_4O_9$ /GC disk electrode in N_2-saturated 0.1 M KOH and Pt ring current (held at 0.4 V vs. RHE) due to oxygen reduction as a function of disk potential.

The faradic efficiency was calculated for $Bi_2Fe_4O_9$, showcasing the lowest overpotential value in comparison to the other Bi-Fe-O-based catalysts. The disk and ring current at 1.9V vs RHE were found to be 46.3 µA and 4.0 µA respectively (Figure 6.13). The faradaic efficiency was calculated as 70.1% for $Bi_2Fe_4O_9$.

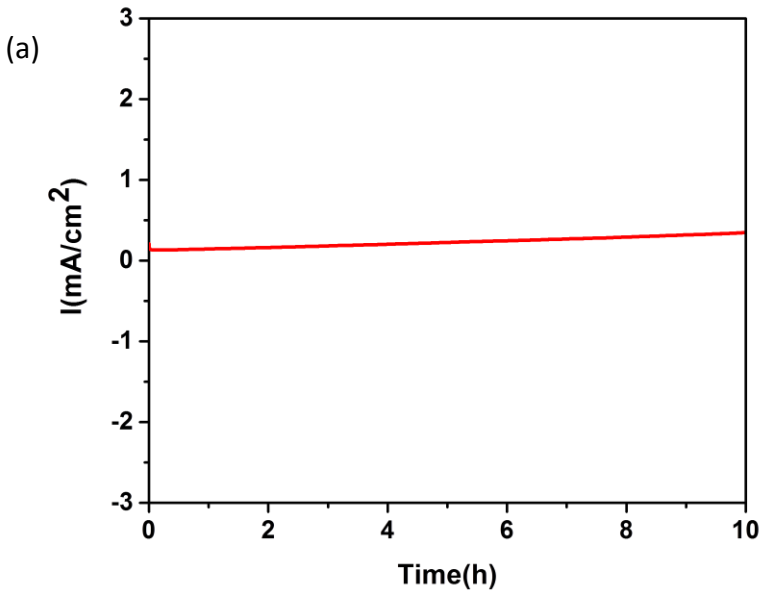

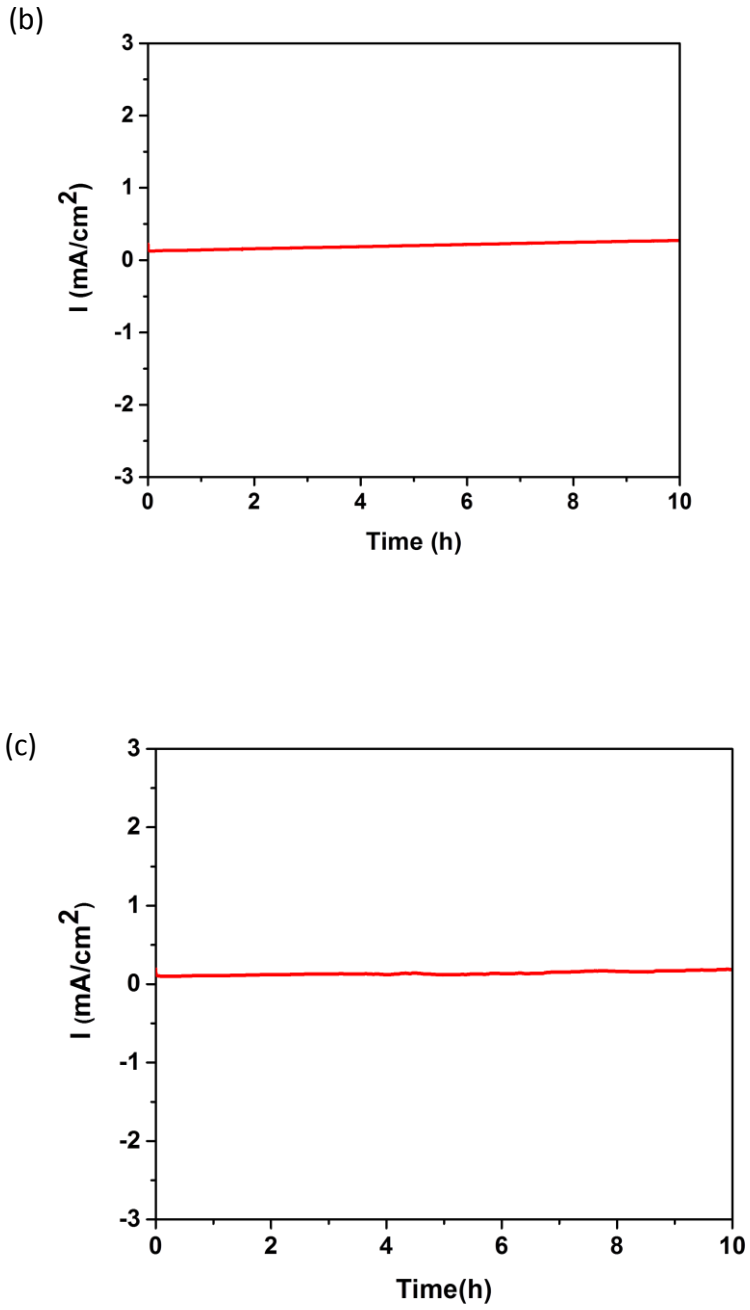

Figure 6.14: Stability curves of (a) $BiFeO_3$, (b) $Bi_2Fe_4O_9$ and (c) $Bi_{25}FeO_{40}$ during electrochemical OER at 1.5 V vs. RHE

The stability of the catalysts was checked for 10 hours at 1.5 V vs RHE. The catalysts were found to be stable for 10 hours during continuous measurement under alkaline conditions (figure 6.14a-c).

Based on the above values of current densities, overpotential, and charge transfer resistance, it was observed that the performance of $Bi_2Fe_4O_9$ was highest amongst the three Bi-Fe-O systems. This could be attributed to the presence of two types of Fe atoms in the unit cell; one forming FeO_6 octahedra and the other kind forming FeO_4 tetrahedra [32]. In mullite structure ($Bi_2M_4O_9$; M: Al^{3+}, Ga^{3+}, Fe^{3+}), there are MO_6 octahedra chains that are interconnected with two MO_4 tetrahedra through a common oxygen atom [33-34]. We have carried out Reitveld refinement for all three oxides and the refined atomic coordinates were used to draw their unit cells. From the unit cell structure of the three oxides, it is quite evident that there are FeO_6 octahedra and FeO_4 tetrahedra units in $Bi_2Fe_4O_9$ (mullite structure), which are connected at corner vide a common oxygen atom, as shown in figure 6.15. Thus, based on earlier reports from literature and through Reitveld refinement studies used for drawing the unit cell structure of the oxides, it can be deciphered that $Bi_2Fe_4O_9$ contains $Fe_{(oct)}$-O-$Fe_{(td)}$ linkages. The increased performance of $Bi_2Fe_4O_9$ towards OER can be correlated to the spinel structures, which are also known to be effective for OER [35]. In spinel structure, $M_{(oct)}$-O-$M_{(td)}$, linkages are present and it has been reported [35] that there occurs a competition of covalency between $M_{(oct)}$-O and $M_{(td)}$-O bond, making one of the weak. This weak bond in $M_{(oct)}$-O-$M_{(td)}$ framework breaks under the bias applied during OER, thus resulting in the formation of M-O and M- units. These M- units are exposed metal sites that act as active sites for the adsorption of OH^- ions present in the medium. The M-OH moieties, formed as a result of covalency competition, formation of M- units, and subsequent adsorption of OH^- ions, become actively involved in OER, thus attributing to the higher efficiency of spinel oxide for OER. Though there is no direct evidence of the relation of $Fe_{(oct)}$-O-$Fe_{(td)}$ linkages present in $Bi_2Fe_4O_9$ and the performance towards electrocatalytic OER, it can be correlated based on the presence of such linkages in spinel structure and their high activity towards OER [35]. It is thus, possible that in $Bi_2Fe_4O_9$ the performance of the oxide towards OER is high amongst all the Bi-Fe-O systems studied here, due to the presence of $Fe_{(oct)}$-O-$Fe_{(td)}$ linkages (figure 6.16), which could probably result in covalency completion, formation of Fe- units and subsequent adsorption of OH^- ions. In addition to the $Fe_{(oct)}$-O-$Fe_{(td)}$ linkages, the plate-like morphology could also have contributed to the increased ECSA, as observed from the value of C_{dl}.

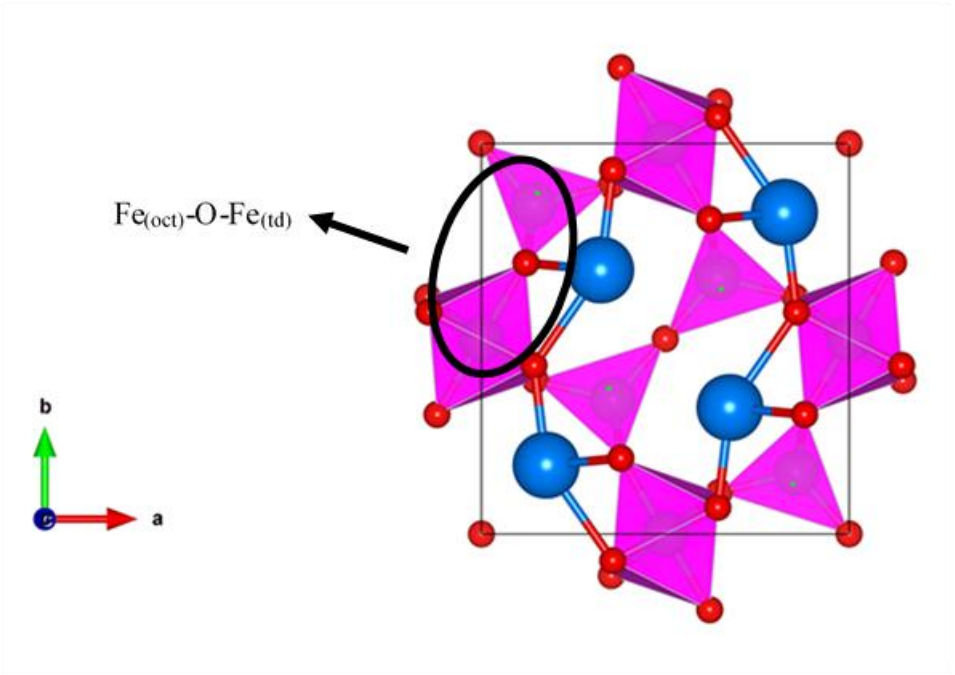

Figure 6.15: Unit cell structure of $Bi_2Fe_4O_9$ showcasing the presence of $Fe_{(oct)}$-O-$Fe_{(td)}$ linkages. (Blue, Green, and Red color are used for depicting Bi, Fe, and O atom respectively. FeO_6 octahedron and FeO_4 tetrahedron is depicted by pink color)

To check the stability of the catalyst after OER, PXRD, and FESEM studies were carried out on the samples obtained after completing the reactions. No change in the crystal structure was observed for the three oxides as observed from the PXRD pattern (figure 6.16 a-c). FESEM studies on the graphite strip containing the catalyst mixed with Nafion are shown in figure 6.17 a-c. The morphology of the catalysts was unaffected, however, agglomeration due to the presence of Nafion can be observed.

(a)

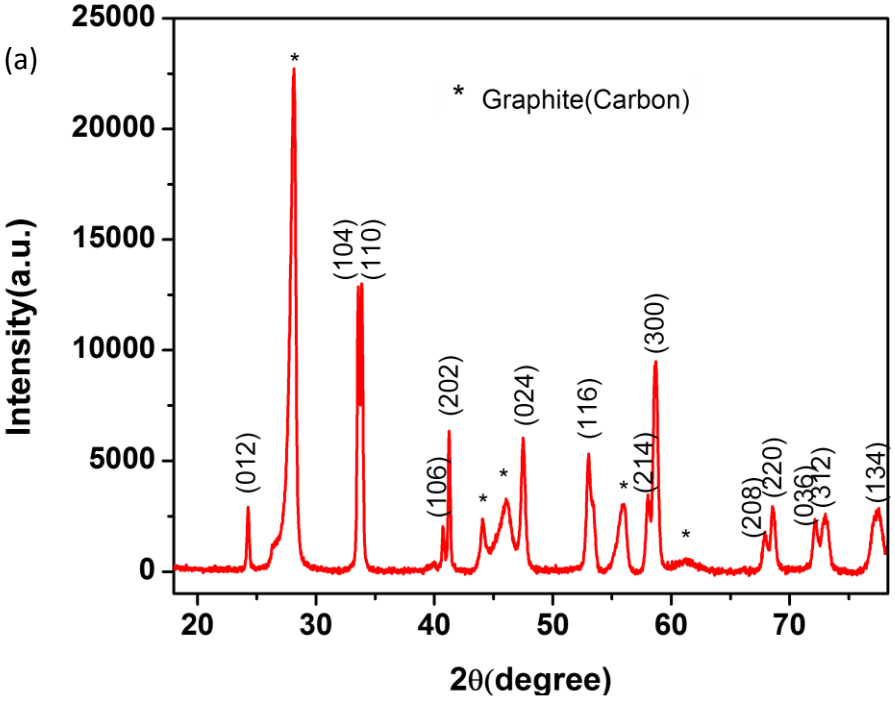
* Graphite(Carbon)
Intensity(a.u.)
2θ(degree)
(012)
(104)
(110)
(106)
(202)
(024)
(116)
(214)
(300)
(208)
(220)
(036)
(312)
(134)

(b)

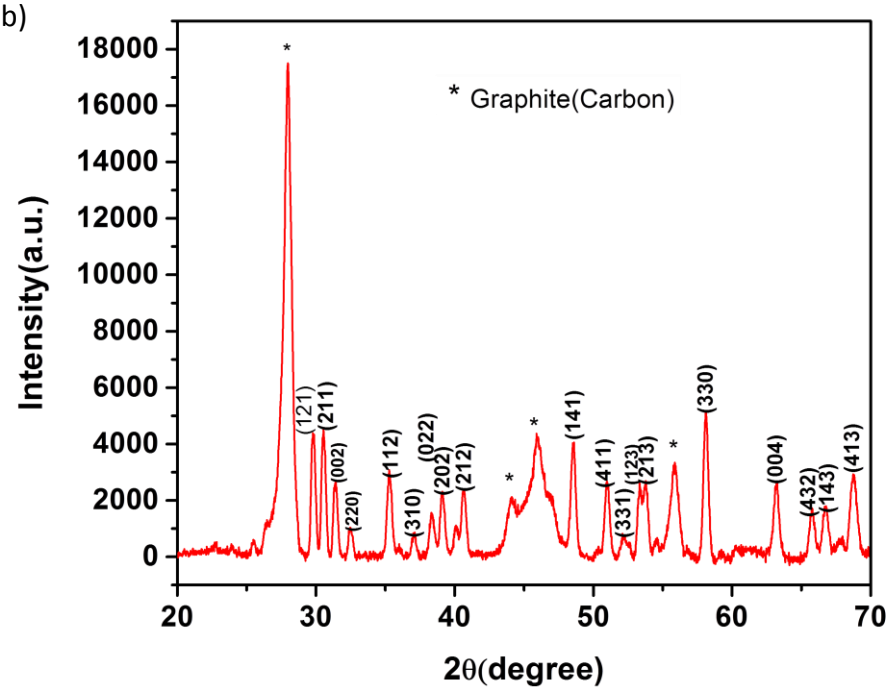
* Graphite(Carbon)
Intensity(a.u.)
2θ(degree)
(121)
(211)
(002)
(220)
(112)
(310)
(022)
(202)
(212)
(141)
(411)
(331)
(123)
(213)
(330)
(004)
(432)
(143)
(413)

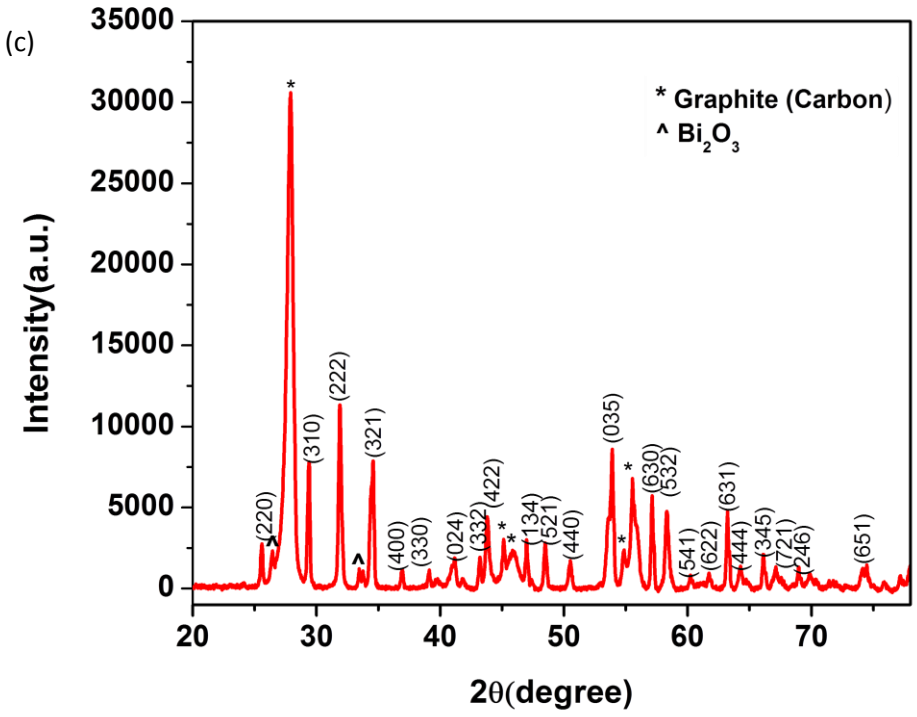

Figure 6.16 PXRD pattern for (a) $BiFeO_3$, (b) $Bi_2Fe_4O_9$, and (c) $Bi_{25}FeO_{40}$ catalysts after performing OER.

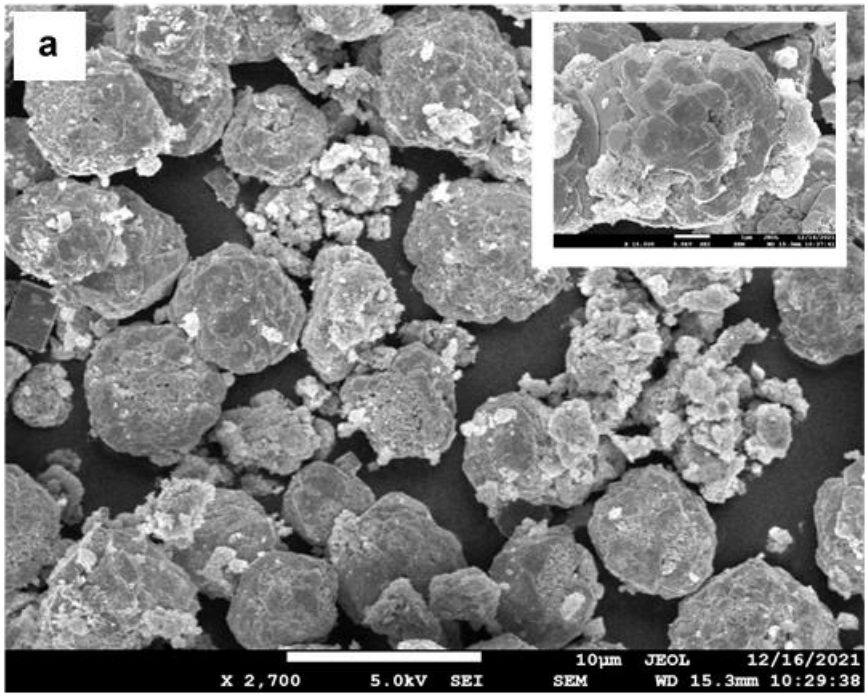

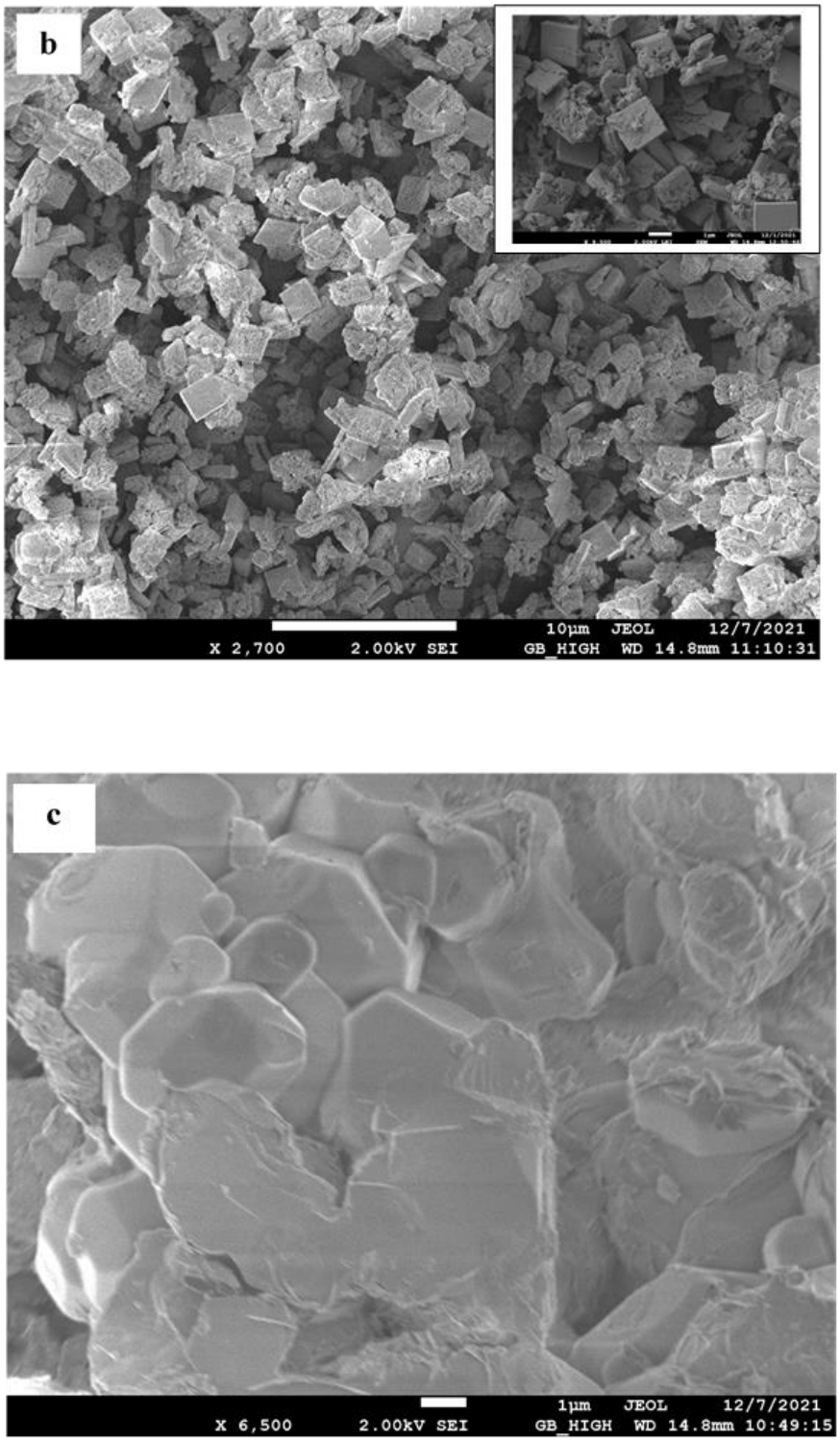

Figure 6.17: FESEM images for (a) $BiFeO_3$, (b) $Bi_2Fe_4O_9$, and (c) $Bi_{25}FeO_{40}$ catalysts after performing OER. Inset in (a) and (b) shows high magnification images.

Polarized working electrode

In polarized semiconductors (polarized by poling), when dipoles are aligned, the polar surfaces attract more charged ions from the outside environment i.e., (electrolyte). For instance, when the semiconductor is positively poled, negative ions are attracted towards the surface and vice-versa. In the case of electrochemical OER, positively poled surfaces lead to adsorption of more $O_2^{\bullet}$ radicals and OH^- ions, thereby enhancing the performance of the catalyst [26-28]. To see the effect of polarization on three different structures of the Bi-Fe-O system, electrochemical water oxidation activity of polarized samples was investigated through LSV curves (scan rate: 10 mV/s) in 0.1M KOH solution. The average current density at 1.9 V vs RHE was observed to be 4.7 mA/cm^2, 8.3 mA/cm^{2,} and 4.9 mA/cm^2 for polarized $BiFeO_3$, $Bi_2Fe_4O_{9,}$ and $Bi_{25}FeO_{40}$ respectively (figure 6.18a). As compared to the as-grown sample, the current density increased by a factor of four for the poled $Bi_{25}FeO_{40}$ while the other two phases showed little difference between as-grown and poled oxides (figure 6.18a). The overpotential for the polarized working electrodes at 1 mA/cm^2 was found to be 510 mV, 430 mV, and 420 mV for polarized $BiFeO_3$, $Bi_2Fe_4O_{9,}$ and $Bi_{25}FeO_{40}$ respectively (figure 6.18b). A significant decrease in the overpotential by 220 mV was observed for the poled $Bi_{25}FeO_{40}$ in comparison to that observed for poled $BiFeO_3$ (by 5 mV) and $Bi_2Fe_4O_9$ (by 30 mV). Further, to analyse, the behavior of the polarized oxides on the electrochemical water oxidation, we looked at the charge transfer abilities of these polarized oxides and compared them with those observed for the as-prepared oxides (figure 6.18 c-e, Table 6.3).

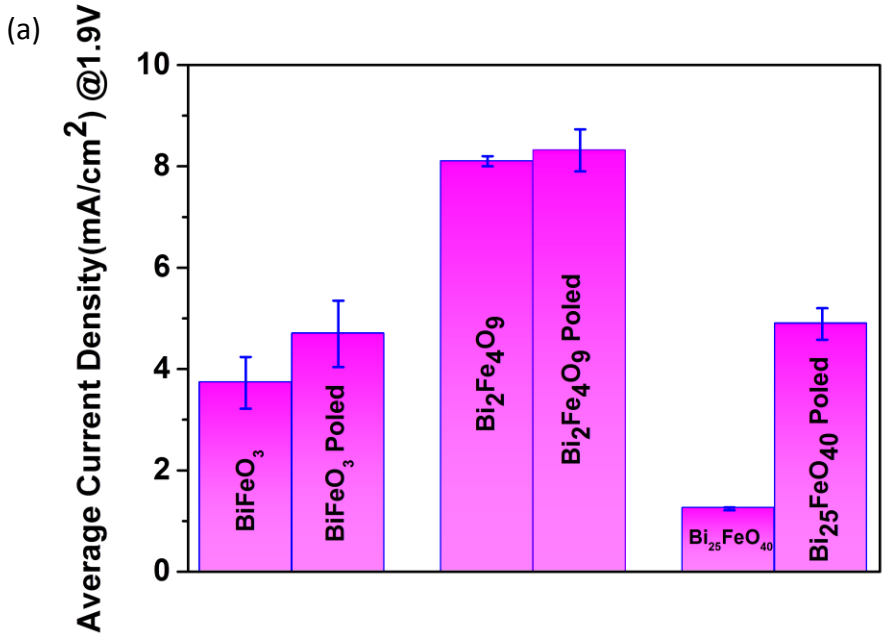

(b)

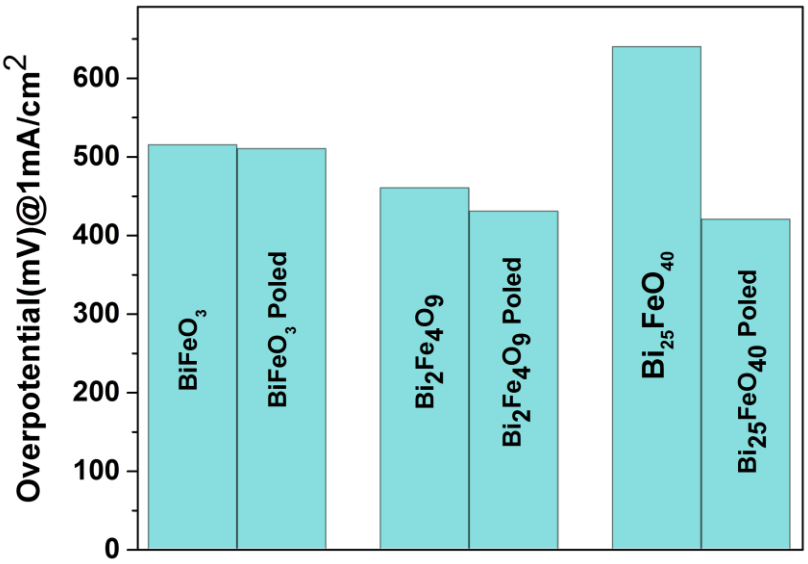
Overpotential(mV)@1mA/cm2
0
100
200
300
400
500
600
BiFeO3
BiFeO3 Poled
Bi2Fe4O9
Bi2Fe4O9 Poled
Bi25FeO40
Bi25FeO40 Poled

(c)

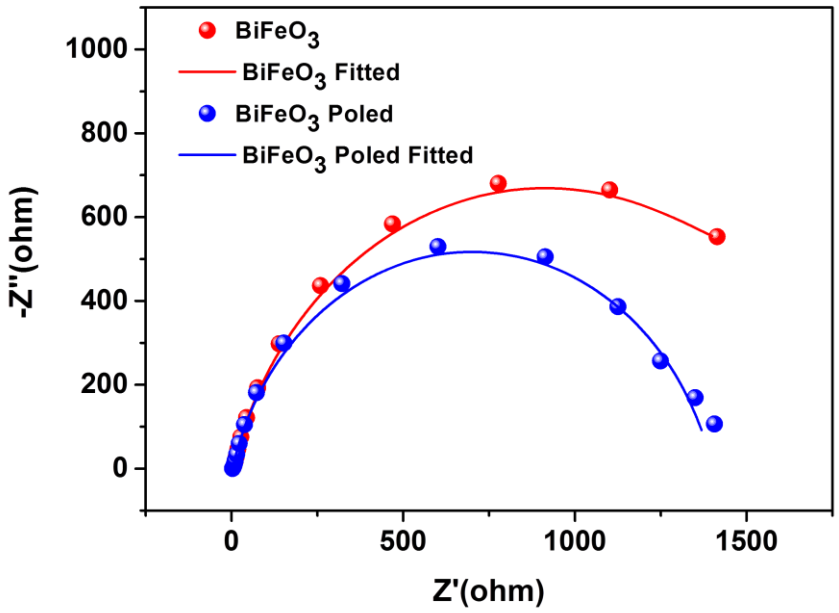
BiFeO3
BiFeO3 Fitted
BiFeO3 Poled
BiFeO3 Poled Fitted
-Z''(ohm)
0
200
400
600
800
1000
0
500
1000
1500
Z'(ohm)

(d)

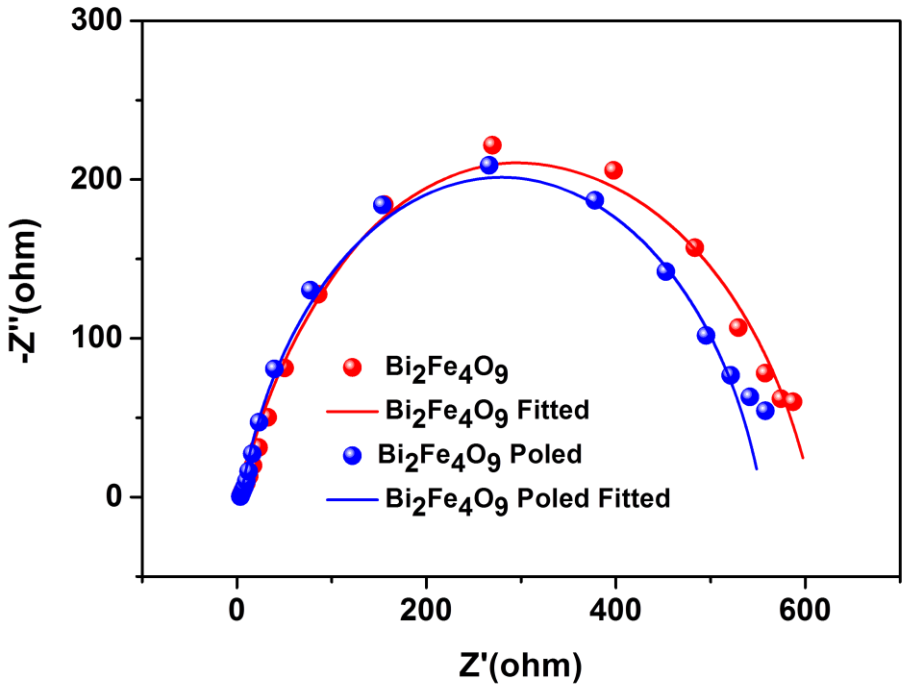

(e)

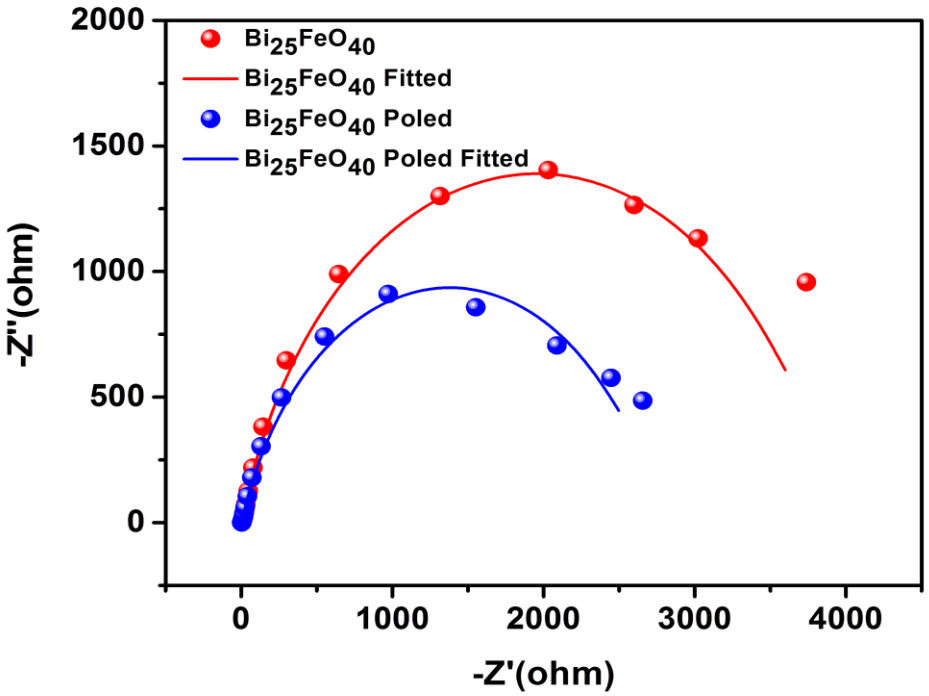

Figure 6.18: Comparison of (a) average current densities and (b) overpotential obtained for $BiFeO_3$, $Bi_2Fe_4O_9$, and $Bi_{25}FeO_{40}$ before and after electrical polarization using corona poling. Nyquist plot of (c) $BiFeO_3$, (d) $Bi_2Fe_4O_9$ and (e) $Bi_{25}FeO_{40}$ before and after electrical polarization using corona poling.

From Mott-Schottky plots (figure 6.19 a-c), the flat band potential (indication of band bending) was calculated to be 2.46 V, 1.70 V, and 2.73 V for $BiFeO_3$, $Bi_2Fe_4O_9$, and $Bi_{25}FeO_{40}$ respectively. The flat band potential (figure 6.19 a-c) was found to be 1.91 V, 1.75 V, and 2.18 V for $BiFeO_3$, $Bi_2Fe_4O_9$, and $Bi_{25}FeO_{40}$ respectively for electrically poled samples. It was observed for $BiFeO_3$ and $Bi_{25}FeO_{40}$ that the flat band potential decreased by ~20%, R_{ct} decreased by ~20% and 30% respectively after poling. C_{dl} was found to increase by ~60% for $BiFeO_3$ and ~25% for $Bi_{25}FeO_{40}$. On the other hand, the changes in the values for $Bi_2Fe_4O_9$ were rather small. Thus, changes in $Bi_{25}FeO_{40}$ are the only ones significant and likely have to do with the surface modification that took place during corona poling. Though there are not many studies available in the literature, we presume that the significant increase in the OER activity of $Bi_{25}FeO_{40}$ could be due to the presence of a large number of Bi^{3+} ions with $6s^2$ lone pair (responsible for ferroelectric behavior in $BiFeO_3$) which could have contributed to increasing the electroconductivity and ECSA (from C_{dl}) on polarization.

(a)

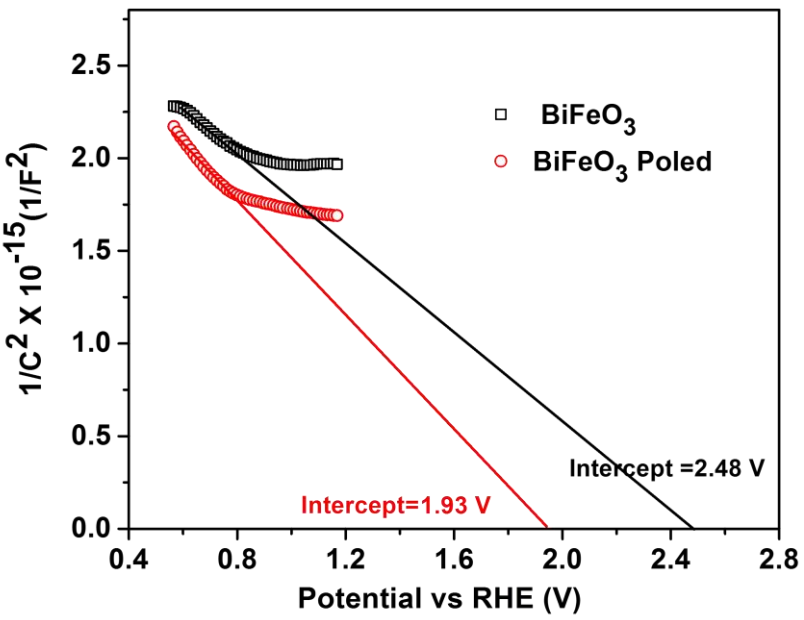

(b)

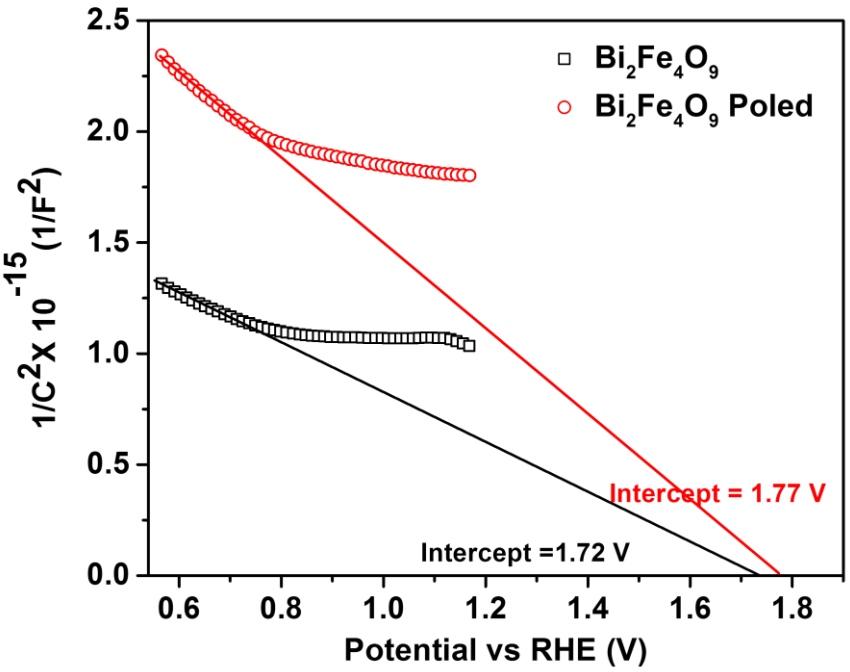

(c)

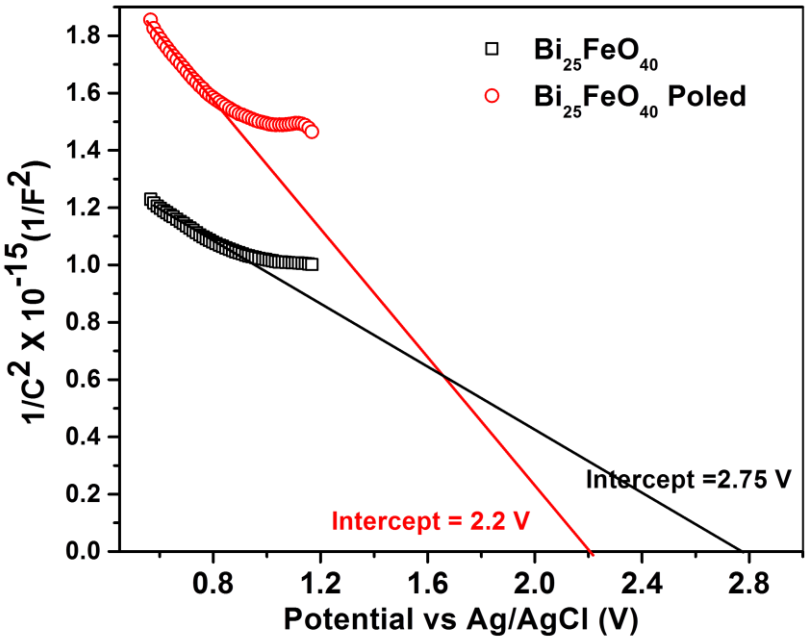

Figure 6.19: Mott Schottky plot of (a) $BiFeO_3$, (b) $Bi_2Fe_4O_9$, and (c) $Bi_{25}FeO_{40}$ before and after electrical polarization using corona poling for obtaining flat band potential (V_{fb}).

Table 6.3: Parameters obtained from Nyquist plot.

Sample	R_{ct} (Ω)	R_s (Ω)	Z_o(CPE)	n (CPE)	C_{dl} (μF/cm^2)
$BiFeO_3$	1820	3.5	375	0.82	174
$BiFeO_3$ Poled	1470	3.32	572	0.83	283
$Bi_2Fe_4O_9$	603	3.90	775	0.79	454
$Bi_2Fe_4O_9$ Poled	563	4.00	797	0.78	481
$Bi_{25}FeO_{40}$	4160	3.94	522	0.78	286
$Bi_{25}FeO_{40}$ Poled	2750	3.51	641	0.78	356

Thus, from our studies, we could observe that there is a clear dependence of the crystal structure (of the oxides in the Bi-Fe-O system) and electrical polarization on OER. Few approaches for designing highly efficient catalysts for OER are to increase the number of active sites on the material, increase their electroconductivity, and increase the rate of the adsorption of the reactant on the surface of the catalyst which facilitates the transfer of charge between the electrode and the reactants. Proper choice of the crystal structure of the catalyst belonging to a set of ternary systems and application of electrical polarization could assist in achieving the parameters desired for designing of efficient catalyst for OER.

6.4 Conclusion :

In summary, we have investigated electrochemical oxygen evolution activity within the Bi-Fe-O system for three phases viz. $BiFeO_3$, $Bi_2Fe_4O_9$, and $Bi_{25}FeO_{40}$. Among the studied materials, $Bi_2Fe_4O_9$ with orthorhombic structure was found to exhibit better OER activity as observed from the current density. Further analysis showed that the oxide possessed the lowest charge transfer resistance and the highest double-layer capacitance. The performance of $Bi_2Fe_4O_9$ was attributed to the presence of Fe_{oct}-O-Fe_{td} linkages and plate-like morphology. It was interesting to observe that the OER activity of $Bi_{25}FeO_{40}$ was increased by a factor of 4 after electrical polarization, which, was the largest enhancement observed among the three oxides. This work demonstrated that the choice of crystal structure within different sets of oxides in a ternary system (showcased here with Bi-Fe-O system as an example) could be an efficient way for the development of a highly active catalyst for oxygen evolution reaction. In addition to the crystal structure, the application of electric polarization could be a constructive strategy to improve the catalytic activity for future energy conversion devices.

Acknowledgments

I would like to thank Prof. K.V. Ramanujachary and Prof. Samuel E. Lofland for the magnetic studies in this work.

This Work has been published as "**Aditi Vijay**, K.V. Ramanujachary, Samuel E. Lofland, Sonalika Vaidya*, Role of crystal structure and electrical polarization of an electrocatalyst in enhancing oxygen evolution performance: Bi-Fe-O system as a case study Electrochimica Acta, Volume 407,2022,139887".

6.5 References:

1. Suen, N.-T.; Hung, S.-F.; Quan, Q.; Zhang, N.; Xu, Y.-J.; Chen, H. M., Electrocatalysis for the oxygen evolution reaction: recent development and future perspectives. *Chemical Society Reviews* **2017,** *46* (2), 337-365.
2. Wang, V. C. C., Exploring the kinetic and thermodynamic aspects of four-electron electrochemical reactions: electrocatalysis of oxygen evolution by metal oxides and biological systems. *Physical Chemistry Chemical Physics* **2016,** *18* (32), 22364-22372.
3. Feng, C.; Faheem, M. B.; Fu, J.; Xiao, Y.; Li, C.; Li, Y., Fe-Based Electrocatalysts for Oxygen Evolution Reaction: Progress and Perspectives. *ACS Catalysis* **2020,** *10* (7), 4019-4047.
4. Wu, K.; Chu, F.; Meng, Y.; Edalati, K.; Gao, Q.; Li, W.; Lin, H.-J., Cathodic corrosion activated Fe-based nanoglass as a highly active and stable oxygen evolution catalyst for water splitting. *Journal of Materials Chemistry A* **2021,** *9* (20), 12152-12160.
5. Gao, R.; Yan, D., Recent Development of Ni/Fe-Based Micro/Nanostructures toward Photo/Electrochemical Water Oxidation. *Advanced Energy Materials* **2020,** *10* (11), Article 1900954.
6. Gao, R.; Zhang, H.; Yan, D., Iron diselenide nanoplatelets: Stable and efficient water-electrolysis catalysts. *Nano Energy* **2017,** *31*, 90-95.
7. Zha, M.; Pei, C.; Wang, Q.; Hu, G.; Feng, L., Electrochemical oxygen evolution reaction efficiently boosted by selective fluoridation of $FeNi_3$ alloy/oxide hybrid. *Journal of Energy Chemistry* **2020,** *47*, 166-171.
8. Osgood, H.; Devaguptapu, S. V.; Xu, H.; Cho, J.; Wu, G., Transition metal (Fe, Co, Ni, and Mn) oxides for oxygen reduction and evolution bifunctional catalysts in alkaline media. *Nano Today* **2016,** *11* (5), 601-625.
9. Gao, R.; Yan, D., Fast formation of single-unit-cell-thick and defect-rich layered double hydroxide nanosheets with highly enhanced oxygen evolution reaction for water splitting. *Nano Research* **2018,** *11* (4), 1883-1894.
10. Gao, R.; Zhu, J.; Yan, D., Transition metal-based layered double hydroxides for photo(electro)chemical water splitting: a mini review. *Nanoscale* **2021,** *13* (32), 13593-13603.
11. Elakkiya, R.; Maduraiveeran, G., Two-Dimensional Earth-Abundant Transition Metal Oxides Nanomaterials: Synthesis and Application in Electrochemical Oxygen Evolution Reaction. *Langmuir* **2020,** *36* (17), 4728-4736.

12. Chen, M.; Lu, S.; Fu, X.-Z.; Luo, J.-L., Core–Shell Structured NiFeSn@NiFe (Oxy)Hydroxide Nanospheres from an Electrochemical Strategy for Electrocatalytic Oxygen Evolution Reaction. *Advanced Science* **2020,** *7* (10), Article 1903777.

13. Bhanja, P.; Kim, Y.; Paul, B.; Kaneti, Y. V.; Alothman, A. A.; Bhaumik, A.; Yamauchi, Y., Microporous nickel phosphonate derived heteroatom doped nickel oxide and nickel phosphide: Efficient electrocatalysts for oxygen evolution reaction. *Chemical Engineering Journal* **2021,** *405*, Article 126803.

14. Gao, J.; Tao, H.; Liu, B., Progress of Nonprecious-Metal-Based Electrocatalysts for Oxygen Evolution in Acidic Media. *Advanced Materials* **2021,** *33* (31), Article 2003786.

15. Wang, X.; Liu, H.; Li, M.; Li, J.; Lu, Y.; Wang, L.; Wang, Z.; Zhang, X.; Ding, X., Modulation of electronic structure and oxygen vacancies of perovskites $SrCoO_{3-\delta}$ by sulfur doping enables highly active and stable oxygen evolution reaction. *Electrochimica Acta* **2021,** *390*, Article 138872.

16. Wang, C.; Wang, Y.; Yang, H.; Zhang, Y.; Zhao, H.; Wang, Q., Revealing the Role of Electrocatalyst Crystal Structure on Oxygen Evolution Reaction with Nickel as an Example. *Small* **2018,** *14* (40), Article 1802895.

17. Garcés, D.; Soldati, A. L.; Troiani, H.; Montenegro-Hernández, A.; Caneiro, A.; Mogni, L. V., La/Ba-based cobaltites as IT-SOFC cathodes: a discussion about the effect of crystal structure and microstructure on the O_2-reduction reaction. *Electrochimica Acta* **2016,** *215*, 637-646.

18. Hu, J.; Li, S.; Chu, J.; Niu, S.; Wang, J.; Du, Y.; Li, Z.; Han, X.; Xu, P., Understanding the Phase-Induced Electrocatalytic Oxygen Evolution Reaction Activity on FeOOH Nanostructures. *ACS Catalysis* **2019,** *9* (12), 10705-10711.

19. Wang, Z.; Gao, W.; Xu, Q.; Ren, X.; Xu, S.; Zhu, S.; Niu, X.; Li, X.; Zhao, R.; Han, Y.; Li, G.; Wang, Q., Influence of the MnO_2 Phase on Oxygen Evolution Reaction Performance for Low-Loading Iridium Electrocatalysts. *ChemElectroChem* **2021,** *8* (2), 418-424.

20. Gupta, G.; Selvakumar, K.; Lakshminarasimhan, N.; Senthil Kumar, S. M.; Mamlouk, M., The effects of morphology, microstructure and mixed-valent states of MnO_2 on the oxygen evolution reaction activity in alkaline anion exchange membrane water electrolysis. *Journal of Power Sources* **2020,** *461*, Article 228131.

21. Wang, Z.; Li, M.; Liang, C.; Fan, L.; Han, J.; Xiong, Y., Effect of morphology on the oxygen evolution reaction for $La_{0.8}Sr_{0.2}Co_{0.2}Fe_{0.8}O_{3-\delta}$ electrochemical catalyst in alkaline media. *RSC Advances* **2016,** *6* (73), 69251-69256.

22. Antoni, H.; Xia, W.; Masa, J.; Schuhmann, W.; Muhler, M., Tuning the oxidation state of manganese oxide nanoparticles on oxygen- and nitrogen-functionalized carbon nanotubes

for the electrocatalytic oxygen evolution reaction. *Physical Chemistry Chemical Physics* **2017,** *19* (28), 18434-18442.

23. Meng, Y.; Song, W.; Huang, H.; Ren, Z.; Chen, S.-Y.; Suib, S. L., Structure–Property Relationship of Bifunctional MnO_2 Nanostructures: Highly Efficient, Ultra-Stable Electrochemical Water Oxidation and Oxygen Reduction Reaction Catalysts Identified in Alkaline Media. *Journal of the American Chemical Society* **2014,** *136* (32), 11452-11464.
24. Zhang, H.; Guan, D.; Gao, X.; Yu, J.; Chen, G.; Zhou, W.; Shao, Z., Morphology, crystal structure and electronic state one-step co-tuning strategy towards developing superior perovskite electrocatalysts for water oxidation. *Journal of Materials Chemistry A* **2019,** *7* (33), 19228-19233.
25. Li, Y.; Li, J.; Yang, W.; Wang, X., Implementation of ferroelectric materials in photocatalytic and photoelectrochemical water splitting. *Nanoscale Horizons* **2020,** *5* (8), 1174-1187.
26. Kakekhani, A.; Ismail-Beigi, S.; Altman, E. I., Ferroelectrics: A pathway to switchable surface chemistry and catalysis. *Surface Science* **2016,** *650*, 302-316.
27. Kushwaha, H. S.; Halder, A.; Vaish, R., Ferroelectric electrocatalysts: a new class of materials for oxygen evolution reaction with synergistic effect of ferroelectric polarization. *Journal of Materials Science* **2018,** *53* (2), 1414-1423.
28. Li, X.; Liu, H.; Chen, Z.; Wu, Q.; Yu, Z.; Yang, M.; Wang, X.; Cheng, Z.; Fu, Z.; Lu, Y., Enhancing oxygen evolution efficiency of multiferroic oxides by spintronic and ferroelectric polarization regulation. *Nature Communications* **2019,** *10* (1), Article 1409.
29. Anantharaj, S.; Ede, S. R.; Sakthikumar, K.; Karthick, K.; Mishra, S.; Kundu, S., Recent Trends and Perspectives in Electrochemical Water Splitting with an Emphasis on Sulfide, Selenide, and Phosphide Catalysts of Fe, Co, and Ni: A Review. *ACS Catalysis* **2016,** *6* (12), 8069-8097.
30. Wang, X.; Zhang, Y. g.; Wu, Z., Magnetic and optical properties of multiferroic bismuth ferrite nanoparticles by tartaric acid-assisted sol–gel strategy. *Materials Letters* **2010,** *64* (3), 486-488.
31. Singh, A. K.; Kaushik, S. D.; Kumar, B.; Mishra, P. K.; Venimadhav, A.; Siruguri, V.; Patnaik, S., Substantial magnetoelectric coupling near room temperature in $Bi_2Fe_4O_9$. *Applied Physics Letters* **2008,** *92* (13), Article 132910.
32. Nlizeki, N.; Wachi, M., The crystal structures of $Bi_2Mn_4O_{10}$, $Bi_2Al_4O_9$ and $Bi_2Fe_4O_9$. *Zeitschrift für Kristallographie* **1968,** *127* (1-4), 173-187.
33. Sadovnikov, S. I.; Gusev, A. I.; Chukin, A. V.; Rempel, A. A., High-temperature X-ray diffraction and thermal expansion of nanocrystalline and coarse-crystalline acanthite α-

Ag_2S and argentite β-Ag_2S. *Physical Chemistry Chemical Physics* **2016,** *18* (6), 4617-4626.

34. Mangir Murshed, M.; Mendive, C. B.; Curti, M.; Šehović, M.; Friedrich, A.; Fischer, M.; Gesing, T. M., Thermal expansion of mullite-type $Bi_2Al_4O_9$: A study by X-ray diffraction, vibrational spectroscopy and density functional theory. *Journal of Solid State Chemistry* **2015,** *229*, 87-96.

35. Sun, Y.; Liao, H.; Wang, J.; Chen, B.; Sun, S.; Ong, S. J. H.; Xi, S.; Diao, C.; Du, Y.; Wang, J.-O.; Breese, M. B. H.; Li, S.; Zhang, H.; Xu, Z. J., Covalency competition dominates the water oxidation structure–activity relationship on spinel oxides. *Nature Catalysis* **2020,** *3* (7), 554-563.

Chapter 7

Conclusion and Future Prospects

Chapter 7

Conclusion and Future Prospects

7.1 Conclusion:

The main aim of the thesis was to investigate the relationship between various structural parameters and the catalytic (photo-and electrocatalytic) activity of the metal oxide catalyst. The role of size, morphology, exposed facets, crystal structure, electric polarization and oriented assembly along a preferred crystalline plane was successfully discussed. The experimental finding of the thesis are summarised below:

In the second chapter, we have discussed the role of ionic flux on the exposed surfaces of ZnO and established their correlation with photocatalytic dye degradation activity. We have synthesized ZnO through the decomposition of zinc oxalate in the absence and presence of various fluxes such as NaCl, KCl, NaCl-KCl, and Na_2SO_4. To find exposed surfaces of the ZnO synthesized in the presence and absence of various fluxes, the value of the texture coefficient of four highly intense planes was calculated from PXRD data. The presence of flux (NaCl, KCl, a mixture of NaCl–KCl, and Na_2SO_4) during decomposition of the oxalate precursor led to the preferential growth of $(11\bar{2}0)$ planes as compared to $(10\bar{1}0)$ surface. The value of texture coefficient was found to be higher for the $(11\bar{2}0)$ plane when the decomposition was carried out in the presence of a mixture of NaCl and KCl in comparison to the ZnO synthesized in the presence of NaCl and KCl as flux. We observed a decrease in the value of texture coefficient for the $(11\bar{2}0)$ plane when Na_2SO_4 was used as a flux, which was similar to the value obtained for ZnO synthesized in the absence of flux. The observations from the analysis of texture coefficient were correlated with the photocatalytic degradation of Rhodamine B dye. The photocatalytic activity of ZnO for the degradation of Rhodamine B dye follows the order: No Flux > Na_2SO_4 > NaCl > NaCl-KCl > KCl which is following the order of value of texture coefficient for polar (0002) plane was No Flux ≈ Na_2SO_4 > NaCl ≈ NaCl-KCl ≈ KCl. DFT (density functional theory) based theoretical studies were also done. Theoretical studies showed that the $(11\bar{2}0)$ surface of ZnO is stabilized more than the $(10\bar{1}0)$ surface in the presence of ionic flux by overcoming the

thermodynamic barrier wherein growth of the $(10\bar{1}0)$ surface is preferred over $(11\bar{2}0)$ surfaces in absence of flux which correlated with the experimental findings.

The third chapter focused on understanding the effect of size, morphology, and exposed facets of $SrTiO_3$ on photocatalytic degradation of RhB dye and the hydrogen evolution activity. Herein, we have synthesized $SrTiO_3$ through the hydrothermal method in the absence and presence of polyols such as ethylene glycol (EG), poly (ethylene glycol)- 300 (PEG-300), and poly (ethylene glycol)-400 (PEG-400). We have observed that the particle size decreased with an increase in the dielectric constant of the solvent (water and polyols). We also observed that the shape of the nanostructures was also affected by the nature of the solvent used during the synthesis (nanocubes with water, nanocuboids with PEG-400, edge-truncated nanocuboids with PEG-300, and hexagonal-shaped particles assembled to form a flower-like nanostructure with EG as solvent). The top exposed facet of the synthesized $SrTiO_3$ nanostructures was observed to be [001] (for $SrTiO_3$ nanostructures synthesized using different solvents). Along with the [001] facet, the $[01\bar{1}]$ facet was also observed in the sample synthesized using EG and PEG-300 as the solvent. Degradation of RhB Dye follows the order EG = water>PEG-300>PEG-400 whereas Hydrogen Evolution follows the order: Water>EG>PEG-300>PEG-400. To understand the photodynamics of charge carriers, we also performed photoluminescence and photo-current studies. Based on experimental observations, we have concluded that the synergistic effect of having maximum surface area, lowest crystallite/particle size, low recombination of photo-generated electron and hole pair, a large value of $I_{photo}/I_{dark,}$ and presence of [001] as the only exposed facet could be the reason for observing the high photocatalytic performance of $SrTiO_3$ nanostructures synthesized in presence of water towards hydrogen evolution reaction. The presence of the $[01\bar{1}]$ facet was found to decrease the photocatalytic hydrogen evolution performance of the catalyst whereas for photodegradation of RhB dye both the facets have active participation.

In the fourth chapter, we concentrated on studying the role of the oriented assembly of $SrTiO_3$ nanostructures (cubic morphology) over a glass substrate on the photocatalytic hydrogen evolution reaction. Assemblies of the $SrTiO_3$ nanostructures on a glass substrate were formed by coating $SrTiO_3$ on a glass substrate under different conditions where IPTMS was used as a linker between the glass substrate and $SrTiO_3$ nanostructures. The orientation of $SrTiO_3$ nanostructures

was checked from the PXRD study. Based on the highest intensity of the crystal plane in the PXRD.

It was observed that the (200) plane was the exposed plane for the assembled nanostructures. High coverage and a uniform layer were observed from the FESEM study for the assembly of $SrTiO_3$ nanostructures formed by depositing non-functionalized oxide on the functionalized glass substrate. Photocatalytic hydrogen evolution was checked on oriented assembly of $SrTiO_3$ nanostructures. Photocatalytic hydrogen evolution performance was found to be highest when the assembly of non-functionalized $SrTiO_3$ nanostructures on the functionalized glass substrate with (200) as the exposed plane was used as the catalyst.

In the fifth chapter, we have established the relation between crystal structure, property, and photocatalytic hydrogen evolution activity of the three members of the Sr-Ti-O system viz. $SrTiO_3$ and $SrO\text{-}(SrTiO_3)_n$ (n= 1 and 2). $SrTiO_3$ belonged to a class of cubic perovskite nanostructure while Sr_2TiO_4 (n=1) and $Sr_3Ti_2O_7$ (n=2) belonged to layered Ruddlesden-Popper based perovskite oxides. A cube-shaped morphology was observed for cubic perovskite nanostructure, $SrTiO_3$ whereas layered morphology was observed for Ruddlesden-Popper based oxides, Sr_2TiO_4, and $Sr_3Ti_2O_7$. Amongst the three nanostructured oxides, the maximum amount of hydrogen was evolved with $Sr_3Ti_2O_7$ as the photocatalyst. These results were explained based on photoluminescence, time-resolved photoluminescence, and Photoelectrochemical study. Synergism of many factors, including the presence of SrO layer, $SrTiO_3$ perovskite unit, layered morphology, and defects, is attributed to the observed photocatalytic performance of the Ruddlesden-popper structure in comparison to cubic perovskite $SrTiO_3$.

In the sixth chapter, we demonstrated the role of crystal structure and electrical polarization in electrochemical oxygen evolution reaction (OER). This effect was studied using the Bi-Fe-O system as a case study. Herein, we synthesized three structures of the Bi-Fe-O system viz. $BiFeO_3$ (perovskite structure), $Bi_2Fe_4O_9$ (mullite structure), and $Bi_{25}FeO_{40}$ (sillenite structure). Rietveld refinement studies was done on these three oxides. We observed that the order for OER activity (using a non-polarized catalyst) of the three stable structures synthesized was $Bi_2Fe_4O_9$ > $BiFeO_3$> $Bi_{25}FeO_{40}$, which was attributed to the presence of $Fe_{(oct)}$-O-$Fe_{(td)}$ linkages in $Bi_2Fe_4O_9$ along with plate-like morphology. After electrical polarization, the OER activity of $Bi_{25}FeO_{40}$ is observed to increase by a factor of four whereas the current density of $Bi_2Fe_4O_9$ and $BiFeO_3$

remained unchanged which could be due to the presence of more number of $6s^2$ lone pairs in $Bi_{25}FeO_{40}$.

In summary, we have successfully studied the role of various factors viz, morphology, exposed facets, crystal structure, orientation, and electrical polarization on the photo and the electrocatalytic performance of the binary and ternary metal oxide. We believe that the study carried out in the thesis would further help one in designing the materials for the desired application.

7.2 Future Prospects:

On the basis of work done in the thesis, the following recommendations can be made for further studies:

i. In the thesis, we have discussed the role of exposed surfaces or facets on photocatalytic activity. Though major advances have been accomplished in the facet engineering field to design a highly efficient catalyst for photocatalysis, still it remains a big challenge to fully utilize this technique for photocatalysis. The major challenge is to control the material's facets in the case of hybrid systems and ternary oxides which involves multiple components. In our opinion, there is still a limitation in synthetic technique as morphology controlling agents such as capping agents, ligands and surfactants are involved in the synthesis. The existence of the ligands and capping agents on the surface of the material would affect the quality of faceted structures. Furthermore, more characterization techniques should be implemented to understand the mechanism of charge transfer kinetics in facet dependent photocatalysis. Also, theoretical simulation and modelling would guide in designing the faceted structures for photocatalysis. Thus, simultaneous efforts on the precise synthesis, use of advanced characterization (such as HAADF-STEM) techniques and theoretical calculations (DFT) would further help in establishing the relationship between faceted structures and photocatalytic activity.

ii. In the fourth chapter of the thesis, the effect of oriented assemblies was studied on the photocatalytic hydrogen evolution activity. Here we have used a glass slide as a substrate

for the formation of oriented assemblies of nanostructures. In our opinion, different kinds of substrates can be used for the formation of different assemblies such as silicon substrates. Also, different linkers such as APTMS (amino-propyl trimethoxy silane) and APTES (amino-propyl trimethoxy silane) could be used instead of IPTMS.

iii. Here, we have demonstrated the role of crystal structure in enhancing photocatalytic hydrogen evolution. Ruddelsden-popper structures were proved to be an efficient catalyst for photocatalysis due to their layered crystal structure where the interlayer allows intercalation of ions and water molecules. Intercalation of ions such as oxyalkyl ions in interlayer space would increase the distance between the layers which further improves the photoinduced charge separation. Therefore, doping of the metal cation either at the A site or B site or co-doping at both the sites would further improve the charge separation as charge carriers would not be expected to cross the different layers which further reduces the number of defects in the structure. Also, the utilization of solar energy instead of using commercial lamps would further reduce the cost of hydrogen production. The optical properties of Ruddelsden-popper structures should be studied deeply with the femtosecond spectroscopy technique. Thus, the proper choice of crystal structure through the theoretical predictions and further modification of them would be a constructive strategy for improving photocatalytic activity.

iv. Role of crystal structure in enhancing the electrocatalytic oxygen evolution has also been discussed in the thesis along with the application of an external electric polarization. In recent past years, serious efforts have been made in reducing the overpotential of the oxygen evolution catalyst. As the OER properties are closely related to the electronic spin states of the electrocatalyst. Therefore, understanding the mechanism of OER on different crystal and electronic structures of transition metal system is important. The role of the external magnetic field on OER can be investigated along with the electric field as it would impact charge transfer and conducting properties of the catalyst.

List of publications from the Thesis:

1. ***Aditi Vijay***, K.V. Ramanujachary, Samuel E. Lofland, Sonalika Vaidya*, Role of crystal structure and electrical polarization of an electrocatalyst in enhancing oxygen evolution performance: Bi-Fe-O system as a case study *Electrochimica Acta*, Volume 407,**2022**,139887.
2. ***Aditi Vijay*** and Sonalika Vaidya*, Tuning the Morphology and Exposed Facets of $SrTiO_3$ Nanostructures for Photocatalytic Dye Degradation and Hydrogen Evolution, *ACS Applied Nanomaterials.* **2021**, 4, 4, 3406–3415.
3. ***Aditi Vijay,*** Aritra Mukhopadhyaya, Vipul Shrivastava, Devanshi Bhardwaj, Ashok K. Ganguli, Md. Ehesan Ali and Sonalika Vaidya*, Understanding the role of ionic flux on the polarity of the exposed surfaces of ZnO, *Physical Chemistry Chemical Phys*ics, **2020**,22,15427-15436.
4. ***Aditi Vijay***, Kadambari Bairagi, Sonalika Vaidya*Relating Structure, Property and Activity of nanostructured $SrTiO_3$ and SrO-($SrTiO_3$) n (n= 1 and 2) for Photocatalytic Hydrogen Evolution. (accepted in Material Advances)
5. ***Aditi Vijay***, Shanmuga Priya S, Santanu Pal, Sonalika Vaidya*, Role of oriented assemblies of $SrTiO_3$ along (200) plane on the glass substrate in enhancing Photocatalytic hydrogen evolution activity. (manuscript under preparation).

List of publications other than thesis

1. ***Aditi Vijay***, Ashwinder Kaur, Sonalika Vaidya*, Synergistic role of model-independent and model-dependent approaches for determining size and shape of Au nanostructures using SAXS, Part. Part. Syst. Charact. **2022**, 2100285.

2. Zakiullah Zaidi, Kalpesh Vaghasiya, ***Aditi Vijay***, Manu Sharma, Rahul Kumar Verma & Sonalika Vaidya*, Hollow ZnO from the assembly of nanoparticles: photocatalytic and antibacterial activity, J Mater Sci, 53, **2018**,14964–14974.

List of conferences attended

❖ *Poster Presentation*

1. Poster Presentation at ICONSAT, 2020, held at SN Bose Institute of Basic Sciences, Kolkata

   Effect of chain length of polyols and influence of flux on the photocatalytic performance of metal oxides, ***Aditi Vijay***, Sonalika Vaidya
2. Poster Presentation at ICONSAT, 2018, held at IISC, Bengaluru

   Small-angle X-ray scattering studies of gold nanostructures**, *Aditi Vijay,*** Sonalika Vaidya
3. Poster Presentation at MRSI National Symposium, 2018

   Photocatalytic Activity of metal oxide nanoparticles, ***Aditi Vijay***, Vipul Srivastava, Zakiullah Zaidi, Sonalika Vaidya
4. **Best Poster Award at Crick Chemistry Symposium, 2019**

   Effect of water intake capacity and ionic strength on the Reverse Micellar System: A SAXS Study, ***Aditi Vijay***, Jasveer Kaur, Sonalika Vaidya

❖ *Oral Presentation*

1. Oral Presentation at 1st Research scholar day, 2021, held at INST Mohali on Self-Assembled Metal Oxide structures for Environmental and Energy application.

2. Oral Presentation at 1st Annual Meeting of School of Energy and Environment Unit, Chem@Nano '21, 2021, held at INST Mohali on Sr-Ti-O based structures for Photocatalytic Hydrogen Evolution Reaction.

3. Oral Presentation at Two days international e-conference on "Recent Advancements in Chemical Sciences: Health, Environment and Society" being organized by the Department of Chemistry, Deshbandhu College, University of Delhi on 8th & 9th April 2022 on Role of Crystal Structure and electrical Polarization in enhancing Electrochemical Oxygen Evolution Performance in Bi-Fe-O system.

CCC Marketplace™

Order Confirmation

Thank you, your order has been placed. An email confirmation has been sent to you. Your order license details and printable licenses will be available within 24 hours. Please access Manage Account for final order details.

This is not an invoice. Please go to manage account to access your order history and invoices.

CUSTOMER INFORMATION

Payment by invoice: You can cancel your order until the invoice is generated by contacting customer service.

Billing Address

Mrs. aditi vijay
1613
phase-10
sector-64
Mohali, Punjab 160062
India

+91 8744823755
aditi.vijay1991@gmail.com

Customer Location

Mrs. aditi vijay
1613
phase-10
sector-64
Mohali, Punjab 160062
India

PO Number (optional)

N/A

Payment options

Invoice

PENDING ORDER CONFIRMATION

Confirmation Number: Pending

Order Date: 04-May-2022

1. Physical chemistry chemical physics

0.00 USD

Article: Understanding the role of ionic flux on the polarity of the exposed surfaces of ZnO.

Special Terms Apply

Order License ID	Pending	**Publisher**	ROYAL SOCIETY OF CHEMISTRY
ISSN	1463-9084		
Type of Use	Republish in a thesis/dissertation	**Portion**	Chapter/article

LICENSED CONTENT

Publication Title	Physical chemistry chemical physics
Article Title	Understanding the role of ionic flux on the polarity of the exposed surfaces of ZnO.
Author/Editor	Royal Society of Chemistry (Great Britain)
Date	01/01/1999
Language	English
Country	United Kingdom of Great Britain and Northern Ireland
Rightsholder	Royal Society of Chemistry
Publication Type	e-Journal
Start Page	15427
End Page	15436
Issue	27
Volume	22
URL	http://firstsearch.oclc.org/journal=1463-9076;screen=info;ECOIP

REQUEST DETAILS

Portion Type	Chapter/article
Page range(s)	15427-15436
Total number of pages	27
Format (select all that apply)	Print, Electronic
Who will republish the content?	Academic institution
Duration of Use	Life of current edition
Lifetime Unit Quantity	Up to 499
Rights Requested	Main product and any product related to main product
Distribution	Worldwide
Translation	Original language of publication
Copies for the disabled?	No
Minor editing privileges?	Yes
Incidental promotional use?	No
Currency	USD

NEW WORK DETAILS

Title	Investigating the role of Structural Parameters influencing Photocatalytic and Electrocatalytic behaviour of Binary and Ternary Metal Oxides
Instructor name	Dr. Sonalika Vaidya
Institution name	Institute of Nano Science and Technology, Mohali
Expected presentation date	2022-05-06

ADDITIONAL DETAILS

Order reference number	N/A
The requesting person / organization to appear on the license	Aditi Vijay/Institute of Nano Science and Technology, Mohali

REUSE CONTENT DETAILS

Title, description or numeric reference of the portion(s)	Full article and supplementary information	**Title of the article/chapter the portion is from**	Understanding the role of ionic flux on the polarity of the exposed surfaces of ZnO.
Editor of portion(s)	Vijay, Aditi; Mukhopadhyaya, Aritra; Shrivastava, Vipul; Bhardwaj, Devanshi; Ganguli, Ashok; Ali, Md. Ehesan; Vaidya, Sonalika	**Author of portion(s)**	Vijay, Aditi; Mukhopadhyaya, Aritra; Shrivastava, Vipul; Bhardwaj, Devanshi; Ganguli, Ashok; Ali, Md. Ehesan; Vaidya, Sonalika
Volume of serial or monograph	22	**Issue, if republishing an article from a serial**	27
Page or page range of portion	15427-15436	**Publication date of portion**	2020-07-21

SPECIAL RIGHTSHOLDER TERMS AND CONDITIONS

Permission is granted as long as the article is fully acknowledged and a link is given back to the article on our Platform. Please go to rsc.li/permissions for details. Please note that if the material specified above or any part of it appears with credit or acknowledgement to a third party then you must also secure permission from that third party before reproducing that material.

Total Items: 1 **Total Due: 0.00 USD**

Accepted: All Publisher and CCC Terms and Conditions

Tuning the Morphology and Exposed Facets of SrTiO3 Nanostructures for Photocatalytic Dye Degradation and Hydrogen Evolution

Author: Aditi Vijay, Sonalika Vaidya
Publication: ACS Applied Nano Materials
Publisher: American Chemical Society
Date: Apr 1, 2021

PERMISSION/LICENSE IS GRANTED FOR YOUR ORDER AT NO CHARGE

This type of permission/license, instead of the standard Terms and Conditions, is sent to you because no fee is being charged for your order. Please note the following:

- Permission is granted for your request in both print and electronic formats, and translations.
- If figures and/or tables were requested, they may be adapted or used in part.
- Please print this page for your records and send a copy of it to your publisher/graduate school.
- Appropriate credit for the requested material should be given as follows: "Reprinted (adapted) with permission from {COMPLETE REFERENCE CITATION}. Copyright {YEAR} American Chemical Society." Insert appropriate information in place of the capitalized words.
- One-time permission is granted only for the use specified in your RightsLink request. No additional uses are granted (such as derivative works or other editions). For any uses, please submit a new request.

If credit is given to another source for the material you requested from RightsLink, permission must be obtained from that source.

BACK CLOSE WINDOW

From the journal:
Materials Advances

Relating Structure, Property and Activity of nanostructured SrTiO3 and SrO-(SrTiO3)n (n= 1 and 2) for Photocatalytic Hydrogen Evolution

Aditi Vijay , Kadambari Bairagi and Sonalika Vaidya

Abstract

This study focuses on relating the structure with their properties and activity and carries out a comparative study amongst the three members of the Sr-Ti-O system for photocatalytic hydrogen evolution. The three oxides focused in this study are based on perovskite structure viz. SrTiO3 and SrO-(SrTiO3)n (n= 1 and 2). We have successfully synthesized these three oxides through a methodology that combined the polymeric citrate precursor method with the hydrothermal method. Their crystal structure, morphology, and optical properties (absorption, and photoluminescence) were systematically explored. SrTiO3 belonged to a class of cubic perovskite while Sr2TiO4 (n=1) and Sr3Ti2O7 (n=2) belonged to layered Ruddlesden-Popper based perovskite oxides. We observed cube-shaped morphology for nanostructured SrTiO3 and layered morphology for Ruddlesden-Popper based oxides, Sr2TiO4 and Sr3Ti2O7. The photocatalytic hydrogen evolution performance of these nanostructured oxides was investigated. Amongst the three nanostructured oxides, the maximum amount of hydrogen was evolved with Sr3Ti2O7 as the photocatalyst. These results were supported by photoluminescence, time-resolved photoluminescence, and Photoelectrochemical study.

Relating Structure, Property and Activity of nanostructured SrTiO3 and SrO-(SrTiO3)n (n= 1 and 2) for Photocatalytic Hydrogen Evolution

A. Vijay, K. Bairagi and S. Vaidya, *Mater. Adv.*, 2022, Accepted Manuscript , **DOI:** 10.1039/D2MA00097K

Search articles by author

- [ ] Aditi Vijay
- [ ] Kadambari Bairagi
- [ ] Sonalika Vaidya

Go

Spotlight

Journals, books & databases

Home

About us

Role of crystal structure and electrical polarization of an electrocatalyst in enhancing oxygen evolution performance: Bi-Fe-O system as a case study

Author: Aditi Vijay,K.V. Ramanujachary,Samuel E. Lofland,Sonalika Vaidya

Publication: Electrochimica Acta

Publisher: Elsevier

Date: 1 March 2022

Journal Author Rights

Please note that, as the author of this Elsevier article, you retain the right to include it in a thesis or dissertation, provided it is not published commercially. Permission is not required, but please ensure that you reference the journal as the original source. For more information on this and on your other retained rights, please visit: https://www.elsevier.com/about/our-business/policies/copyright#Author-rights